

AD-760 799

**PROTOTYPE MOVING BASE GRAVITY
GRADIOMETER**

Charles B. Ames, et al

Hughes Research Laboratories

Prepared for:

**Air Force Cambridge Research Laboratories
Advanced Research Projects Agency**

January 1973

DISTRIBUTED BY:



**National Technical Information Service
U. S. DEPARTMENT OF COMMERCE
5285 Port Royal Road, Springfield Va. 22151**

AD 760799

PROTOTYPE MOVING BASE GRAVITY GRADIOMETER

CHARLES B. AMES, ROBERT L. FORWARD, PHILIP M. LA HUE,
ROBERT W. PETERSON, AND DAVID W. ROUSE

HUGHES RESEARCH LABORATORIES
3011 MALIBU CANYON ROAD
MALIBU, CALIFORNIA 90265

CONTRACT F19628-72-C-0222
PROJECT NO. 1838
TASK NO. 183800
WORK UNIT NO. 18380001
SEMIANNUAL TECHNICAL REPORT NO. 2

JANUARY 1973

CONTRACT MONITOR: BELA SZABO
TERRESTRIAL SCIENCES LABORATORY

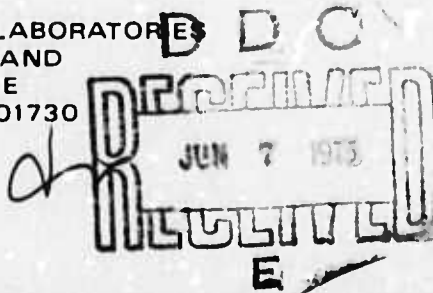
APPROVED FOR PUBLIC RELEASE; DISTRIBUTION UNLIMITED.

Reproduced by
**NATIONAL TECHNICAL
INFORMATION SERVICE**

U.S. Department of Commerce
Springfield VA 22151

Sponsored by
ADVANCED RESEARCH PROJECTS AGENCY
ARPA NO.1838

Monitored by
AIR FORCE CAMBRIDGE RESEARCH LABORATORIES
AIR FORCE SYSTEMS COMMAND
UNITED STATES AIR FORCE
BEDFORD, MASSACHUSETTS 01730



UNCLASSIFIED

Security Classification

DOCUMENT CONTROL DATA - R&D

(Security classification of title, body of abstract and indexing annotation must be entered when the overall report is classified)

1. ORIGINATING ACTIVITY (Corporate author)

Hughes Research Laboratories
3011 Malibu Canyon Road
Malibu, California 90265

2a. REPORT SECURITY CLASSIFICATION

Unclassified

2b. GROUP

N/A

3. REPORT TITLE

PROTOTYPE MOVING BASE GRAVITY GRADIOMETER

4. DESCRIPTIVE NOTES (Type of report and inclusive dates)

Scientific Interim

5. AUTHORISI (First name, middle initial, last name)

Charles B. Ames	Robert W. Peterson
Robert L. Forward	David W. Rouse
Philip M. LaHue	

6. REPORT DATE

January 1973

7a. TOTAL NO. OF PAGES

416 448

7b. NO. OF REPS

5

8a. CONTRACT OR GRANT NO. ARPA Order No.
F19628-72-C-0222 1838

8a. ORIGINATOR'S REPORT NUMBER(S)

Semiannual Technical Report No. 2

8b. PROJECT, TASK, WORK UNIT NOS.

1838-00-01

8b. OTHER REPORT NO(S) (Any other numbers that may be assigned this report)

c. DOD ELEMENT

62701D

AFCRL-TR-73-0141

d. DOD SUBELEMENT

10. DISTRIBUTION STATEMENT

Approved for public release; distribution unlimited.

11. SUPPLEMENTARY NOTES

This research was supported by the Defense Advanced Research Projects Agency

12. SPONSORING MILITARY ACTIVITY

Air Force Cambridge Research Laboratories (LW)
L.G. Hanscom Field
Bedford, Mass 01730

13. ABSTRACT

This report covers the technical studies accomplished during the second six months of this contract to design and develop a prototype moving base gravity gradiometer with a sensitivity of better than 1 EU (10^{-9} sec 2) for a 10 sec integration time. Since the end of this second report period coincided with the end of the first phase of the contract, this report is a complete summary of the Phase I design and analysis work. The report is self-contained in that all material pertinent to the analytical and design phase is contained herein with the exception of references to certain specific sections in the previous Semiannual Technical Report (August 1972).

The selected rotating gravity gradiometer (RGG) baseline design has an arm length and inertia of 12 cm and 35,600 gm-cm 2 , and an overall size and weight of 22 cm by 16 cm dia. and 9.6 kg. The sensor spin speed is 1050 rpm (17.5 rps), which is compatible with the sensor resonant frequency of 35 Hz with a Q of 300. These parameters, in turn, determine the sensor time constant to be 2.71 sec; the remainder of the system integration time (7.29 sec) is determined by the data processing filtering.

In the fully integrated RGG prototype design, we have chosen: hydrodynamic oil spin bearings; asynchronous drag cup motor drive with photoelectric position and tachometer speed pickoffs; mechanically isolated piezoelectric transducer; similarly shaped isolastic interlaced double-strut sensing arms; electrolytic fine balance adjustment; multiple torsion bar supports formed from a single rod; internal AM-FM conversion with external power supply; air core transformer data feedthrough; external FM-digital conversion; digital plus analog data reduction; and solid mounting of the sensor case to the stable element of the angular isolation platform.

In addition to the gradiometer design studies, the report contains specifications for a vibration isolation, alignment and leveling system (VIALS) for support of the gradiometers during use. For the vehicle and mission we assumed a C-135 carrying out an airborne gravity survey. The components of a VIALS that would meet the system performance specifications are shown to be state-of-the-art components.

An extensive error analysis was carried out on the various error terms introduced by the assumed environment, the VIALS, and the gradiometer itself. The estimated errors from all sources are shown to be less than 0.65 EU for a 10 sec integration time, which is well within the design goal.

We can report achievement of our goals for this study phase. The sensor design is complete, and we are proceeding into the engineering phase where detailed drawings will be prepared prior to fabrication and laboratory test of the first prototype.

UNCLASSIFIED

Security Classification

14. KEY WORDS	LINK A		LINK B		LINK C	
	ROLE	WT	ROLE	WT	ROLE	WT
Gravity gradiometer						
Gravitational mass sensor						
Gravitational gradient sensor						
Gravity mapping						
Mass detection						
Navigation						
Inertial guidance						
Airborne gradiometer						
Vertical deflection						
Motion isolation and stabilization						

1b

UNCLASSIFIED

Security Classification

AFCRL-TR-73-0141

PROTOTYPE MOVING BASE GRAVITY GRADIOMETER

by

Charles B. Ames
Robert L. Forward
Philip M. LaHue
Robert W. Peterson
David W. Rouse

HUGHES RESEARCH LABORATORIES
3011 Malibu Canyon Road
Malibu, California 90265

Contract F19628-72-C-0222

Project No. 1838
Task No. 183800
Work Unit No. 18380001

Semiannual Technical Report No. 2

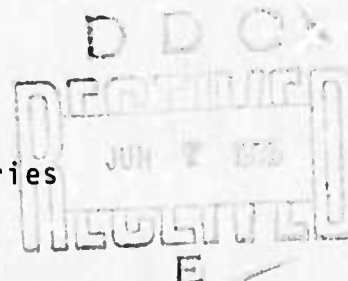
January 1973

Contract Monitor: Bela Szabo
Terrestrial Sciences Laboratory

Approved for public release; distribution unlimited

Sponsored by
Advanced Research Projects Agency
ARPA No. 1838

Monitored by
Air Force Cambridge Research Laboratories
Air Force Systems Command
United States Air Force
Bedford, Massachusetts 01730



IC

ARPA ORDER No. 1838

Program Code No. 1F10

Contractor: Hughes Aircraft Company

Effective Date of Contract: 1 February 1972

Contract No. F19628-72-C-0222

Principal Investigator and Phone No.

Dr. Robert L. Forward, (213)456-6411

AFCRL Project Scientist and Phone No.

Mr. Bela Szabo, (617)861-3654

Contract Expiration Date: 31 March 1974

Qualified requestors may obtain additional copies from the Defense Documentation Center. All others should apply to the National Technical Information Service.

TABLE OF CONTENTS

	LIST OF ILLUSTRATIONS	ix
I	INTRODUCTION	1
II	SENSOR DESIGN INTEGRATION	7
III	STATEMENT OF WORK COMPLIANCE	15
A.	Line Item 0001	15
B.	Sub-Line Item 0001AA	16
C.	Sub-Line Item 0001AB	17
D.	Sub-Line Item 0001AC	17
E.	Sub-Line Item 0001AD	18
F.	Sub-Line Item 0001AE	18
IV	RGG CONFIGURATION SELECTION SUMMARY	19
A.	Configuration A - Neutrally Buoyant Rotating Sphere	20
B.	Configuration B - Two-Axis Air Bearing Gimbal	20
C.	Configuration C - Restrained Tetrahedron Air Pads	21
D.	Configuration D - Direct Mounted Sensor	21
E.	Tradeoff Comparisons	21
F.	Conclusion	23
V	RGG PROTOTYPE DESIGN SUMMARY	25
A.	Tabulation of Design Parameters	25
B.	RGG Drawing	25
C.	Semiannual Technical Report No. 1	34
D.	Prototype Moving Base Gravity Gradiometer Proposal	34

VI	ERROR ANALYSIS SUMMARY	35
	A. Brief Error Descriptions	35
VII	CONFIGURATION SELECTION RATIONALE	43
	A. General	43
	B. Pertinent Design Goals	43
	C. Angular Isolation Requirements	45
	D. Sensor Configurations Studied	46
	E. Trade-Off Comparisons of Alternate Configurations	59
	F. Conclusion	67
VIII	VIBRATION ISOLATION, ALIGNMENT AND LEVELING SYSTEM (VIALS) REQUIREMENTS	71
	A. General	71
	B. Worst Case Environment	72
	C. VIALS Requirements for Prototype RGG Sensor	72
	D. Basis for VIALS Requirements	80
	E. Vibration Isolation Mount Design Considerations	84
	F. Stable Platform Design Considerations . .	87
	G. Anisoelastic Compensation Accelerometers	100
IX	ERROR ANALYSIS	105
	A. Arm Mass Unbalance Errors	105
	B. Phase Error Propagation in the RGG . . .	117
	C. Transducer Load Study Thermal Noise . . .	126
	D. Rotational Field Errors	134
	E. Sum-Mode Mismatch Errors	146

F.	Anisoelastic Errors	151
G.	Platform Orientation Error Propagation	180
X	SENSOR ROTOR DESIGN	187
A.	Description	187
B.	Stiffness, Mass, and Inertia Calculations	189
XI	SENSOR STATOR DESIGN	191
A.	General	191
B.	Stiffness, Mass and Inertia Calculations . .	192
XII	SPIN BEARINGS	193
A.	Bearing Candidates	194
B.	Bearing Selection	194
C.	Prototype Bearing Design	195
XIII	SENSOR ARM DESIGN	199
A.	General	199
B.	Form-Factor Tradeoffs	200
C.	Arm, Mass, and Inertia Efficiency	201
D.	Isoelastic Arm Design	207
E.	Arm Design Characteristics	210
F.	Operational Anisoelastic Error Coefficient	210
XIV	PIVOTS AND TRANSDUCER DESIGN	221
A.	General	221
B.	Pivots, Arm Support	225
C.	Piezoelectric Transducers	228
D.	Sensor Thermal Sensitivity	251
E.	Transducer Mounting Structure	272

XV	ROTOR POWER SUBSYSTEM	273
XVI	ROTOR SPEED CONTROL SUBSYSTEM	275
	A. General	275
	B. Speed Control Servo	275
	C. Spin Motor/Tachometer	278
	D. Frequency Reference	285
	E. Position Pickoff	286
XVII	REMOTE ARM BALANCE SUBSYSTEM	291
	A. General	291
	B. Mass Transport Devices	293
	C. Vibration Driver	298
	D. Sensor Test Signal	299
XVIII	TEMPERATURE CONTROL SUBSYSTEM	303
	A. Temperature Control Requirements on Critical Components	303
	B. Thermal Model	303
	C. Transient Analysis Results	308
	D. Subsystem Specifications	313
	E. Conclusions	315
	F. Recommendations	316
XIX	SIGNAL READOUT SUBSYSTEM	317
	A. General Description	317
	B. Rotor Mounted Electronics Size Estimates	319
XX	ANALOG DATA REDUCTION SUBSYSTEM	321

XXI	DIGITAL DATA REDUCTION SUBSYSTEM	323
A.	General	323
B.	FM Signal Decoding	324
C.	Rotor Position	327
D.	Anisoelastic Compensation	328
E.	Computer Interface and Specification . .	329
XXII	PHASE II DIGITAL SYSTEM BENEFITS	333
A.	Computational Requirements Coordination	333
B.	Digital Rotor Speed Control	333
C.	Active Compensation of the RGG	334
XXIII	RGG CALIBRATION TECHNIQUES	337
A.	Bias Adjustment and Anisoelastic Coefficient Determination	337
B.	Scale Factor Calibration	338
C.	Arm Mass and Inertia Balancing	338
D.	Rotor Mass Balancing	340
XXIV	LABORATORY EXPERIMENTS	341
A.	Vibration Sensitivity Measurements . . .	341
B.	Analysis of Gradient Strain Level . . .	341
C.	Analysis of Transducer Mismatch	344
D.	Tension-Compession Due to Axial Acceleration	345
E.	Analysis of Congruent Arm Mass Unbalance Effects	350
	REFERENCES	355

APPENDIX A - Sensor Arm Anisoelastic Deflection Analysis	357
APPENDIX B - Estimation of Upper Bound of Stable Platform Angular Rate	365
APPENDIX C - Spin Motor Specification	371
APPENDIX D - Spin Bearing Design Specification	387

LIST OF ILLUSTRATIONS

FIGURE		PAGE
I-1	Rotating Gravity Gradiometer Cross-Section View	4
II-1	System Breakdown Structure	8
V-1	Layout of RGG Prototype Design	27
VII-1	Configuration A	48
VII-2	Configuration B	55
VII-3	Configuration B	56
VII-4	Configuration C	57
VII-5	Restraint System Schematic For Tetrahedron Air Pad Sensor Configuration C	58
VIII-1	Acceleration Power Spectra	73
VIII-2	Angular Rate Power Spectrum	74
VIII-3	Acceleration Power Spectra	82
VIII-4	Angular Rate Power Spectrum	83
VIII-5	Six-Element Axisymmetric Linkage Air Column Vibration Isolation Mount	86
VIII-6	Hipernas IIB IRU Specification	89
VIII-7	Three-Axis Air Bearing Stabilizer Platform	99
VIII-8	Estimated Platform Angular Rate Response to Normalized Torque Disturbance	119
IX-1	Equivalent Block Diagram of Signal Process	128
IX-2	Equivalent Circuit of Signal Sensing and Transducing Process	133

IX-3	Standard Deviation Cross Gradient Thermal Noise (θ_{ij}) Versus Effective Q	133
IX-4	An Assumed Probability Density Function	145
XII-1	Spin Bearing Final Design Cross- Sectional View	197
XIII-1	Solid Bar Structure of Rectangular Cross Section	202
XIII-2	Arm Configuration A	202
XIII-3	Arm Configuration B	203
XIII-4	Arm Configuration - Interleaved	204
XIII-5	Arm Inertia Parameter Versus Width to Radius Ratio	206
XIII-6	Arm Mass With Added Cylindrical Sector Portion	208
XIII-7	Prototype RGG Isoelastic Arm Design	211
XIV-1	RGG Sensor-Transducer Equivalent Circuit	222
XIV-2	Sensor Computer Program	226
XIV-3	Voltage and Phase of Sensor- Transducer Output Voltage	227
XIV-4	Axis Definition for Piezoelectric Ceramics	230
XIV-5	Piezoelectric Bender Transducer	233
XIV-6	Moment and Shear Diagram for One Type of Transducer Loading	235
XIV-7	Moment and Shear Diagram for Second Type of Transducer Loading	237
XIV-8	Equivalent Circuits for Piezoelectric Bender Transducers With Interrelating Equations	240

XIV-9	RGG Sensor Equivalent Circuit	243
XIV-10	Piezoelectric Transducer Computations	247
XIV-11	Piezoelectric Bender Transducer, Series Polarized	248
XIV-12	Computer Program to Evaluate RGG Sensor Temperature Sensitivity	258
XV-1	Rotor Power Subsystem	274
XVI-1	Functional Block Diagram of Servo	277
XVI-2	Speed Control Servo Gain Versus Phase	279
XVI-3	Speed Control Servo Error Response	280
XVI-4	Encoder Disk	289
XVII-1	Remote Arm Balance Subsystem	292
XVII-2	Mass Balance Device	295
XVII-3	Mass Balance Device Mounting	296
XVII-4	Test Signal Generator, Schematic and Waveforms	302
XVIII-1	Thermal Model	304
XVIII-2	Hughes TAP-3 Thermal ANalysis Program	306
XVIII-3	Node 12 Temperature Curve	309
XVIII-4	Node 12 Temperature Curve Without Boundary Temperature Fluctuation	310
XVIII-5	Lower Heater Power Curve With Lower Control Temperature	311
XVIII-6	Oil Film Temperature	312
XVIII-7	Plot of Control Temperature During 10th Operation Hour	314

XIX-1	Signal Readout Subsystem Schematic Diagram	318
XIX-2	Full Scale Mockup of Rotor Mounted Electronics	320
XXI-1	Encoder Disk	325
XXI-2	AM to FM and Signal Counter Switching	326
XXI-3	Minicomputer and I/O For RGG Prototype Design	330
XXIV-1	Sensor Model - Axial Acceleration Effect	345

GLOSSARY OF TERMS

a = acceleration; meters/sec², ft/sec², cm/sec²

a_g = gravitational acceleration at the surface of the earth

A_{xx} = moment of inertia of a body about the x axis

A = constant (s); ampere; compliance

Å = Angstrom unit = 10⁻⁸ cm

A_{ij} = generalized second rank tensor

B = compliance

B_{yy} = moment of inertia of a body about the y axis

B_N = noise bandwidth

C = capacitance, farad

c = Viscous damping, dyne cm/rad/sec; or compliance
1/K of a mechanical system

cm = centimeters

C = compliance

C_{zz} = moment of inertia of a body about the z axis

d = diameter; dynes force; pendulosity distance

dcm = dyne centimeter

D = viscous damping

EU = Eötvos Unit = 10⁻⁹ sec⁻² = 10⁻⁹ (ft/sec²)/ft
= 10⁻⁹ gal/cm \cong 10⁻¹² g's/cm

e_o = temperature coefficient of modulus of elasticity

e, Δe = mass center eccentricity

E = Young's modulus of elasticity

f = force; dyne; newton (10⁵ dynes = 1 newton);
pounds; frequency

ft = foot

GLOSSARY

F = force; a parameter in surface tension equations; farad

g = earth's gravity

g = 32.1724 ft/sec^2
= 980.616 cm/sec^2
 $\approx 10^6$ milligals

gal = (Galileo) unit of acceleration = 1 cm/sec^2

gm = grams

G = Newtonian gravitational constant
= $6.67 \times 10^{-11} \text{ m}^3/\text{kg sec}^2$ = $34.4 \times 10^{-9} \text{ ft}^4/\text{lb-sec}^4$
= $6.67 \times 10^{-8} \text{ cm}^3/\text{gm sec}^2$

G = shear modulus

GG = gravity gradient

G_{ij} = gravity plus inertial gradient tensor

hr = hours

Hz = Hertz (2π radians/sec)

H = transmittance function; angular momentum; inductance in henry; transfer function

h = Planck's constant, mass unbalance distance

I = moment of inertia

I_N = noise current

I = in-phase subscript

j = imaginary operator

J = polar moment of inertia; joule

$^\circ\text{K}$ = degrees Kelvin

k = Boltzmann Constant = 1.38062×10^{-23} joule/ $^\circ\text{K}$
= 1.38062×10^{-16} ergs/ $^\circ\text{K}$

$kT_{290^\circ\text{K}}$ = $kT_{17^\circ\text{C}}$ = 4×10^{-14} ergs = 4×10^{-21} joules

GLOSSARY

kg = kilogram

K, k = constant; or spring stiffness; or torsional stiffness

lb = unit of force

l = length; or separation between masses

L = torque

M or m = mass or meters

m = meter

M_e = mass of the earth = 5.975×10^{24} kg, 4.08×10^{23} slugs

mgal = milligal = 10^{-3} gal = 10^{-3} cm/sec²

N = newton; piezoelectric transducer coefficient

P = power

P_N = noise power

P_S = signal power

p = pendulosity

pF = picofarads = 10^{-12} farads

P = dm = pendulosity

Q = quality factor of a tuned system

$Q = \frac{I\omega_n}{D} = \frac{\sqrt{IK}}{D} = \frac{\omega_n}{2\tau} = \frac{1}{2\xi} = \frac{\pi}{\delta} = 2\pi$ times peak
energy stored in sensor/(energy dissipated per cycle)

Q = quadrature phase subscript

R or r = radius

R = Radius of the earth (mean) = 2.09×10^7 ft

RGG = Rotating Gravity Gradiometer

rad = radian

GLOSSARY

r = radius of sensor arm
R_g = radius of gyration
S = Laplace transform differential operator, power spectral density
s = second
S_{ij} = rotation matrix
t = time in seconds; t₁, t₂ - t₁ = time index points or intervals
T = temperature, °C, °K or °F, torque
T_s = time of signal
T_o = time of absence of signal
T_{ave} = averaging time
T_{int} = integration time
V = volts, velocity, volume
W = watt
XYZ, x, y, z = used to designate coordinate systems

GREEK CHARACTERS

α = angle; angular acceleration; thermal coefficient of expansion; generalized mode coordinate.
β = angle, angular rate, sum-mode resonant frequency
 $\Gamma = \frac{GM}{R^3}$ in general
 Γ_e = gradient error
 $\Gamma_{eq} = \frac{3GM}{R^3}$ = equivalent gradient

GLOSSARY

Γ_{ij} = gravitational force gradient

η = inertia efficiency ratio $\frac{B_{yy} - A_{xx}}{C_{zz}}$

ν = frequency; Poisson's ratio

ϕ = gravitational potential; phase angle

Φ = rotation matrix; inertial tensor

θ = angle; radians or degrees

Θ = rotation matrix

τ = time constant

λ = wavelength

ψ = angle, compliance tensor

Ψ = rotation matrix

ω = angular rate or natural frequency

ζ = damping ratio = $\frac{\text{actual damping}}{\text{critical damping}}$

μ = micro; magnetic permeability

μF = microfarads = 10^{-6} farads

γ = surface tension, cynes/cm, eccentricity ratio

γ_{ij} = anomalous gradient tensor

δ = $\Delta f/f_0$, ratio of frequency change to resonant frequency;
differential angle between sensor arms

ρ = density

$\bar{\rho}$ = transport angular rate

Ω = Earth's angular rate; natural frequency; ohms

ϑ = angle, radians or degrees

Δ = increment or difference

GLOSSARY

δ = angle

ϵ = gyro drift rate, bearing anisoelasticity

σ = standard deviation

MATHEMATICAL SYMBOLS

= equal to

\triangleq equal to by definition

\equiv identically equal to

\approx approximately equal to

∇ del or nabla, differential vector operator

PREFIXES

The names of multiples and submultiples of SI Units may be formed by application of the prefixes:

Factor by which unit is multiplied	Prefix	Symbol
10^{12}	tera	T
10^9	giga	G
10^6	mega	M
10^3	kilo	k
10^2	hecto	h
10	deka	da
10^{-1}	deci	d
10^{-2}	centi	c
10^{-3}	milli	m
10^{-6}	micro	μ
10^{-9}	nano	n
10^{-12}	pico	p
10^{-15}	femto	f
10^{-18}	atto	a

GLOSSARY

PIEZOELECTRIC SYMBOLS

(See Section XIV.)

ABSTRACT

This report covers the technical studies accomplished during the second six months of this contract to design and develop a prototype moving base gravity gradiometer with a sensitivity of better than 1 EU (10^{-9} sec $^{-2}$) for a 10 sec integration time. Since the end of this second report period coincided with the end of the first phase of the contract, this report is a complete summary of the Phase I design and analysis work. The report is self-contained in that all material pertinent to the analytical and design phase is contained herein with the exception of references to certain specific sections in the previous Semi-annual Technical Report (August 1972).

The selected rotating gravity gradiometer (RGG) baseline design has an arm length and inertia of 12 cm and 35,600 gm·cm 2 , and an overall size and weight of 22 cm by 16 cm diameter, and 9.6 kg. The sensor spin speed is 1050 rpm (17.5 rps), which is compatible with the sensor resonant frequency of 35 Hz with a Q of 300. These parameters, in turn, determine the sensor time constant to be 2.71 sec; the remainder of the system integration time (7.29 sec) is determined by the data processing filtering.

In the fully integrated RGG prototype design, we have chosen: hydrodynamic oil spin bearings; asynchronous drag cup motor drive with photoelectric position and tachometer speed pickoffs; mechanically isolated piezoelectric transducer; similarly shaped isoelastic interleaved double-strut sensing arms; electrolytic fine balance adjustment; multiple torsion bar supports formed from a single rod; internal AM-FM conversion with external power supply; air core transformer data feed-through; external FM-digital conversion; digital plus analog data reduction; and solid mounting of the sensor case to the stable element of the angular isolation platform.

In addition to the gradiometer design studies, the report contains specifications for a vibration isolation, alignment and leveling system (VIALS) for support of the gradiometers during use. For the

vehicle and mission we assumed a C-135 carrying out an airborne gravity survey. The components of a VIALS that would meet the system performance specifications are shown to be state-of-the-art components.

An extensive error analysis was carried out on the various error terms introduced by the assumed environment, the VIALS, and the gradiometer itself. The estimated errors from all sources are shown to be less than 0.65 EU for a 10 second integration time, which is well within the design goal.

We can report achievement of our goals for this study phase. The sensor design is complete, and we are proceeding into the engineering phase where detailed drawings will be prepared prior to fabrication and laboratory test of the first prototype.

SECTION I

INTRODUCTION

This report presents the culmination of the Phase I work carried out under Contract F 19628-72-C-0222 during the period from 1 February 1972 through 19 January 1973.

The reader will note that Sections IV, V, and VI summarize the configuration selection rationale, the sensor design, and the error analyses. The summaries are intended to provide an overview of the accomplishments without detailed elaboration or references to other material.

The Semiannual Technical Report No. 1, dated August 1972, is included by reference throughout this document to avoid duplication of previous efforts and to reduce the bulk and cost of this report. Thus, these two reports are complementary and are intended not only to meet the contractual requirements but to serve as useful, working documents.

The philosophy of a two-phase program, i. e., study followed by a review and then hardware, generally proves to be very beneficial when the state of the art is being advanced. The work under this contract has reaffirmed this desirability. Phase I has provided the answers to the many tradeoff questions involved in the complex task of designing a new sensor which incorporates the extraordinary capabilities that a moving base gravity gradiometer must possess.

The efforts of this past year have provided visibility in previously unexplored areas. Many problems were uncovered during the early months, but solutions were found. New problem discovery has virtually disappeared in recent months, which attests to the progress

SECTION I

that has been made and the present status of the development. Of course, analyses and studies cannot provide all the answers; any practical program must leave the paper phases at an appropriate time and enter a hardware phase. Only then can an unequivocal statement be made that all problems have been discovered and solutions found.

We can report achievement of our goals for this study phase. The sensor design is complete, and we are ready to proceed into the engineering phase where detailed drawings will be prepared prior to fabrication and laboratory test of the first prototype.

We have met the Statement of Work error-sensitivity design goals. The resulting sensor is a sophisticated, logical design based upon: (1) a great deal of prior analytical and experimental work funded by AFCRL, NASA, and Hughes, and (2) the analytical and design tasks of this first contractual phase. The design is a feasible concept requiring available, or readily obtainable machine tools, test equipment, and test facilities for both manufacture and laboratory testing.

We have retained most of our original sensor concepts, thereby building upon an already proven base of technology. We have utilized the services of specialists in certain relatively narrow fields where it was not cost effective for Hughes to attain new levels of knowledge.

This study phase has reaffirmed the importance of designing a sensor within the context of the total, integrated system. A gradiometer design study cannot be carried out in isolation from considerations of the complete gravity gradient measurement system and its ultimate application. The application sets the desired sensitivity and time constant (these were predetermined by the contract as 1 EU at 10 sec), while the using vehicle determines the environmental conditions. However, the coupling of the sensor design is strongest to the isolation and stabilization platform, and there are many tradeoffs possible between the sensor and platform parameters. We have taken these tradeoffs into consideration during this design phase and discuss them further in Sections VII and VIII.

SECTION I

In summary, the system concept described in this report, and the RGG sensor design, depicted in Fig. I-1 and I-2, are fully justifiable. We are confident that Phase I results reflect very well upon a broad foundation of knowledge and warrant immediate continuation into the hardware phases of this program to construct the first prototype moving base gravity gradiometer.

Figure I-1, next page, is 76% of full-scale cross sectional drawing. The weight is calculated to be 9.6 kg (\approx 21 lb).

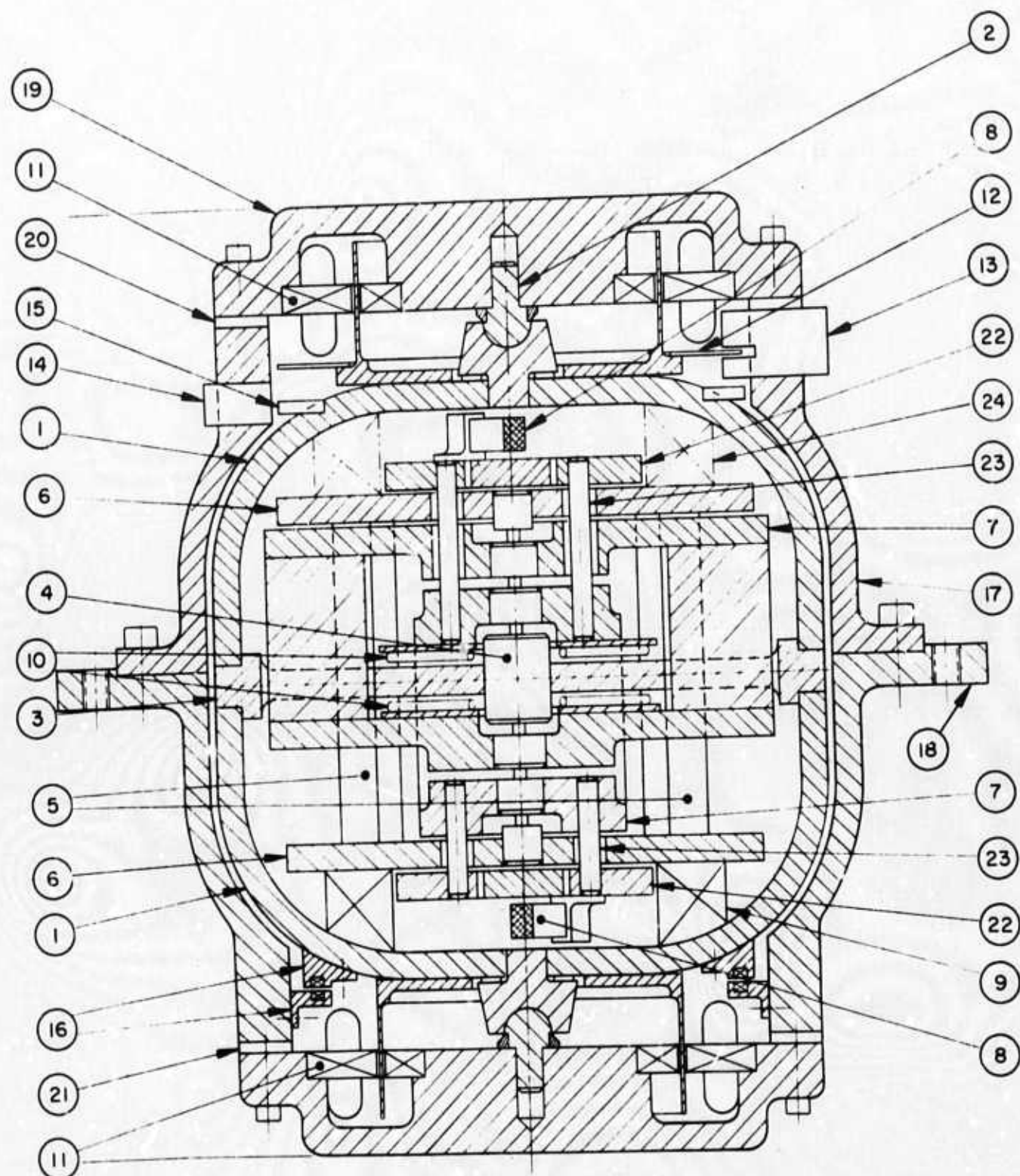


Fig. I-1. Rotating Gravity Gradiometer Cross-Section View
(76% of Full Scale).

SECTION I

ROTATING GRAVITY GRADIOMETER COMPONENT IDENTIFICATION

- (1) Rotor
- (2) Spin bearings
- (3) Circular central plate of rotor
- (4) Pivot assembly
- (5) Brace posts (8 total)
- (6) End plates
- (7) Central assembly and sensor arms
- (8) Piezoelectric transducers
- (9) Rotor electronics
- (10) Mass balance adjusting devices
- (11) Motor/tachometer
- (12) Position encoder disk
- (13) Light source and photo cell
- (14) Second light source
- (15) Photocells (2 ea.)
- (16) FM transmitter output transformer
- (17) Stator
- (18) Mounting bosses
- (19) Motor end cup
- (20) Insulator
- (21) Lapped shim
- (22) Transducer concentric mounting plates
- (23) Transducer assembly mounting posts
- (24) Electronic growth area

M9390

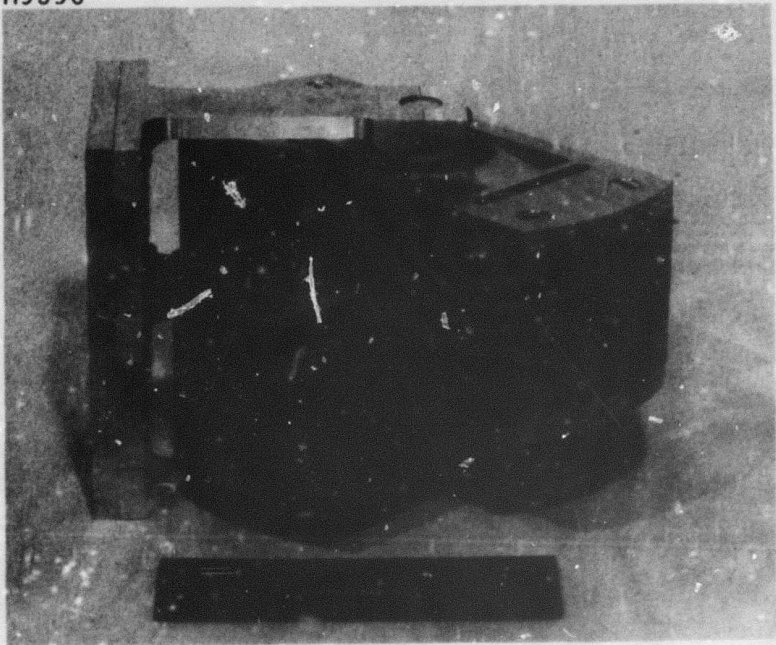


Fig. I-2. Mass Model of Sensor Arm Structure.

SECTION II

SENSOR DESIGN INTEGRATION

A moving base rotating gravity gradiometer measurement system consists of many subsystems; one of these is the Rotating Gravity Gradiometer (RGG), which itself has many subcomponents (see Fig. II-1). All of these subsystems and their interactions must be considered in the design integration task throughout the design phases. Hughes' 8 years of RGG design and test experience has established a number of viable concepts for each of the subcomponents of the RGG. Specific examples of the alternate concepts for some of the major subsystems in the gradiometer are shown in Table II-1. All of these alternate concepts were considered many times during this program.

Before a sensor baseline design could be evaluated, a set of basic parameters had to be selected. These basic parameters are: desired system sensitivity and integration time; size and weight (arm inertia); sensor resonant frequency and damping ratio; resonant frequencies and damping ratios of the other major mechanical components (support pivots, brackets, and arms); and coupling ratio of the transducer.

The system sensitivity and integration time were set by the contract requirements: 1 EU (10^{-9} sec $^{-2}$) at 10 sec (1 σ). With these fixed, the remainder of the basic parameters were then determined (with some tradeoff possible between some of the parameters). The tradeoffs and selection of the basic parameters were made early in the program and are given in detail in the Semiannual Technical Report No. 1 (Section III-C).

During the initial phases of the program, various combinations of the alternate concepts (Table II-1) were combined into a series of baseline sensor designs with each design carried out in sufficient detail to allow the complete sensor to be evaluated.

1943-12RI

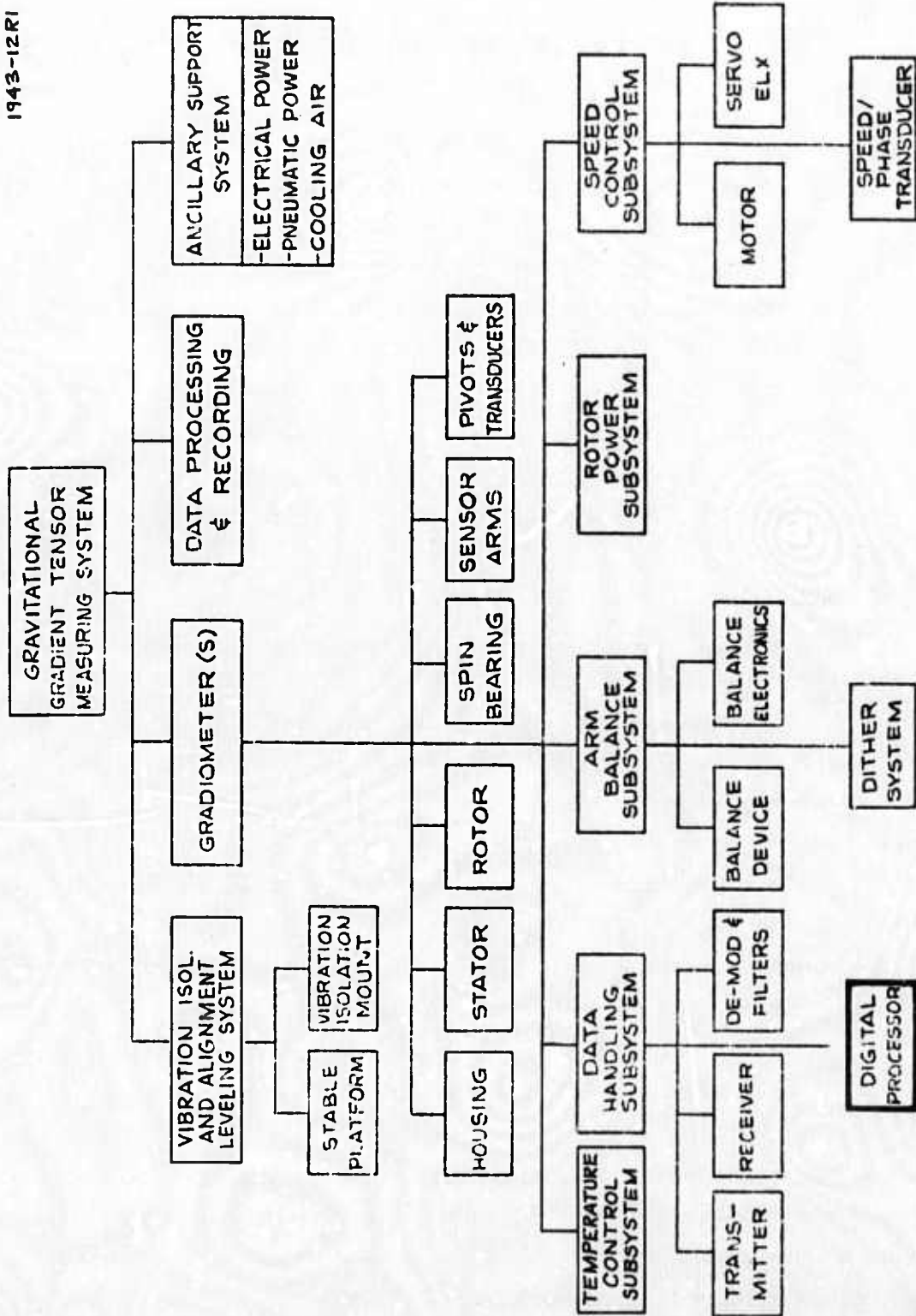


Fig. II-1. System Breakdown Structure.

SECTION II

TABLE II-1

Viable Alternate Design Approaches for RGG Subsystems

Subsystem	Alternate Concept
Spin bearing	Magnetic Oil - hydrodynamic and hydrostatic Air - hydrostatic and squeeze film
Sensor arms	Single strut Interleaved double strut similar shape different shape
Pivots	Torsional - single and double ended Longitudinal flex leaf (reel) Transverse flex leaf (Bendix)
Transducers	Capacitive Piezoelectric Optical Magnetostrictive Magnetic flux Mutual inductance
Speed control	Synchronous Asynchronous - ac and dc Photoelectric, magnetic or mutual inductance pickoff
Data handling	Analog Digital FM PCM Combinations of above
Housing	Hard mounted Floated - oil air - pressurized, squeeze film springs various combinations of above
Arm balancing	Piezoelectric Mechanical Sputtering Electrolytic

T874

SECTION II

For each of these baseline sensor designs, we studied the effect of the known error excitation sources acting on the sensor error sensitivity estimated for the particular baseline design. (See Tables II-2 and II-3; they are condensed from pages 11 to 17 in the Semiannual Technical Report No. 1. These show, in more detail, the many factors involved in the evaluation of a sensor design). From this series of evaluation studies, we have chosen a sensor design.

The selected RGG baseline design has an arm size and inertia of 12 cm long and $35,600 \text{ gm-cm}^2$, and an overall size and weight of 16 cm by 22 cm, and 9.6 kg. (This size and weight will be approximately the same for all gradiometers with a 1 EU at 10 sec sensitivity, since the thermal noise contribution of the sensor alone becomes larger than the required sensitivity for smaller sensors.) The sensor spin speed is 1050 rpm (17.5 rps), which is compatible with the sensor resonant frequency of 35 Hz with a Q of 300. These parameters, in turn, determine the sensor time constant to be 2.71 sec; the remainder of the system integration time (7.29 sec) is determined by the data processing filtering.

In the fully integrated RGG prototype design, we have chosen: hydrodynamic oil spin bearings; asynchronous drag cup motor drive with photoelectric position and tachometer speed pickoffs; mechanically isolated piezoelectric transducer; similarly shaped isoelastic interleaved double-strut sensing arms; electrolytic fine balance adjustment; multiple torsion bar supports formed from a single rod; internal AM-FM conversion with external power supply; air core transformer data feedthrough; external FM-digital conversion; digital plus analog data reduction; and solid mounting of the sensor case to the stable element of the angular isolation platform.

This last feature deserves comment as it illustrates the fact that a sensor design cannot be isolated from the design of a complete system. Our studies showed that the sensor sensitivity to angular rate jitter and alignment errors is the same for all gradiometers, and that all gradiometers with the same sensitivity will have similar size and weight.

SECTION II

TABLE II-2
Error Excitation Sources

- | | |
|------|---|
| (1) | <u>Translational Acceleration</u> |
| (2) | <u>Angular Rates and Accelerations</u> |
| (3) | <u>Temperature</u> — (Nominal operating temperature results in thermal noise effects) |
| (4) | <u>Temperature Variation</u> |
| (5) | <u>Ambient Pressure Variations</u> |
| (6) | <u>Ambient Humidity Variations</u> |
| (7) | <u>Magnetic Fields</u> |
| (8) | <u>Electric Fields</u> |
| (9) | <u>Acoustic Fields</u> |
| (10) | <u>Angular Orientation</u> |
| (11) | <u>Mass Proximity Gravity Gradients</u> (including earth) |
| (12) | <u>Prime Power Variations</u> |
| (13) | <u>Time Standard Variations</u> |
| (14) | <u>Component Inherent Characteristics</u> |
| (15) | <u>Material Stability</u> — This includes stability of dimensional properties as well as other parameter changes (e.g., transistor β 's, Young's modulus, damping coefficient, etc.) resulting from creep, aging, crystal growth, temperature cycling, etc. |

T875

SECTION II

TABLE II-3
Error Mechanisms

- (1) Translational Acceleration Sensitivity
- (2) Angular Acceleration Sensitivity
- (3) Thermal Noise Generation - (Sensitivity to nominal operating temperature)
- (4) Temperature Sensitivity - (Sensitivity to variations in operating temperature)
- (5) Ambient Pressure Sensitivity
- (6) Humidity Sensitivity
- (7) Electromagnetic Sensitivity
- (8) Electrostatic Sensitivity
- (9) Acoustic Sensitivity
- (10) Angular Orientation Error Sensitivity

Sensor

VIALS

- (11) Gravity Gradient Sensitivity
- (12) Prime Power Sensitivity
- (13) Time Standard Sensitivity
- (14) Component Inherent Characteristics
- (15) Material Instability Sensitivity

SECTION II

The sensitivity to angular rate jitter and alignment errors produces a conflicting set of requirements that cannot be met by a simple flotation system for a gradiometer sensor. If a gradiometer is to be floated to isolate it from angular rate jitter, it would require a servo system to maintain the orientation of the sensitive axis of the sensor with respect to the platform coordinates. If we use a simple case-oriented servo system that is tight enough to reduce the error contribution from the coupling of the error in angular orientation to the background bias of the earth's field, then the servo is so tight that it will transmit angular rate jitter. Thus, either a floated gradiometer with a complex servo system or a platform with better bearings or an angular rate jitter measurement and compensation system is indicated.

The size and weight of a three-axis gravity gradiometer system, along with the system sensitivity to angular alignment errors, produce a conflicting set of requirements for the stabilization platform. Available stable platforms with the required angular orientation capability do not have a payload capability to carry one or more gravity gradiometers in addition to their own inertial instruments. Therefore, a new stable platform capable of carrying the weight is required. It must also possess the desired characteristics of presently available inertial navigation systems. Fortunately, a new stable platform can be made easily with bearings providing the required angular rate steadiness, thus allowing the gradiometer to be hard mounted directly to the stable element. The design and manufacture of such a stable platform with the required orientation accuracy, payload capacity, and a high level of angular rate steadiness is within the state of the art and is a relatively straightforward engineering task.

The above discussion is but a brief overview. The details of the design features of the fully integrated RCG prototype design are covered in Sections IV, V, and VI of this report. Other sections of this report and the Semiannual Technical Report No. 1 treat each aspect of the design in detail.

SECTION II

The design integration tasks are not completed. They will continue into Phase II of this program as long as the fine-grained details of the manufacturing and assembly processes are being examined and remain open for refinement.

SECTION III

STATEMENT OF WORK COMPLIANCE

This section reviews the work that has been done during Phase I of this contract and demonstrates that the technical requirements of Section F, Description/Specifications, of the Statement of Work have been completed. Each line item of Section F is reproduced for convenience. Following each line item and sub-line item is a brief discussion which demonstrates that the requirements of the line item have been met. In many cases, specific sections of the Semiannual Technical Report No. 1 and of this report are referenced to demonstrate specific compliance.

A. LINE ITEM 0001

Design a moving base gravity gradiometer capable of measuring directly the horizontal and vertical gradients of gravity and serve as the basic sensor(s) for the following applications: marine, airborne and satellite gravimetry: determination and recording of the variation of the deflection of the vertical along the path of a vessel; augmenting on real time basis an inertial navigation system of a submarine, ship or aircraft; and in static mode of operation for mass detection.

Discussion

The one rotating gravity gradiometer sensor (RGG) design summarized in Sections IV, V, VI, and VII will measure directly the horizontal or vertical gravity gradient tensor elements. The tensor elements measured will depend on the orientation of the spin axis. Three sensors are required to measure all of the unrelated gravity gradient tensor components. The same sensor and electronics can be used for marine and airborne gravimetry. The same sensor

SECTION III

(three required) and electronics, along with other necessary computers, stable platforms, and recorders can be used to determine and record the variation of the deflection of the vertical along the path of a vessel and to augment on real-time basis an inertial navigation system of a submarine, ship, or aircraft. The RGG sensor can be used in the static mode for mass detection.

Satellite gravimetry would require a sensor of greater sensitivity than that specified by this Statement of Work. A preliminary design has been completed by Hughes for NASA. The design is based upon the same basic RGG concept of a torsionally resonant pair of rotating arms, but which are much larger in their dimensions. It also differs because a spinning, orbiting satellite vehicle is assumed, which eliminates the need for the spin bearings and the isolation subsystems.

In summary, the one RGG that has been designed meets all of the requirements of Line Item 0001.

B. SUB-LINE ITEM 0001AA

Perform analytical studies for the determination of design parameters and configuration of a gradiometer capable of measuring any horizontal and vertical gravity gradient components to a one standard deviation accuracy of one EU (EU = Eotvos Unit = 10^{-9} sec^{-2}) or better for a 10 second integration time. If a design requires different sensors for the measurement of horizontal and vertical components both types of sensors will be included.

Discussion

Analytical studies of several gradiometer configurations have been made. These are reviewed and summarized in Section VII of this report. Extensive error analyses have been made; some of these are given in the Semiannual Technical Report No. 1, and others are shown in Section IX of this report. In addition to these analyses, the errors

SECTION III

due to each component or subsystem are evaluated as part of the subsystem design, and this material appears in the appropriate sections. Section VI provides an error analysis summary which demonstrates that the Prototype RGG Design used in a three-sensor system has a 1-sigma error of less than 1 EU at the gravity gradient tensor element. The one sensor design can be used in any orientation.

The requirements of Sub-Line Item 0001AA have been fulfilled.

C. SUB-LINE ITEM 0001AB

Conduct laboratory experiments with existing instruments (if any) to complement and substantiate the results of analytical studies.

Discussion

Laboratory experiments were conducted on an existing RGG. Specific acceleration sensitivities were measured and studied. These are discussed in Section XXIV of this report. The prototype RGG design avoids the problems encountered in the older design. Sub-Line Item 0001AB requirement has been satisfied.

D. SUB-LINE ITEM 0001AC

Study the stabilization and motion isolation requirements for the recommended gradiometer design considering the most critical application. Determine required platform and isolation systems parameters. Demonstrate in form of studies that any component of the motion isolation system, external to the basic gradiometer, required for the support and isolation of the sensor is within the current state-of-the-art technology.

SECTION III

Discussion

This requirement has been studied since the receipt of the RFP. The final summary is in Section VIII of this report. The airborne environment is considered to be the worst case, and all components are within the current state of the art.

Sub-Line Item 0001AC requirements have been fulfilled.

E. SUB-LINE ITEM 0001AD

Determine design parameters and final configuration of the proposed gravity gradient sensor(s).

Discussion

The design parameters of the RGG Prototype Design are tabulated in Section V of this report. The final configuration is also shown in that section.

Sub-Line Item 0001AD requirements have been met.

F. SUB-LINE ITEM 0001AE

Data in accordance with Contract Data Requirements List (CDRL) DD Form 1423, Exhibit "A" (Revised) dated 72JAN19.

Discussion

Data has been provided in accordance with this list. This requirement has been met.

SECTION IV

RGG CONFIGURATION SELECTION SUMMARY

This section is a summary of Section VII which describes our rationale which led to the selection of the prototype configurations of both the RGG sensor and its required motion isolation system.

A large portion of this study effort has been devoted to selecting the most cost-effective configuration of the required moving base gravity gradient measurement system. Because of the inherent sensitivities of any realizable gravity gradient sensor to translational and rotational motions induced by the carrying vehicle, design of the prototype RGG sensor is heavily linked with the characteristics of the vibration isolation, alignment, and leveling system (VIALS) used to support a three-sensor group. Although design of the VIALS has not been required, study of its performance requirements and characteristics, as well as demonstration of its state-of-the-art feasibility, has been a contractual requirement of this study (see Section VIII).

Because of the inherent rotational field error sensitivity of any gravity gradiometer to angular rates of its measurement reference frame, primary consideration was given to selecting an RGG VIALS system combination which leads to the most cost-effective solution of this problem. Indications from earlier Hughes studies, reconfirmed during this study, showed that stabilized platforms, utilizing conventional ball-type gimbal bearings, do not provide the required angular rate steadiness. Thus, our original design goal was to seek a solution to this problem by incorporating an angular rate isolation capability in the RGG sensor.

During studies conducted in preparation for our proposal for this study contract, many alternative sensor configurations were considered that could provide this angular rate isolation. A neutrally buoyant rotating sphere configuration appeared the most promising

SECTION IV

and was the recommended baseline configuration in our September 1971 proposal, although its practical design details had not been studied in depth.

Several of the other alternative configurations still remained practical and feasible. It was realized that more detailed studies would have to be carried out in order to learn the pitfalls and advantages of each. After receipt of the contract, preliminary design studies of the proposed baseline and the most promising alternatives were undertaken. The four configurations studied are briefly described below.

A. CONFIGURATION A - NEUTRALLY BUOYANT ROTATING SPHERE

The basic RGG arm pair is mounted in a spherical float centered in a spherical, fluid-filled rotor. The rotor is spun on its spin bearings at the required sensor spin frequency. The transverse-to-polar moment of inertia ratio of the float is designed such that the preferred axis of spin of the float results in the sensitive axis of the sensor arm pair maintaining its average alignment coincident with the spin bearing axis. Any angular vibrations of the spin bearing stator are isolated from the float via the small viscous coupling between the float and the rotor.

B. CONFIGURATION B - TWO-AXIS AIR BEARING GIMBAL

The sensor arm pair is mounted directly to the rotor and rotates in the spin bearings. The angular isolation is provided by supporting the stator by an air bearing, two-axis ring gimbal, similar to the suspension of a 2 degree-of-freedom gyro.

SECTION IV

C. CONFIGURATION C - RESTRAINED TETRAHEDRON AIR PADS

The sensor arm pair, rotor, and spin bearings are identical to that of Configuration B. The sensor stator is spherical and the angular isolation is provided by supporting the spherical stator by four spherical-segment hydrostatic air bearing thrust pads located at the outer surface of the stator. Each pad is placed at the corner of a circumscribed equilateral tetrahedron which provides an isoelastic support for the stator. The suspension is constrained to have only 2 rotational degrees-of-freedom by a system of taut restraint wires connected from the stator to the housing.

D. CONFIGURATION D - DIRECT MOUNTED SENSOR

The sensor arm pair, rotor, and spin bearings are identical to Configurations B and C. The sensor stator is mounted directly to the stable element of the VIALS stable platform. The required RGG sensor angular rate isolation is provided by the stable platform via substitution of hydrostatic air bearings for the conventional ball-type gimbal bearings.

E. TRADEOFF COMPARISONS

Although the neutrally buoyant rotating sphere intuitively appeared the simplest and most straightforward of the configurations which incorporate self-contained angular isolation, it subsequently was proven to be the least attractive. Computer simulation results showed its angular isolation to be marginally adequate and that it would require very fine adjustment of the float's polar-to-transverse inertia ratio. These computer results were questioned because previous experience in fluid-rotor gyroscope development has indicated large discrepancies between the analytically predicted and

SECTION IV

experimentally determined damping coefficient. Also, apparent disturbance torques were observed, although their cause has not been understood. Other practical design and assembly problems were found which are more numerous and their solutions more complex, technically questionable, and costly than any of the other configurations.

Initially, it was thought that both configurations B and C could be mechanized using only passive, mechanical spring and damper elements to provide the necessary spin-axis alignment and stabilization.

Dynamic analysis, however, showed that this was not the case and that an active servo feedback system employing torquers and angle transducers on the two axes would be required. The conflicting requirements of providing a low-bandwidth servo response to external angular rates, but high-bandwidth response to torque disturbances, implied that a multiple-loop servo design would be required. The only conceptually feasible method of implementing this multiple-loop design would be to employ two single-degree-of-freedom integrating gyros, or their equivalent, in the servo design. Aside from the impractical, complex, and costly servo system required, no other significant design or assembly problems were formed for either Configuration B or C. Configuration C is preferred over Configuration B because of its inherently isoelastic suspension of the rotor and its somewhat smaller size and weight.

The direct mounted Configuration D sensor is, of course, the least complex and costly of all the configurations studied. In this configuration, the stable platform gyros provide the necessary isolation and stabilization for all three RGG's simultaneously, instead of requiring two additional gyros per RGG as would be necessary for Configurations B or C.

Considerable effort has been expended to determine the availability of a stable platform having the required level and azimuth accuracy and the space and weight carrying capacity for mounting three RGG sensors. No such platform meeting all of these requirements

SECTION IV

in one system is known to be operational or under development, thus it has become obvious that a new platform will be required.

The stable platform long-term level and azimuth accuracy requirements are stringent and can only be met by careful design of the platform and use of very high quality, "inertial grade" gyros and accelerometers. These requirements hold for all of the RGG configurations studied and for any other type of gravity gradiometer as well.

A study has been made to determine the feasibility, practicality, and costs associated with the additional angular rate steadiness requirement imposed on the stable platform if the direct mounted Configuration D sensor is utilized. Incorporation of hydrostatic air gimbal bearings in the new platform design would provide the required angular isolation; it is feasible and within the current state of the art, and it is not a major cost factor (approximately 5 to 10% of the total platform cost).

F. CONCLUSION

The least complex and most cost-effective solution to the angular rate isolation problem has been sought. Schedule requirements and budget limitations precluded selection of a system configuration requiring significant development effort or high technical risk items.

Complexity and technical risk considerations ruled out Configuration A. Configurations B and C require a complex, costly mechanization using two integrating rate gyros per sensor (a total of six rate gyros per system in addition to the VIALS stable platform gyros); B and C are considered impractical.

Configuration D imposes the least technical risk and cost of development of the RGG sensor itself. The additional angular rate steadiness requirement imposed on the stable platform does not

SECTION IV

represent a significant incremental cost or a technical risk. Complexity, technical risk, and cost effectiveness of the total operational system being considered, Hughes selected the direct mounted configuration to build in Phase II of this contract.

SECTION V

RGG PROTOTYPE DESIGN SUMMARY

A. GENERAL

This section provides a brief tabulation of the RGG Prototype Design parameters, provides a sensor layout, and incorporates the Semiannual Technical Report No. 1 and the original Prototype Moving Base Gravity Gradiometer proposal as parts of this report. The purpose of this section is to provide a ready reference of important parameters. Detailed calculations, tradeoffs and assumptions are given in the sections relating to each parameter. Table V-1 provides the parameter summary.

B. RGG DRAWING

A layout of the RGG prototype design is shown in Fig. V-1. The rotor (1) is generally spherical, but is slightly flattened at the ends to provide a mount for the spin bearings (2). The main member of the rotor is the circular central plate (3). The pivot assembly (4) is fastened in the center of the central plate. Eight brace posts (5), four on each side, are fastened to the central plate (3), and end plates (6) are in turn fastened to the brace posts. The outboard end of the pivots are fastened to the end plates.

This central assembly forms a rigid cage-like structure that completely supports the arms (7), the pivots, and the transducers (8). Thus the central rotor structure can be assembled, balanced, and tested before the rotor end bells (1) are put in place. The rotor electronics assembly (9) is fastened to the previously mentioned end plates (6). The sensor arms (7) are interleaved during assembly so that the arms are identical. The mass balance adjusting devices (10) are mounted on circular disks and these disks are fastened to the arms

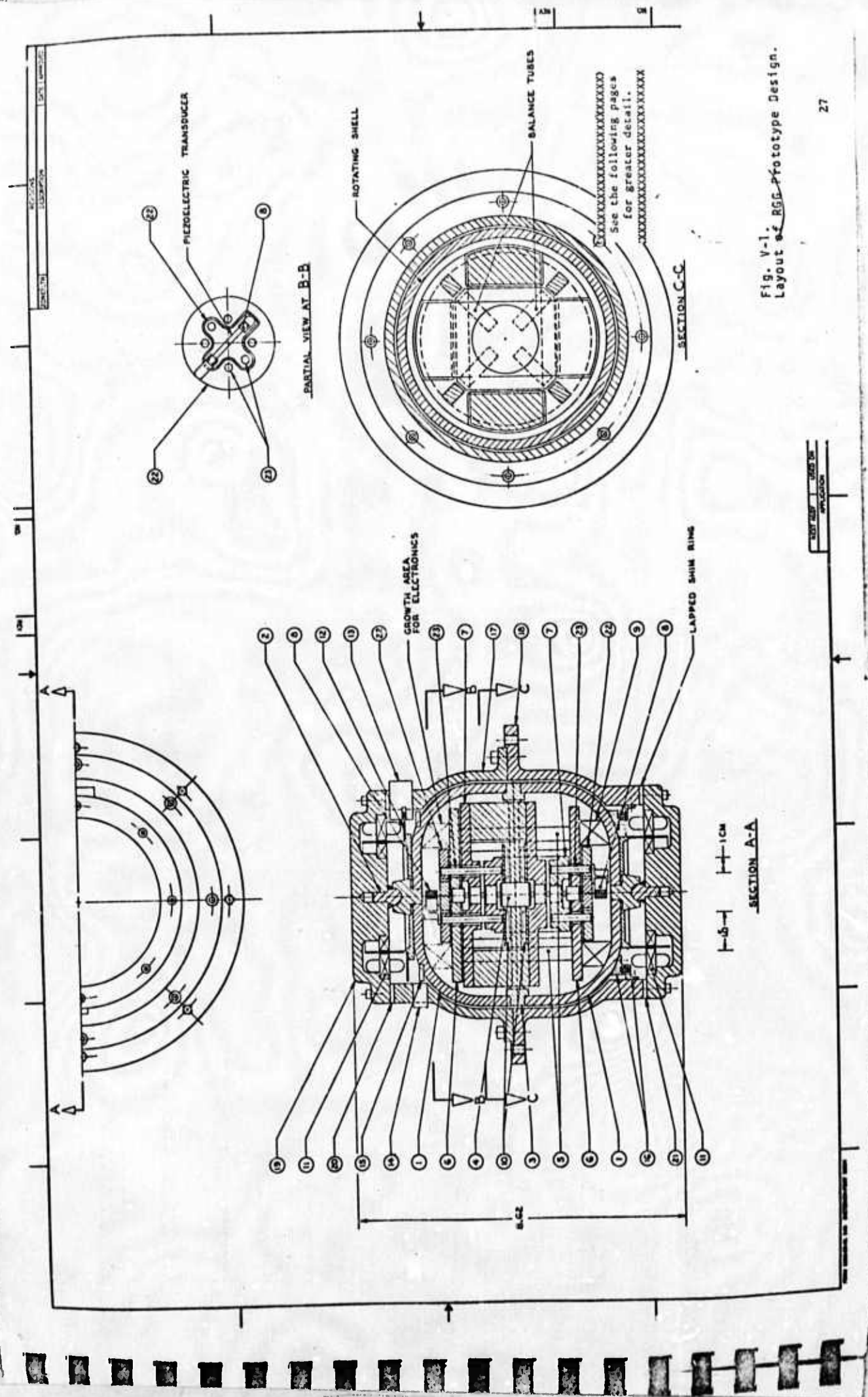


Fig. V-1. Layout of RSG-P Prototype Design.

SECTION V

TABLE V-1
RGG Prototype Design Parameters

1. Sensor Undamped Natural Frequency	
ω_o	220 rad/sec
f_o	35.014 Hz
2. Sensor Rotational Speed	
ω_s	110 rad/sec
f_s	17.507 Hz
3. System Integration Time, τ_i	
$\tau_i = \tau_s + \tau_F$	10 sec
τ_s = sensor time constant = $2Q/\omega_o$	2.73 sec
τ_F = filter time constant = $\tau_i - \tau_s$	7.27 sec
4. Sensor Q with Output Load	
Q Unloaded Sensor	320.9
Q Unloaded Sensor	640.9
5. Sensor Arms, each	
Material	6061 Al
Mass	1.563 kg
Inertia A	4.990×10^{-4} kg m ²
Inertia B	35.610×10^{-4} kg m ²
Inertia C	35.600×10^{-4} kg m ²
Inertia Efficiency, $\eta = (B-A)/C$	0.861
6. Sensor Arm Torque and Energy	
Gradient input torque = $M_o = \eta C \Gamma_{eq}/2$	1.533×10^{-12} Nm/EU
Peak arm torque = $\eta C Q \Gamma_{eq}/2$	4.599×10^{-10} Nm/EU
7. Rotor, Including Arms	
Material	6061 Al
Mass	5.876 kg
Inertia I _{zz}	203.9×10^{-4} kg m ²
Inertia I _{xx} = I _{yy}	144×10^{-4} kg m ²

SECTION V

TABLE V-1
RGG Prototype Design Parameters (Continued)

Mass unbalance about spin, allowed	0.03 gm cm
Angular momentum at 1050 rpm	22.4×10^6 gm·cm ² /sec
8. Stator	
Material	6061 Al
Mass	3.766 kg
Inertia I_{zz}	252.6×10^{-4} kg m ²
Inertia $I_{xx} = I_{yy}$	289.2×10^{-4} kg m ²
9. Transducer	
Material	PZT-5A
Output capacity, C_o	3.491 nF
Output impedance at $\omega = 220$	1.302×10^6 ohm
Output load resistor, R_o	9.55 M ohm
Output volts, E_o	95.86 nV/EU
10. Preamplifier and FM Transmitter	
Carrier frequency	200 kHz
Average frequency deviation per EU	2.78 Hz/EU
11. Rotor Power Supply	
Input power frequency	500 kHz
Filtered dc output	10.7 V
Output current	16.0 mA
12. Rotor Logic	
States available	8
States used	6
States spares	2
Logical 1, interrupt power supply	0.1 ms
Logical 0, interrupt power supply	0.3 ms

SECTION V

TABLE V-1
RGG Prototype Design Parameters (Continued)

13. Arm Mass Balance and Balance Devices	
Balance devices per arm per axis	10
Range of balance adjustment per arm per axis, Δm_h	$\pm 57 \times 10^{-4}$ gm cm
Balance adjustment resolution	$\pm 4 \times 10^{-5}$ gm cm
Differential arm mass unbalance allowed,	
Bias	$\pm 2 \times 10^{-4}$ gm cm
10 hour variation, 3σ	2×10^{-4} gm cm
Arm unbalance sum allowed,	
Bias	$\pm 8 \times 10^{-3}$ gm cm
10 hour variation, 3σ	2×10^{-4} gm cm
Balance device balance change speed	1.78×10^{-4} gm cm/hr
14. Arm Anisoelasticity	
Percent mismatch allowed	0.1%
Prime Anisoelastic Coefficient at Tensor Element	1800 EU/g^2
Stability of Prime Aniso-Coefficient	0.0075 EU/g^2
Natural Frequencies (Includes pivot spring rates)	
Lateral Bending or Longitudinal Mode	779 Hz
Flapping (Axial) Bending Mode	673 Hz
See-Saw (Rocking) Mode	567 Hz
15. Temperature Control	
Nominal operating temperature	53°C
Temperature variation of arms, pivots, and transducer allowed,	
1σ over 3 hr	0.00114°C

SECTION V

TABLE V-1
RGG Prototype Design Parameters (Continued)

16. Spin Motor/Tachometer	
Type	Two-phase, drag cup
Excitation frequency, nominal	140 Hz
Stall torque, 2 motors	7.68×10^5 dcm
Stall watts, 2 motors	30.2 W
Running torque at 1050 rpm, 1 motor	6.7×10^4 dcm
Running watts at 1050 rpm, 1 motor	9.94 W
Tachometer scale factor	1.29×10^{-2} V/rad/sec
17. Spin Bearing	
Type	Hydrodynamic oil
Form	Hemispherical
Running torque at 1050 rpm, 2 bearings	5×10^4 dcm
Breakaway torque, 2 bearings	5×10^5 dcm
Bearing radial clearance	220 μ in.
Bearing stiffness	1.63×10^5 lb/in.
18. Sensor Pivots, All Pivots Identical	
Material	Beryllium-Copper
Shear modulus	4.5×10^{10} N/m ²
Temperature coefficient of shear modulus	-330 ppm/ $^{\circ}$ C
Active length, each pivot	0.05563 in.
Active diameter, each pivot	0.05563 in.
Torsional Spring Rate	12.5 Nm/rad
19. Digital Computer	
Word length	16 bit
Memory	8K of 16 bit
Add or subtract	2.5 μ sec
Multiply	12 μ sec

SECTION V

TABLE V-1
RGG Prototype Design Parameters (Continued)

Divide	15 μ sec
Access I/O Channels	10 μ sec
20. Frequency Reference	
Type	Quartz Crystal
Make	Hewlett-Packard
Model number	10544-A
Frequency	10 MHz
Drift	
per day	$<5 \times 10^{-10}$ Hz
per year	$<1.5 \times 10^{-7}$ Hz
Stabilize to 5×10^{-9}	15 min

as shown. The rotor end bells (1) are sealed to the central plate after the central assembly is complete. A motor/tachometer (11) is fixed to the stator and encloses the spin bearings. At one end of the rotor is the position encoder disk (12) with its associated light source and photocell (13), which is attached to the stator. At this same end of the stator is another light source (14) that excites two photocells (15) on the rotor. These two photocells provide the reference for the sensor test signal.

At the sensor end opposite that used for the photocells and the encoder disk is the FM transmitter output transformer (16). This transformer is made up of two concentric coils, one fixed to the rotor and one fixed to the stator. The stator (17) is made in two parts and has mounting bosses (18). Rotor input power is provided by insulating one motor end cup (19) with insulator (20). The capacitance between the motor and drag cup and between the two halves of one spin bearing conducts the electric power to the rotor. End play of the spin bearings is adjusted by means of the lapped shim (21). The piezoelectric

SECTION V

transducers (8) are mounted on concentric plates (22). These plates are in turn fastened to the sensor arms by means of posts (23).

C. SEMIANNUAL TECHNICAL REPORT NO. 1

The Semiannual Technical Report No. 1, Contract F19628-72-C-D222, Project Code P1F10, August 1972, is considered to be a part of this Design Evaluation Report when referenced herein.

D. PROTOTYPE MOVING BASE GRAVITY GRADIOMETER PROPOSAL

The Prototype Moving Base Gravity Gradiometer, Hughes Research Laboratories Proposal 71M-1593/C3755, Parts 2 and 3, Technical Proposal, September 1971, is considered to be a part of this Design Evaluation Report when referenced herein.

SECTION VI

ERROR ANALYSIS SUMMARY

This section provides a concise summary of all errors of an operational RGG Prototype Design System. The errors due to a state-of-the-art navigation and vibration isolation system are shown, as well as the errors due to the RGG itself. The estimated errors for the system as a whole are well below 1 EU, 1 sigma. The errors for the RGG sensor are only about one-half EU, 1 sigma. Thus a large safety factor is available in the sensor design. In paragraph A, each error term is briefly described so that the terms in the RGG System Error Summary (Table VI-1) can be easily understood.

A. BRIEF ERROR DESCRIPTIONS

1. Thermal Noise

The main source of thermal noise is associated with the dissipative elements of the signal sensing and transducing process of the RGG. An additional minor source is associated with the signal processing electronics. Both noise sources are assumed to have white spectra at their origin, and they enter the RGG signal process in the carrier domain. The selective RGG filter process passes the thermal noise power located in narrow frequency bands centered at the positive and negative tuned frequencies of the carrier filter process, nominally twice the RGG spin frequency. In this analysis, the noise power is evaluated for a temperature of 326°K, which corresponds to 127.4°F.

2. Sum Mode Mismatch

The "sum mode mismatch" error mechanism provides an excitation of the RGG differential mode through RGG rotor spin axis

SECTION VI

TABLE VI-1
RGG Prototype Design System
Error Summary

Error Sources	Gravity Gradient Tensor Element Errors, 1σ					
	σ_{XX}	σ_{YY}	σ_{ZZ}	σ_{XY}	σ_{XZ}	σ_{YZ}
<u>RGG Errors</u>						
Thermal noise	0.338	0.338	0.338	0.358	0.358	0.358
Arm mass unbalance	0.218	0.218	0.218	0.231	0.231	0.231
Sum mode mismatch	0.093	0.093	0.093	0.098	0.098	0.098
Scale factor	0.150	0.150	0.212	0.045	0.002	0.002
Phase Errors	0.003	0.003	0.003	0.033	0.325	0.325
Rotational field	0.027	0.027	0.027	0.028	0.028	0.028
Anisoelastic	0.017	0.017	0.020	0.014	0.010	0.010
RSS of RGG Errors	0.441	0.441	0.465	0.442	0.547	0.547
<u>VIALS Errors</u>						
Arm mass unbalance	0.036	0.036	0.036	0.036	0.038	0.038
Rotational field	0.086	0.086	0.086	0.079	0.079	0.079
Anisoelastic	0.069	0.069	0.135	0.016	0.011	0.011
Platform orientation	0.368	0.368	0.212	0.352	0.327	0.327
RSS of VIALS Errors	0.386	0.386	0.286	0.377	0.339	0.339
RSS of RGG and VIALS	0.586	0.586	0.546	0.581	0.643	0.643

SECTION VI

accelerations occurring in a narrow frequency band centered at twice the spin frequency ($2\omega_s$). This error sensitivity is proportional to the difference of the squares of the torsional natural frequencies defined by each arm polar inertia and its associated torsional elastic coupling to the rotor case (end pivot). Both deterministic and random excitation of this error mechanism may occur. Deterministic excitations produce bias errors that may be compensated during RGG calibration to the extent that these excitations remain stable after calibration. Changes of the deterministic excitations after calibration produce both bias and random errors depending on the statistical character of the changes. All excitations of this error mechanism occur by virtue of disturbance torques acting on the RGG rotor about its spin axis in a narrow frequency band centered at twice the spin frequency. Potential excitation sources are the spin bearing; the spin motor; the speed control servo; and the vibration isolation, alignment, and leveling system (VIALS).

3. Axial Torsional Coupling

This error mechanism is sometimes called "The Yankee Screwdriver Effect" for obvious reasons. It is characterized by a coupling between RGG axial translational acceleration and RGG differential mode excitation in a narrow frequency band centered at twice the spin frequency. Its potential excitation sources are the spin bearing, the spin motor, and the VIALS. In the RGG prototype design, the pivots, transducer mount and the transducers have all been designed to eliminate this effect. The sensitivity is assumed to be negligible.

4. Transducer Axial Acceleration Sensitivity

Axial translational acceleration of the RGG rotor in a narrow frequency band centered at twice the spin frequency will produce stresses in the differential mode transducers that may generate error signals due to differences in the electromechanical characteristics of

SECTION VI

the transducers. The potential excitation sources are the spin bearing, the spin motor, and the VIALS. It is shown in Section XIV that, to the first order the transducers are insensitive to axial acceleration.

5. Transducer Transverse Acceleration Sensitivity

Accelerations normal to the RGG spin axis in narrow frequency bands centered at the spin frequency and its third harmonic will produce stresses in the differential mode transducers which may generate error signals due to differences in their electromechanical characteristics. The potential excitation sources are the spin bearing, the spin motor, RGG rotor mass unbalance, and the VIALS. It is shown in Section XIV that, to the first order, the transducers are insensitive to transverse acceleration.

6. Differential Arm Mass Unbalance

When the mass centers of the RGG arms do not coincide with a line parallel to the torsional elastic axis of the arm support structure, a differential arm mass unbalance condition exists. Case-referenced accelerations of the RGG rotor normal to its spin axis in narrow frequency bands centered at the spin frequency and its third harmonic will act on the differential arm mass unbalance to produce error signals at twice the spin frequency in the carrier domain. The potential excitation sources are the spin bearing, the spin motor, the RGG rotor mass unbalance, and the VIALS.

7. Axial Arm Mass Unbalance

When the mass centers of the RGG arms are separated axially and in addition are displaced normal to the torsional elastic axis of the RGG, case-referenced angular accelerations of the RGG rotor about axes normal to the spin axis in narrow frequency bands centered at the spin frequency and its third harmonic will produce error signals

SECTION VI

at twice the spin frequency in the carrier domain. The potential excitation sources are the spin bearing, the spin motor, the RGG rotor mass unbalance, and the VIALS.

8. Cross Anisolelasticity

When the principal transverse elastic axes of the arms are not exactly normal to the RGG torsional elastic axis, and, in addition, the principal compliances of each arm are unequal or unequal to each other, a cross-anisoelastic condition exists. Under these circumstances, case-referenced accelerations of the RGG rotor normal to the spin axis in narrow frequency bands centered at the spin frequency and its third harmonic will produce differential error moments at twice the spin frequency. The potential excitation sources are the spin bearing, the spin motor, the RGG rotor mass unbalance, and the VIALS.

9. Prime Anisoelasticity

When the principal transverse compliances of the arms are unequal, a prime anisoelastic condition is said to exist. Under these circumstances, the low frequency components of the squares and products of the RGG case-referenced rotor specific forces normal to the spin axis will produce error moments in a narrow frequency band, centered at twice the spin frequency. Potential sources of excitation are the spin bearing, the spin motor, rotor mass unbalance, and the VIALS. The most significant errors are those involving the gravitational specific force. It is anticipated that these error terms will be of sufficient magnitude to require active compensation. After active compensation, both deterministic and random errors must be considered. The deterministic errors can be compensated during RGG initialization to the extent that they remain stable after initialization. Changes of the deterministic errors after initialization produce trend effects primarily, e.g., bias changes directly proportional to altitude. The most significant random errors after the compensation and initialization processes are due to the random vertical accelerations of the VIALS.

SECTION VI

10. Rotational Field Errors

The rotational field errors of any gravity gradient instrument are not the result of an error mechanism within the basic instrument itself. All gravity gradiometers which are based on mass attraction phenomena (this includes all presently known instrument types) are in reality specific-force gradiometers. As a consequence, such instruments sense the specific force gradient of the rotational field of their measurement frames in addition to that of the mass attraction (gravity) field. All such instruments must be compensated for the known deterministic rotational field gradients. The errors remaining after compensation are primarily random in nature and the result of the random angular velocities of the VIALS. Rotational field specific force gradients that arise from self-excitation of the RGG due to its spin bearing, spin motor, and rotor mass unbalance are primarily deterministic and are compensated during the RGG system initialization process.

11. Signal-Dependent Scale Factor and Phase Errors

Within the class of signal-dependent errors are those due to RGG instrument scale factor, RGG instrument phase, and uncertainty in orientation and position of the RGG system measurement frame. The first two error mechanisms are instrument-related (scale factor and phase), and the latter two are related to the uncertainty in angular orientation of the VIALS and the position uncertainty of the navigation system associated with the RGG measurement system. The initial scale factor and phase of the RGG measurement system are established and calibrated during the system initialization process. Changes of RGG scale factor and phase after calibration are due primarily to temperature sensitivity and aging of the instrument parameters associated with the signal sensing and transducing process. In addition, phase variations associated with the signal modulation and demodulation

SECTION VI

processes contribute to this class of errors. Phase variations associated with the speed control servo as compensated by the signal demodulation process are the result of torque disturbances and servo position measurement noise. There are two classes of phase errors in the RGG signal process. Phase errors that are the result of speed control servo torque disturbances, by virtue of the servo design and the method of signal detection, occur in a narrow low frequency band centered near a frequency of 0.3 rad/sec (approximately 0.05 Hz). There is no dc transmission of this class of phase error. The other class of phase errors is low frequency (below 0.05 Hz to dc) in character. This class is the result of changes in the RGG carrier filter transfer function after initial alignment and changes in the alignment of the various mechanical elements associated with the RGG position measurement for the speed control servo. Potential sources of speed control servo torque disturbances are the spin bearing, the spin motor, and the tachometer. Potential sources of the second class of phase errors are resonant frequency variations of RGG differential mode, changes in the transducer and electronics, variations in the following alignments: RGG arms to rotor case, speed control servo position index disk to rotor case, and speed control servo position pick-off to stator case, and variations in the position pick-off threshold. Variations in frequency of the time standard ($\approx 10^{-9}$) produces a negligible error.

12. Extraneous Fields

A general class of possible errors of an RGG measurement system may be considered in relation to its sensitivity to various fields of the external environment. Perhaps the most obvious error source in this class is the time-varying mass attraction field in the immediate vicinity of the measurement system due to the presence of the mass of the carrying vehicle and its payload. Generally speaking,

SECTION VI

the gravity gradient magnitudes associated with various parts of the vehicle and payload must be examined to determine the necessity of real-time compensation for this effect. Due to the close proximity of the stable platform gimbal structure to the RGG instruments, it is highly probable that a deterministic compensation will be required for changes in the relative mass distribution of the stable platform.

Most materials suitable for use in the construction of an RGG are paramagnetic, and magnetic fields can produce error moments at the even harmonic of the spin frequency. It is believed that all magnetic fields except that due to the earth can be kept negligibly small in the vicinity of the RGG. It is planned to determine experimentally the magnetic field sensitivity of the RGG and to provide sufficient magnetic shielding, if necessary.

It is believed that excitation of the RGG differential mode by electrostatic fields will be negligible. Electrostatic charge buildup on the rotor may produce torques on the rotor, but this effect will not produce a differential moment on the RGG arms.

13. Ambient Effects

It is believed that RGG sensititity to ambient humidity, ambient pressure, and acoustic pressure will be negligible. Temperature effects and prime power variations are considered in relation to all previously listed error mechanisms.

SECTION VII

CONFIGURATION SELECTION RATIONALE

A. GENERAL

Selection of the prototype RGG sensor and the prototype vibration isolation, alignment, and leveling system (VIALS) configuration for an operational gravity gradient sensing system has been a significant portion of this Phase I study effort. Because of the inherent error sensitivities of any realizable gravity gradient sensor to translatory and rotational motion induced by the carrying vehicle, design of a prototype sensor capable of operating in a moving base environment is strongly linked with the characteristics of the VIALS used to support the sensor. Although design of the VIALS has not been required, study of its performance requirements and characteristics, as well as demonstration of its state-of-the-art feasibility, have been a contractual requirement of this study. This section discusses the design goals and the many trade-offs considered in selecting the prototype configurations of both the Hughes RGG sensor and the VIALS.

B. PERTINENT DESIGN GOALS

The primary consideration in selecting an optimum configuration of both the RGG and the VIALS has been cost and operational effectiveness of the total system. The requirement of this study was to develop a gradiometer which would serve as the basic sensing element in an operational system that will provide for measurement of all vertical and horizontal gravity gradient components. It requires three Hughes RGG sensors operating with mutually orthogonal spin-axes to provide all of these specified components. Hence, this study has been confined to optimizing a system consisting of a VIALS and three RGG

SECTION VII

sensors. The fact that this specific system configuration was optimized is important. In some potential applications, a single RGG sensor could provide the necessary measurement, hence the angular isolation portion of the system might take a considerably different form.

It had become apparent that one of the very dominant problems in developing an operational moving base gradiometer was to provide a feasible and practical solution to the inherent rotational field error sensitivity of a gradiometer. Hence, a primary design goal was to develop a system that would solve this problem in the most cost-effective way.

Earlier study results, which were reconfirmed during this study, indicated that conventional, inertially-stabilized platforms transmit sufficient angular rate jitter that they would be unsuitable for direct mounting of a gradiometer. Thus, our original design goal was to seek a solution to this problem by providing a self-contained angular rate isolation capability within the RGG sensor. (It has turned out that this solution was not cost effective, as shown in succeeding discussions.)

Another design goal was that the sensor was to be made as small and lightweight as possible. This would result in many beneficial effects; a significant one would be to reduce the payload requirements of the VIALS.

Hughes' earlier work in RGG development had utilized a hydrostatic air bearing as the sensor spin bearing. Although this type of bearing had provided good results in the laboratory, it was recognized that a significant problem would result if a compressed air supply was required for the moving base operational system. This is because piping high pressure air to the sensors could add significant mass unbalance and spring restraint disturbance torques to the required inertial platform. Thus, a design goal was to eliminate the need for an air bearing supply system.

SECTION VII

C. ANGULAR ISOLATION REQUIREMENTS

Estimates of the angular vibration power spectra of vehicle motion have been made, assuming the vehicle to be a C-135 type of aircraft. These estimates are detailed in the Semiannual Technical Report No. 1 (Section III-C-4, pages 102 to 109). That report also presents an estimated angular rate spectra of the stable element of an inertial platform using conventional ball-type gimbal bearings.

The analysis contained in the Semiannual Report estimates the gradient error if a gravity gradiometer were to be rigidly attached to the stable element. The resulting gradient error is estimated to be approximately 2.5 EU. The method of analysis was approximate, however, and it is expected that the result was not a conservative estimate.

In recent months we have developed another analytical method for estimating the resultant gradient field error, assuming the sensor to be rigidly attached to the stable element of a conventional platform. Appendix B of this report presents the details. This second method produced a significantly different result, but it can be demonstrated that it provides a worst-case estimate. This worst-case estimate indicates the rotational field error of a ball bearing platform to be approximately 40 EU.

The purpose of presenting the second analysis is to place a worst-case boundary on the estimate. Thus, if a worst-case situation were to exist, there is absolutely no doubt as to the need for additional angular rate isolation or compensation. Our error analysis has assumed that the residual rotational field error must be limited to 0.2 EU. Thus, the 40 EU worst-case figure would require a factor of 200 attenuation or compensation, or an attenuation of rms angular rate by a factor equal to $\sqrt{200} \approx 14$.

Further analyses and testing programs would be possible and would result in establishing the probable rotational field error with a corresponding increased level of confidence. Such a series of tasks is beyond the scope of this contract; also, it would really not be a

SECTION VII

cost/effective effort. It is our considered opinion that the probability is low that such efforts would indicate that a conventional ball bearing platform could meet the angular rate steadiness requirements.

D. SENSOR CONFIGURATIONS STUDIED

Prior to and during the preparation of our September 1971 proposal, much consideration was given to configuring a gradiometer which would provide for isolation of angular vibrations from the rotating sensor arm pair, thus providing the desired reduction of the inherent rotational field errors induced by the moving base environment. After considering many alternative schemes, we recommended the neutrally buoyant rotating sphere in our proposal. However, practical details of the design had not been studied in depth. Because it was realized that many of the other alternate schemes also appeared feasible and practical, it was apparent that a more detailed study of the practical design, fabrication, and assembly problems of the most promising alternates would be required to ferret out the pitfalls and advantages of each. Hence, during the initial period of this Study Phase, preliminary design studies of several sensor configurations were undertaken. Four sensor configurations were studied and are described below.

1. Configuration A — Neutrally Buoyant Rotating Sphere

In this design, the sensor arm pair is encased in an evacuated spherical float. The float is suspended in a neutrally buoyant fluid contained within a spherical rotor via a small torsion-bar pivot located at the center of the float. The spherical rotor is supported on a pair of hemispherical gas spin bearings. The drive motor spins the rotor at the desired spin frequency. The axis of maximum inertia of the float is designed to be parallel to the torsionally sensitive axis of the sensor arm pair. Thus, after spin-up, this axis precesses into alignment

SECTION VII

with the bearing spin axis. Isolation of oscillatory angular rate normal to the arm pair torsional axis is provided by the low-friction spherical degree-of-freedom between the float and the rotor.

Design of the sensor arm pair and their suspension torsional pivots has not been worked out in detail. Conceptually, the arms would be similar to the other RGG designs except that the arm pair would be hollow in the center to fit over the center post of the float. Pivots to support the arms and transduce the differential arm motion would be of the quadrilever type as illustrated in our September 1971 proposal, p. 140.

Details of the design of the float, rotor, and outer case are shown in Fig. VII-1. The basic structure is almost entire 6061 aluminum, stress-relieved after final machining. Most screws and balance weights are brass, which has almost the same coefficient of expansion as aluminum. The following notes describe the numbered callouts in the figure.

- (1) Alternate screws and taper pins. Approximately 24 around outer case. Approximately 6 around air bearing.
- (2) O-rings. Used as temporary seal only.
- (3) Brass balance screws. Their coefficient of thermal expansion is almost identical to aluminum and can get adequately low magnetic susceptibility. Will not gall with aluminum.
- (4) Spanner nuts each end. Note that lower one provides a gimbal tilt stop that just matches the pivot to float clearance at top. Select top nut for balance. Proper seals not yet provided at these points.
- (5) Outer case of float. 6061 aluminum.
- (6) Flex leads - 4 required.
(Pivot = Gnd); 1 + Battery; 1 - Battery; 1 Signal;
1 Logic.
- (7) Bellows. Can only install at one end. Bellows shown is not adequate.

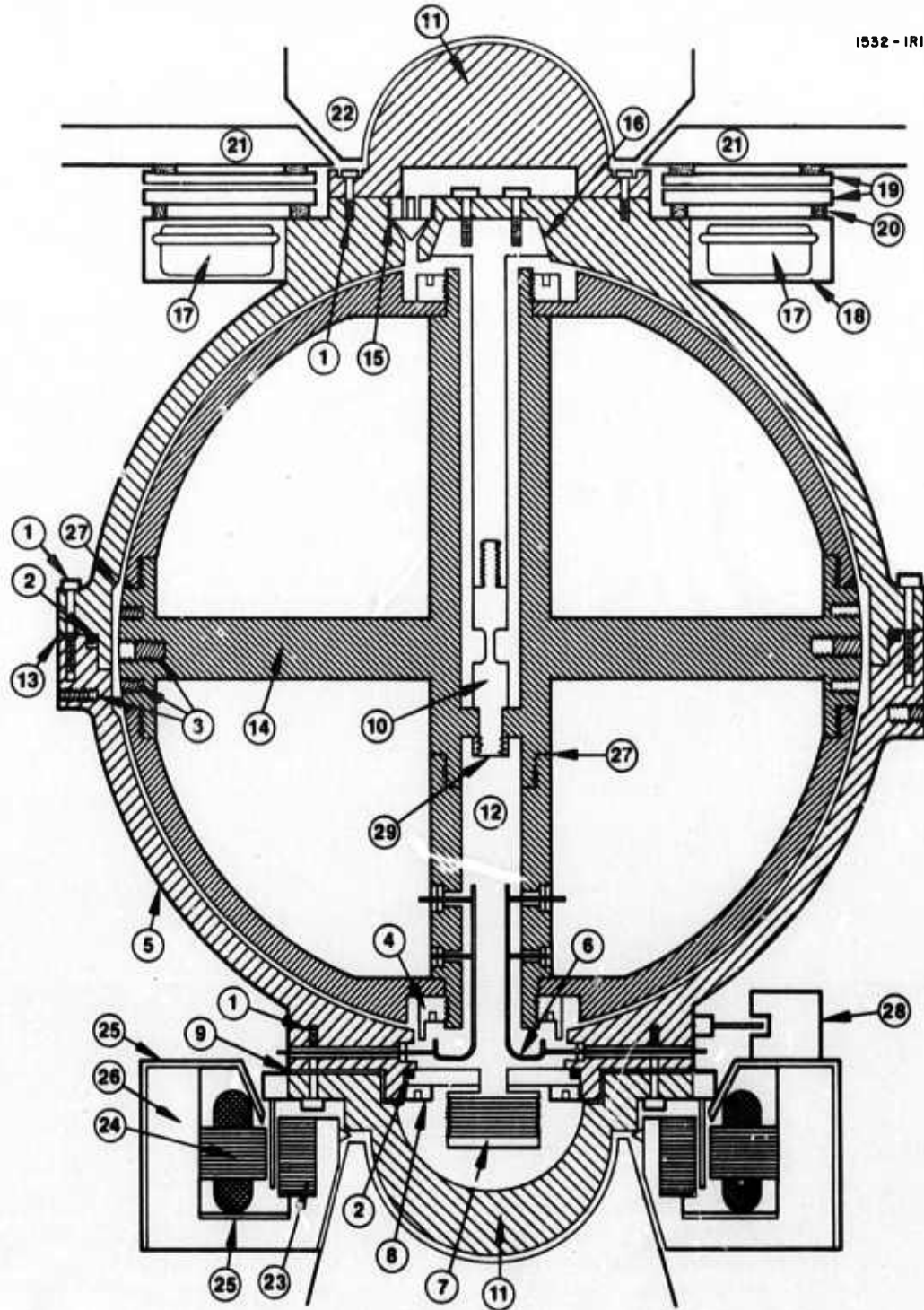


Fig. VII-1. Configuration A.

SECTION VII

- (8) Spanner nut.
- (9) Insulator if needed or desired.
- (10) Beryllium copper pivot with aluminum or brass extender. Extender keeps float control centered as temperature varies. This may not be necessary. Pivot itself can be shortened. This will help reduce suspension point shift as temperature varies.
- (11) Air bearing rotors.
- (12) Flotation fluid. Carbon tetrachloride in present design but there are a number of other possibilities.
- (13) May have to change slightly so that we have a half-sphere as a cup for half-flotation during assembly. Have not provided a good seal yet at this point.
- (14) Central plate and central post. 6061 aluminum, of course. Make these first and assemble and balance arms and add internal guts to these. Will want to make a handling fixture. The central plate can have large holes, bosses, posts, etc., as required. Internal structure not yet designed.
- (15) Fill port with non-locking taper plug. Held in place by spanner nut with hole to accommodate extractor post of plug.
- (16) Non-locking taper, centers and levels pivot post.
- (17) Batteries. 12 - 0.225 A-h, 1.3 V/cell. Nickel-cadmium. Must be provided with case-fixed magnetic shield.
- (18) Battery carrier. Visualize batteries epoxy-set in an aluminum ring.
- (19) Power input capacitor plates.
- (20) Stand-off insulators for 19.
- (21) Exhaust air deflector attached to main frame.
- (22) Air bearing stators attached to main frame.

SECTION VII

- (23) Backup motor stator iron. Overlaps stator stack to act as magnetic shield.
- (24) Motor stator. TranCore T, 0.007 in. thick. Should be able to buy standard punching.
- (25) Magnetic leakage shield.
- (26) Motor stator mount attached to main case.
- (27) Epoxy seals.
- (28) Float angle pickoff.
- (29) Pivot nut with Allen wrench socket.

Additional data describing the design Configuration A are as follows:

a. Float

Material	6061 aluminum	
Outside diameter	(6.50 in.)	16.51×10^{-2} m
Inside diameter	(6.00 in.)	15.24×10^{-2} m
Displaced volume	(2356 cc)	2.356×10^{-3} m ³
Average density	(1.6 gm/cc)	1.6×10^{-9} kg/m ³
Mass (3770 gms)		3.7 kg
Polar inertia	$(1.02 \times 10^5$ gm cm ²)	1.02×10^{-2} kg/m ²
Diameter inertia	$(8.0 \times 10^4$ gm cm ²)	8.00×10^{-3} kg/m ²

b. Arms

Mass (Mallory 1000 & Al)	(700 gms)	0.7 kg
Inertia	(20,000 gm cm ²)	2.0×10^{-3} kg/m ²
Inertia efficiency		0.7 η

SECTION VII

Peak torque 1 EU field	7.0×10^{-13} Nm
---------------------------	--------------------------

Balance screws	Brass
----------------	-------

c. Central Pivot

Material	Beryllium Copper
----------	------------------

Length, active	(0.100 in.)
----------------	-------------

Diameter	(0.010 in.)
----------	-------------

K_t , torsional stiffness	$(7.2 \times 10^7 \text{ dcm}/\text{rad})$ $7.2 \times 10^{-3} \text{ Nm/rad}$
--------------------------------	--

K_b , bending stiffness	$(9.4 \times 10^4 \text{ dcm}/\text{rad})$ $9.4 \times 10^{-3} \text{ Nm/rad}$
------------------------------	--

Stress when lifting float	(106,000 psi)
------------------------------	---------------

Torsional freedom	(2.39 deg) $\pm 0.0417 \text{ rad}$
----------------------	-------------------------------------

Bending freedom	(2.39 deg) $\pm 0.0417 \text{ rad}$
-----------------	-------------------------------------

Max tension stress bend	(34,400 psi)
----------------------------	--------------

Max shear stress torsion	(~12,000 psi)
-----------------------------	---------------

Hang-off at $20^\circ/\text{hr}$ input rate	(0.61 deg) 0.010 rad
--	--------------------------------

d. Fluid

Carbon tetrachloride (tentative selection)

Density, 20°C	(1.6 gms/cc)	$1.6 \times 10^{-9} \text{ kg/m}^3$
-----------------------------	--------------	-------------------------------------

Viscosity, μ	(0.009 poise)	$9.0 \times 10^{-4} \text{ Nsec/m}^3$
------------------	---------------	---------------------------------------

Germanium tetrachloride

Density	(1.84 gms/cc)	$1.84 \times 10^{-9} \text{ kg/m}^3$
---------	---------------	--------------------------------------

Viscosity, μ	
------------------	--

SECTION VII

Damping gap, h

Physical	(0.025 in.)	6.35×10^{-4} m
Effective, 10 Hz		2.7×10^{-4} m
Effective, 20 Hz		1.9×10^{-4} m
Effective, 40 Hz		1.35×10^{-4} m

Damping coefficient

Low frequency	(5,950 dcm sec)	5.95×10^{-4} Nm sec
10 Hz	(8.340 dcm sec)	8.34×10^{-4} Nm sec
20 Hz	(11,800 dcm sec)	11.80×10^{-4} Nm sec
40 Hz	(16,680 dcm sec)	16.68×10^{-4} Nm sec
Volume of fluid	(55 cc)	5.5×10^{-6} m ³
Coefficient of expansion	(1.2×10^{-3} °C)	
Net Volume Change $\Delta T = (124 - 70)$ = 54°F = 30°C	(1.8 cc)	1.8×10^{-6} m ³

e. Natural Frequencies and Damping Ratios

Torsional undamped	(0.135 Hz)	0.85 rad/sec
Bending undamped	(0.172 Hz)	1.08 rad/sec
Damping ratio torsion	ζ	0.024 (low frequency)
Damping ratio bending	ζ	0.034 (low frequency)

SECTION VII

f. Spin Motor Estimates

Excitation frequency		180 Hz
Number of poles		12
Synchronous speed		30 rps
Stator and rotor material		Tran-Core T 0.007 in.)
Mass of iron	(1.83 lb)	0.828 kg
Mass of copper	(0.60 lb)	0.414 kg
Power during run-up		20 W
Power during operation		10 W
Locked rotor torque	(3.0 in.-oz)	2.12×10^{-3} Nm
Running torque	(0.5 in.-oz)	3.54×10^{-4} Nm

2. Configuration B - Two-Axis Air Bearing Gimbal

In this and the remaining two configurations studied, the sensor arm pair, torsional support pivots, differential arm motion transducer, rotor, spin bearings, and case would be similar. Although not worked out during the configuration trade-off study, the details of this portion of the sensor are described in Section IV, RGG Prototype Design Summary. These last three configurations differ in the method of suspension of the sensor case. In Configuration B, the arms and rotor rotate in the spin bearing and the angular isolation is provided by supporting the stator on a two-axis air bearing ring gimbal, similar to that of a 2 degree-of-freedom gyro. (Initially, it was thought that tefrural pivots could be used as gimbal bearings. It was found that they were not feasible because to accomplish the required angular rate isolation, the torsional spring rate had to be so low that pivots could

SECTION VII

not be designed to carry the 1g load of the sensor.) Rough preliminary sketches of this air bearing gimbal configuration are shown in Figs. VII-2 and VII-3. The gimbal air bearings, although perfectly feasible, are quite large to support the sensor weight with adequate margin. The gimbal ring is quite large and massive. This is required to provide for adequate stiffness and to reduce anisoelastic disturbance torques. Damping coefficient of the air gimbal bearings is estimated to be less than 50 dyne-cm-sec. Provision for adding torquers and angular pickoffs in each axis is made.

3. Configuration C - Restrained Tetrahedron Air Pads

The sensor stator suspension of Configuration C is functionally similar to that of Configuration B in that a 2 degree-of-freedom support is provided. In Configuration C, the sensor stator is spherical and the suspension is provided by a set of four spherical-segment, hydrostatic gas-bearing thrust pads. The pads are located at the outer surface of the spherical stator. Each pad is placed at the corners of a circumscribed equilateral tetrahedron. This suspension provides an isoelastic support for the stator and is illustrated in Fig. VII-4. The suspension is restrained by a system of restraint wires (as depicted in the sketch of Fig. VII-5) so that it has only 2 rotational degrees-of-freedom about axes normal to the spin axis. In Section III-C-6 of the Semiannual Technical Report No. 1, a derivation is shown which demonstrates that this tetrahedron support geometry provides an isoelastic suspension. The damping coefficient of the tetrahedron air pads is estimated to be 500 dyne-cm-sec.

4. Configuration D - Direct-Mounted Sensor

In Configuration D, the sensor stator is direct mounted to the stable element of the VIALS inertial platform. The required angular rate isolation and/or compensation is provided by the inertial platform via the use of hydrostatic gas gimbal bearings rather than the conventional ball-type bearings and/or special angular rate sensors. This

1943-19

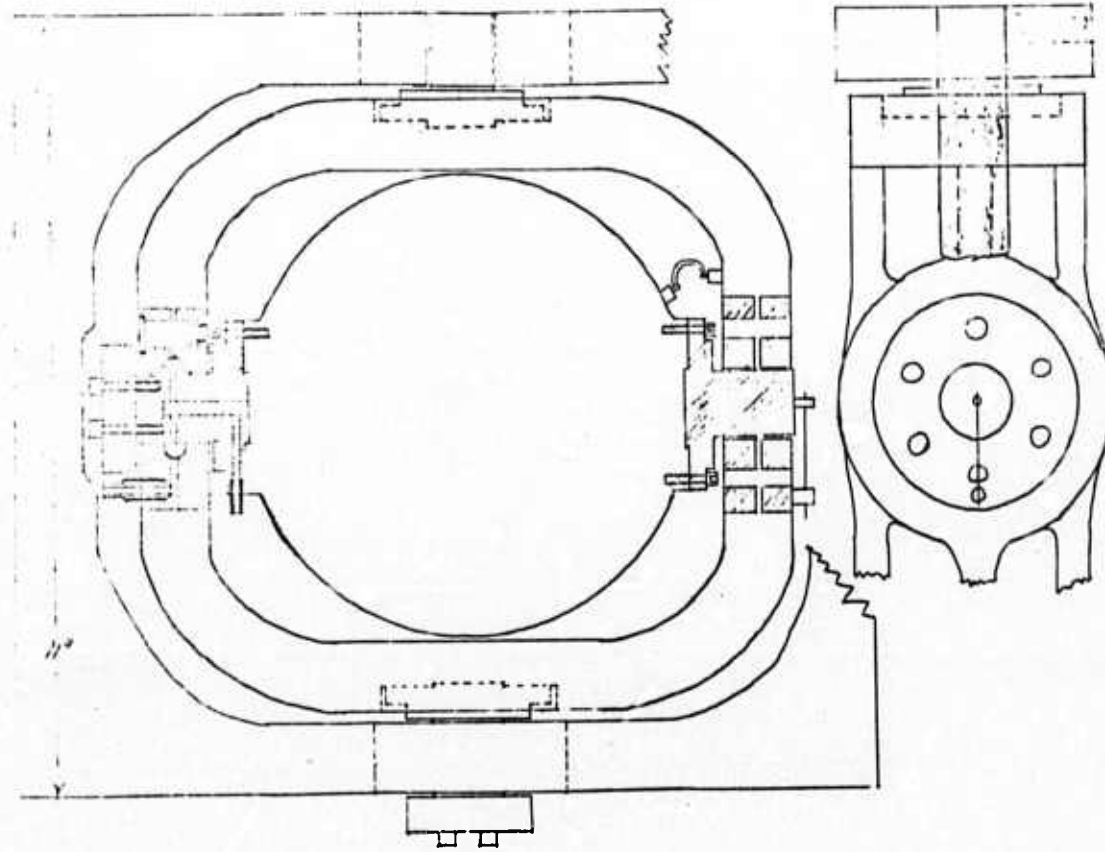


Fig. VII-2. Configuration B.

1943-20

AFCRL Gimbal
Mounted PGG

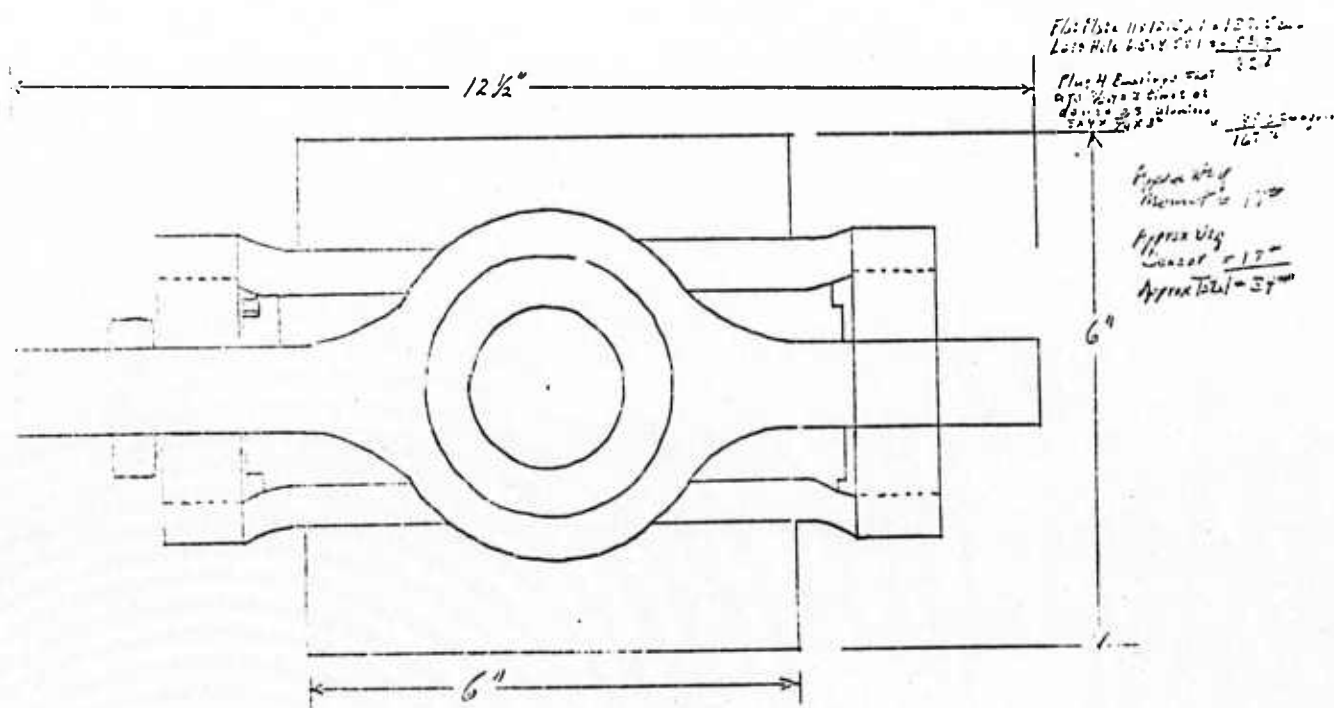


Fig. VII-3. Configuration B.

1943-21

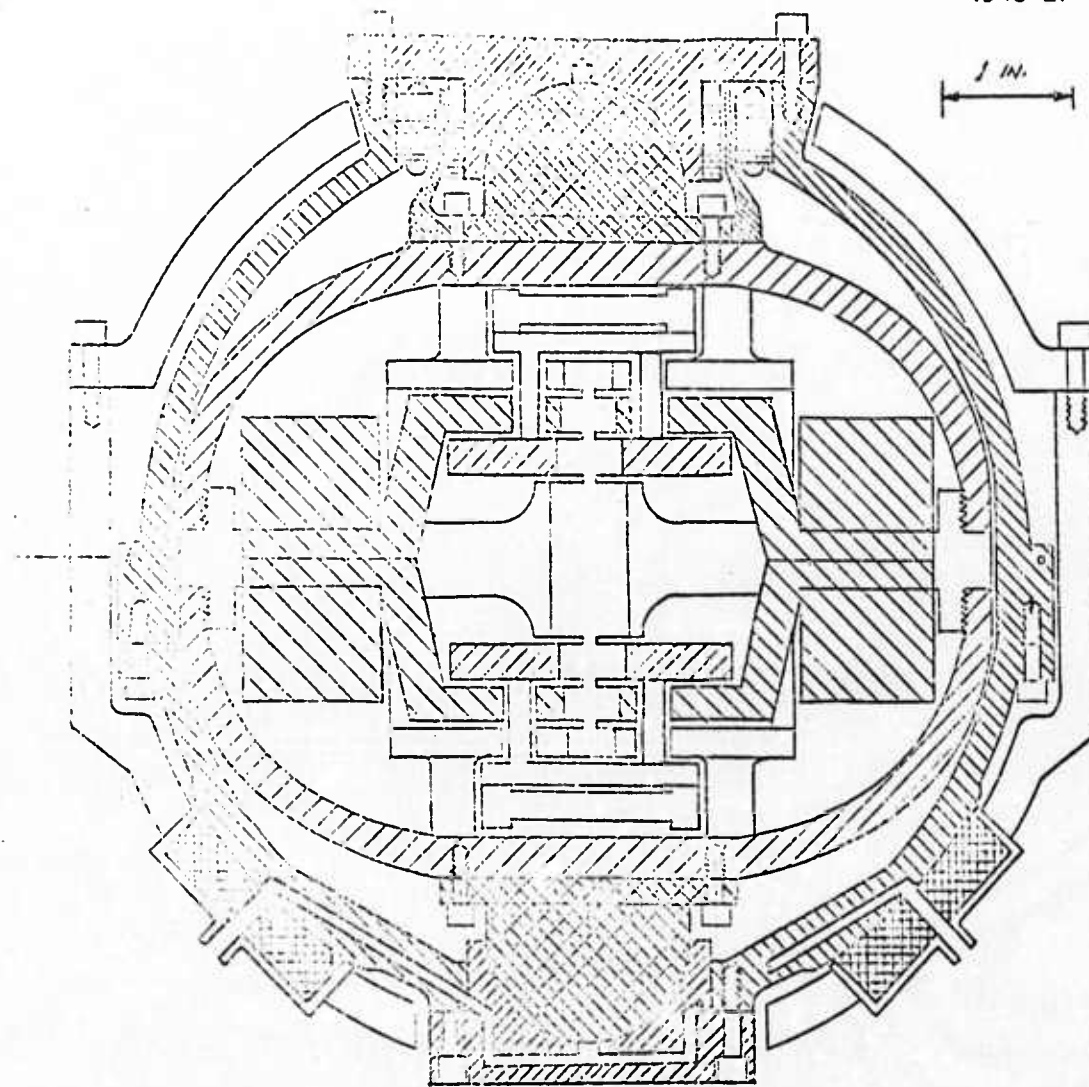
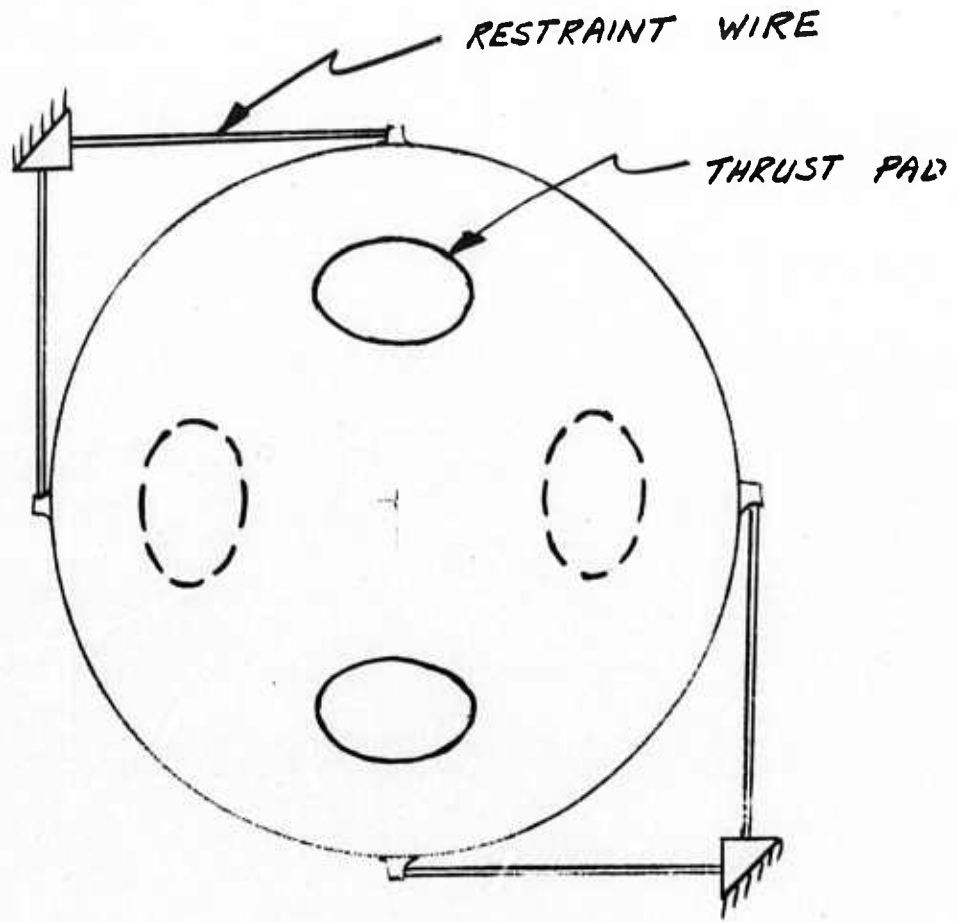


Fig. VII-4. Configuration C.

1943-16



RESTRAINT SYSTEM SCHEMATIC
FOR TETRAHEDRON AIR PAD SENSOR
(CONFIGURATION "C")

Fig. VII-5. Restraint System Schematic for Tetrahedron Air Pad Sensor.

SECTION VII

configuration is our recommended prototype system. The sensor configuration is described in Section V, RGG Prototype Design Summary, and the inertial platform requirements and characteristics are described in Section VIII, VIALS Requirements.

E. TRADE-OFF COMPARISONS OF ALTERNATE CONFIGURATIONS

This section discusses the many pros and cons of each of the four above-described sensor configurations. Common criteria which the four configurations are evaluated against and a summary of the pertinent comments are shown in Table VII-1. In some instances, the space available in the summary table is not sufficient to fully describe the considerations and hence such details are provided in the following paragraphs.

1. Angular Rate Isolation Capability

Configurations A, B, and C inherently provide for angular rate isolation. For Configuration A, computer simulation results show angular isolation capability is marginally adequate. Very fine adjustment of the ratio of polar to transverse moment of inertia of the float is required to attain the required isolation. Computer simulation results are questionable. This is because previous experience in fluid-rotor gyroscope development has indicated large discrepancies between the analytically predicted and the experimentally verified damping coefficient. Also, apparent disturbance torques were observed whose cause was not understood. This lack of in-depth understanding of the behavior of rotating fluids weighs heavily against considering this approach at this time. It was felt that the many other RGG development problems should be given priority. If a future system application requirement could be met most favorably with this approach, a separate research and development program to implement it could then be considered.

SECTION VII

For Configurations B and C, the viscous coupling torques of their air bearing suspensions are minuscule and hence their inherent angular rate isolation capability is very good.

In Configuration D, all of the required angular rate isolation and/or compensation must be provided within the VIALS inertial platform. Our studies show that this is entirely feasible and practical. The required angular rate attenuation of a factor of 14 as shown above is achieved by substitution of hydrostatic air gimbal bearings. A detailed description of this mechanization and the supporting analysis is provided in Section VIII, VIALS Requirements.

2. Angular Alignment Capability

In Configuration A, angular phase error about spin-axis could develop. Angular spin rate of the rotor would be closely controlled as in all other configurations. An additional servo control loop probably would be required to provide accurate phase alignment between the rotor and float. This servo would be feasible, but would add additional complexity.

Angular alignment of the sensor arms about axes normal to the rotor-defined spin axis is accomplished by mass balancing the float so that its principal axis of maximum moment of inertia is parallel to the torsional axis of the sensor arms. Thus any disturbance torques about transverse axes are balanced by gyroscopic reaction torques in such a manner that the float maximum moment of inertia axis tends to align itself with the spin axis. This alignment accuracy can be no better than that provided by the float mass balance trimming operation.

In Configurations B and C, angular alignment of the sensor about axes normal to the nominal spin axis must be provided by servo control. The need for and requirements of this servo control system is discussed in the following item.

In Configuration D, angular alignment about all axes is inherent because of the direct mounting to the inertial platform stable element. In all configurations, the angular alignment requirements of the inertial

SECTION VII

platform stable element are similar. Because of the inherent alignment capability of Configuration D, the inertial platform alignment (and drift) requirement could be somewhat less stringent than for any of the other configurations.

3. Sensor Alignment Servo Control

In Configuration A, a spin-axis phase control servo might be required. Implementation difficulties would arise as noted in the comparison table.

In both Configurations B and C, it was initially anticipated that the required angular rate isolation and spin-axis alignment could be achieved using only passive elastic and viscous restraints. Dynamic analysis of this passive restraint system revealed two lightly damped oscillatory modes whose characteristic frequencies were related to the RGG spin momentum, H, the elastic restraint coefficient, K, and the RGG transverse moment of inertia, A, as in eqs. (1) and (2).

$$\Omega_p \triangleq K/H \quad (1)$$

$$\Omega_n \triangleq H/A \quad (2)$$

The normalized damping coefficients, ζ , of both of these oscillatory modes are equal to the ratio of the viscous damping coefficient, D, to the RGG spin momentum as in (3).

$$\zeta_p = \zeta_n = D/H \quad (3)$$

The equivalent damping time constant, τ_p , of the precessional mode characteristic frequency, Ω_p , is defined by (4).

$$\tau_p = H^2/DK \quad (4)$$

SECTION VII

Substitution of the appropriate numerical parameters into (4) revealed a fundamental problem of the passive restraint system; its damping time constant was in excess of 1000 hr. This calculation is shown in (5).

$$\tau_P = \frac{\left(2.039 \times 10^5 \text{ g-cm}^2 \times 110 \frac{\text{rad}}{\text{sec}}\right)^2}{\left(500 \text{ dyne-cm-sec}\right)\left(2 \times 10^5 \text{ dyne-cm/rad}\right)} \cong 5 \times 10^6 \text{ sec.} \quad (5)$$

Consideration was given to parametric changes that could reduce this time constant to an acceptable level of about one minute. This implied an increase in the DK product by a factor greater than 10^5 . Angular rate isolation requirements limit the practical increase of the elastic constant, K, to less than two orders of magnitude. This implies a required increase of the damping coefficient, D, by several orders of magnitude (10^3 to 10^4). An increase in damping of this magnitude was not considered feasible, and the passive restraint system was abandoned on this basis.

This led to considering active restraint configurations that require the addition of torque generators and angle pickoffs between the RGG stator and its case. The performance requirements of these components were investigated, and it was determined that the addition of components of suitable performance and size was feasible. The dynamics of active restraint configurations based on the angle measurement only were investigated, and it became apparent that a single-loop design could not satisfy the conflicting requirements of a low bandwidth response to external angular rates and a high bandwidth response to torque disturbances. It was concluded that a multiple-loop design would be necessary to provide the required performance. To implement a multiple-loop design, it is necessary to employ some form of RGG stator inertial angular velocity feedback. One obvious method is to add two single-degree of freedom rate integrating gyros to the RGG stator to provide the rate measurements. Other sensors could be utilized, such as opposed accelerometers or angular differentiating accelerometers. A mechanization using any of these types of sensors would result in a

SECTION VII

conceptually feasible system; however, it would be impractical, complex, and costly. Another outwardly attractive scheme would be to employ a passive inertia damper, such as a mercury ring affixed to the stator. However, preliminary examination of the characteristics of such a device of acceptable size indicates that it would provide only a marginally adequate amount of inertial rate feedback. Also, an inherent problem associated with this device is that an expansion bellows would be required to accommodate the fluid expansion. Because of the low stiffness associated with any bellows arrangement, large center of mass shifts could result, thus increasing the magnitude of vibration-induced disturbance torques. Thus, implementation of a passive inertia damper appeared unattractive and at best would probably require a development effort to assure its feasibility.

4. Sensor Mass Balance

In Configuration A, static and dynamic mass balance of the float will have to be performed with the flotation fluid surrounding the float and controlled to the nominal operating temperature. Static balance can be accomplished using techniques similar to that used for balancing floated gyros. No known technique has been devised to accomplish the required dynamic balance, i.e., to bring the float principal axes into alignment with the sensor arm's torsional axis. This could be a serious problem and might result in building up expensive test gear.

Also, in Configuration A, fluid expansion bellows would be required. Because of the low stiffness of the bellows, a potential instability of the rotor mass balance might result.

Mass balancing of Configurations B, C, and D appears to be relatively straightforward.

SECTION VII

5. Vibration Susceptibility

As described earlier, a cylindrical hole passing through the spherical float of Configuration A is required to provide for C. G. attachment of the centering pivot. Thus, the arm suspension was required to be hollow to fit over the center post of the float, and the quadrilever-type arm support pivots were envisioned as an appropriate pivot design. Since completing this preliminary design study, it has been learned that this type of pivot results in an unusually large error sensitivity to spin-axis translational vibration. This is discussed in Section XXIV. Thus, this pivot configuration is no longer considered appropriate. It would appear that for the same reasons the quadrilever pivot is susceptible to spin-axis vibrations, any other hollow arm suspension pivot might very well have similar characteristics.

Design of the gimbal ring of Configuration B to reduce potential anisoelastic error torques could result in a large, massive structure. Configuration C overcomes this difficulty because of isoelastic characteristics of a spherical structure. In Configuration B, rotor dynamic mass unbalance would have to be very tightly controlled to prevent self-induced rotational field errors. In Configuration C, such self-induced errors are minimized. This is because a dynamically unbalanced rotor will cause a coning-type motion of the sensor spin axis. It can be shown that no rotational field error results if this coning motion is purely circular, but it does result if the motion is elliptical. The motion would nominally be circular in Configuration C, because of the inherently equal moment of inertia of its stator about any transverse axis. In Configuration B, the motion would be elliptical because of the anisoinertial properties of the reacting inertia, i. e., the moment of inertia of the stator and gimbal ring is different about the two suspension axes.

6. Spin Bearing Selection

In the initial phase of this study when the sensor configuration selection study was undertaken, the design of the spin bearing had not been started. At that time, a hydrostatic air spin bearing appeared

SECTION VII

the most promising type. Hence, avoiding the high-pressure supply problem was an important consideration. For that reason, Configuration A appeared the most attractive since increased spring restraint or mass unbalance disturbance imposed on the inertial platform would not seriously affect its performance; nor could they directly couple into the gradiometer. The problem of series feeding an air supply via the sensor stator suspension bearings to the spin bearing in Configurations B or C did not appear unfeasible, but was an added design complexity. Configuration D would result in a similar design complexity.

The hydrodynamic oil sensor spin bearing design, now completed, requires no external excitation source. Hence, the above tradeoffs are no longer a concern.

7. Overall Sensor Size

The table is self-explanatory.

8. Piece-part Fabrication

The table is self-explanatory.

9. Assembly

The table is self-explanatory.

10. Relative Sensor Cost

The table is self-explanatory.

11. VIALS Cost

Considerable effort has been expended in conducting surveys of industry, DOD, and NASA to ascertain the availability of an inertial platform having the required long-term level and azimuth accuracy with the load carrying capacity suitable for supporting the required

SECTION VII

three RGG sensors. The results of these surveys have been frustrating because no system meeting both the accuracy and payload requirements has been found. For this reason, it has become obvious that a platform development will be required for an operational system of three sensors.

The performance requirements of the inertial platform for any of the sensor configurations are stringent. The long-term level and azimuth accuracy requirements can be met only by the best of inertial-grade gyroscopes and accelerometers. A very careful design of the stable element and gimbal structure and gimbal bearings will be required to limit anisoelastic errors. The additional angular rate steadiness requirement imposed with sensor Configuration D will not significantly increase either the development or hardware manufacturing cost of the platform. It is shown in Section VIII that incorporation of hydrostatic air gimbal bearings in the new platform design will provide the required angular rate steadiness. Use of air gimbal bearings is feasible, within the current state of the art, and is not a major cost factor. It is estimated that the incremental cost would be 10 to 20% at most. This type of bearing has a significant advantage over the conventional ball-type gimbal bearing because it inherently provides a much stiffer bearing, which helps alleviate the anisoelastic drift errors.

Alternatively, compensation of the rotational field error has been considered. Angular rate sensors having the required accuracy are feasible. This laternative is treated in more detail in the VIALS section.

A secondary advantage of selecting the Configuration D sensor is that the long-term level and azimuth accuracy requirement can be somewhat less stringent than that required for any of the other configurations. This is because the other configurations have additional angular alignment uncertainties due to their additional angular degrees of freedom.

SECTION VII

There would be no major differences in the requirements imposed on the vibration isolation mount of VIALS for any of the sensor configurations. Because of the size differences between sensor configurations, the size and payload weight would be somewhat altered, but this is inconsequential in terms of technical feasibility or cost.

F. CONCLUSION

The dominant criteria used in selecting the prototype sensor configuration are complexity and cost effectiveness of the operational gradient sensing system. Solution of the angular rate isolation problem is the primary consideration affecting this selection. Schedule requirements and budget limitations preclude selection of a system configuration requiring significant development effort or high technical risk items.

Complexity and technical risk considerations rule out Configuration A. Configurations B and C require either a complex mechanization using two inertial angular velocity feedback sensing devices per RGG sensor (a total of six devices per system), or they involve development of a passive damper whose technical feasibility and practicality are questionable.

Configuration D imposes the least technical risk and cost in development of the RGG sensor. The additional angular rate steadiness/compensation requirement imposed on the VIALS inertial platform does not represent a significant incremental cost or technical risk. The simplicity and cost effectiveness of the total operational system is by far the greatest for Configuration D, hence Hughes has selected Configuration D as the prototype sensor configuration.

SECTION VII

TABLE VII-1
Configuration Tradeoff Comparison Summary

Criteria	Configuration A Naturally-Buoyant Rotating Sphere	Configuration B Two-Axis Air Bearing Gimbal	Configuration C Retrained Tetrahedron Air Pads	Configuration D Direct Mounted to Inertial Platform
1. Angular Rate Isolation Capability	APP's adequate; however, analytical prediction of performance uncertain because previous experience reveals lack of correlation of analysis with experimental results.	More than adequate. Lends itself to straightforward, well-understood analysis. Requires servo control, see below.	More than adequate. Lends itself to straightforward, well-understood analysis. Requires servo control, see below.	None. VIALS inertial platform must provide angular rate vibration isolation.
2. Angular Alignment Capability	Angular phase error about spin-axis might require use of pickoff and torque to reduce phase error.	Angular alignment about axes normal to spin-axis inherently automatic; however, alignment accuracy dependent upon mass and moment of inertia balance of the float.	Angular alignment about spin-axis is accurate and straightforward.	Angular alignment about all axes is accurate and straightforward.
3. Sensor Alignment Servo Control	Spin-axis phase control servo might be required. Implementation of pickoff and torque would be straightforward; however, control electronics and power supply would be difficult because relatively high power levels would have to be transmitted to rotating members.	Servo control required to provide simultaneous angular rate isolation and transverse axis alignment. See text discussion.	Servo control required to provide simultaneous angular rate isolation and transverse axis alignment. See text discussion.	None required. Azimuth and level accuracies of VIALS platform somewhat less stringent.
4. Sensor Mass Balance	Mass balance difficult because: 1. Float would have to be suspended in fluid controlled to operating temp.; ure. 2. Dynamic balance of float to bring principal axes into coincidence with sensor arms' torsional axis difficult (No known technique has yet been established). 3. Required expansion bellows could cause serious rotor C.G. instability.	Rotor and gimbal mass balancing is straightforward.	Rotor and rotor housing mass balancing is straightforward.	Rotor mass balancing is straightforward.
5. Vibration Susceptibility	Hollow arm suspension pivot may induce large error torques caused by vibrations along sensor spin-axis.	Potential anisoclasticity of ring gimbal could result in a large massive structure. Anisoclastic characteristics of suspension could result in self-induced rotational field error.	Anisoclastic errors are minimized due to spherical structure.	Least susceptible of all.
6. Spin Bearing Selection	Hydrodynamic oil spin bearing has been selected, hence no high pressure air feed problem. See text.	Hydrodynamic oil spin bearing has been selected, hence no high pressure air feed problem. See text.	Hydrodynamic oil spin bearing has been selected, hence no high pressure air feed problem. See text.	Hydrodynamic oil spin bearing has been selected, hence no high pressure air feed problem. See text.
7. Over-all Sensor Size	Upper limit of density of practical flotation fluids (1.6 g/c.c.) forces float size to larger package than necessary to hold sensor. This results in largest sensor size of all.	Smaller than A, but larger than C or D due to larger size required for stably stiff gimbal ring and air bearings.	Smallest configuration of all.	

SECTION VII

TABLE VII-1
Configuration Tradeoff Comparison Summary (Continued)

Criteria	Configuration A Naturally-Buoyant Rotating Sphere	Configuration B Two-Axis Air Bearing Gimbal	Configuration C Restrained Tetrahedron Air Pads	Configuration D Direct Mounted to Inertial Platform
8. Piece-Part Fabrication	Largest quantity of precision piece parts, however generally straightforward.	Medium quantity of piece parts. High precision required on gimbal air bearings.	Medium quantity of piece parts. High precision required on bearing spherical surfaces.	Smallest quantity of piece parts and generally straightforward.
9. Assembly	Extreme difficulty of assembly: 1. Delicate handling required to assemble centering spring to float and housing requiring temperature control of fluid and extreme care to avoid breakage of spring. 2. Sealing of both float and housing required. 3. Nuisance of handling flotation fluid.	Straightforward assembly.	Straightforward assembly.	Straightforward assembly.
10. Relative Sensor Cost	Highest hardware cost because of larger quantity of piece parts and difficulties of mass balance and assembly. Highest development cost and uncertainty because of little understood fluid damping characteristics.	Medium to high hardware cost dependent on use of rate sensors versus passive damper. Medium development cost. Uncertainty due to hardware and development cost to implement inertial damping feedback.	Medium to high hardware cost dependent on use of rate sensors versus passive damper. Medium development cost. Uncertainty due to hardware and development cost to implement inertial damping feedback.	Lowest hardware cost. Lowest development cost and development cost uncertainty.
11. VITALS Cost	New inertial platform development required to obtain large payload capability with required azimuth and level accuracy.	New inertial platform development required to obtain large payload capability with required azimuth and level accuracy.	New inertial platform development required to obtain large payload capability with required azimuth and level accuracy.	New inertial platform development required. Cost higher than A, B, or C to obtain required azimuth rate steadieness.

SECTION VIII

VIBRATION ISOLATION, ALIGNMENT, AND LEVELING SYSTEM

A. GENERAL

The need for a vibration isolation, alignment and leveling system (VIALS) for support of the three-RGG sensor cluster has been recognized for some time. Earlier studies conducted by Hughes have ascertained the requirements and characteristics for the VIALS. Two basic functions are provided by the VIALS: (1) establishment of a gradient measurement reference frame via providing azimuth and level stabilization of the three-sensor cluster, and (2) attenuation of translational and angular vibrations to reduce induced errors resulting from vibration sensitivity of the RGG to these motions.

These earlier studies have considered the tradeoffs of various mechanization approaches. These studies resulted in establishing a basic building block approach to provide the two basic functional requirements. It consists of the following: The three sensors are mounted to the stable element of an inertially stabilized three-axis platform. The platform in turn is supported by a softly sprung vibration-isolation mount, which is affixed to the carrying vehicle. This softly sprung mount provides for isolation of translational vibrations induced by the carrying vehicle. It also serves to attenuate vehicle-induced angular vibrations. The three-axis platform provides long-term azimuth and level stabilization of the RGG cluster.

Contractual requirements of this Phase I study have been to determine the characteristics and requirements of the VIALS and to demonstrate that any of its components are within the current state of the art. As such, detailed design of the VIALS was not carried out. The Hughes recommendation for the VIALS configuration, although not backed up by an in-depth detail design, will be referred to as the prototype VIALS configuration. (It is referred to as "prototype" in the

SECTION VIII

sense that it is compatible with our selected prototype RGG sensor configuration).

B WORST CASE ENVIRONMENT

Hughes has selected an airborne environment typified by a KC-135 aircraft as the "most critical application." This is discussed in the Technical Report No. 1. Therein, we have presented data showing the power spectral density for aircraft angular acceleration and for aircraft angular rate. A minor transcription error was made in the presentation of these data in that report. Hence, the corrected data is re-presented herein (see Figs. VIII-1 and VIII-2).

C. VIALS REQUIREMENTS FOR PROTOTYPE RGG SENSOR

The performance characteristics and design requirements of the vibration isolation mount and the stable platform are stated herein. These are the minimum requirements necessary to insure that operation of the RGG sensors in the aircraft environment for durations up to 10 hr will result in measurement of the gravity gradient tensor elements to an accuracy of 1 EU, 1 sigma. These requirements are presented in a specification format.

1.0 Vibration Isolation, Alignment and Leveling System

This specification states the requirements for a vibration isolation, alignment and leveling system to be used to support three orthogonally mounted RGG sensors. This system shall consist of a vibration isolation mount subsystem and a stabilized platform subsystem. The requirements stated herein shall apply for the total assembled system consisting of the vibration isolation mount, the stable platform, and three RGG sensors including sensor electronics. The system shall be capable of meeting the specified performance throughout a 10,000-hr operating life, with a minimum of 1000 warm-up cycles,

2075-42

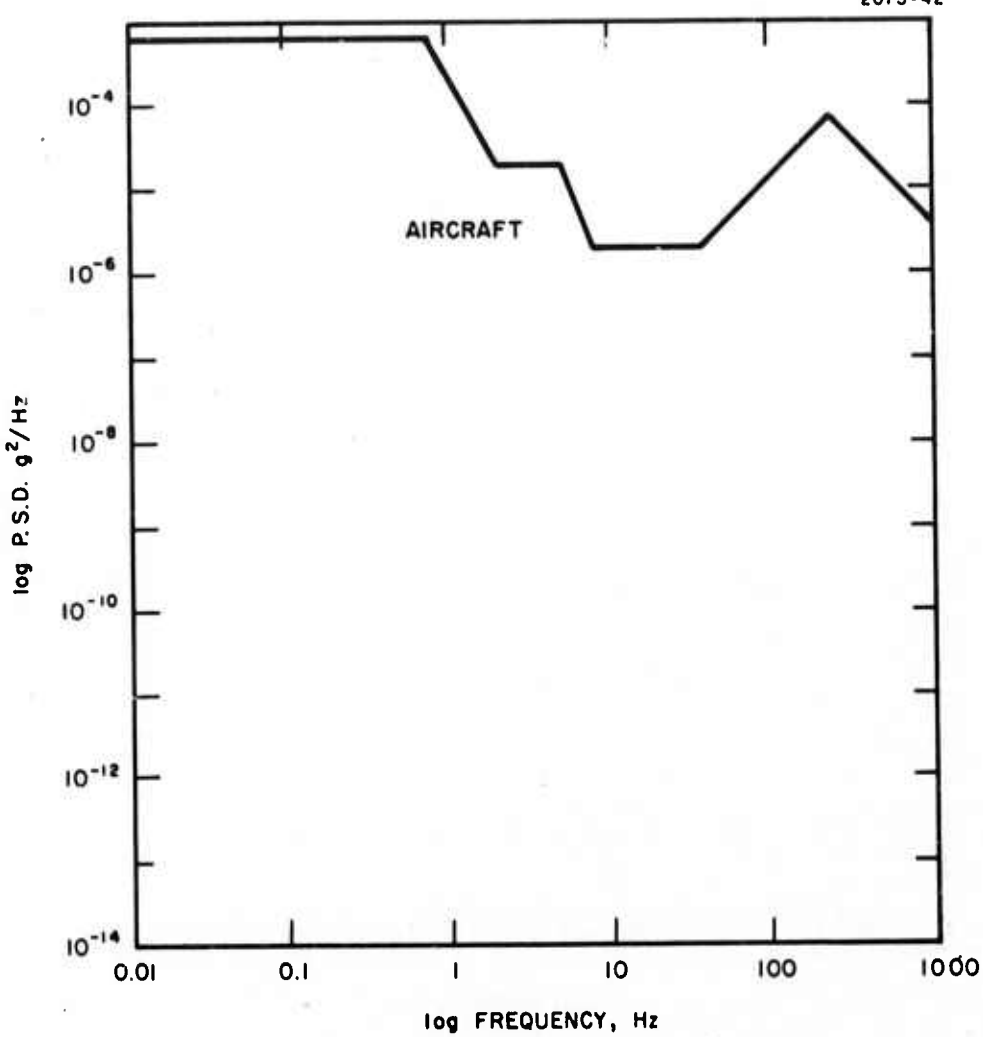


Fig. VIII-1. Acceleration Power Spectra.

2075-41

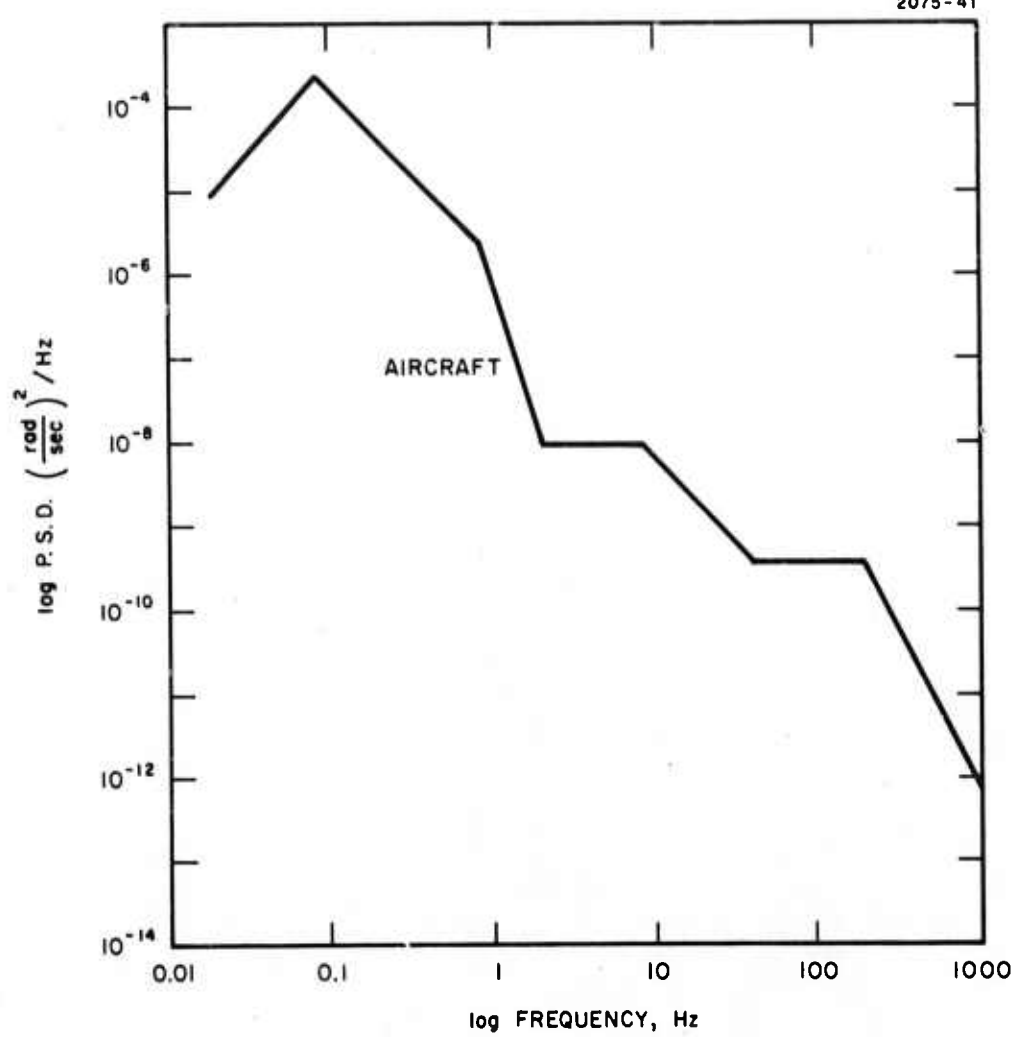


Fig. VIII-2. Angular Rate Power Spectrum.

SECTION VIII

at any time during a 2-year period following delivery, when exposed to any and all combinations of the aircraft operating environment specified herein.

2.0 Environment-Operating

The VIALS system will be used to support the three RGG sensors for collection of gravity gradient data in a jet aircraft. After takeoff and climb to cruise altitude, the aircraft will be flown in a straight and level cruise condition during non-turbulent weather conditions while data is being taken. The airborne operation is at a subsonic speed, approximately 400 to 500 mph at a constant cruise altitude of between 25,000 to 35,000 ft in a multiengine jet aircraft such as the KC-135. A nominal cabin temperature of $72^{\circ}\text{F} \pm 3^{\circ}$ will be maintained. The aircraft motion environment shown in Figures VIII-1 and VIII-2 is applicable and applies to all axes. A cabin pressure of between sea level and 10,000 ft equivalent pressure altitude will be maintained at all times.

3.0 Functional and Performance Requirements

3.1 Vibration Isolation Mount - The vibration isolation mount shall support the weight of the stable platform and 3 RGG sensors and sensor electronics. It shall provide isolation in six degrees-of-freedom of the isolated load with respect to the aircraft mounting reference. A right-handed x, y, z aircraft body-fixed orthogonal reference coordinate system centered at the aircraft mounting reference is defined with x along the aircraft's fuselage reference line, z along the nominal vertical and y normal to x and z. The isolated load is defined to consist of the portion of the vibration mount rigidly affixed to the base of the stable platform, the stable platform, and its 3 RGG sensor and electronics payload. The mount shall provide three translational degrees-of-freedom along x, y, and z and three rotational degrees-of-freedom

SECTION VIII

about x, y, and z of the isolated load with respect to the aircraft mounting reference.

3.1.1 Load Capacity and Dynamic Range Requirements - The vibration isolation mount shall provide the specified vibration attenuation while supporting its payload and while being exposed to the vibration spectra specified in paragraph 2.0. Additionally, it must provide the specified vibration attenuation and not exceed the inertial and elastic coupling limits specified in paragraph 3.1.2 when exposed to aircraft maneuver loads of 0.1 g.

3.1.2 Inertial and Elastic Coupling - The vibration isolation mount shall limit inertial and elastic coupling between the six degrees-of-freedom as required below.

3.1.2.1 Elastic Center - The vibration isolation mount shall have a nominal elastic center defined by a point such that application of an incremental force (not to exceed 0.1 g maneuver load factor) at that point in any direction shall result in pure translation of that point and no rotation about that point of the isolated load with respect to the aircraft mounting reference.

Deviations from this defined nominal elastic center shall be limited as follows. The elastic center may not vary by more than ± 0.2 in. from its average location as a function of the direction of the incremental load. Its average location shall be defined by determining the average of the elastic center locations found by applying 0.1 g incremental loads, one at a time, in each of the three cardinal x, y, and z directions.

3.1.2.2 Mass Balance - The vibration isolation mount shall be equipped to provide for mass balancing of its isolated load. This required mass balance adjustment equipment shall be capable of adjusting the isolated load's center of mass to within ± 0.1 in. of the average elastic center as defined in paragraph 3.1.2.1.

SECTION VIII

3.1.3 Translational Vibration Attenuation - The vibration isolation mount shall provide for isolation of translational vibration in all three axes. The translational isolation performance in any axis shall be equal to or exceed the performance characterized by a second-order linear system having an undamped natural frequency of 1 Hz and a damping ratio of 0.4.

3.1.4 Rotational Vibration Attenuation - The vibration isolation mount shall provide for isolation of rotational vibration about all three axes. The isolation performance in any axis shall be equal to or exceed the performance characterized by a second-order linear system having an undamped natural frequency of 2.5 Hz and a damping ratio of 1.0.

3.2 Stable Platform - The stable platform shall meet the following performance requirements while supporting the three RGG sensors and electronics and when mounted on the vibration isolation mount whose characteristics are specified in paragraph 3.1 above.

3.2.1 Reference Stabilization Axes - The stable platform shall provide three-axis stabilization such that a locally level, true north referenced stable element orientation is maintained. (It is only required that a true north reference be available, e.g., an "azimuth wander" system mechanization is fully acceptable.)

3.2.2 Angular Freedom - The stable platform shall be capable of accommodating aircraft motion excursions of $\pm 30^\circ$ in pitch and roll while in any heading orientation. Aircraft heading variations of more than 360° shall be accommodated.

3.2.3 Gimbal Readout - Angle transducers providing an output signal proportional to gimbal angle for each of the three axes will be required for compensation of the RGG output due to mass proximity effects. These transducers shall have an over-all accuracy of at least one (1) arc minute. Note that this requirement is in addition to

SECTION VIII

any resolvers associated with the stabilization servo loops of the platform.

3.2.4 Angular Alignment Accuracy - Initial alignment accuracy and allowable drift limits are as specified below.

3.2.4.1 Platform and RGG Initialization - The accuracies required for initial alignment of the three-sensor cluster are as follows:

Vertical: 2.5×10^{-4} radian, 1 sigma, with respect to the local plumb-bob vertical.

Azimuth: 5×10^{-4} radian, 1 sigma, with respect to the reference stabilization axes north reference.

After initial alignment of the three-sensor cluster, RGG initialization will be accomplished. This RGG initialization process may require up to one hour to complete. The platform drift and angular motion steadiness requirements of paragraphs 3.2.4.2 and 3.2.5 shall apply during this RGG initialization period. No retrimming or adjustment of the stable platform can be allowed at any time during the ensuing 10-hr operational run after RGG initialization has commenced.

3.2.4.2 Allowable Drift - The stable element angular orientation shall not drift from the initially aligned reference stabilization axes orientation by more than the following amounts for flight durations of up to 10 hr:

Level: 5×10^{-5} radian, 1 sigma.

Azimuth: 5×10^{-4} radian, 1 sigma.

3.2.5 Angular Motion Steadiness - In addition to the long-term drift stability specified in paragraph 3.2.4.2, angular oscillations of the stable element shall be limited by the following criteria.

3.2.5.1 - The integral overall frequencies of the angular rate power spectral density about any axis of the three-sensor cluster shall not exceed $10^{-10} (\text{rad/sec})^2$.

SECTION VIII

3.2.5.2 - The requirement specified in paragraph 3.2.5.1 above is a simplified statement of the angular rate steadiness requirement. The above requirement is based upon somewhat conservative assumptions regarding spectral co- and cross-correlations of angular rates about the three orthogonal axes. In Section IX, "Error Analysis" and in Technical Report No. 1, pp 38-46, "Covariance Functions of the Rotational Field Errors of the RGG," the precise relationship between these angular rate spectral properties and the resultant gravity gradient tensor element errors are defined. It is required that the rotational field error, induced as a result of angular rate jitter of the three-sensor cluster, of any of the gravity gradient tensor elements be limited to 10^{-10} (rad/sec)², 1 sigma. If desired the above requirements may be substituted for the simplified requirement of paragraph 3.2.5.1.

3.2.5.3 Angular Rate Compensation - The angular rate steadiness requirements of paragraph 3.2.5.1 or 3.2.5.2 may be relaxed if a suitable system of angular rate sensors is provided. This system of angular rate sensors shall be capable of measuring and providing compensation signals to each RGG sensor with measurement and data processing accuracies consistent with the angular rate steadiness specified in paragraphs 3.2.5.1 or 3.2.5.2.

3.2.6 Stable Platform Computer - A stable platform computer will be required whose accuracy is compatible with meeting the angular alignment accuracy requirements of paragraph 3.2.4 and the angular motion steadiness of paragraph 3.2.5.

3.2.7 Payload Description - The weight and size of the three RGG sensors and their associated stable element mounted electronics is as follows:

SECTION VIII

Sensor:	Weight - 25 lb Size - 6-in. dia x 8-in. long cylinder
Electronics:	Weight - approx 10 lb Size - volume $\cong 0.2 \text{ ft}^3$ may be packaged to accommodate stable element design
Compensation Accelerometer:	3 required. Wt - 1 lb Size - 2-in. dia x 1-in. long

3.2.8 Power and Signal Transmission - Slip rings or their equivalent will be required to transmit power to and signals to and from the specified payload equipment as follows:

ac power: a. 100 V, 60 to 100 Hz, 2-phase (90° phase shift) power

0.25 A run per leg plus 0.3 A return.

b. 28 V, 400 Hz, 3-phase, 100 W.

dc power: 2 A at 28 V dc.

signals: Provision for approximately 32 signal channels.

3.2.9 Mechanical Impedances:

3.2.9.1 Vibration Isolation Mount - The stable platform shall be capable of meeting the performance specified herein when mounted on the vibration isolation mount specified in paragraph 3.1.

3.2.9.2 Reaction Torques from Payload

- a. **Sensor Rotor Mass Unbalance** - Each sensor's rotor mass unbalance shall not exceed 7.5×10^{-5} lb-in. Each sensor is operated at a nominal spin frequency of 1050 rpm.
- b. **Sensor Angular Momentum** - The angular momentum of each sensor is 2.24×10^7 gm-cm²/sec.

SECTION VIII

4.0 Test Requirements - Due to the preliminary nature of this specification, no detailed qualification or acceptance test requirements are included herein. Because the intended application of this system is for military purposes, appropriate military specifications will be applicable.

D. BASIS FOR VIALS REQUIREMENTS

This section summarizes the basis of the important performance requirements imposed by the above VIALS specification.

The vibration isolation mount is required primarily to attenuate aircraft translational vibration. The predominant RGG sensor errors caused by translational vibration are arm differential mass unbalance and arm anisoelastic properties. A secondary benefit of the vibration isolation mount is to reduce the oscillatory angular motions of the aircraft from the base of the inertial platform. This aids in reducing friction-coupled disturbance torques to the platform's stable element.

The requirements to minimize the inertial and elastic coupling are necessary to: (1) limit the amount of angular motion of the stable platform's base induced by aircraft translational vibration, and (2) to limit the amount of translational motion of the stable platform's base induced by aircraft angular vibration.

The specified 1.0 Hz translation natural frequency with 0.4 damping ratio second order transmissibility requirement limits the translational vibration spectra of the stable platform. Similarly, the specified 2.5 Hz rotational natural frequency with 0.4 damping ratio along with the specified elastic center/mass balance requirements limits the rotational vibration spectra. A system designed with these specified characteristics will attenuate the aircraft translational and rotational vibration spectra as shown in Figs. VIII-3 and VIII-4. The resultant translation spectra has been used to estimate the RGG errors associated with translational vibration. These results are shown to be within the required limits consistent with the over-all accuracy requirement of 1 EU in the Error Analysis, Section IX.

SECTION VIII

The stable platform is required to provide azimuth and vertical stabilization and the final stage of angular rate isolation. An analysis of the errors resulting from initial misalignment and drift of the stable platform is shown in Section IX. Briefly, angular orientation errors cause fictitious inputs to the gradiometer which result in apparent gradient component values that would be interpreted as true gravity gradient signals. Because of the relatively large nominal gradients of the earth (3000 EU vertical and 1500 EU horizontal), relatively large errors of the off-diagonal gradient tensor components (which are proportional to the sine of the tilt error angle times these large nominal gradient values) can result.

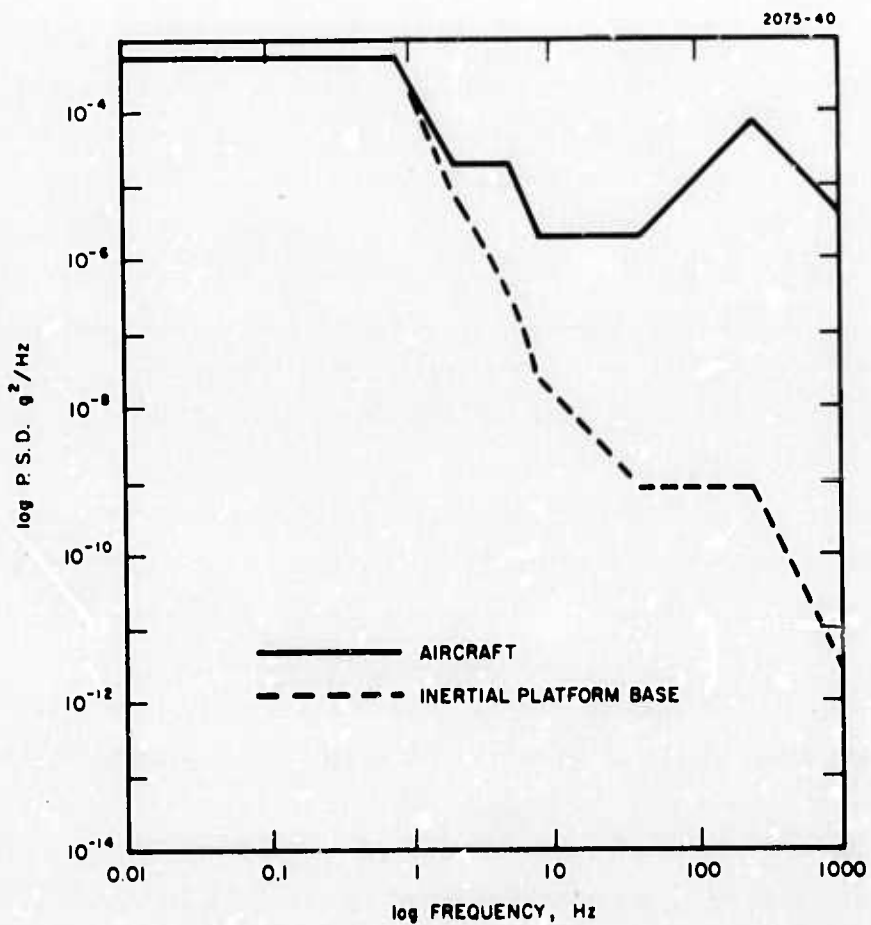


Fig. VIII-3. Acceleration Power Spectra.

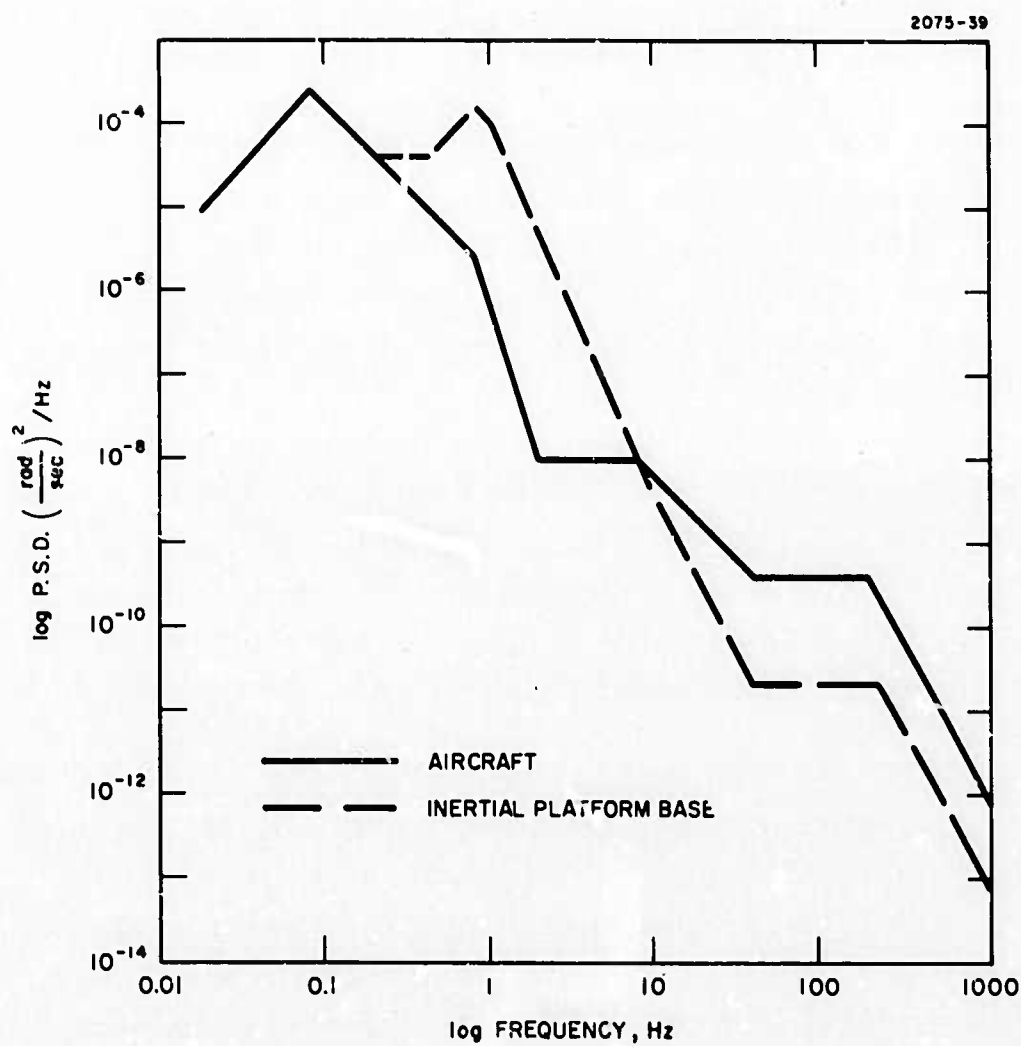


Fig. VIII-4. Angular Rate Power Spectrum.

SECTION VIII

The specified angular rate steadiness requirement is imposed primarily to limit rotational field errors of the gradiometer. The specified requirement translates to limiting these rotational field errors of the tensor components to 0.1 EU, 1 sigma.

The requirement for $\pm 30^\circ$ gimbal travel in pitch and roll is consistent with aircraft attitudes which can occur during takeoff and landing. The full freedom in azimuth is required to not limit the survey aircraft's heading. During an operational run, it might be desired to retrace a course or fly a criss-cross pattern for purposes of data correlation.

Gimbal angle transducers are required to compensate for the effects of proximate masses aboard the aircraft as heading and attitude change. The influence of aircraft proximate masses has been studied in detail and is discussed in the September 1971 HRL Technical Proposal, Appendix I (see Section V-D). This study shows that the primary item of concern is the proximate mass effects of the stable platform gimbals.

E. VIBRATION ISOLATION MOUNT DESIGN CONSIDERATIONS

Hughes has conducted earlier studies of three types of softly sprung vibration isolation systems. Detailed results are shown in the September 1971 HRL Technical Proposal, Appendix F (see Section V-D). These studies have considered three types of spring-damper elements and several linkage arrangements utilizing these elements. The three elements considered were: (1) a coil spring with a parallel viscous damper, (2) an elastomer element (Bungee chords), and (3) an air-column isolator.

The results of these studies have indicated the use of an air-column spring-damper element to be the most appropriate. Elements of this type are readily available. They are in widespread usage in bus suspension systems. Laboratory vibration isolation test tables using the bus type suspension for support of a granite-top table, with a pneumatic servo controlled leveling feature, are available from several

SECTION VIII

manufacturers, including Modern Optics Corp., Barry Corp., and Newport Research Corp. Barry Corp. also makes a smaller unit referred to as Barry Servo-Level, which also has a similar pneumatic servo that utilizes a simple mechanical linkage feedback control. All air-column isolators of this type have the desirable characteristics of providing vibration isolation efficiency equal to that of a virtually unamped second-order system at high frequencies while providing near critical damping (transmissibility of less than 1.5) at the system resonant frequency.

An arrangement of six of these isolators in an axisymmetric linkage is proposed. The arrangement is depicted in Figure VIII-5. Each end of each isolator element is connected by a spherical joint, one end to the stable platform and its opposite end to the aircraft floor. This arrangement is novel, because if the axis of each adjacent isolator is extended, they meet at a point. These intersections of each adjacent set of isolator axes form six of the eight corners of a cube, while the isolators themselves lie along six of the edges of the cube. The dotted lines of Figure VIII-5 indicate the remaining six edges of the cube. Therefore, any given vibration force directed parallel to one of the edges of this cube cause equal loads on the two isolators that lie along these parallel edges. The result of such an arrangement is an isoelastic structure in the sense that it has equal translational spring rates in all directions of force application. Similarly, it has equal rotational spring rates, regardless of torque direction. By proper placement of the center of mass of the supported load, this structure also will not induce angular rates into the load caused by linear vibrations of the vehicle, nor will it induce linear vibrations into the load caused by angular vibrations of the vehicle.

Each of the six isolators is supplied with air via a simple mechanically actuated servo valve. The mechanical linkage is arranged so that if the isolator extends beyond a certain point in one direction, the valve bleeds air out of the isolator, and if the isolator extends beyond a certain point in the opposite direction, the valve bleeds supply air into the isolator. The time constant of this servo action is

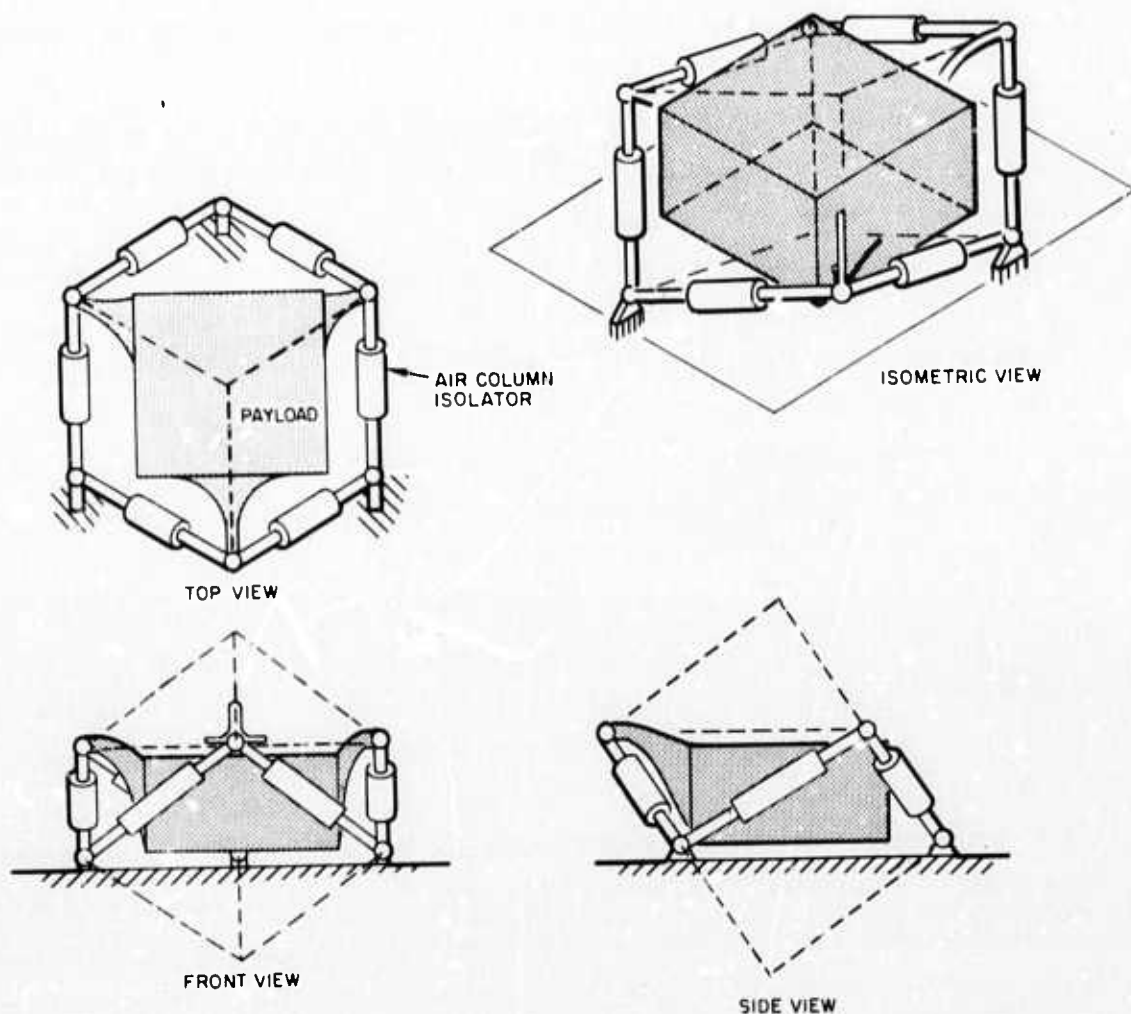


Fig. VIII-5. Six-Element Axisymmetric Linkage Air Column Vibration Isolation Mount.

SECTION VIII

long compared with the period of the vibration disturbances of concern. The predominant error sensitivity of the RGG is caused by vibration at one and three times its spin frequency of 17.5 Hz. In the previous subsection, it was indicated that sufficient isolation would be provided with a linear second-order system with a natural frequency of 1.0 Hz and a damping ratio of 0.4. Use of the air-column element with its natural frequency set at 1.0 Hz would provide more than adequate attenuation of the sensitive frequencies of 17.5 and 52.5 Hz.

F. STABLE PLATFORM DESIGN CONSIDERATIONS

As discussed in Section VII, it has been determined by surveys of industry and Government inventories that a stable platform meeting the combined long-term accuracy and payload requirements is not currently available. It has, therefore, been assumed that a platform development will be necessary to meet this dual requirement.

A requirement of this study is to demonstrate the current state-of-the-art feasibility of components of the required VIALS. Two areas of the stable platform performance requirements were considered potentially difficult: (1) the level and azimuth accuracies, and (2) the angular rate isolation requirements. These subjects are discussed below. These topics are followed by a discussion of the design approach and a brief physical description of the recommended operational system prototype design concept.

1. Level and Azimuth Stabilization Accuracy

Three approaches are available to provide the required level and azimuth accuracies. These methods consist of: (a) a pure (unaided) inertial mechanization, (b) an aided inertial mechanization, and (c) a master-slave mechanization.

a. Pure Inertial Mechanization

The gyros and accelerometers necessary to produce the level and azimuth stabilization accuracies for a pure inertial

SECTION VIII

mechanization approach are high quality inertial components, but they are well within the state of the art.

The required inertial component accuracies would be typified by the following performance parameters:

Gyros

Systematic drift rate uncertainty	$\pm 0.003^\circ/\text{hr}$
Random drift rate	$\pm 0.003^\circ/\text{hr}$

Accelerometers

Long-term bias stability	$\pm 10^{-4} \text{ g}$
Bias repeatability, warmup to warmup	$\pm 5 \times 10^{-5} \text{ g}$

The AN/USQ-28 Geodetic Mapping and Survey Subsystem uses a Bell Aerosystems Hipernas II-B stable platform with a Nortronics CP-720 digital computer. This system has demonstrated 10 arc sec, 1 sigma ($\approx 5 \times 10^{-5} \text{ rad}$) vertical accuracy and better than 60 arc sec ($\approx 2.5 \times 10^{-4} \text{ rad}$) azimuth accuracy in numerous flight tests on an RC135A aircraft. Results of this flight test program conducted at Eglin Air Force Base, Florida, are documented in a Bell Aerosystems report "Technical Note, Hipernas IIB 1969 Flight Test Performance, Eglin Missile Range", Report No. 6208-936002, February 1970. A copy of the Bell Aerosystems Hipernas II-B specification is reproduced herein as Figure VIII-6. It is understood that seven of these systems are presently available for appropriate Department of Defense programs. These inertial sensors and computer, mounted on a suitable RGG stable platform, would provide the necessary level and azimuth accuracy.

Several other classified inertial navigation systems which are now in operational usage are known to exist and could provide the necessary pure inertial level and azimuth accuracies. Performance specifications for these systems are not shown to avoid the necessity of placing security classification restrictions on this report.

b. Aided Inertial Mechanization

An aided inertial system utilizing high precision Loran, Transit, Doppler Navigation Radar, Position Fixes, and Star



III. HIPERNAS IIB

A. SPECIFICATION

The following is a specification defining the primary characteristics of the Hipernas IIB IRU:

1. Performance

Position error rate (CEP) 0.1 n.mi./hr for 12 hr
(See Figure III-1 for typical performance. Additional data in Appendix B)

Velocity error dc < 1 ft/sec
 0.001 ft/sec

Azimuth < 60 arcsec in 10 hr

Verticality 10 arcsec rms in 30 hr

Gimbal readout accuracy 30 arcsec max error

2. Number of gimbals

three

3. Reaction time

< 2.5 hr

4. Weight

150 lb

5. Size

3.7 cu ft

6. Inherent MTBF

500 hr

7. Packaging

Discrete components

8. Power Requirements

120/208 v rms, 3 phase, 400 Hz primary power in accordance with MIL-STD-704, provided the abnormal voltage transients are between limits 3 and 4 of that standard and do not occur more often than once per hour.

Power Consumption:

1500w start and warmup

450 w operate at 25°C

9. Mechanization

See Appendix A

Fig. VIII-6. Hipernas IIB IRU Specification.

SECTION VII

Trackers can be utilized. The extent to which these aids can reduce the accuracy requirements of the inertial sensors is dependent on the particular type of aids used, their inherent accuracy, and the degree of sophistication used to "marry" these aids to the pure inertial system. Incorporation of such aids adds considerably to the over-all system complexity. Because several pure inertial systems have the proven capability to meet the RGG requirement, a pure inertial mechanization is favored by Hughes.

c. Master-Slave Mechanization

This mechanization approach is attractive especially if the survey aircraft or carrying vehicle has or must have a primary inertial navigation system aboard for providing precision navigation station-keeping information. If this system itself had the specified long-term azimuth and level accuracy, it would serve as the master system to which the RGG stable platform would be slaved.

With this approach, only modestly accurate gyros and accelerometers would be required for the RGG stable platform system, typically level axis gyro bias stability of 0.01 deg/hr, azimuth axis gyro bias stability of 0.02 deg/hr, and accelerometer bias short-term stability of 1×10^{-4} g. The RGG platform would be a Schuler tuned mechanization. The slaving of the RGG platform to the master navigator would be accomplished using Kalman filter technique. The number of error states employed in this Kalman filter probably would be about eight or ten. The digital computer requirements to implement the required number of Kalman filter states would be modest. This filter would be implemented as part of the RGG platform management computer or possibly could be programmed in the management computer of the master navigator.

This master-slave approach could result in a satisfactory and attractive over-all system mechanization. Detailed studies would be required to determine the specific mechanization requirements of this approach and to compare its cost effectiveness to that of the pure inertial mechanization once the specific RGG application is defined.

SECTION VIII

2. Angular Rate Isolation Feasibility

Hughes has performed studies to determine the potential problems which might arise if the bulk of the angular rate isolation capability is to be provided by the RGG stable platform. In addition to the studies conducted by Hughes, an outside firm, Aeroflex Laboratories, Inc., Plainview, Long Island, New York, was hired to consult on this over-all angular rate isolation problem. Aeroflex was chosen as a consultant because of their very applicable experience in similar systems. They have developed many camera mounts and other large-payload airborne stabilization systems. They also have developed a product line of large capacity dc torque motors which are required by such systems.

The Hughes and Aeroflex studies revealed four potentially significant sources of platform stable-element disturbances:

- a. Platform stable-element and gimbal mass unbalance
- b. RGG rotor mass unbalance
- c. Stabilization gyro signal noise
- d. Platform gimbal bearing coulomb-type friction torque.

The most predominant disturbance source would result from platform friction if ball-type platform gimbal bearings were to be used. In Section VII, the amount of angular rate disturbance that could occur has been estimated to be approximately 14 times the amount that can be tolerated. Hence, ball-type bearings were ruled out. Several alternate gimbal suspension techniques have been considered. These all employ the use of hydrostatic gas bearings. Three types of mechanizations were considered: One suspension essentially replaces the conventional three-axis platform ball-type gimbal bearings with air bearings; the second type would utilize a hemispherical knuckle air bearing that would provide the required three-axis isolation; the third type would utilize a conventional three-axis ball bearing gimbal platform with a hemispherical knuckle air bearing between the

SECTION VIII

stable element of the ball bearing platform and the gradiometer and inertial sensor payload.

In any of these mechanizations, some form of slip rings or their equivalent are required to provide power inputs and signal inputs to and signal outputs from the inertial sensors and the three RGG's mounted on the stabilized element. Low-level signals could be transmitted via a telemetry link; however, the power inputs would require the use of slip rings or direct wires. Either would result in undesirably large disturbance torques. The use of slip ring follow-up servos, which essentially reduce the coulomb friction torque to zero, appear to be the best solution to this problem. Implementation of the slip ring follow-up servo is direct and straightforward for the three-axis gimbal bearing mechanization.

It is felt that torquing and angular motion detection of the three axes of freedom of the hemispherical air bearing mechanization would present very difficult design problems because of the relatively large ($\pm 30^\circ$) roll and pitch freedom and full azimuth freedom requirements. This problem would be reduced if the third mechanization were employed. However, even then, providing the power and signal communication between the three-gimbal platform stable element and the gradiometer and inertial sensor payload would be difficult.

Because of the above considerations, the three-gimbal air bearing approach has been selected as the preferred mechanization approach for the operational system prototype stable platform.

To estimate the magnitude of the four disturbance sources mentioned earlier, the pertinent design characteristics of the prototype stable platform were required. A preliminary design of the prototype platform was made, and estimates of these characteristics were generated. A description of the prototype platform and its design characteristics are presented in the next subsection.

The basis of computing the disturbance torques, the angular rates they produce, and the resultant rotational field errors of the gravity gradient components follows.

SECTION VIII

a. Platform Mass Unbalance

The presence of gimbal bearing coulomb friction torque masks the induced mass unbalance torques created by the earth's 1 g field. Hence, because of the very low friction torques associated with the use of air bearing gimbals, significantly better static mass balance of the gimbals and stable element can be achieved compared to a ball bearing gimbal suspension. As shown in a subsequent section, residual coulomb-type friction torques will remain even with air gimbal bearings. The estimated magnitude of these residual normalized friction torques (ratio of torque to platform moment of inertia) is 7.8×10^{-4} rad/sec². Ideally, the mass unbalance of the platform gimbals and stable element could be adjusted down to a level equaling this residual torque. Conservatively, it is estimated that adjustment to within ten times this level could be achieved, resulting in a normalized mass unbalance torque ratio of 7.8×10^{-3} rad/sec² per g.

The resultant rotational field error caused by angular rates induced by the aircraft vibration acting on the platform mass unbalance is estimated as follows. The power spectral density of the platform's mass unbalance normalized disturbance torque is given by the product of the square of the normalized disturbance torque ratio, 7.8×10^{-3} rad/sec² per g, and the estimated platform base acceleration power spectral density, S_A , from Fig. VIII-3, or

$$S_{T_d} = (7.8 \times 10^{-3})^2 S_A \quad (1)$$

disturbance torque, H_p , has been estimated and is shown in Fig. VIII-8. The power spectral density of the platform angular rate, S_ω , is obtained as shown in eq. 2.

$$S_\omega = |H(j2\pi f)|^2 S_{T_d} \quad (2)$$

The variance of the platform angular rate, σ_ω^2 , is obtained by integration of its power spectra over all frequencies as shown in eq. 3.

SECTION VIII

$$\sigma_{\omega}^2 = \int_0^\infty |H(j2\pi f)|^2 S_{T_d} df \quad (3)$$

The platform stable element angular rate variance has been evaluated using the estimated normalized mass unbalance and the data of the two figures. The resulting variance is 27.8×10^{-14} (rad/sec)² or a standard deviation of 5.3×10^{-7} rad/sec.

The worst case gradient tensor component error due to this rotational field input can be approximated by eq. 4.

$$\sigma_{\Gamma}^2 = \sigma_{\omega}^2 \quad (4)$$

Thus the estimated rotational field gradient error due to platform mass unbalance is 27.8×10^{-14} (rad/sec)² $\times 10^9$ EU/sec⁻² = 0.000278 EU and is negligible.

b. R. G. G. Rotor Mass Unbalance

The RGG rotor mass unbalance is expected to be trimmed and to remain stable within 2μ in., which corresponds to a pendulosity of 0.03 gm-cm. Results similar to this have been achieved on the earlier Hughes RGG experimental hard bearing sensor. The small centrifugal force resulting from rotor mass unbalance can create a disturbance torque at the sensor spin frequency proportional to the distance from the sensor rotor center of mass to the stable element center of rotation. This disturbance torque can create angular rates of the stable element, which in turn result in rotational field error. This error has been estimated and is very small. The basis of this estimate is as follows: The amplitude of the platform disturbance torque is given by the product of the distance from the sensor center of mass to the stable element center of rotation, d, times the pendulosity, p, times the square of the sensor spin frequency, ω_s , or

$$T_d = pd\omega_s^2 \quad (5)$$

SECTION VIII

The amplitude of the angular acceleration of the stable element is the torque divided by platform inertia, J , or

$$\ddot{\theta} = \frac{T_d}{J} = \frac{pd\omega_s^2}{J} \quad (6)$$

The angular rate response of the platform can be approximated by assuming a one-to-one correspondence between disturbance acceleration (normalized torque disturbance, T_d/J) and resultant platform angular acceleration. Thus the platform angular rate, $\dot{\theta}$, is just the integral of the angular acceleration, or its peak value is given by

$$\dot{\theta}_{peak} = \frac{\ddot{\theta}_{peak}}{\omega_s} = \frac{pd\omega_s}{J} \quad (7)$$

The root-mean-square angular rate will be

$$\dot{\theta}_{rms} = \frac{\dot{\theta}_{peak}}{\sqrt{2}} = \frac{pd\omega_s}{J\sqrt{2}} \quad (8)$$

Equation 8 is evaluated using for values of d and J , the values for the prototype platform shown in Table VIII-1:

$$p = 0.03 \text{ gm-cm} = 2.6 \times 10^{-5} \text{ lb-in.}$$

$$d = 5 \text{ in.}$$

$$J = 5,095 \text{ lb-in.}^2$$

$$\omega_s = 110 \text{ rad/sec}$$

$$\dot{\theta}_{rms} = \frac{2.6 \times 10^{-5} \times 5 \times 110}{5,095 \times \sqrt{2}} = 2.0 \times 10^{-6} \text{ rad/sec}$$

This will result in a rotational field error of $(2 \times 10^{-6})^2 \times 10^9 = 0.004 \text{ EU}$ which is negligible.

SECTION VIII

It should be noted that the assumed one-to-one correspondence between normalized torque disturbance and the resulting platform acceleration could be erroneous unless proper care is used in designing the platform servo transfer characteristics. The sensor spin frequency is in the range near the peak of the assumed servo transfer characteristic. Thus, the servo should be designed to avoid amplification of disturbance torques occurring near the sensor spin frequency.

c. Stabilization Gyro Signal Noise

Noise appearing at the output of the signal generator of the RGG stable platform gyro has been conservatively estimated to be no greater than $1.0^{\circ}/\text{hr rms}$ (or $4.85 \times 10^{-6} \text{ rad/sec}$) in the range of the platform servo bandwidth. This estimate is based on the use of an inertial quality gyro such as the BRIG-II-B used in the Hipernas II system. Due to its use of a gas spin bearing, subharmonics of its spin frequency (24,000 rpm = 400 Hz) will not be present as they are in a ball-type gyro spin bearing. Thus, gyro noise resulting from rotor mass unbalance, occurring at the spin frequency, will be significantly removed from the platform servo bandwidth and thus highly attenuated.

d. Platform Coulomb Friction Torque

With the predominant coulomb-type friction torques associated with ball-type gimbal bearings removed, other residual sources of coulomb torque must be examined. The two remaining residual torques estimated by Aeroflex are those created by slip rings and residual platform gimbal torque motor torques.

A rough count was made of the number of power and signal slip rings that would be required. The estimated number of slip rings was 80, and their anticipated coulomb friction torque was estimated to be 8 oz-in. This friction torque estimate is based on assuming a normal contact pressure of 2 oz per ring with two contacts per ring to prevent contact noise by redundancy, a coefficient of friction of 0.05 and a friction radius area of 0.5 in.

SECTION VIII

The torque motor torque is characterized by a coulomb friction torque and a positional torque varying periodically with rotation as a result of residual error of symmetry in the magnetic path. This coulomb torque is due to hysteresis in the soft magnetic stator and is dependent on its material. For conventional materials in the size torquers that would be suitable for this application, a coulomb torque of about 0.0035 in.-lb would be expected. The equivalent coulomb friction associated with the positional torque would be of the level of 0.007 in.-lb.

The subsequent analysis shows that the 8 oz-in. estimated coulomb friction of the slip-rings would result in intolerable rotational field errors. A significant reduction of these torques can be obtained through the use of follow-up servos on each axis of the stable platform. A proprietary device produced by Aeroflex, known as a Rotary Electro-Bridge, could also be used to reduce the usual friction associated with slip rings. This device, used in conjunction with a follow-up servo, would result in a very attractive mechanization. This technique has been used on a number of platforms recently manufactured by Aeroflex. This would essentially reduce the friction torques produced by wiring across the gimbals to negligible values.

The residual torques associated with the gimbal torque motors can be reduced by using higher quality laminations and materials in the torque motors. However, this does not appear to be necessary.

An estimate of the angular rate and the resultant gravity gradient component rotational field error associated with the estimated coulomb friction torques can be made as follows: The total estimated coulomb friction torque is the sum of the two types of torque motor torques or 0.0105 in.-lb. The normalized disturbance torque, using the minimum azimuth axis platform moment of inertia, is

$$\frac{T_d}{J} = \frac{0.0105 \times 386.4}{5,095} = 7.8 \times 10^{-4} \text{ rad/sec}^2.$$

A method of computing a worst-case, upper bound of the standard deviation of platform angular rate is shown in Appendix B. Using this

SECTION VIII

technique, the above normalized torque disturbance, and the estimated prototype platform servo bandwidth of 100 rad/sec, the resultant standard deviation of friction induced angular rate is 7.8×10^{-6} rad/sec. The corresponding gravity gradient component rotational field error is 0.061 EU.

Summarizing, the induced rms angular rates and the resultant gravity gradient component rotational field errors have been estimated for the four sources of stable platform disturbance considered potentially significant. These estimates are summarized below.

<u>Disturbance Source</u>	<u>rms Angular Rate ~ rad/sec</u>	<u>Rotational Field Error ~ EU</u>
Platform mass unbalance	0.53×10^{-6}	0.00028
RGG rotor mass unbalance	2.0×10^{-6}	0.004
Stabilization gyro signal noise	4.85×10^{-6}	0.024
Platform coulomb friction	7.8×10^{-6}	0.061

3. Angular Rate Compensation Alternative

We have considered as an alternative, use of compensation techniques to reduce the rotational field error induced by vehicle motion. A cursory examination of the angular rate sensing requirements reveals the following. Sensors to measure the low frequency angular rates are readily available. Such sensors would take the form of floated rate-integrating gyros used in a closed loop mode. These sensors would be capable of sensing relatively large angular rates (up to approximately $300^\circ/\text{hour}$ or 1.5×10^{-3} rad/sec). However, their sensing bandwidth is limited to approximately 10 to 15 Hz. To sense oscillatory angular rates above the rate gyro bandwidth, angular accelerometers could be used. Such devices also are feasible and available.

The question of feasibility of the angular rate compensation scheme lies in the quality and characteristics of the stable platform. This platform would have to be of high quality, have high stiffness gimbals and an especially stiff, high resonant frequency stable element

SECTION VIII

design for mounting the three RGG's. High frequency angular rates would have to be limited since their measurement would be difficult.

Processing of the measured angular rate data is required to form the squares and products of angular rate components. Limitations on the amplitude and frequency of the allowable angular rate jitter would have to be imposed to limit the bandwidth of the required data processing equipment.

The Hughes preference regarding angular rate isolation versus compensation for an operational system of three RGG sensors would be to limit angular rate jitter by appropriate platform design. Angular rate compensation could be considered as a back-up.

For early moving base vehicle testing of the RGG, utilization of angular rate compensation techniques could be an attractive approach, since a crude angular rate compensation system would undoubtedly be less expensive than development of the ultimate operational system platform.

4. Prototype Platform Characteristics

A preliminary design of the prototype operational system platform has been made. The three-view sketch in Fig. VIII-7 illustrates the design concept. The basic platform configuration is a pseudo inside-out gimbal arrangement. Because of the relatively large size of the air bearings, this inside-out arrangement is not very obvious.

The dumbbell-type arrangement of the stable element payload provides for mounting of the two horizontal (x and y) spin-axis RGG's on the lower side and the vertical spin-axis (z) sensor, its electronics, the inertial components and their electronics on the upper side. The space between the upper and lower sensor groups provides room for the azimuth air bearing, torquer, resolver, and slip ring follow-up servo. The stable element structure would be an aluminum casting. The azimuth air bearing would be of the spool type providing thrust and radial support in the single bearing.

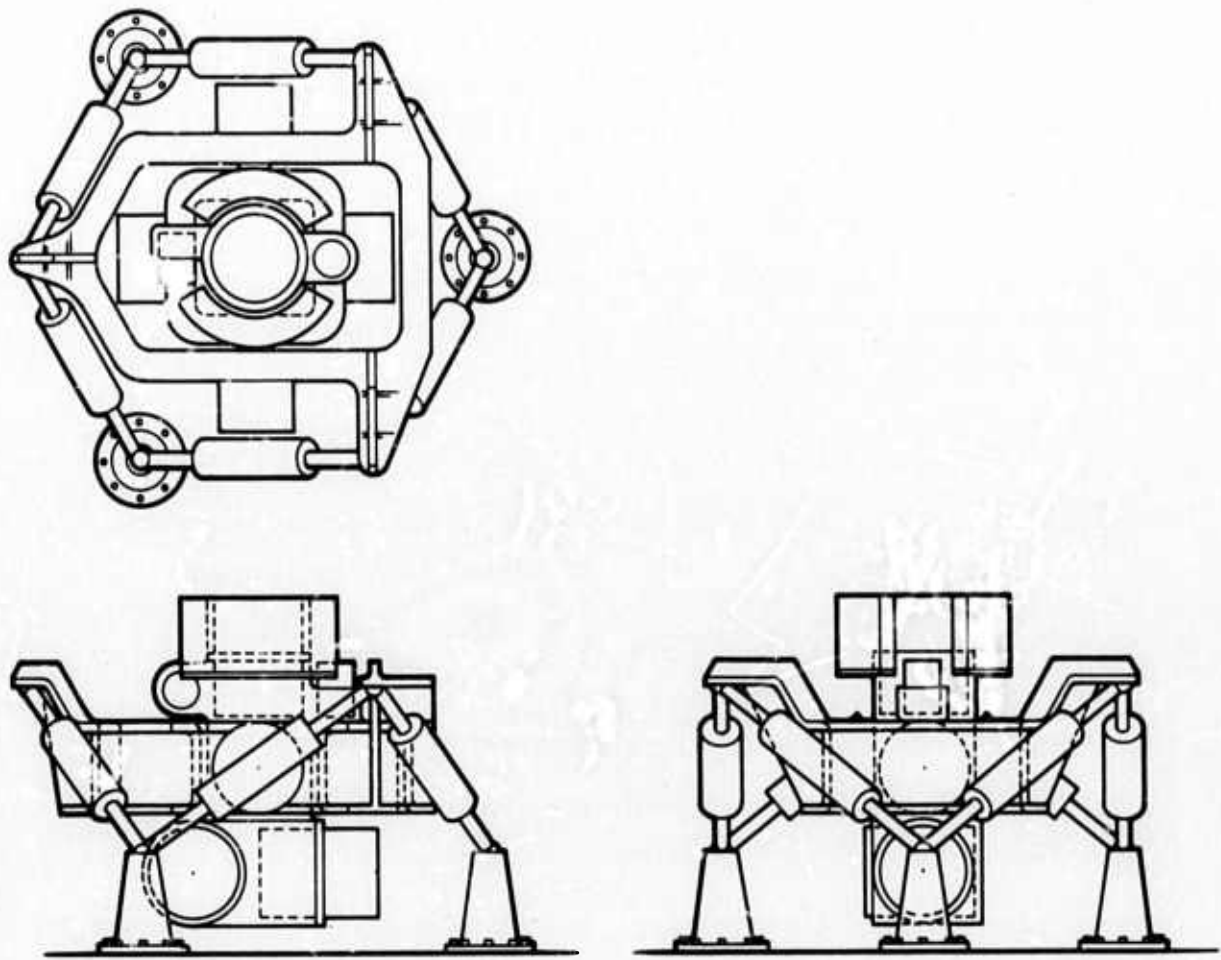


Fig. VIII-7. Three-Axis Air Bearing Stabilized Platform.

SECTION VIII

Dual air bearings for the middle and outer gimbal ring members also would be of the cylindrical type. One end would be a simple cylindrical bearing, while the opposite end would be a spool-type to accommodate thrust loads. The middle and outer ring members would be fabricated from a box or channel section to provide maximum stiffness possible.

Mass, center of gravity, and moment of inertia estimates have been generated and are shown in Table VIII-1.

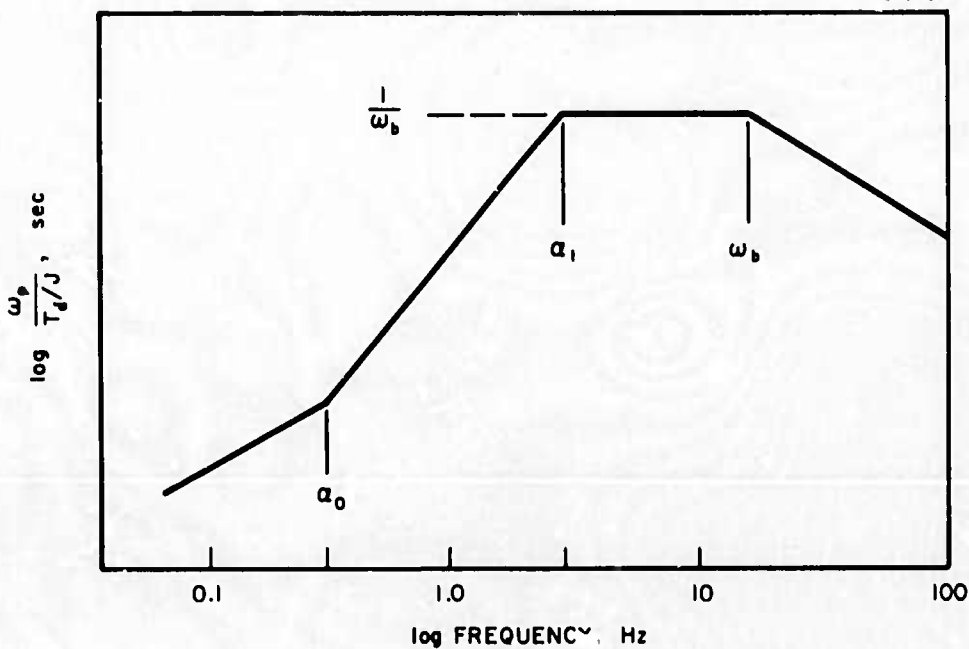
Design of the stabilization servo loops has not been undertaken. An estimate of the approximate angular rate to disturbance torque transfer function and a plot of its asymptotes is shown in Fig. VIII-8. The gyroscopic feedback torques resulting from the angular momentum of the three RGG sensors is negligible compared to the platform servo feedback gain; however, this momentum should be considered in the detailed servo design to avoid instabilities.

G. ANISOELASTIC COMPENSATION ACCELEROMETERS

It is proposed, as discussed in Sections IX and XXIII, to compensate the anisoelastic errors of the RGG by using active acceleration compensation. Accelerometers used to serve as the basic sensing element for this compensation scheme are required to be of a good inertial quality. The accuracy requirements for anisoelastic compensation and for stable platform alignment and stability are similar. However, the feasibility and practicality of using the platform's inertial reference system accelerometer signals for anisoelastic compensation will depend on the particular method selected to mechanize the platform's inertial reference system.

In the event that it is not desirable to make dual use of the platform's inertial reference system accelerometers, separate anisoelastic compensation accelerometers will be required. An accelerometer whose performance is typical of that required is the Bell Aerospace

1075-38



$$\frac{\omega_p}{T_d/J} = \frac{s(s + \alpha_0)(s + \omega_b)}{(s + \alpha_1)^2(s^2 + 2\xi\omega_b s + \omega_b^2)}$$

$$\alpha_0 = 0.3 \text{ Hz}$$

$$\alpha_1 = 3.0 \text{ Hz}$$

$$\omega_b = 16 \text{ Hz}$$

$$\xi = 0.7$$

Fig. VIII-8. Estimated Platform Angular Rate Response to Normalized Torque Disturbance.

SECTION VIII

TABLE VIII-1

**Prototype Stable Platform - Preliminary Weight,
c, g, and Moment of Inertia Estimates**

- x = Outer gimbal axis
- y = Inner gimbal axis
- z = Stable element azimuth axis
- I_x, I_y, I_z = Moments of inertia of individual gimbals or stable element
- I'_x, I'_y, I'_z = Moments of inertia of composite system assuming gimbal angles are zero
- W = Weight of individual gimbals or stable element

	W (lb)	\bar{x} (in.)	\bar{y} (in.)	\bar{z} (in.)	I_x (lb-in. ²)	I_y (lb-in. ²)	I_z (lb-in. ²)
Stable Element							
x Spin Axis RGG	21.3	0	-5	-9.5	2,610	2,070	680
y Spin Axis RGG	21.3	0	+5	-9.5	2,602	2,078	688
z Spin Axis RGG	21.3	0	0	+9.5	2,070	2,070	148
Electronics & Inertial Components	21.3	0	0	+9.5	3,051	2,536	1,129
Air Brg & Structure	50.0	0	0	0	1,250	1,250	2,450
Total	135.2	0	0	0	11,583	10,004	5,095
Inner Gimbal	24.5	0	0	0	654	237	725
Outer Gimbal	37.4	0	0	0	1,624	816	1,554
$I'_x = 11,583 + 654 + 1624 = 13,861 \text{ lb-in.}^2$							
$I'_y = 10,004 + 237 = 10,241 \text{ lb-in.}^2$							
$I'_z = 5,095 \text{ lb-in.}^2$							

SECTION VIII

Model IX Acceleration Transducer. Its performance is characterized by the following:

Long-term bias stability	$\pm 10^{-4}$ g
Short-term (10 hr) bias stability	$\pm 10^{-5}$ g
Threshold and resolution	5×10^{-7} g

SECTION IX

ERROR ANALYSIS

The following subsections treat specific RGG error mechanisms in detail. The propagation of the various errors differs considerably. Some of the errors are correlated and others are independent. Each of the subsections deals with a particular class or type of error and shows how these are propagated to the gravity gradient tensor.

A. ARM MASS UNBALANCE ERRORS

When the center of mass of an arm does not lie on the principal torsional axis (\bar{k}) of the RGG, an error moment is developed by acceleration of the arm center of support. The difference of the mass unbalance moments of each arm which act about the torsional axis constitutes an input error moment to the differential mode of the RGG. This input error moment may be expressed as the difference of the vector products of the arm center of support accelerations (\bar{a}_i) and the arm "pendulosities" (\bar{p}_i) as (1).

$$L_k = \bar{k} [\bar{a}_1 \times \bar{p}_1 - \bar{a}_2 \times \bar{p}_2] \quad (1)$$

where

$$\bar{p}_i = m_i \bar{h}_i$$

and

m_i = arm mass

\bar{h}_i = center of arm mass position vector normal to \bar{k} .

L_k = input error moment about \bar{k}

SECTION IX

The error moment of (1) contains two types of mass unbalance errors, "differential arm mass unbalance" and "axial arm mass unbalance." This error decomposition is illustrated in (2) and (3).

$$L_d \triangleq \bar{k} \cdot [\bar{a}_o \times (\bar{p}_1 - \bar{p}_2)] \quad (2)$$

$$L_a \triangleq \bar{k} \cdot [\bar{\Delta a} \times (\bar{p}_1 + \bar{p}_2)] \quad (3)$$

where

$$\bar{a}_1 \triangleq \bar{a}_o + \bar{\Delta a}$$

$$\bar{a}_2 \triangleq \bar{a}_o - \bar{\Delta a}$$

The average acceleration (\bar{a}_o) of the arm structure is taken at a point on the torsional axis midway between the arm mass centers, and the differential arm acceleration ($\bar{\Delta a}$) becomes a function of the axial mass center separation (\bar{l}) along the torsional axis as defined by (4).

$$2\bar{\Delta a} = \dot{\omega} \times \bar{l} + [\bar{\omega} \times (\bar{\omega} \times \bar{l})] \quad (4)$$

The difference and sum of the arm "pendulosities" that appear in (2) and (3) are defined, for analytical convenience, as the "differential arm mass unbalance" and the "axial arm mass unbalance" by (5) and (6).

$$\bar{p}_d \triangleq (\bar{p}_1 - \bar{p}_2) \quad (5)$$

$$\bar{p}_a \triangleq \frac{1}{2} (\bar{p}_1 + \bar{p}_2) \quad (6)$$

Substitution of (5) and (6) into (2) and (3) yields the two types of arm mass unbalance error moments as (7) and (8).

$$L_d = \bar{k} \cdot [\bar{a}_o \times \bar{p}_d] \quad (7)$$

SECTION IX

$$L_a = \bar{k} \cdot [2\bar{\Delta a} \times \bar{p}_a] \quad (8)$$

Observe that the mass unbalance vectors, \bar{p}_d and \bar{p}_a , are both normal to the torsional axis (\bar{k}). For convenience in error evaluation, expansions of the differential arm mass unbalance input error moment of (7) in both the rotor reference frame (ijk) and the stator reference frame (xyz) are presented as (9) and (10).

$$L_d = a_i p_{dj} - a_j p_{di} \quad (9)$$

$$L_d = a_x p_{dy} - a_y p_{dx} \quad (10)$$

The rotor-referenced mass unbalances, (p_{di}, p_{dj}) are constants, and the stator-referenced mass unbalances, (p_{dx}, p_{dy}) are periodic functions of the rotor spin frequency (ω_s).

Similarly, expansion of the axial arm mass unbalance input error moment of (8), employing (4), yields (11) and (12) in rotor and stator reference frames, respectively.

$$L_a = l p_{ai} [\dot{\omega}_i - \omega_j \omega_k] + l p_{aj} [\dot{\omega}_j + \omega_i \omega_k] \quad (11)$$

$$L_a = l p_{ax} [\dot{\omega}_x - \omega_y \omega_z] + l p_{ay} [\dot{\omega}_y + \omega_x \omega_z] \quad (12)$$

The input error moments to the RGG signal process in a narrow frequency band centered at twice the spin frequency ($2\omega_s$) will propagate to output gravity gradient measurement errors. This property of the RGG signal process infers a particular spectral sensitivity to the mass unbalance driving functions. For example, the differential arm mass unbalance error is sensitive to the second spin harmonic of the rotor-referenced accelerations (a_i, a_j) and to the fundamental and third spin harmonic of the stator-referenced accelerations (a_x, a_y).

SECTION IX

These same statements apply to the angular velocity and acceleration driving functions of the axial mass unbalance error functions of (11) and (12).

Consideration of the different spectral properties of the error driving functions in both the rotor and stator reference frames may seem an unnecessary complexity at this point. However, the added complexity here provides a flexibility in the evaluation of the errors later on since both rotor-referenced and stator-referenced specifications of the driving functions may be treated directly without the necessity of coordinate conversion.

In order to evaluate the RGG arm mass unbalance errors, consideration must be given to the various excitation sources. There are four potential excitation sources, the spin bearing, the spin motor, RGG rotor mass unbalance, and the vibration-isolation system (VIALS). Of the first two excitation sources, only the spin bearing is considered significant. Of the latter two excitation sources, the VIALS is the most significant. The main result of RGG rotor mass unbalance is a small bias (less than 0.1 EU) with an uncertainty less than 0.01 EU. These figures are predicated on a rotor unbalance of approximately 0.03 gm-cm, a stable platform inertia of approximately $2 \text{ #}\cdot\text{ft}\cdot\text{sec}^2$, and an offset of the RGG mass center from the stable platform axes of approximately 10 inches.

Spin bearing excitations of the arm mass unbalance error mechanism contain both coherent and random components which lead to bias and random errors, respectively. The initial bias errors are compensated by the RGG-system initialization process, and the bias uncertainty thereafter contributes to the output error variance. The VIALS excitations of the arm mass unbalance error mechanisms are assumed to be random-only, since the RGG rotor mass unbalance excitations are considered separately.

In order to evaluate the output errors which result from random excitations of the arm mass unbalance error mechanisms, it is convenient to form the power spectra of the resultant error moments. These power spectra are then transformed by the RGG signal process

SECTION IX

to form the resultant power spectra of the output errors in each RGG channel. The error variances are then obtained by integration of the output error spectra. The basis for performing these operations is documented in Semiannual Technical Report No. 1 and will not be repeated here. In Technical Report No. 1, it was demonstrated that when the accelerations on each axis of the RGG stator reference frame (\bar{xyz}) are assumed to be statistically independent and to have equal power spectra at the spin frequency and its third harmonic, the "differential arm mass unbalance" error variances of each RGG channel are equal and of magnitude stated in (13), where the power spectral magnitudes, $S_a(f)$, are the "two-sided" values of a single axis, and Δf_e is the equivalent bandwidth of the RGG signal process.

$$\sigma_c^2 = \sigma_s^2 = \left[\frac{p_d g}{\eta C} \right]^2 [S_a(f_s) + S_a(3f_s)] \Delta f_e \quad (13)$$

By a similar process, the "axial arm mass unbalance" error variances of each RGG channel are obtained to first order as (14) since the products of the angular velocities in (12) are small compared to the angular acceleration terms in the frequency regions of the spin and third harmonic.

$$\sigma_c^2 = \sigma_s^2 = \left[\frac{p_a \ell}{\eta C} \right]^2 [S_{\dot{\omega}}(f_s) + S_{\dot{\omega}}(3f_s)] \Delta f_e \quad (14)$$

When the output error variances of each RGG in a system of three are equal and the inter-instrument error correlations are zero (uncorrelated), the standard deviations of the gravity gradient tensor errors are given by (15) for the trace elements and by (16) for the cross-elements.

$$\sigma_{ii} = \frac{\sqrt{2}}{3} \sigma_c \quad (15)$$

$$\sigma_{ij} = \frac{1}{2} \sigma_s \quad (16)$$

SECTION IX

Thus, the tensor element standard errors due to differential and axial arm mass unbalance are given as (17), (18), (19), and (20).

$$\sigma_{ii} \Big|_d = \frac{\sqrt{2}}{3} \left[\frac{p_d g}{\eta C} \right] \sqrt{[S_a(f_s) + S_a(3f_s)] \Delta f_e} \quad (17)$$

$$\sigma_{ij} \Big|_d = \frac{1}{2} \left[\frac{p_d g}{\eta C} \right] \sqrt{[S_a(f_s) + S_a(3f_s)] \Delta f_e} \quad (18)$$

$$\sigma_{ii} \Big|_a = \frac{\sqrt{2}}{3} \left[\frac{p_a \ell}{\eta C} \right] \sqrt{[S_{\dot{\omega}}(f_s) + S_{\dot{\omega}}(3f_s)] \Delta f_e} \quad (19)$$

$$\sigma_{ij} \Big|_a = \frac{1}{2} \left[\frac{p_a \ell}{\eta C} \right] \sqrt{[S_{\dot{\omega}}(f_s) + S_{\dot{\omega}}(3f_s)] \Delta f_e} \quad (20)$$

The error coefficients in (17) through (20) are estimated on the basis of the following parameters:

$$p_d = 2 \times 10^{-4} \text{ gm-cm}$$

$$p_a = 4 \times 10^{-3} \text{ gm-cm}$$

$$\eta C = 3.066 \times 10^4 \text{ gm-cm}^2$$

$$\ell = 2.16 \text{ cm}$$

$$g = 980 \text{ cm/sec}^2$$

$$[p_d g / \eta C] \approx 6390 \text{ EU/g} \quad (21)$$

$$[p_a \ell / \eta C] \approx 282 \text{ EU-sec}^2 \quad (22)$$

SECTION IX

The estimated two-sided spectral values of acceleration due to VIALS at the spin and its third harmonic are stated in (23) and (24).

$$S_a(f_s) + S_a(3f_s) \cong 26.8 \times 10^{-10} g^2/\text{Hz} \quad (23)$$

$$S_\omega(f_s) + S_\omega(3f_s) \cong 4.84 \times 10^{-8} \frac{(\text{rad/sec})^2}{\text{Hz}} \quad (24)$$

Substitution of the appropriate values in (21) through (24) into (17) through (20) (for $\Delta f_e = 0.05 \text{ Hz}$) yields the VIALS-induced arm mass unbalance standard errors given in (25) through (28).

$$\sigma_{ii}|_d \cong 0.035 \text{ EU} \quad (25)$$

$$\sigma_{ij}|_d \cong 0.037 \text{ EU} \quad (26)$$

$$\sigma_{ii}|_a \cong 0.007 \text{ EU} \quad (27)$$

$$\sigma_{ij}|_a \cong 0.007 \text{ EU} \quad (28)$$

The arm mass unbalance errors attributable to the spin bearing fall into three categories: (1) bias, (2) bias change, and (3) random. The bias errors are the result of coherent accelerations at the spin frequency and/or its harmonics. To the extent that these bias-type errors do not change after the system initialization process, they do not contribute to errors of the operating system. The bias-type errors change after initialization for two reasons: (1) the coherent vibrations of the spin bearing change and/or (2) the RGG mass unbalance coefficients change.

SECTION IX

The maximum bias errors as limited by the spin bearing specification of 10^{-4} g are given by (29) and (30) wherein the bias outputs of two RGG's are assumed to add in the worst way

$$M_{ii} \Big|_{\max} = \left(\frac{2}{3} \right) \left(\frac{P_d g}{\eta C} \right) (10^{-4}) = 0.426 \text{ EU} \quad (29)$$

$$M_{ij} \Big|_{\max} = \left(\frac{1}{2} \right) \left(\frac{P_d g}{\eta C} \right) (10^{-4}) \approx 0.320 \text{ EU} \quad (30)$$

The bias variations are assumed to be statistically independent due to the spin bearing and to RGG error coefficient changes after initialization. These bias variations contribute to the standard error as described by (31) and (32).

$$\sigma_{ii} \Big|_{BIAS} = \frac{\sqrt{2}}{3} \left(\frac{P_d g}{\eta C} \right) \sqrt{\sigma_a^2 + \frac{\sigma_d^2}{P_d^2} (10^{-4} g)^2} \quad (31)$$

$$\sigma_{ij} \Big|_{BIAS} = \frac{1}{2} \left(\frac{P_d g}{\eta C} \right) \sqrt{\sigma_a^2 + \frac{\sigma_d^2}{P_d^2} (10^{-4} g)^2} \quad (32)$$

where

σ_a^2 = spin bearing coherent acceleration variance

σ_d^2 = RGG error coefficient variance

Evaluation of (31) and (32) for the specified values of $\sigma_a = 10^{-5}$ g and $\sigma_d = 2/3 \times 10^{-4}$ gm-cm yields the bias error standard deviations given by (33) and (34).

SECTION IX

$$\sigma_{ii} \Big|_{BIAS} = 3020 \sqrt{\left(10^{-10}\right) + \left(\frac{1}{9}\right)\left(10^{-8}\right)} = 0.105 \text{ EU} \quad (33)$$

$$\sigma_{ij} \Big|_{BIAS} = 3195 \sqrt{\left(10^{-10}\right) + \left(\frac{1}{9}\right)\left(10^{-8}\right)} = 0.111 \text{ EU} \quad (34)$$

The standard errors due to random accelerations of the spin bearing are similar in form to (17) and (18) as stated by (35) and (36) wherein these equations are re-written in terms of the spin bearing acceleration power at the spin second harmonic.

$$\sigma_{ii} \Big|_d = \frac{\sqrt{2}}{3} \left(\frac{P_d g}{\eta c} \right) \sqrt{2[S_a(2f_s)] \Delta f_e} \quad (35)$$

$$\sigma_{ij} \Big|_d = \frac{1}{2} \left(\frac{P_d g}{\eta c} \right) \sqrt{2[S_a(2f_s)] \Delta f_e} \quad (36)$$

For a specified single-axis random acceleration power of $(10^{-5} \text{ g})^2$ in the effective band around the spin second harmonic, the standard errors are stated as (37) and (38).

$$\sigma_{ii} \Big|_d = \frac{6390}{3} \sqrt{2} \times 10^{-5} \cong 0.030 \text{ EU} \quad (37)$$

$$\sigma_{ij} \Big|_d = \frac{6390}{2} \times 10^{-5} \cong 0.032 \text{ EU} \quad (38)$$

A summary of the standard errors due to differential arm mass unbalance is given in Table IX-1.

SECTION IX

TABLE IX-1
Differential Arm Mass Unbalance Errors

Error Type	σ_{ii} - EU	σ_{ij} - EU
Bias Uncertainty (1σ)	0.105	0.111
Bearing Random	0.030	0.032
VIALS Random	0.035	0.037

T830

The axial mass unbalance errors attributable to the spin bearing may be examined in an analogous manner. The maximum bias error as limited by the spin bearing specification of 10^{-2} rad/sec 2 for deterministic transverse angular accelerations are stated by (39) and (40).

$$M_{ii} \Big|_{max} = \left(\frac{2}{3}\right) \left(\frac{p_a \ell}{\eta C}\right) \left(10^{-2}\right) = 1.88 \text{ EU} \quad (39)$$

$$M_{ij} \Big|_{max} = \left(\frac{1}{2}\right) \left(\frac{p_a \ell}{\eta C}\right) \left(10^{-2}\right) = 1.41 \text{ EU} \quad (40)$$

The bias variations are assumed to be statistically independent due to the spin bearing and due to RGG error coefficient changes. The standard errors which result from these uncertainties are described by (41) and (42).

$$\sigma_{ii} \Big|_{BIAS} = \frac{\sqrt{2}}{3} \left(\frac{p_a \ell}{\eta C}\right) \sqrt{\sigma_{\dot{\omega}}^2 + \left(\frac{\sigma_{p_a}}{p_a}\right)^2 \left(10^{-2}\right)^2} \quad (41)$$

SECTION IX

$$\sigma_{ij} \Big|_{\text{BIAS}} = \frac{1}{2} \left(\frac{p_a \ell}{\eta C} \right) \sqrt{\sigma_{\dot{\omega}}^2 + \left(\frac{\sigma_{pa}}{p_a} \right)^2 (10^{-2})^2} \quad (42)$$

where

$\sigma_{\dot{\omega}}^2$ = Spin bearing coherent angular acceleration variance

σ_{pa}^2 = RGG error coefficient variance

Evaluation of (41) and (42) for the specified values of $\sigma_{\dot{\omega}} = 10^{-3}$ rad/sec² and $\sigma_{pa} = 2/3 \times 10^{-4}$ gm-cm yields the bias error standard deviations of (43) and (44).

$$\sigma_{ii} \Big|_{\text{BIAS}} = \frac{\sqrt{2}}{3} (282) \sqrt{\left(10^{-3}\right)^2 + \left(\frac{10^{-2}}{60}\right)^2} \approx 0.133 \text{ EU} \quad (43)$$

$$\sigma_{ij} \Big|_{\text{BIAS}} = \left(\frac{1}{2}\right) (282) \sqrt{\left(10^{-3}\right)^2 + \left(\frac{10^{-2}}{60}\right)^2} \approx 0.141 \text{ EU} \quad (44)$$

The standard errors due to random angular accelerations of the spin bearing are expressed similarly to (35) and (36) in terms of total angular acceleration power on a single axis by (45) and (46).

$$\sigma_{ii} \Big|_a = \left(\frac{\sqrt{2}}{3}\right) \left(\frac{p_a \ell}{\eta C}\right) \sqrt{2 [S_{\dot{\omega}} (2f_s)] \Delta f_e} \quad (45)$$

$$\sigma_{ij} \Big|_a = \left(\frac{1}{2}\right) \left(\frac{p_a \ell}{\eta C}\right) \sqrt{2 [S_{\dot{\omega}} (2f_s)] \Delta f_e} \quad (46)$$

SECTION IX

For a specified single-axis random angular acceleration power of $(10^{-3} \text{ rad/sec}^2)^2$ in the effective band around the spin second harmonic, the standard errors are stated as (47) and (48).

$$\sigma_{ii} \Big|_a = \left(\frac{282}{3} \right) \sqrt{2} \times 10^{-3} \cong 0.133 \text{ EU} \quad (47)$$

$$\sigma_{ij} \Big|_a = \left(\frac{282}{2} \right) \times 10^{-3} \cong 0.141 \text{ EU} \quad (48)$$

A summary of the standard errors due to axial arm mass unbalance is given in Table IX-2.

TABLE IX-2
Axial Arm Mass Unbalance Errors

Error Type	σ_{ii} - EU	σ_{ij} - EU
Bias Uncertainty (1σ)	0.133	0.141
Bearing Random	0.133	0.141
VIALS	0.007	0.007

T831

The standard errors due to both differential and axial arm mass unbalance from Tables IX-1 and IX-2 may be combined on the basis of statistical independence to yield an instrument-associated standard error and a VIALS-associated standard error for all arm-mass unbalances. This result is presented in Table IX-3.

SECTION IX

TABLE IX-3.
Arm Mass Unbalance Error Summary

Error Source	σ_{ii} - EU	σ_{ij} - EU
RGG Instruments	0.218	0.231
VIALS.	0.036	0.038

T832

B. PHASE ERROR PROPAGATION IN THE ROTATING GRAVITY GRADIOMETER

In this section the phase error sensitivity equations are first derived. The gradient tensor error is then evaluated for the various contributing effects.

1. Phase Error Propagation Derivations

Phase errors in the RGG signal process are similar to coordinate misalignments in that they create effective rotations of the "signal vector" at the particular locations in the signal process where they occur. For the purposes of system error analysis, these phase errors may be modelled as error functions associated with either the modulation or demodulation functions of the RGG signal process. The modulation process is implemented by spinning the sensor at nominally constant speed with respect to the measurement reference frame, and the demodulation process is implemented electronically by phase sensitive detection. The detection process is referenced to the measured relative position of the sensor with respect to the measurement reference frame. This method of detection provides a certain amount of correlation between the modulation and demodulation phase errors and a resultant net reduction in the total effective phase error of the

SECTION IX

RGG signal process. In addition, as part of the initial alignment of the system, the detection phase reference must be adjusted to match the initial phase shift ($\psi(0)$) of the signal process between the spatially modulated signal and the input to the demodulation process. Changes of the phase shift ($\Delta\psi$) in this part of the signal process after initial alignment are considered to be part of the net phase error of the total signal process.

In order to develop a phase error model for the RGG signal process, it is necessary to examine the modulation, carrier filter, and demodulation functions in greater detail. The spatially modulated input gravity gradient signal (Γ_i) may be expressed in terms of the instantaneous angular position, $\alpha(t)$, of the sensor with respect to the stator reference frame ($\bar{x}\bar{y}\bar{z}$) for a (\bar{z}) spin axis as (1).

$$\Gamma_i = (\Gamma_{yy} - \Gamma_{xx}) \cos 2\alpha(t) + 2\Gamma_{xy} \sin 2\alpha(t) \quad (1)$$

The instantaneous angular position, $\alpha(t)$, of the sensor may be modelled in terms of the constant reference speed command, ω_R , to the speed control servo and a modulation phase error function, $\phi(t)$, as (2).

$$\alpha(t) = \omega_R t + \phi(t) \quad (2)$$

Note that the modulation phase error, $\phi(t)$, is identically the position error of the speed control servo.

The output signal of the carrier filter process, Γ_o , may be expressed in terms of the input signal, Γ_i , and the carrier filter transfer, $H_1(s)$, as (3).

$$\Gamma_o(S) = H_1(S) \Gamma_i(S) \quad (3)$$

The carrier filter process may be characterized in terms of its phase shift at the carrier frequency, $\psi(t)$, and its "equivalent envelope transfer function," $H_e(s)$. This equivalent envelope transfer function may be modelled as a low pass filter with a single time constant, τ_e , as in (4).

SECTION IX

$$H_e(S) \triangleq \frac{1}{\tau_s S + 1} \quad (4)$$

The carrier filter output signal ($\hat{\Gamma}_c$) is demodulated by the instantaneous angular position of the sensor, $\alpha(t)$, as compensated by the initial carrier phase shift, $\psi(0)$, to form the in-phase and quadrature signals which are then processed by low pass filters, $H_o(S)$. An equivalent block diagram of the entire signal process, based on the input signals of (1), is shown in Fig. IX-1.

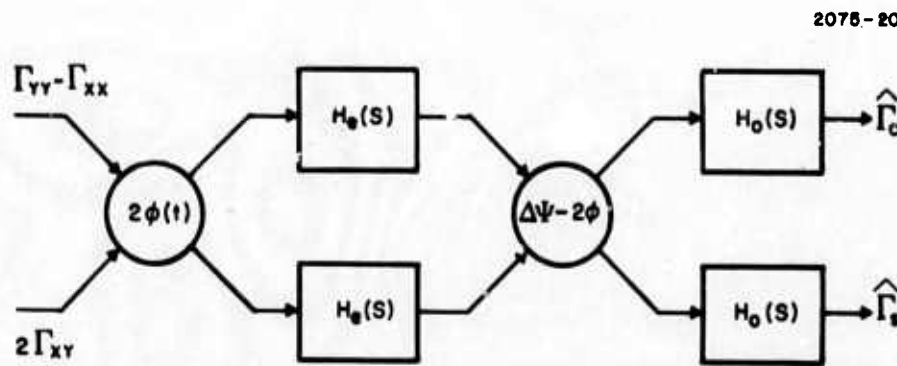


Fig. IX-1. Equivalent Block Diagram of Signal Process.

The input signals are resolved by the phase error, $2\phi(t)$, of the modulation process, and the resultant signals are filtered by the "equivalent envelope transfer function", $H_e(S)$, of the carrier filter process. These filtered signals are resolved by the phase error of the demodulation process, $\Delta\psi - 2\phi(t)$, and the resultant signals are processed by the low pass filters, $H_o(S)$, to form the in-phase and quadrature output signals, $\hat{\Gamma}_c$ and $\hat{\Gamma}_s$.

The phase-induced errors in the output signals are defined as the difference between the actual output signals and those that would occur in the absence of phase errors as in (5) and (6).

SECTION IX

$$\epsilon_c \triangleq \hat{\Gamma}_c - H_e(S) H_o(S) [\Gamma_{yy} - \Gamma_{xx}] \quad (5)$$

$$\epsilon_s \triangleq \hat{\Gamma}_s - H_e(S) H_o(S) [2\Gamma_{xy}] \quad (6)$$

The phase-induced output errors may be expressed to first order by assuming the gravity gradient signals, $\Gamma_{yy} - \Gamma_{xx}$ and $2\Gamma_{xy}$, to be constant and the phase errors to be very small angles. Substitution of (4) into (5) and (6) and application of these assumptions yields the first order phase-induced errors as (7) and (8).

$$\epsilon_c \cong [2\Gamma_{xy}] [H_o(S)] \left[\left(\frac{1}{\tau_e S + 1} \right) (2\phi) + \Delta\psi - (2\phi) \right] \quad (7)$$

$$\epsilon_s \cong [\Gamma_{xx} - \Gamma_{yy}] [H_o(S)] \left[\left(\frac{1}{\tau_e S + 1} \right) (2\phi) + \Delta\psi - (2\phi) \right] \quad (8)$$

Rearrangement of (7) and (8) reveals differences in the propagation of phase errors depending on the error source as shown in (9) and (10).

$$\epsilon_c \cong [2\Gamma_{xy}] [H_o(S)] \left[\Delta\psi - \left(\frac{\tau_e S}{\tau_e S + 1} \right) (2\phi) \right] \quad (9)$$

$$\epsilon_s \cong [\Gamma_{xx} - \Gamma_{yy}] [H_o(S)] \left[\Delta\psi - \left(\frac{\tau_e S}{\tau_e S + 1} \right) (2\phi) \right] \quad (10)$$

Phase errors originating in the modulation process (speed control servo position errors) do not propagate at low frequency. This is the direct result of the correlation between the modulation and demodulation phase errors associated with the previously described method of detection. Phase errors associated with the carrier filter process ($\Delta\psi$) do propagate at low frequencies and as a result, phase stability in the carrier filter process is an important design parameter. Note that the form of both (9) and (10) are identical except for the background gradient signal parameters which serve as scale factors in these error equations.

SECTION IX

In a locally-level oriented measurement system, the most significant phase-induced errors occur in the sensors with horizontal spin axes. In this case, the background gradient coefficient ($\Gamma_{xx} - \Gamma_{yy}$) has a magnitude of 4500 EU, and the significant output error is given by (10). This represents an error in the measurement of the cross-gradient signal ($2\Gamma_{xy}$). To obtain the cross-gradient tensor element from the quadrature phase measurement, $\hat{\Gamma}_s$, one must divide by two, i.e.

$$\hat{\Gamma}_{xy} = \frac{1}{2} \hat{\Gamma}_s \quad (11)$$

The phase-induced cross gradient tensor element error from (10) and (11) is stated as (12).

$$\epsilon_{xy} = [\Gamma_{xx} - \Gamma_{yy}] [H_o(S)] \left[\frac{\Delta\psi}{2} - \left(\frac{\tau_e S}{\tau_e S + 1} \right) (\phi) \right] \quad (12)$$

The low-pass output filter, $H_o(S)$, is defined by (13).

$$H_o(S) \triangleq \left[\frac{1}{\tau_o S + 1} \right]^2 \quad (13)$$

In the present design the time constants, τ_e and τ_o , are approximately equal to each other and to one-third the integration time of the total signal process. In this analysis, for analytical convenience, they are assumed to be identically equal such that equation (12) may be expressed as (14), where

$$\alpha_o = \frac{1}{\tau_o} \triangleq \frac{1}{\tau_e}$$

$$\epsilon_{xy} = [\Gamma_{xx} - \Gamma_{yy}] \left[\frac{\alpha_o}{S + \alpha_o} \right]^2 \left(\frac{\Delta\psi}{2} \right) - [\Gamma_{xx} - \Gamma_{yy}] \left[\frac{\alpha_o^2 S}{(S + \alpha_o)^3} \right] (\phi) \quad (14)$$

SECTION IX

2. Gradient Tensor Error Evaluation

Equation (14) describes the cross-gradient tensor errors which are the result of misalignments, phase shift variations in the carrier filter process, and position errors of the speed control servo. All of these errors, with the exception of the servo position error, propagate in accordance with the phase uncertainty parameter, ($\Delta\psi/2$), in (14). Errors of this type are assumed to change slowly so that no real benefit is obtained from the filter process acting on ($\Delta\psi/2$) in (14). Table I contains a summary from other sections of this report of the estimated standard deviations of the phase uncertainties in this category ($\Delta\psi/2$). All listed sources are assumed to be statistically independent.

TABLE IX-4
Estimated Standard Deviations

<u>Phase Error Source</u>	<u>Std. Dev. ($\Delta\psi/2$)</u>
Sensor Resonant Frequency Variation	6×10^{-5} rad
Arm to Rotor Alignment Variation	1×10^{-5} rad
Disk to Case Alignment Variation	1×10^{-5} rad
Readout Shift	1×10^{-5} rad
Electronics Including Frequency Reference	1×10^{-5} rad
RSS Total of ($\Delta\psi/2$)	6.3×10^{-5} rad
Tensor Element Standard Deviation	0.28 EU

T833

The servo position error (ϕ), according to (14), propagates in a limited low frequency band positioned near the filter frequency, $\alpha_0 \approx 0.3$ rad/sec. Equations (2) and (3) of Section XVI-B describe the speed control servo position error responses to torque disturbances and tachometer measurement noise. The resultant cross-gradient

SECTION IX

tensor error due to servo torque disturbances and tachometer measurement errors may be expressed from (14) and the speed control servo position error responses as (15).

$$\epsilon_{xy} = (\Gamma_{yy} - \Gamma_{xx}) \left[\frac{\alpha_0^2 s^2 (s + 16)}{(s + \alpha_0)^3 (s^4 + 16s^3 + 90s^2 + 170s + 160)} \right] \left[\frac{T_d}{J} + \left(\frac{80}{s+16} \right) \Delta\omega_t \right] \quad (15)$$

Equation (15) may be cast in a form more convenient for spectral analysis by normalizing the equivalent filter processes. These forms are defined by (16), (17), and (18).

$$\epsilon_{xy} = (\Gamma_{yy} - \Gamma_{xx}) \left[\left(\frac{\alpha_0}{10} \right) \left(H_{T_d}(s) \frac{T_d}{J} \right) + \left(\frac{\alpha_0}{2} \right) \left(H_{\Delta\omega}(s) \right) \Delta\omega_t \right] \quad (16)$$

$$H_{T_d}(s) \triangleq \left[\frac{10\alpha_0 s^2 (s + 16)}{(s + \alpha_0)^3 (s^4 + 16s^3 + 90s^2 + 170s + 160)} \right] \quad (17)$$

$$H_{\Delta\omega}(s) \triangleq \left[\frac{160 \alpha_0 s^2}{(s + \alpha_0)^3 (s^4 + 16s^3 + 90s^2 + 170s + 160)} \right] \quad (18)$$

The mean square cross-gradient tensor errors are obtained from (16), (17), and (18) for the torque disturbance and tachometer measurement spectra, $S_T(f)$ and $S_{\Delta\omega}(f)$, by the integrals of (19) and (20).

$$\sigma_{xy}^2 \Big|_{T_d} = \left[\frac{(\Gamma_{yy} - \Gamma_{xx}) \alpha_0}{10J} \right]^2 \int_{-\infty}^{\infty} \left| H_{T_d}(s) \right|^2 S_T(f) df \quad (19)$$

$$\sigma_{xy}^2 \Big|_{\Delta\omega_t} = \left[\frac{(\Gamma_{yy} - \Gamma_{xx}) \alpha_0}{2} \right]^2 \int_{-\infty}^{\infty} \left| H_{\Delta\omega}(s) \right|^2 S_{\Delta\omega}(f) df \quad (20)$$

SECTION IX

Assuming that the disturbance torque and tachometer measurement error spectra of (19) and (20) are "regionally constant" within the effective bands of the filter transfer functions of (17) and (18), The integration of (19) and (20) may be approximated to yield the error of (21) and (22).

$$\sigma_{xy}^2 \Big|_{T_d} \approx \left[\frac{(\Gamma_{yy} - \Gamma_{xx}) \alpha_0}{10J} \right]^2 \left[S_{T_d}(f_o) f_o \right] \quad (21)$$

$$\sigma_{xy}^2 \Big|_{\Delta\omega_t} \approx \left[\frac{(\Gamma_{yy} - \Gamma_{xx}) \alpha_0}{2} \right]^2 \left[S_{\Delta\omega_t}(f_o) f_o \right] \quad (22)$$

where

$$f_o = \frac{\alpha_0}{2\pi} = \frac{0.3}{2\pi} \approx 0.048 \text{ Hz}$$

Note that the integrals of (19) and (20) are based on "two-sided" spectra for the variables, T_d and $\Delta\omega_t$, such that the spectral amplitudes, $S_{T_d}(f_o)$ and $S_{\Delta\omega_t}(f_o)$, in (21) and (22) are one-half the magnitude of spectral amplitudes based on "one-sided" spectra. The combined upper limit of random torque variation allowed by the spin motor and spin bearing specifications translates to a maximum allowable "one-sided" magnitude of 3.75×10^6 (dyne-cm)²/Hz or a maximum "two-sided" spectral magnitude of 1.875×10^6 (dyne-cm)²/Hz. Thus, the effective mean-square random torque from (21) is bounded by (23).

$$\sigma_{T_d}^2 \leq S_{T_d}(f_o) f_o = 1.875 \times 10^6 \times 0.048 = 9 \times 10^4 (\text{dcm})^2 \quad (23)$$

Then from (21) and (23), the standard deviation of the cross gradient error due to speed control servo torque disturbances is bounded by (24).

SECTION IX

$$\sigma_{xy} \Big|_{T_d} \leq \left[\left[\frac{(\Gamma_{yy} - \Gamma_{xx})\alpha_o}{10J} \right] \right] \left[\sigma_{T_d} \right]_{max} \quad (24)$$

Evaluation of (24) for $(\Gamma_{yy} - \Gamma_{xx}) = 4500$ EU, $\alpha_o = 0.3$ rad/sec, and $J = 2.5 \times 10^5$ gm-cm yields the bounding value of (25).

$$\sigma_{xy} \Big|_{T_d} \leq \left[\left[\frac{(4500)(0.3)}{2.5 \times 10^6} \right] [300] \right]_{max} \approx 0.161 \text{ EU} \quad (25)$$

The cross-gradient error associated with a vertical spin axis sensor due to speed control servo phase errors depends on the effective difference of the principal horizontal gradient elements. Normally this gradient difference is only a small fraction of the vertical gradient "difference" of 4500 EU. Assuming that it is as large as 10% of 4500 EU yields an error less than 0.02 EU. In general, this error will be even smaller than this figure.

Estimation of the cross-gradient error variance due to tachometer measurement noise in the effective low frequency band near α_o is more difficult. To the first order, it is zero by virtue of the design of the tachometer. The tachometer is described in Section XVI-C wherein it is estimated that the tachometer measurement noise in the low frequency region will have an rms value in a 0.1 Hz band of 0.1 mrad/sec. This translates to a "two-sided" spectral density magnitude of $5 \times 10^{-8} (\text{rad/sec})^2/\text{Hz}$ in the low frequency region. Thus the effective mean-square random tachometer noise from (22) is evaluated in (26).

$$\begin{aligned} \sigma_{\Delta\omega_t}^2 &= S_{\Delta\omega_t} (f_o) f_o = 5 \times 10^{-8} \times 0.048 \\ &= 24 \times 10^{-10} (\text{rad/sec})^2 \end{aligned} \quad (26)$$

SECTION IX

Then, from (22) and (26), the standard deviation of the cross-gradient error due to low frequency tachometer noise is evaluated in (27).

$$\sigma_{xy} \Big|_{\Delta\omega_t} = \left[\frac{(4500)(0.3)}{2} \right] (4.9 \times 10^{-5}) = 0.033 \text{ EU} \quad (27)$$

The total cross-gradient standard deviation due to all phase errors in the horizontal spin axis sensors may be computed from the values given in Table I and in equations (25) and (27) as shown in (28).

$$\sigma_{xy} \Big|_{\text{All Phase Errors}} = \sqrt{(0.28)^2 + (0.161)^2 + (0.033)^2} = 0.325 \text{ EU} \quad (28)$$

Similarly, for the vertical spin axis sensor, the cross-gradient standard deviation due to all sources of phase error will be less than 0.03 EU if the principal horizontal gradient difference is less than 400 EU.

C. TRANSDUCER LOAD STUDY - THERMAL NOISE

Previous analyses of thermal noise employed a single equivalent dissipative element in the model of the electromechanical signal sensing and transducing process. A more accurate representation of this process requires at least two dissipative elements: one to represent the mechanical losses and one to represent the electrical losses associated with the signal transducing process. The intent of this study is to examine the relation between thermal noise on the gravity gradient tensor elements and the "effective Q" of the signal sensing and transducing process when the total signal process is constrained to have a fixed integration time of 10 sec in terms of signal transmission. The results of the study for transducer load resistances in the range 2.86 to 28.6 megohms indicate a small increase in thermal noise (about 5%)

SECTION IX

with respect to the no-load case for the same "effective Q" of the signal sensing and transducing process.

1. Sensing and Transducing Equivalent Circuit

An equivalent circuit of the signal sensing and transducing process is shown in Fig. IX-2. The resistors, R_1 and R_o , represent the mechanical damping and transducer loading, respectively. The reactive elements, L_1 and C_1 , represent the equivalent inertia and elasticity of the mechanical system, and C_o is the electrical capacity of the transducer.

For convenience, the electrical equivalents of the mechanical components have been transformed to the output side of the equivalent circuit in this figure. The mechanical impedances have been divided by N^2 and the primary voltages divided by N, where N is the system transformation ratio discussed in Section XIV-A. Therefore, except for C_o , R_o , and ω_o , the magnitudes of the various elements are not the same as in other sections of this report. The noise calculations are in normal units. The voltage generators, e_1 and e_2 , represent the white noise sources associated with R_1 and R_o , and E_s represents the input gravity gradient signal at scale factor K_s as in eq. (1).

$$E_s \triangleq K_s (2 \Gamma_{ij}) \quad (1)$$

The output signal (e_o) of Fig. IX-2 is processed by the remainder of the RGG signal process to yield the gravity gradient tensor elements. This latter process must be selected according to the parameters in Fig. IX-2 so that the total process acting on the signal ($2 \Gamma_{ij}$) satisfies the 10-sec integration time requirement. To select this process, we state the input-output signal transfer as eq. (2).

2075-22

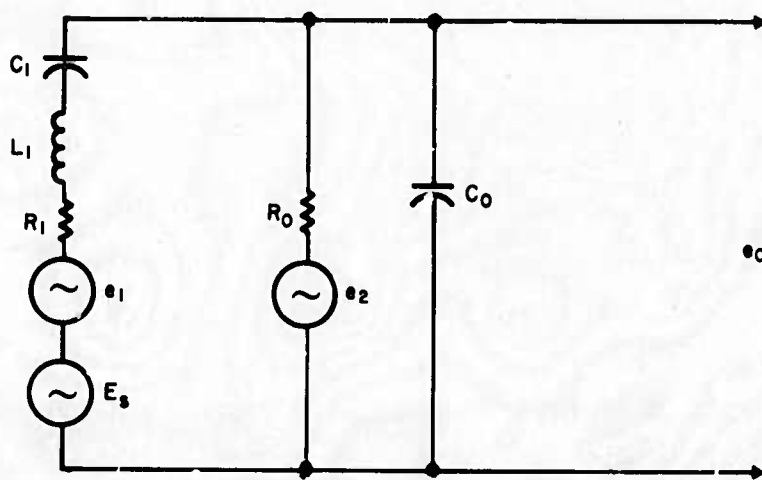


Fig. IX-2. Equivalent Circuit of Signal Sensing and Transducing Process.

SECTION IX

$$\frac{e_o}{E_s} = H_1(s) = \frac{\left(\frac{C_1}{C_1+C_o}\right) \omega_o^2 s}{s^3 + (\alpha_o + \alpha_1)s^2 + (\omega_o^2 + \alpha_o \alpha_1)s + \alpha_o \beta_1^2} \quad (2)$$

where

$$\alpha_o \triangleq \frac{1}{R_o C_o}$$

$$\alpha_1 \triangleq \frac{R_1}{L_1}$$

$$\beta_1^2 \triangleq \frac{1}{L_1 C_1}$$

$$\omega_o^2 \triangleq \frac{1}{L_1} \left(\frac{C_1 + C_o}{C_1 C_o} \right) \text{ the undamped natural frequency.}$$

The signal transfer, $H_1(s)$, may be restated as eq. (3) in factored form

$$H_1(s) = \frac{\left(\frac{C_1}{C_1+C_o}\right) \omega_o^2 s}{(s + \lambda_o)(s^2 + \frac{\beta_o}{Q_o}s + \beta_o^2)} \quad (3)$$

In (3), by definition, β_o is the resonant frequency of signal transmission, and Q_o is the "effective Q" of the signal sensing and transducing system. The equivalent carrier filter process, $H_o(s)$, for the remainder of the signal process to either the RGG in-phase or quadrature outputs, Γ_c and Γ_s , is stated as (4).

SECTION IX

$$H_o(s) = \frac{1}{K_s} \left(\frac{C_1 + C_o}{C_1} \right) \left(\frac{\beta_o \sqrt{\lambda_o^2 + \beta_o^2}}{Q_o \omega_o^2} \right) \left(\frac{\frac{\beta_o}{Q_2} s}{s^2 + \frac{\beta_o}{Q_2} s + \beta_o^2} \right) \quad (4)$$

The parameter, Q_2 , of eq. (4) must be selected to satisfy the integration time requirement.

2. Thermal Noise Evaluation

The thermal noise variances on each RGG output channel, $\sigma_{c_1}^2$ and $\sigma_{s_1}^2$, due to R_1 are computed as in (5).

$$\sigma_{c_1}^2 = \sigma_{s_1}^2 = 2kTR_1 \int_{-\infty}^{\infty} |H_1(s)H_o(s)|^2 df \quad (5)$$

The variances, $\sigma_{c_2}^2$ and $\sigma_{s_2}^2$, due to R_o are computed as in (6).

$$\sigma_{c_2}^2 = \sigma_{s_2}^2 = 2 kTR_o \int_{-\infty}^{\infty} |H_2(s)H_o(s)|^2 df \quad (6)$$

where

$$H_2(s) = \frac{\alpha_o(s^2 + \alpha_1 s + \beta_1^2)}{(s + \lambda_o)(s^2 + \frac{\beta_o}{Q_o} s + \beta_o^2)} \quad (7)$$

The total channel variances are simply the sums of the individual variances due to the statistical independence of e_1 and e_2 .

$$\sigma_c^2 = \sigma_{c_1}^2 + \sigma_{c_2}^2 \quad (8)$$

SECTION IX

$$\sigma_s^2 = \sigma_{s_1}^2 + \sigma_{s_2}^2 \quad (9)$$

The gravity gradient tensor element standard deviations for a system of three orthogonal sensors are stated as eq. (10) for the trace elements and as (11) for the cross-gradient elements.

$$\sigma_{ii} = \frac{\sqrt{2}}{3} \sigma_c \quad (10)$$

$$\sigma_{ij} = \frac{1}{2} \sigma_s. \quad (11)$$

The noise integrals of (5) and (6) were evaluated for a fixed set of reactive elements, (L_1 , C_1 , C_o), and a variable set of dissipative elements, i. e.,

$$125 \text{ k}\Omega \leq R_1 \leq 1.25 \text{ M}\Omega$$

$$2.86 \text{ M}\Omega \leq R_o \leq 28.6 \text{ M}\Omega$$

$$C_1 = 41 \text{ pF}$$

$$C_o = 3490 \text{ pF}$$

$$\omega_o^2 = (220)^2 \text{ rad/sec}$$

This set gave a range of mechanical quality factor, Q_m , from 88 to 880 and a range of effective quality factor, Q_{eff} , from 62 to 589 where

$$Q_m \triangleq \frac{1}{\omega_o R_1} \left(\frac{1}{C_1} + \frac{1}{C_o} \right)$$

SECTION IX

The parametric results of these computations for a typical operating point are as follows:

$$R_1 = 175 \text{ k}\Omega \quad \beta_o = 219.98 \text{ rad/sec}$$

$$R_o = 9.55 \text{ M}\Omega \quad Q_{\text{eff}} = 307.5$$

$$\sigma_{ii} = 0.318 \text{ EU} \quad \sigma_{ij} = 0.337 \text{ EU for } 290^\circ\text{K}$$

$$\sigma_{ii} = 0.337 \text{ EU} \quad \sigma_{ij} = 0.357 \text{ EU for } 326^\circ\text{K}$$

In the simple, single dissipative element model, the resultant noise figures for the same value of Q are slightly less (about 2.5%):

$$\sigma_{ii} = 0.328 \text{ EU} \quad \sigma_{ij} = 0.349 \text{ EU for } 326^\circ\text{K}$$

At other load conditions, particularly at lower effective Q 's, the thermal noise increases above that of the simple model by about 6%. A plot of the cross-gradient standard deviation, σ_{ij} , as a function of "effective Q " is shown in Fig. IX-3 for the range of load conditions considered. The individual values for each load condition are not plotted because of their close proximity. Rather, the upper and lower boundaries are shown.

SECTION IX

$$\sigma_s^2 = \sigma_{s_1}^2 + \sigma_{s_2}^2 \quad (9)$$

The gravity gradient tensor element standard deviations for a system of three orthogonal sensors are stated as eq. (10) for the trace elements and as (11) for the cross-gradient elements.

$$\sigma_{ii} = \frac{\sqrt{2}}{3} \sigma_c \quad (10)$$

$$\sigma_{ij} = \frac{1}{2} \sigma_s. \quad (11)$$

The noise integrals of (5) and (6) were evaluated for a fixed set of reactive elements, (L_1 , C_1 , C_o), and a variable set of dissipative elements, i. e.,

$$125 \text{ k}\Omega \leq R_1 \leq 1.25 \text{ M}\Omega$$

$$2.86 \text{ M}\Omega \leq R_o \leq 28.6 \text{ M}\Omega$$

$$C_1 = 41 \text{ pF}$$

$$C_o = 3490 \text{ pF}$$

$$\omega_o^2 = (220)^2 \text{ rad/sec}$$

This set gave a range of mechanical quality factor, Q_m , from 88 to 880 and a range of effective quality factor, Q_{eff} , from 62 to 589 where

$$Q_m \triangleq \frac{1}{\omega_o R_1} \left(\frac{1}{C_1} + \frac{1}{C_o} \right)$$

SECTION IX

The parametric results of these computations for a typical operating point are as follows:

$$R_1 = 175 \text{ k}\Omega \quad \beta_o = 219.98 \text{ rad/sec}$$

$$R_o = 9.55 \text{ M}\Omega \quad Q_{\text{eff}} = 307.5$$

$$\sigma_{ii} = 0.318 \text{ EU} \quad \sigma_{ij} = 0.337 \text{ EU for } 290^{\circ}\text{K}$$

$$\sigma_{ii} = 0.337 \text{ EU} \quad \sigma_{ij} = 0.357 \text{ EU for } 326^{\circ}\text{K}$$

In the simple, single dissipative element model, the resultant noise figures for the same value of Q are slightly less (about 2.5%):

$$\sigma_{ii} = 0.328 \text{ EU} \quad \sigma_{ij} = 0.349 \text{ EU for } 326^{\circ}\text{K}$$

At other load conditions, particularly at lower effective Q 's, the thermal noise increases above that of the simple model by about 6%. A plot of the cross-gradient standard deviation, σ_{ij} , as a function of "effective Q " is shown in Fig. IX-3 for the range of load conditions considered. The individual values for each load condition are not plotted because of their close proximity. Rather, the upper and lower boundaries are shown.

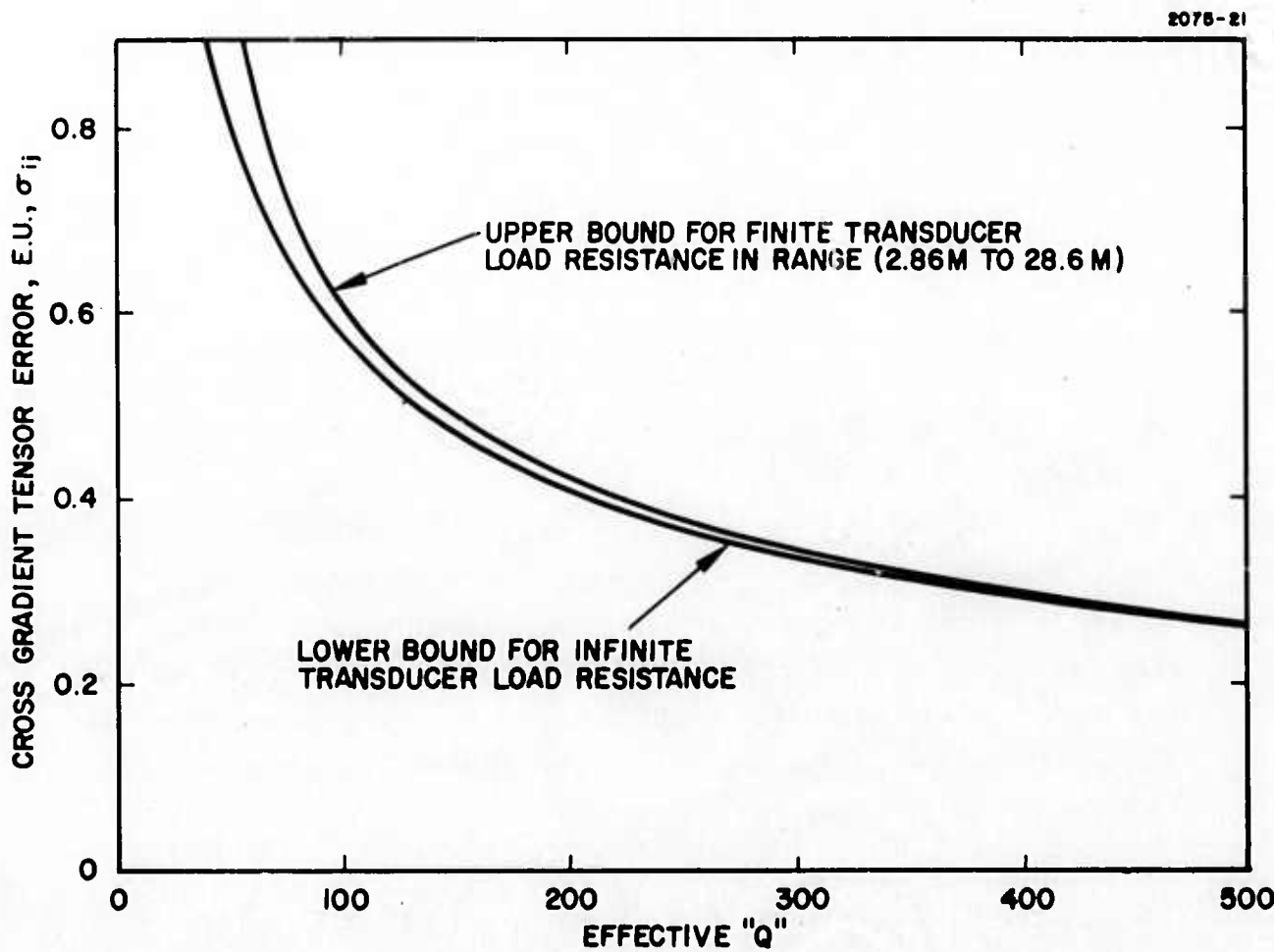


Fig. IX-3. Standard Deviation Cross-Gradient Thermal Noise (σ_{ij}) Versus Effective Q . (These Curves were Plotted for 290°K. For 326°K, Multiply σ_{ij} by 1.06.)

SECTION IX

D. ROTATIONAL FIELD ERRORS

In Section III-B-2 of Technical Report No. 1, the equivalent input power spectra of the rotational field errors to each RGG channel were derived and presented as eqs. (30) and (31), and the bias errors were presented in eqs. (9) and (10). When a system of three mutually orthogonal RGG's are subjected to the same inertial angular velocity, the resultant rotational field errors of each instrument are correlated. When this is the case, this correlation must be considered in the calculation of the rotational field trace element errors of the gravity gradient tensor. Since only one RGG is employed in the measurement of each cross-gradient tensor element, inter-instrument error correlation is not a consideration in the determination of the cross-gradient tensor errors.

For common inertial angular velocity excitation, the equivalent input rotational field error spectra to the RGG signal process for calculation of the trace element errors may be derived using the method employed in Technical Report No. 1 to obtain the equivalent input error spectra to each RGG channel. As an example, the complete input rotational field error spectrum for the \overline{XX} trace element error is presented in (1) for the correlated case.

$$\begin{aligned} S_{XX_{in}}(f) = & \frac{8}{9} [S_x(f) * S_x(f)] + \frac{2}{9} [S_y(f) * S_y(f) + S_z(f) * S_z(f)] \\ & - \frac{4}{9} [S_{xy}(f) * S_{xy}(f) + S_{yx}(f) * S_{yx}(f)] \\ & - \frac{4}{9} [S_{xz}(f) * S_{xz}(f) + S_{zx}(f) * S_{zx}(f)] \\ & + \frac{2}{9} [S_{yz}(f) * S_{yz}(f) + S_{zy}(f) * S_{zy}(f)] \\ & + \frac{4}{9} [4M_x^2 S_x(f) + M_y^2 S_y(f) + M_z^2 S_z(f)] \end{aligned}$$

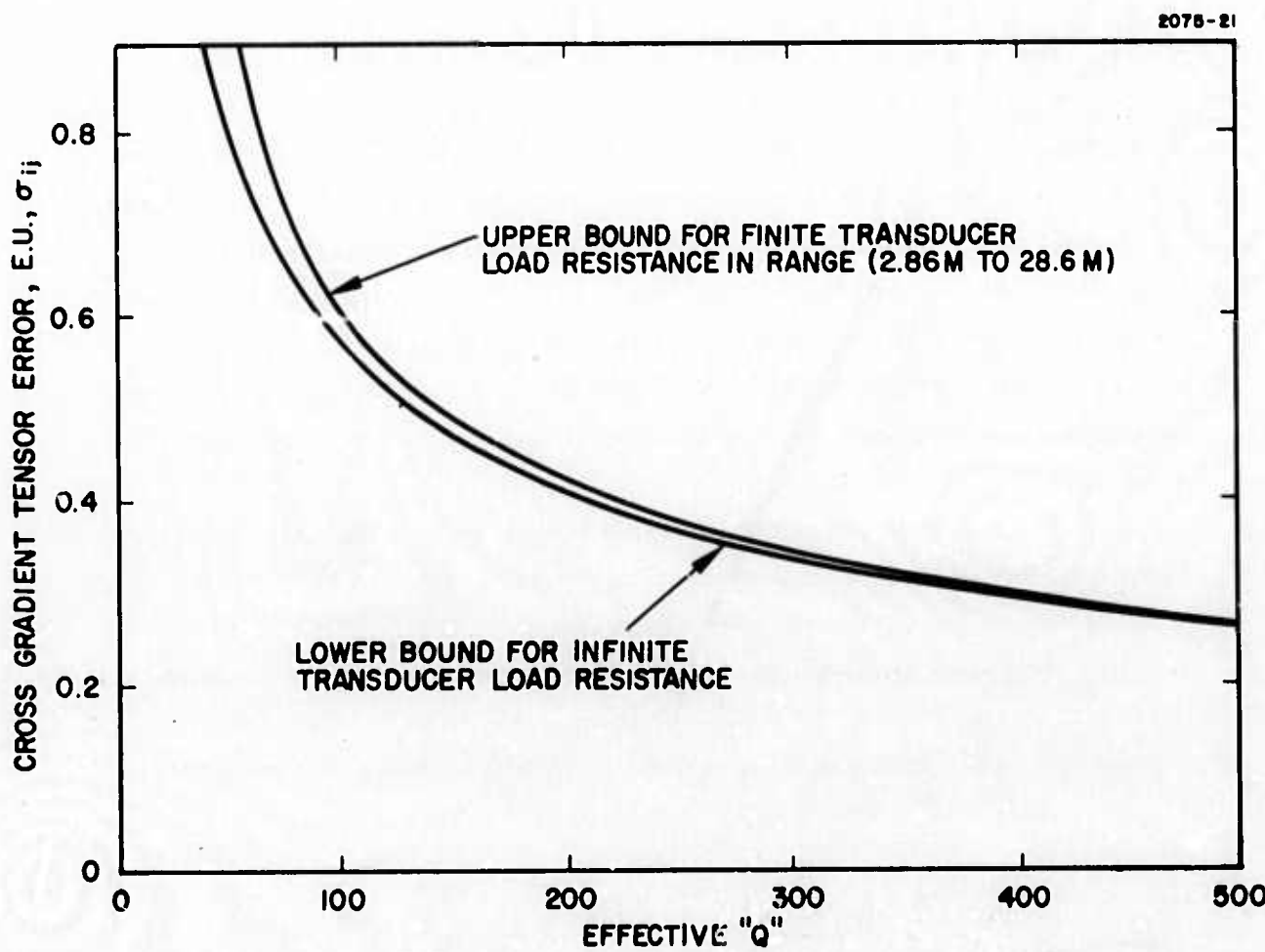


Fig. IX-3. Standard Deviation Cross-Gradient Thermal Noise (σ_{ij}) Versus Effective Q. (These Curves were Plotted for 290°K. For 326°K, Multiply σ_{ij} by 1.06.)

SECTION IX

D. ROTATIONAL FIELD ERRORS

In Section III-B-2 of Technical Report No. 1, the equivalent input power spectra of the rotational field errors to each RGG channel were derived and presented as eqs. (30) and (31), and the bias errors were presented in eqs. (9) and (10). When a system of three mutually orthogonal RGG's are subjected to the same inertial angular velocity, the resultant rotational field errors of each instrument are correlated. When this is the case, this correlation must be considered in the calculation of the rotational field trace element errors of the gravity gradient tensor. Since only one RGG is employed in the measurement of each cross-gradient tensor element, inter-instrument error correlation is not a consideration in the determination of the cross-gradient tensor errors.

For common inertial angular velocity excitation, the equivalent input rotational field error spectra to the RGG signal process for calculation of the trace element errors may be derived using the method employed in Technical Report No. 1 to obtain the equivalent input error spectra to each RGG channel. As an example, the complete input rotational field error spectrum for the \overline{XX} trace element error is presented in (1) for the correlated case.

$$\begin{aligned} S_{XX_{in}}(f) = & \frac{8}{9} [S_x(f) * S_x(f)] + \frac{2}{9} [S_y(f) * S_y(f) + S_z(f) * S_z(f)] \\ & - \frac{4}{9} [S_{xy}(f) * S_{xy}(f) + S_{yx}(f) * S_{yx}(f)] \\ & - \frac{4}{9} [S_{xz}(f) * S_{xz}(f) + S_{zx}(f) * S_{zx}(f)] \\ & + \frac{2}{9} [S_{yz}(f) * S_{yz}(f) + S_{zy}(f) * S_{zy}(f)] \\ & + \frac{4}{9} [4M_x^2 S_x(f) + M_y^2 S_y(f) + M_z^2 S_z(f)] \end{aligned}$$

SECTION IX

$$\begin{aligned}
 & + \frac{4}{9} \left[M_y M_z \left\{ S_{yz}(f) + S_{zy}(f) \right\} - 2M_x M_y \left\{ S_{xy}(f) + S_{yx}(f) \right\} \right. \\
 & \left. - 2M_x M_z \left\{ S_{xz}(f) + S_{zx}(f) \right\} \right] \quad (1)
 \end{aligned}$$

When the rotational field environment of each RGG is statistically independent of the others, eq. (30) of Technical Report No. 1 may be applied to each individual RGG to obtain the error variances of each RGG channel, and the resultant error variances of pairs of instruments may be combined on the basis of statistical independence to obtain the gravity gradient trace element error variances. Self-induced rotational fields of each RGG, e.g., from each spin bearing, have inter-instrument statistical independence. On the other hand, the common angular velocities of the vibration-isolation system (VIALS) produce inter-instrument correlation, and this requires employment of input error spectra of the form of eq. (1) to obtain the trace element variances.

The correlated trace element rotational field bias errors are stated as (2), (3), and (4), where the σ_x^2 , σ_y^2 , σ_z^2 are the angular rate variances of the common rotational field environment.

$$M_{XX} = \frac{1}{3} \left[2\sigma_x^2 - (\sigma_y^2 + \sigma_z^2) \right] \quad (2)$$

$$M_{YY} = \frac{1}{3} \left[2\sigma_y^2 - (\sigma_x^2 + \sigma_z^2) \right] \quad (3)$$

$$M_{ZZ} = \frac{1}{3} \left[2\sigma_z^2 - (\sigma_x^2 + \sigma_y^2) \right] \quad (4)$$

In the uncorrelated case, the trace element bias errors depend on the rate variances associated with pairs of RGG's. As an example,

the uncorrelated \overline{XX} trace element bias is presented as (5) where the superscript is used for RGG spin axis identification.

$$M_{XX} = \frac{1}{3} \left[\sigma_x^2 - \sigma_z^2 \right]^Y + \frac{1}{3} \left[\sigma_x^2 - \sigma_y^2 \right]^Z \quad (5)$$

Observe that the rate variances, σ_x^2 , in each term of (5) are two different variances; the first is related to the RGG with a \overline{Y} spin axis, and the second is related to the RGG with a \overline{Z} spin axis.

The cross-gradient bias errors are of the same form for both uncorrelated and inter-instrument correlated cases as shown in (6), (7), and (8), where the $C_{ij}(o)$ are the angular rate covariance functions evaluated at zero time shift.

$$M_{XY} = C_{xy}(o) \quad (6)$$

$$M_{XZ} = C_{xz}(o) \quad (7)$$

$$M_{YZ} = C_{yz}(o) \quad (8)$$

For the purpose of estimating the rotational field error variances of the gravity gradient tensor elements, it is convenient to assume the angular rate cross spectra to be zero for two reasons: (1) a great simplification of the equivalent input error spectra is achieved, and (2) at present there is no sound basis for estimation of the cross spectra. This assumption may be justified by considering that the basic effect of non-zero angular rate cross spectra is to redistribute the rotational field errors between RGG channels without appreciably altering the total system error for a given angular rate power. When the cross spectra are zero, eq. (1) reduces to (9) for the correlated case.

SECTION IX

$$S_{XX_{in}}(f) = \frac{8}{9} [S_x(f) * S_x(f)] + \frac{2}{9} [S_y(f) * S_y(f) + S_z(f) * S_z(f)] \\ + \frac{4}{9} [4M_x^2 S_x(f) + M_y^2 S_y(f) + M_z^2 S_z(f)] \quad (9)$$

In the uncorrelated case, the equivalent input error spectrum of the \overline{XX} trace element is just the weighted sum of the error spectra of the \overline{Y} and \overline{Z} spin axis RGG in-phase channel error spectra as defined by (10).

$$S_{XX_{in}}(f) = \frac{1}{9} [S_c^Y(f) + S_c^Z(f)] \quad (10)$$

When the cross spectra are zero, eq. (10) may be expressed (from eq. (30) of Technical Report No. 1) as (11) wherein the superscript spin-axis identification is employed.

$$S_{XX_{in}}(f) = \frac{2}{9} [S_x(f) * S_x(f) + S_y(f) * S_y(f)]^Z \\ + \frac{2}{9} [S_x(f) * S_x(f) + S_z(f) * S_z(f)]^Y \\ + \frac{4}{9} [M_y^2 S_y(f) + M_x^2 S_x(f)]^Z \\ + \frac{4}{9} [M_z^2 S_z(f) + M_x^2 S_x(f)]^Y \quad (11)$$

The equivalent input error spectrum of the \overline{XY} cross-gradient tensor element for either the correlated or uncorrelated cases is just the weighted spectrum of eq. (31) in Technical Report No. 1. When the cross spectra are zero, the equivalent input \overline{XY} cross-gradient error spectrum is given by (12).

SECTION IX

$$S_{XY_{in}}(f) = S_x(f) * S_y(f) + M_y^2 S_x(f) + M_x^2 S_y(f) \quad (12)$$

For the purposes of error estimation, a further simplification results when all of the rate spectra and average rates of each axis are assumed to be equal to $S_\omega(f)$ and M_ω , respectively. When these assumptions are applied to (9), (11), and (12), the equivalent input error spectra of (13), (14), and (15) are the result.

$$S_{ii}(f) \Big|_{corr} = \frac{12}{9} [S_\omega(f) * S_\omega(f)] + \frac{8}{3} M_\omega^2 S_\omega(f) \quad (13)$$

$$S_{ii}(f) \Big|_{uncorr} = \frac{8}{9} [S_\omega(f) * S_\omega(f)] + \frac{16}{9} M_\omega^2 S_\omega(f) \quad (14)$$

$$S_{ij}(f) \Big|_{all} = [S_\omega(f) * S_\omega(f)] + 2M_\omega^2 S_\omega(f) \quad (15)$$

Observe that the correlated case of (13) is a little larger than the uncorrelated case of (14). The gradient tensor error variances are estimated by integration of the equivalent output error spectra obtained from the equivalent filter of the RGG signal process acting on the appropriate input error spectra as defined by (16) and (17) where $H_e(s)$ is the equivalent lowpass filter of the RGG signal process.

$$\sigma_{ii}^2 = \int_{-\infty}^{+\infty} |H_e(j2\pi f)|^2 S_{ii}(f) df \quad (16)$$

$$\sigma_{ij}^2 = \int_{-\infty}^{+\infty} |H_e(j2\pi f)|^2 S_{ij}(f) df \quad (17)$$

SECTION IX

The significant error variances are produced by the terms in (13), (14), and (15) involving the convolution of the rate spectra. The remaining terms involving the average rate (M_ω) when filtered by the RGG signal process produce extremely small contributions to the standard error. It is estimated that these error variance contributions will be less than $(0.002 \text{ EU})^2$ and as a result they will not be given further consideration.

Proper evaluation of the convolved spectral error contributions requires knowledge of the form of the rate spectra; however, it is possible to place an upper bound on these errors without knowledge of the exact spectral form, providing that an upper bound on the rate variance (σ_ω^2) is known. To make such an estimate, consider a model power spectrum consisting of pairs of impulse functions containing power, σ_i^2 . Further, assume that each pair is displaced from every other pair by a frequency increment larger than the equivalent bandwidth of the signal process and that the total rate power is the sum of the power contained in each pair of impulses. When this model spectrum is convolved with itself and passed through the equivalent filter of the RGG signal process, the resultant spectrum, to first order, is a single impulse of weight equal to one-half the square of the total rate variance. For any other rate spectrum containing the same total rate variance (σ_ω^2), the power of the convolved spectrum within the equivalent RGG bandwidth (centered at zero frequency) will be less than or equal to one-half the square of the rate variance. This result is stated as (18).

$$\int_{-\infty}^{\infty} \left| H_e(j2\pi f) \right|^2 \left\{ S_\omega(f) * S_\omega(f) \right\} df \leq \frac{1}{2} \sigma_\omega^4 \quad (18)$$

Thus, a set of gradient tensor error variance bounds may be computed from (16) and (17) using (18). These bounds are stated as (19) and (20) for the correlated and uncorrelated trace element cases and as (21) for the cross-gradient variance bound.

SECTION IX

$$\left. \sigma_{ii}^2 \right|_{\text{corr}} \leq \frac{6}{9} \sigma_\omega^4 \quad (19)$$

$$\left. \sigma_{ii}^2 \right|_{\text{uncorr}} \leq \frac{4}{9} \sigma_\omega^4 \quad (20)$$

$$\left. \sigma_{ij}^2 \right|_{\text{all}} \leq \frac{1}{2} \sigma_\omega^4 \quad (21)$$

Finally, the standard deviation bounds of the rotational field errors are stated as (22), (23), and (24).

$$\left. \sigma_{ii} \right|_{\text{corr}} \leq \frac{\sqrt{6}}{3} \sigma_\omega^2 \quad (22)$$

$$\left. \sigma_{ii} \right|_{\text{uncorr}} \leq \frac{2}{3} \sigma_\omega^2 \quad (23)$$

$$\left. \sigma_{ij} \right|_{\text{all}} \leq \frac{1}{\sqrt{2}} \sigma_\omega^2 \quad (24)$$

It is interesting to observe that all of these standard error bounds are approximately equal.

SECTION IX

Having developed these standard error bounds, it is a simple task to evaluate the rotational field error contributions from the various error sources. First, let us consider the errors induced by the VIALS. In Section VII, an upper bound on the rate variance of the stable platform was established and is restated in (25).

$$\sigma_{\omega}^2 \Big|_{VIALS} \leq \left(9.27 \times 10^{-6} \text{ rad/sec} \right)^2 \quad (25)$$

Substitution of (25) into (22) and (24), yields the VIALS-induced rotational field errors as (26) and (27).

$$\sigma_{ii} \leq \frac{\sqrt{6}}{3} \left(9.27 \times 10^{-6} \right)^2 \times 10^9 \approx 0.070 \text{ EU} \quad (26)$$

$$\sigma_{ij} \leq \frac{1}{\sqrt{2}} \left(9.27 \times 10^{-6} \right)^2 \times 10^9 \approx 0.061 \text{ EU} \quad (27)$$

Transverse angular velocity induced by the spin bearing of each RGG causes rotational field errors that are statistically independent between instruments. The spin bearing specification requires that the transverse angular rates produced by the bearing be limited so that the induced bias of each instrument channel does not exceed ± 4 EU with a maximum bias uncertainty of 0.04 EU. In addition, it is required that the standard error of each channel due to random bearing-induced rates be limited to 0.04 EU in each instrument channel. The 0.04 EU bound translates to an equivalent rate variance bound of $0.283 \times 10^{-10} (\text{rad/sec})^2$. The statistical combination of the bias uncertainty and the random standard error bounds translates to an equivalent rate variance bound of $0.4 \times 10^{-10} (\text{rad/sec})^2$. Using this

SECTION IX

rate variance bound in (23) and (24), we obtain the spin bearing-induced rotational field errors as (28) and (29).

$$\sigma_{ii} \leq \left(\frac{2}{3}\right) \left(0.4 \times 10^{-10}\right) \left(10^9\right) \approx 0.027 \text{ EU} \quad (28)$$

$$\sigma_{ij} \leq \left(\frac{1}{\sqrt{2}}\right) \left(0.4 \times 10^{-10}\right) \left(10^9\right) \approx 0.028 \text{ EU} \quad (29)$$

Spin motor-induced rates normal to the spin axis are assumed to be negligible in comparison to the bearing-induced rates because of the high bearing stiffness and the small motor forces.

Platform angular rates due to RGG rotor mass unbalance of (0.03 gm-cm) produce bias errors to the extent that they remain constant after initialization. It is estimated that the RGG rotor mass-unbalance induced platform rates on each axis will be less than 3×10^{-6} rad/sec and that the amplitudes will be stable to better than 10% of their values. This leads to the rate variance bound defined by (30).

$$\sigma_{\omega}^2 \Big|_{\substack{\text{RGG} \\ \text{MU}}} \leq 2 \left(3 \times 10^{-6}\right) \left(0.3 \times 10^{-6}\right) \quad (30)$$

Substitution of this rate variance into (22) and (24) yields standard errors of approximately 0.001 EU. It is concluded that RGG rotor mass unbalance causes negligible rotational field errors.

In summary, only the spin bearing and the VIALS produce significant rotational field errors. To complete the rotational field error analysis, consideration must be given to the bias uncertainty of the VIALS-induced errors. The bias errors are defined by (2), (3), and (4) and by (6), (7), and (8) for the trace and cross-gradient tensor elements, respectively. When the previous assumptions of equal and

SECTION IX

independent rate spectra are applied to these bias equations, the resultant biases are zero. To estimate bias uncertainty, a departure from the previous assumptions is required. One possibility is to assume non-stationary statistics for the VIALS-induced angular rates and then to compute the bias variances on the basis of the variances of the rate variances. For this purpose, let the rate variances, σ_x^2 , σ_y^2 , σ_z^2 , be represented by the independent random variables, α , β , γ . Further, assume that the probability density function of each of these random variables is of the same form and equal to zero outside of the positive region zero to ω_{\max}^2 . Under these conditions, the expected value of the bias is zero. This may be demonstrated by substitution of the random variables, α , β , γ , into (2) as shown in (31).

$$M_{xx} = \frac{1}{3} [2\alpha - \beta - \gamma] \quad (31)$$

$$E[M_{xx}] = \frac{1}{3} [2E[\alpha] - E[\beta] - E[\gamma]] \quad (32)$$

Since the random variables all have the same probability density, their expected values are equal leading to an expected bias of zero from (32). The variance of the bias, σ_m^2 , is defined by (33) when the random variables are statistically independent.

$$\sigma_m^2 = \frac{1}{9} [4E[\alpha^2] + E[\beta^2] + E[\gamma^2]] \quad (33)$$

Since the probability densities are assumed to be the same, (33) may be expressed as (34).

$$\sigma_m^2 = \frac{2}{3} E[\alpha^2] \quad (34)$$

SECTION IX

The expectation in (34) is the variance of the rate variance. This expectation may be calculated on the basis of an assumed probability density function. For this purpose, let's select arbitrarily the density shown in Fig. IX-4. The second moment of α is evaluated in (35) for the density function of Fig. IX-4.

$$E[\alpha^2] = \int_0^{2/\sigma_\omega^2} \alpha^2 p_\alpha(\alpha) d\alpha = \frac{1}{2} \sigma_\omega^4 \Big|_{\max} \quad (35)$$

From (34) and (35), the resultant variance of the bias is given in (36).

$$\sigma_m^2 = \frac{1}{3} \sigma_\omega^4 \Big|_{\max} \quad (36)$$

The standard error is given by (37).

$$\sigma_m = \frac{1}{\sqrt{3}} \sigma_\omega^2 \Big|_{\max} \quad (37)$$

An upper bound of the VIALS rate variance was defined by (25). Substitution of this value into (37) yields an estimate of the bias uncertainty due to VIALS-induced rate errors.

$$\sigma_m = \frac{(9.27)^2 \times 10^{-12} \times 10^9}{\sqrt{3}} \cong 0.050 \text{ EU} \quad (38)$$

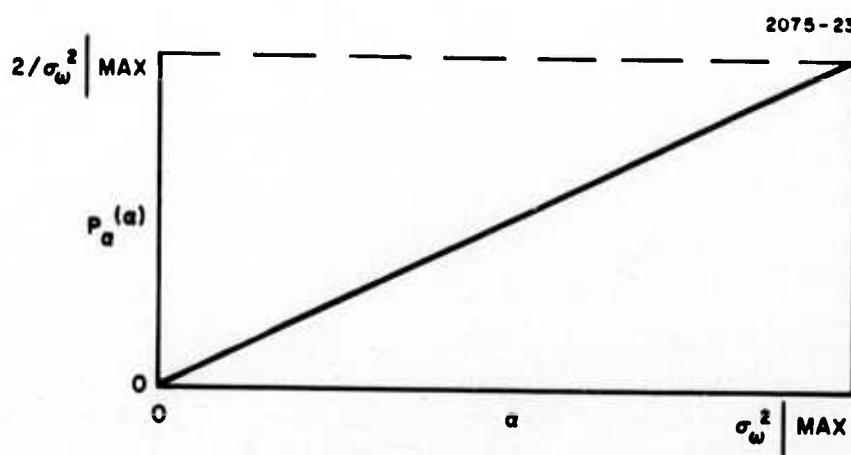


Fig. IX-4. An Assumed Probability Density Function.

SECTION IX

A summary of the rotational field errors is given in Table IX-5. It is recognized that the method of estimating the VIALS-induced bias uncertainty is quite arbitrary, but it does provide some indication of the size of this error source based on an upper bound for the angular rate variance.

TABLE IX-5
Summary of Rotational Field Errors

Error Source	σ_{ii} -EU	σ_{ij} -EU
Spin bearing total	0.027	0.028
VIALS random	0.070	0.061
VIALS bias uncertainty	0.050	(0.050)*
Total VIALS	0.086	0.079

*Actually this value should be zero for the stated assumptions but the same value was used here as was derived for the trace element bias uncertainty, because the stated assumptions are quite arbitrary.

T868

E. SUM-MODE MISMATCH ERRORS

The sum-mode mismatch error mechanism provides an excitation of the RGG differential mode through RGG rotor spin axis accelerations occurring in a narrow frequency band centered at twice the spin frequency ($2\omega_s$). In Technical Report No. 1, it was demonstrated that errors of this type can be represented in terms of an equivalent input error to the RGG carrier signal process, which is proportional to the RGG rotor spin axis disturbance torques in a narrow frequency band centered at twice the spin frequency as described by (1), wherein " T_d " represents the narrow band spin axis disturbance torque, $K\beta$ is the

SECTION IX

sum-mode mismatch factor, η is the arm inertia efficiency, β_0 is the nominal sum mode frequency, and J is the total polar inertia of the RGG rotor.

$$\Gamma_{\epsilon_{in}} = \left[\frac{k_\beta}{\eta} \right] \left[\frac{\beta_0^2}{(2\omega_s)^2 - \beta_0^2} \right] \left[\frac{T_d}{J} \right] \quad (1)$$

Both deterministic and random excitations of this error mechanism are possible. Deterministic excitations produce bias errors which may be compensated during RGG system initialization to the extent that these excitations remain stable. Changes in the bias errors after initialization and random excitations contribute to the total error variance. Potential excitation sources are the spin bearing, the spin motor, the speed control servo, and the vibration-isolation system (VIALS).

It is convenient to analyze the errors of each channel of an individual RGG instrument in this case and then to determine the gravity gradient tensor element standard errors from the individual instrument errors. The bias errors of each RGG channel will be determined on the basis of the spin bearing and spin motor specifications and an estimate of the tachometer disturbance through the speed control servo. When the speed control servo position error is sampled only once per revolution, no significant torque disturbances at twice the spin frequency due to sampling noise are anticipated, and the load torque disturbance from the VIALS is considered to be random only.

The random errors of each channel will be determined on the basis of (1) bias uncertainty due to both excitation uncertainty and RGG error coefficient uncertainty, and (2) random excitations acting on the nominal RGG error coefficient. The resultant random errors of each channel will then be converted to gravity gradient tensor standard errors on the basis of inter-instrument statistical independence.

SECTION IX

The first logical step in the analysis is to establish the bias errors of each channel. To accomplish this, it is convenient to evaluate the RGG error coefficient of (1) for the following parametric values:

$$k_\beta = 10^{-6}$$

$$\eta = 0.86$$

$$\beta_0 = 128 \text{ rad/sec}$$

$$2\omega_s = 220 \text{ rad/sec}$$

$$J = 2.5 \times 10^5 \text{ gm-cm}^2$$

The resultant error coefficient is evaluated in (2).

$$\left(\frac{k_\beta}{\eta} \right) \left(\frac{\beta_0^2}{(2\omega_s)^2 - \beta_0^2} \right) \left(\frac{1}{J} \right) = 2.37 \times 10^{-3} \frac{\text{EU}}{\text{dcm}} \quad (2)$$

The spin bearing specification allows a deterministic disturbance torque of 1000 dcm at twice the spin frequency. Assuming this disturbance torque to have equal contributions of 707 dcm to each RGG channel, the resultant spin bearing bias is given by (3) from (1) and (2).

$$M_c = M_s = (2.73 \times 10^{-3})(707) \cong 1.68 \text{ EU} \quad (3)$$

Similarly, the specification for each motor allows a deterministic disturbance torque of 500 dcm. There are two motors, and the probable net disturbance torque is 707 dcm. Assuming this is distributed equally in each RGG channel, the resultant spin motor bias is given by (4) from (1) and (2).

$$M_c = M_s = (2.73 \times 10^{-3})(500) \cong 1.19 \text{ EU} \quad (4)$$

SECTION IX

Finally, it is assumed that the deterministic tachometer signal noise acting through the speed control servo will be less than 1% of the signal amplitude. This assumption results in an equivalent deterministic disturbing torque of 1000 dcm, and an expected bias in each channel equal to that in (3).

Since the bias values from the spin bearing, the spin motor, and the tachometer may be considered, to be statistically independent, the probable bias is just the root-sum-square of the individual biases. This bias value is given in (5).

$$M_c = M_s = \sqrt{2(1.68)^2 + (1.19)^2} = 2.66 \text{ EU} \quad (5)$$

The value of (5) may be employed to determine the error due to RGG coefficient uncertainty. It is estimated that in a 10-hr period the standard deviation of k_β from its nominal value (10^{-6}) will be 3.75×10^{-9} ; this is a per-unit uncertainty of 3.75×10^{-3} . Using this figure in conjunction with (5), a standard error for RGG coefficient uncertainty is given by (6).

$$\sigma_c = \sigma_s = 2.66 \times 3.75 \times 10^{-3} \approx 0.008 \text{ EU} \quad (6)$$

The spin bearing and spin motor specifications allow a 5% uncertainty in the deterministic torque disturbances. With a similar allowance for the tachometer signal-induced disturbing torque, the bias uncertainty of the spin bearing, spin motor, and tachometer may be scaled as 5% of the probable bias given in (5), as stated in (7).

$$\sigma_c = \sigma_s = 0.05 \times 2.66 \approx 0.133 \text{ EU} \quad (7)$$

Having established the bias uncertainties, it is in order to consider the random variations of the various excitation sources. The spin

SECTION IX

bearing specification allows a random disturbing torque of 50 dcm, rms in each channel, and the spin motor specification allows a random disturbing torque from each motor of 25 dcm, rms. These specifications produce the standard errors in each RGG channel from (1) and (2) stated in (8).

$$\sigma_c = \sigma_s = 2.37 \times 10^{-3} \sqrt{(50)^2 + 2(25)^2} = 0.145 \text{ EU} \quad (8)$$

The other potential contributors to the standard error are the tachometer and the VIALS. It is assumed that all the tachometer disturbances have been considered in the bias variations, so that there are no additional random tachometer disturbances to be treated. The load-induced torque disturbances at twice the spin frequency due to VIALS are estimated to be less than 1 dyne-cm and are considered to be a negligible excitation source of the sum-mode mismatch error mechanism.

The total standard error of each RGG channel is obtained as the root sum square of (6), (7), and (8) as stated in (9).

$$\sigma_c = \sigma_s = \sqrt{(0.008)^2 + (0.133)^2 + (0.145)^2} \cong 0.196 \text{ EU} \quad (9)$$

When the inter-instrument errors are statistically independent, the standard gradient tensor errors are given by (10) and (11).

$$\sigma_{ii} = \frac{\sqrt{2}}{3} \sigma_c = \frac{\sqrt{2}}{3} (0.196) \cong 0.093 \text{ EU} \quad (10)$$

$$\sigma_{ij} = \frac{1}{2} \sigma_s = \frac{1}{2} (0.196) \cong 0.098 \text{ EU} \quad (11)$$

SECTION IX

F. ANISOELASTIC ERRORS

Body forces that result from acceleration of the centers of support of the RGG arms will cause a relative deflection of the center of mass of each arm with respect to its center of support. When this deflection has a component normal to the acceleration vector, an anisoelastic moment is developed about the center of support. The equations describing the deflection and the resultant anisoelastic moment of the i^{th} arm may be expressed in terms of the arm mass, m_i , the arm compliance tensor, $\bar{\Psi}_i$, and the center of support acceleration, \bar{a}_i , by eqs. (1), (2), and (3).

$$\bar{\delta}_i = -m_i \bar{\Psi}_i \cdot \bar{a}_i \quad (1)$$

$$\bar{L}_i = -m_i \bar{\delta}_i \times \bar{a}_i \quad (2)$$

$$\bar{L}_i = (m_i)^2 [\bar{\Psi}_i \cdot \bar{a}_i] \times \bar{a}_i \quad (3)$$

The differential moment (of the two RGG arms) acting about the principal torsional axis (\bar{k}) of the arm support structure may excite the RGG differential mode and produce errors in the gravity gradient measurement. This differential moment is expressed as eq. (4) on the basis of (3).

$$\bar{k} \cdot (\bar{L}_1 - \bar{L}_2) = \bar{k} \cdot [(m_1)^2 \bar{\Psi}_1 \cdot \bar{a}_1] \times \bar{a}_1 - [m_2]^2 \bar{\Psi}_2 \cdot \bar{a}_2] \times \bar{a}_2 \quad (4)$$

The accelerations of each arm support center may be expressed in terms of a "common mode" and a "differential" acceleration as defined by eqs. (5) and (6).

$$\bar{a}_o \triangleq \frac{1}{2} (\bar{a}_1 + \bar{a}_2) \quad (5)$$

SECTION IX

$$\overline{\Delta a} \triangleq (a_1 - a_2) \quad (6)$$

Substitution of (5) and (6) into (4) leads to the expanded form of the anisoelastic differential moment presented as (7).

$$\begin{aligned} L_k &= \bar{k} \cdot \left[\left\{ (m_1^2 \psi_1 - m_2^2 \psi_2) \cdot \bar{a}_o \right\} \times \bar{a}_o \right] \\ &\quad + \bar{k} \cdot \left[\left\{ (m_1^2 \psi_1 - m_2^2 \psi_2) \cdot \frac{\overline{\Delta a}}{2} \right\} \times \frac{\overline{\Delta a}}{2} \right] \\ &\quad + \bar{k} \cdot \left[\left\{ \left(\frac{m_1^2 \psi_1 + m_2^2 \psi_2}{2} \right) \cdot \bar{a}_o \right\} \times \overline{\Delta a} \right] \\ &\quad + \bar{k} \cdot \left[\left\{ \left(\frac{m_1^2 \psi_1 + m_2^2 \psi_2}{2} \right) \cdot \overline{\Delta a} \right\} \times \bar{a}_o \right] \end{aligned} \quad (7)$$

Normalization of (7) by the principal arm transverse inertia difference (ηC) yields the equivalent input gradient error to the RGG signal process. This normalized error function is presented as (8) wherein the arm compliance tensor functions have been replaced by the "differential" and "average" anisoelastic error coefficient tensors, \bar{K}_o and \bar{K}_a , as defined by (9) and (10).

$$\begin{aligned} (2r_{ij})_e &= \bar{k} \cdot \left[(\bar{K}_o \cdot \bar{a}_o) \times \bar{a}_o + (\bar{K}_o \cdot \frac{\overline{\Delta a}}{2}) \times \frac{\overline{\Delta a}}{2} \right] \\ &\quad + \bar{k} \cdot [(\bar{K}_a \cdot \bar{a}_o) \times \overline{\Delta a} + (\bar{K}_a \cdot \overline{\Delta a}) \times \bar{a}_o] \end{aligned} \quad (8)$$

$$\bar{K}_o \triangleq \frac{1}{\eta C} \left[(m_1)^2 \psi_1 - (m_2)^2 \psi_2 \right] \quad (9)$$

SECTION IX

$$\bar{K}_a \stackrel{\Delta}{=} \frac{1}{\eta C} \left[\frac{(m_1)^2 \bar{\psi}_1 + (m_2)^2 \bar{\psi}_2}{2} \right] \quad (10)$$

The differential acceleration, $\bar{\Delta}a$, is a function of the axial separation, \bar{l} , of the arm centers of mass and may be expressed in terms of the RGG angular acceleration and velocity vectors as (11).

$$\bar{\Delta}a = \dot{\bar{\omega}} \times \bar{l} + \bar{\omega} \times (\bar{\omega} \times \bar{l}) \quad (11)$$

It is anticipated that the second term in (8) involving the product of $\bar{\Delta}a$ with itself will be a second order effect and that the errors associated with this term will be less than 0.001 EU for all excitation sources. For this reason and for later analytical convenience, eq. (8) is decomposed into the separate input error functions of (12) and (13).

$$(2\Gamma_{ij})_o \stackrel{\Delta}{=} \bar{k} \cdot \left[(\bar{K}_o \cdot \bar{a}_o) \times \bar{a}_o \right] \quad (12)$$

$$(\gamma\Gamma_{ij})_a \stackrel{\Delta}{=} \bar{k} \cdot \left[(\bar{K}_a \cdot \bar{a}_o) \times \bar{\Delta}a + (\bar{K}_a \cdot \bar{\Delta}a) \times \bar{a}_o \right] \quad (13)$$

Expansion of (12) in the RGG rotor-fixed frame ($\bar{i}\bar{j}\bar{k}$) yields (14).

$$(2\Gamma_{ij})_o = [K_{ii} - K_{jj}] a_i a_j + K_{ij} a_j^2 - K_{ji} a_i^2 + a_k [K_{ik} a_j - K_{jk} a_i] \quad (14)$$

Transformation of the acceleration terms in (14) to RGG stator-referenced acceleration components yields (15).

SECTION IX

$$\begin{aligned}
 (2\Gamma_{ij})_o &= \left[\frac{K_{ii} - K_{jj}}{2} \right] \left[\left(a_y^2 - a_x^2 \right) \sin 2\omega_s t + 2a_x a_y \cos 2\omega_s t \right] \\
 &+ \left[K_{ij} - K_{ji} \right] \left[\frac{a_x^2 + a_y^2}{2} \right] \\
 &- \left[\frac{K_{ij} + K_{ji}}{2} \right] \left[a_x a_y \sin 2\omega_s t + \left(a_x^2 - a_y^2 \right) \cos 2\omega_s t \right] \\
 &+ a_z \left[\left(K_{ik} a_y - K_{jk} a_x \right) \cos \omega_s t - \left(K_{ik} a_x + K_{jk} a_y \right) \sin \omega_s t \right]
 \end{aligned} \tag{15}$$

Equation (15) contains an unmodulated term whose coefficient, $[K_{ij} - K_{ji}]$, is zero because the anisoelastic tensor is symmetric. The third term in (15) is negligible because its coefficient is more than three orders of magnitude smaller than the coefficient of the first term in (15). The cross-anisoelastic coefficients, K_{ij} and K_{ji} , are proportional to the product of $(K_{ii} - K_{jj})$ and the angle of orthogonal deficiency of the principal elastic axes of the two arms about the torsional axis (\bar{k}). This non-orthogonality is expected to be less than 1 milliradian. Thus, eq. (15) may be further decomposed into what we shall describe as the "prime anisoelastic" error function of (16) and the "cross-anisoelastic" error function of (17).

$$(2\Gamma_{ij})_{op} \triangleq \left[\frac{K_{ii} - K_{jj}}{2} \right] \left[\left(a_y^2 - a_x^2 \right) \sin 2\omega_s t + 2a_x a_y \cos 2\omega_s t \right] \tag{16}$$

$$(2\Gamma_{ij})_{oc} \triangleq a_z \left[\left(K_{ik} a_y - K_{jk} a_x \right) \cos \omega_s t - \left(K_{ik} a_x + K_{jk} a_y \right) \sin \omega_s t \right] \tag{17}$$

The "prime anisoelastic" error function of (16) is of a non-linear form similar to the rotational field error function; it is

SECTION IX

sensitive to the low frequency components of the squares and products of the accelerations normal to the RGG spin axis. Analysis of these errors is facilitated by viewing these functions as separate input errors to each channel of the RGG signal process in the non-spinning domain as described by (18) and (19).

$$\epsilon_c \Big|_{op} \triangleq K_o \left[a_y^2 - a_x^2 \right] \quad (18)$$

$$\epsilon_s \Big|_{op} \triangleq K_o \left[2a_x a_y \right] \quad (19)$$

where

$$K_o \triangleq \left[\frac{K_{ii} - K_{jj}}{2} \right]$$

The "cross-anisoelastic" error function of (17) is sensitive to frequency components of the acceleration products in narrow frequency bands centered at the spin frequency and its third harmonic. The most significant terms in (17) are those involving the product of scalar gravity and a vibrational acceleration at one and three times the spin frequency. The non-linear terms of (17) produce negligibly small errors for the anticipated RGG vibration environment. The linearized forms of (17) are expressed as (20), (21), and (22) for each RGG spin axis orientation in the locally level measurement frame (\overline{XYZ}).

$$(2\Gamma_{ij})_{oc} \Big|_X = g \left[K_{ik} a_X \cos \omega_s t - K_{jk} a_X \sin \omega_s t \right] \quad (20)$$

$$(2\Gamma_{ij})_{oc} \Big|_Y = g \left[-K_{jk} a_Y \cos \omega_s t - K_{ik} a_Y \sin \omega_s t \right] \quad (21)$$

SECTION IX

$$(2\Gamma_{ij})_{oc} \Big|_Z = g \left[(K_{ik}a_Y - K_{jk}a_X) \cos \omega_s t - (K_{ik}a_X + K_{jk}a_Y) \sin \omega_s t \right] \quad (22)$$

An interesting property of these linearized equations is that the sensors with horizontal spin axes are sensitive to axial vibrations only (i. e., vibrations along their spin axes) while the vertical spin axis sensor is sensitive to radial accelerations only.

Certain cross-anisoelastic errors are more conveniently viewed in the rotor-fixed frame (\bar{ijk}). For example, the last term in (14) for the vertical spin axis sensor may be linearized as in (23).

$$(2\Gamma_{ij})_{oc} \Big|_Z = g \left[K_{ik}a_j - K_{jk}a_i \right] \quad (23)$$

This equation is useful in estimating the cross-anisoelastic errors induced by radial accelerations of the spin bearing at twice the spin frequency in RGG rotor-fixed coordinates. Similarly, the spin-bearing-induced axial vibrations at one and three times the spin frequency for horizontal spin axes may be readily estimated from the linearized forms of (24) and (25).

$$(2\Gamma_{ij})_{oc} \Big|_X \approx g a_k \left[K_{ik} \cos \omega_s t - K_{jk} \sin \omega_s t \right] \quad (24)$$

$$(2\Gamma_{ij})_{oc} \Big|_Y \approx -g a_k \left[K_{jk} \cos \omega_s t + K_{ik} \sin \omega_s t \right] \quad (25)$$

In summary, (18) through (25) provide the basis for the evaluation of the gravity gradient input errors due to the coefficients of the "differential" anisoelastic tensor defined by (9).

The errors defined by (13) may be approximated to first order by equating the "common mode" acceleration vector (\bar{a}_o) to the

SECTION IX

negative gravity vector ($-\bar{g}$). An expansion of (13) under this constraint is given by (26) wherein the elements of \bar{K}_a are identified by numerical subscripts and the gravity vector scalar elements are expressed in the rotor-fixed frame (\bar{ijk}).

$$\begin{aligned} (2\Gamma_{ij})_a &\equiv -g_i \left[(K_{11} - K_{22}) \Delta a_j - 2K_{12}\Delta a_i - K_{23}\Delta a_k \right] \\ &- g_j \left[(K_{11} - K_{22}) \Delta a_i + 2K_{12}\Delta a_j + K_{13}\Delta a_k \right] \quad (26) \\ &- g_k \left[K_{13}\Delta a_j - K_{23}\Delta a_i \right] \end{aligned}$$

Transformation of the gravity and differential acceleration components in (26) to RGG stator-referenced coordinates (\bar{xyz}) yields (27).

$$\begin{aligned} (2\Gamma_{ij})_a &\equiv - (K_{11} - K_{22}) \left[(g_x \Delta A_y - g_y \Delta A_x) \cos 2\omega_s t \right. \\ &+ \left. (g_y \Delta a_y - g_x \Delta a_x) \sin 2\omega_s t \right] \\ &- 2K_{12} \left[(g_y \Delta a_y - g_x \Delta a_x) \cos 2\omega_s t \right. \\ &- \left. (g_x \Delta a_y + g_y \Delta a_x) \sin 2\omega_s t \right] \quad (27) \\ &- \Delta a_z \left[(K_{13}g_y + K_{23}g_x) \cos \omega_s t \right. \\ &+ \left. (K_{23}g_y - K_{13}g_x) \sin \omega_s t \right] \\ &- g_k \left[(K_{13}\Delta a_y - K_{23}\Delta a_x) \cos \omega_s t \right. \\ &- \left. (K_{13}\Delta a_x + K_{23}\Delta a_y) \sin \omega_s t \right] \end{aligned}$$

SECTION IX

In (27), the cross-anisoelastic tensor coefficient, K_{12} , is estimated to be much smaller than the diagonal element, $K_{11} - K_{22}$, and since both coefficients operate on identical terms it is justifiable to neglect the K_{12} tensor coefficient. The coefficients of the second harmonic terms in (27) may be viewed as input errors to each channel of the RGG signal process in the manner of (18) and (19). These input error terms are defined by (28) and (29).

$$\epsilon_c \Big|_{ap} \triangleq - (K_{11} - K_{22}) [g_y \Delta a_y - g_x \Delta a_x] \quad (28)$$

$$\epsilon_s \Big|_{ap} \triangleq - (K_{11} - K_{22}) [g_x \Delta a_y + g_y \Delta a_x] \quad (29)$$

The remaining cross-anisoelastic terms of (27) are sensitive to the one and three times spin frequency components of the differential accelerations. Considerable simplification of these error functions is achieved when they are specialized to the locally level reference frame (\overline{XYZ}) for each individual sensor as in (30), (31), and (32).

$$(2\Gamma_{ij})_{ac} \Big|_X = g \Delta a_X [K_{13} \cos \omega_s t + K_{23} \sin \omega_s t] \quad (30)$$

$$(2\Gamma_{ij})_{ac} \Big|_Y = g \Delta a_Y [K_{23} \cos \omega_s t - K_{13} \sin \omega_s t] \quad (31)$$

$$(2\Gamma_{ij})_{ac} \Big|_Z = g [(K_{13} \Delta a_Y - K_{23} \Delta a_X) \cos \omega_s t - (K_{13} \Delta a_X + K_{23} \Delta a_Y) \sin \omega_s t] \quad (32)$$

It is interesting to observe that the horizontal spin axis sensors are sensitive to the axial components of differential

SECTION IX

acceleration only. Since the arm mass center separation vector (\bar{l}) is also in the axial direction, only the centrifugal term of (11) in the axial direction contributes to the errors of the horizontal spin sensors. It is estimated that the axial components of these centrifugal accelerations will be significantly less than $10^{-6} g$ for all excitation sources in the operational environment. It is concluded that the cross-anisoelastic error due to differential acceleration of the horizontal spin sensors is negligible and may be dropped from further consideration.

The differential acceleration components of the vertical spin axis sensor at one and three times the spin frequency are primarily the result of the angular acceleration term in (11). The vibration-isolation, alignment, and leveling system (VIALS) contribution to these angular accelerations in narrow frequency bands centered at one and three times the spin frequency is extremely small, i. e., of the order of $7 \times 10^{-5} \text{ rad/sec}^2$ rms. The resulting differential acceleration is substantially less than $10^{-6} g$ and may be neglected. The self-induced coherent, transverse angular acceleration of the vertical spin sensor at its spin frequency due to rotor mass unbalance is estimated to be less than $5 \times 10^{-4} \text{ rad/sec}^2$. The resultant transverse differential acceleration components for an axial mass center separation of approximately 2 cm is less than $10^{-6} g$. Rotor mass unbalance is a negligible excitation source of this error. Finally, we consider the spin bearing. A deterministic transverse angular acceleration of $10^{-2} \text{ rad/sec}^2$ is allowed by specification. This translates to approximately $2 \times 10^{-5} g$ for the vertical spin axis sensor. It is estimated that this will produce a bias-type error less than 0.005 EU with a 1% uncertainty. It is concluded that cross-anisoelastic error due to differential acceleration is negligible for all RGG orientations, and that only the prime anisoelastic errors due to eqs. (28) and (29) need further consideration. Equations (28) and (29) are zero for a vertical spin axis sensor, so only the

SECTION IX

the horizontal spin sensors need consideration. The errors of the \bar{X} -spin sensor are expressed as eqs. (33) and (34) from (28) and (29).

$$\epsilon_c \left| \frac{X}{ap} \right. = (K_{11} - K_{22}) [g\Delta a_z] \quad (33)$$

$$\epsilon_s \left| \frac{X}{ap} \right. = (K_{11} - K_{22}) [g\Delta a_y] \quad (34)$$

Only the differential acceleration components of (33) and (34) within the low frequency passband of the RGG signal process will propagate as errors. Only the spin bearing and the VIALS can produce angular accelerations in this frequency region. The spin bearing specification allows a low-frequency power spectral density of $10^{-4} (\text{rad/sec}^2)^2/\text{Hz}$ on a one-sided basis between 0 and 1 Hz. This translates to an effective angular acceleration within the RGG bandwidth of approximately $1.5 \times 10^{-3} \text{ rad/sec}^2$ and an effective differential acceleration (for $\ell \approx 2 \text{ cm}$) of about $3 \times 10^{-6} \text{ g}$. It is estimated that this will produce a standard error at the gravity gradient tensor of less than 0.004 EU. This is quite small but within the arbitrarily selected error resolution of 0.001 EU. Low-frequency angular accelerations attributable to VIALS are estimated to produce negligible differential accelerations. It is concluded that the anisoelastic errors associated with the error differential acceleration ($\bar{\Delta}a$) are negligible and that only the "prime anisoelastic" and "cross-anisoelastic" errors that result from (12) need further consideration.

First, let us examine the cross-anisoelastic errors defined by (20) through (25). These errors are all spin-frequency dependent. When the spin frequencies of all pairs of RGGs in a system differ by more than the equivalent bandwidth of the signal process it is reasonable to combine the individual instrument errors on the basis

SECTION IX

of statistical independence in determining the standard errors of the gravity gradient tensor elements. Therefore, the cross-anisoelastic errors at the output of each RGG instrument channel will be determined prior to determining the tensor element errors. The errors of the horizontal spin axis sensors are given by (20), (21) and (24), (25), and the vertical spin axis sensor errors are given by (22) and (23). The spin bearings and the VIALS are the main excitation sources.

The cross-anisoelastic error coefficients, K_{ik} and K_{jk} , are bounded to the same magnitude (1931 EU/g^2) and are zero mean random variables over an instrument population. In a single instrument, each may take any positive or negative value within the bound. An estimate of the standard output error of each RGG channel may be made using the bounding value (K_c) in place of K_{ik} and K_{jk} as in (35), (36), and (37).

$$\sigma_c^X \triangleq \sigma_s^X = K_c g^2 \frac{\sqrt{2}}{2} \sigma_{nX} \quad (35)$$

$$\sigma_c^Y \triangleq \sigma_s^Y = K_c g^2 \frac{\sqrt{2}}{2} \sigma_{nY} \quad (36)$$

$$\sigma_c^Z \triangleq \sigma_s^Z = K_c g^2 \frac{\sqrt{2}}{2} \sqrt{\sigma_{nX}^2 + \sigma_{nY}^2} \quad (37)$$

The VIALS effective accelerations in narrow bands centered at the spin and its third harmonic may be estimated on a per-axis basis from the VIALS acceleration power spectral density as in (38).

$$\begin{aligned} \sigma_n &= \sqrt{2 \left[S_a(f_s) + S_a(3f_s) \right] \Delta f_e} \\ &\approx 16.4 \times 10^{-6} g \end{aligned} \quad (38)$$

SECTION IX

Substitution of this value for the effective acceleration values in (35), (36), and (37) with $K_c = 1931 \text{ EU/g}^2$ yields the RGG instrument channel errors of (39) and (40) for the VIALS excitation.

$$\left. \begin{array}{l} \sigma_c^X = \sigma_s^X \\ \sigma_c^Y = \sigma_s^Y \end{array} \right\} = (1931) \left(\frac{\sqrt{2}}{2} \right) (16.4 \times 10^{-6}) \text{ EU} \equiv 0.022 \text{ EU} \quad (39)$$

$$\sigma_c^Z = \sigma_s^Z = (1931) (16.4 \times 10^{-6}) \text{ EU} \equiv 0.032 \text{ EU} \quad (40)$$

The associated tensor element errors on the basis of statistical independence are given by (41) through (46).

$$\sigma_{XX} = \frac{1}{3} \sqrt{\sigma_{cy}^2 + \sigma_{cz}^2} \equiv 0.013 \text{ EU} \quad (41)$$

$$\sigma_{YY} = \frac{1}{3} \sqrt{\sigma_{cx}^2 + \sigma_{cz}^2} \equiv 0.013 \text{ EU} \quad (42)$$

$$\sigma_{ZZ} = \frac{1}{3} \sqrt{\sigma_{cx}^2 + \sigma_{cy}^2} \equiv 0.010 \text{ EU} \quad (43)$$

$$\sigma_{XY} = \frac{1}{2} \sigma_s^Z \equiv 0.016 \text{ EU} \quad (44)$$

$$\sigma_{XZ} = \frac{1}{2} \sigma_s^Y \equiv 0.011 \text{ EU} \quad (45)$$

$$\sigma_{YZ} = \frac{1}{2} \sigma_s^X \equiv 0.011 \text{ EU} \quad (46)$$

The instrument errors due to spin bearing excitation may be determined in a similar manner; however, a large part of the spin bearing excitation is coherent with the spin. This produces bias errors that are compensated during the initialization process. It is estimated that deterministic accelerations of the order of 10^{-4} g

SECTION IX

with a stability of 10^{-5} g are possible. In addition, a random level of 10^{-5} g is assumed. Substitution of these acceleration uncertainties into (35), (36), and (37) yields the estimated instrument channel errors of (47) and (48) for the spin bearing excitation.

$$\left. \begin{array}{l} \sigma_c^X = \sigma_s^X \\ \sigma_c^Y = \sigma_s^Y \end{array} \right\} \cong (1931) \left(\frac{\sqrt{2}}{2} \right) \sqrt{2 \times (10^{-5})^2} \cong 0.019 \text{ EU} \quad (47)$$

$$\sigma_c^Z = \sigma_s^Z \cong (1931) \left(\frac{\sqrt{2}}{2} \right) \sqrt{4 \times (10^{-5})^2} \cong 0.027 \text{ EU} \quad (48)$$

When these errors are combined on the basis of inter-instrument statistical independence, the resultant gravity gradient tensor element standard errors due to spin-bearing excitation are given by (49) through (54).

$$\sigma_{XX} \cong \frac{1}{3} \sqrt{(0.019)^2 + (0.027)^2} \cong 0.011 \text{ EU} \quad (49)$$

$$\sigma_{YY} \cong \frac{1}{3} \sqrt{(0.019)^2 + (0.027)^2} \cong 0.011 \text{ EU} \quad (50)$$

$$\sigma_{ZZ} \cong \frac{1}{3} \sqrt{(0.019)^2 + (0.019)^2} \cong 0.009 \text{ EU} \quad (51)$$

$$\sigma_{XY} \cong \frac{1}{2} (0.027) \cong 0.014 \text{ EU} \quad (52)$$

$$\sigma_{XZ} \cong \frac{1}{2} (0.019) \cong 0.010 \text{ EU} \quad (53)$$

$$\sigma_{YZ} \cong \frac{1}{2} (0.019) \cong 0.010 \text{ EU} \quad (54)$$

This completes the evaluation of the cross-anisoelastic errors, and the prime anisoelastic errors are considered next.

SECTION IX

The prime anisoelastic input errors to each instrument channel in the RGG stator reference frame (\bar{xyz}) are defined by (18) and (19). These errors are of a non-linear form similar to the rotational field errors; however, their characteristics are quite different. The important rotational field errors result from the convolved rate spectra, and the terms whose coefficients are the average rates contribute a negligible error. The prime anisoelastic errors have just the opposite behavior in the $1 - g$ field. In this case, the important errors result from the terms whose coefficients are the average accelerations, and the errors which are the result of the convolved acceleration spectra are of minor importance.

It is estimated that the prime anisoelastic error coefficients, K_o , of each instrument will be of a magnitude (2695 EU/g^2) that will necessitate active compensation of these errors on the basis of the measured coefficient of each instrument. It is estimated that the error coefficient can be determined to about 1% leaving a coefficient uncertainty of about 27 EU/g^2 with a stability of about $5 \times 10^{-3} \text{ EU/g}^2$. Inertial quality accelerometers with a long term stability of 10^{-4} g and a short term stability of 10^{-5} g are assumed for active compensation of the VIALS-induced errors. It is estimated that active compensation of the spin-bearing accelerations is not necessary. Spin-bearing accelerations are assumed to be uncorrelated between instruments such that spin-bearing induced errors may be treated on the basis of statistical independence in determining the standard gravity gradient tensor element errors. It is recognized that due to the non-linear form of the prime-anisoelastic error functions, rigorous analysis does not permit separate treatment of the VIALS and spin-bearing induced errors. When these excitation sources are treated separately, terms containing convolutions of the VIALS and spin-bearing acceleration spectra are omitted. Fortunately, in this case, the significant power of each spectrum has a large frequency separation in relation to the bandwidth of the RGG signal process, and the error incurred by separate treatment of the two excitation sources is negligible. Therefore, in the interest of analytical simplicity, each error source will be examined separately.

SECTION IX

Let us begin with the spin bearing as an excitation source of the horizontal spin axis sensors. Specializing (18) and (19) to the \bar{X} -spin RGG yields (55) and (56), where the n_x and n_y are the normalized radial accelerations of the spin bearing.

$$\epsilon_{cX} = K_{oX} \left[\left(g + gn_y \right)^2 - \left(gn_x \right)^2 \right] \quad (55)$$

$$\epsilon_{sX} = 2K_{oX} \left[\left(gn_x \right) \left(g + gn_y \right) \right] \quad (56)$$

Expansion of (55) yields (57).

$$\epsilon_{cX} = K_{oX} \left[g^2 + 2g^2 n_y + g^2 n_y^2 - g^2 n_x^2 \right] \quad (57)$$

The first term in (57) is mainly a bias term which will be compensated by the initialization procedure for the value of "g" at the initialization point. The change in "g" from the initialization point will be measured by the active compensation system and will propagate as an error to the extent of the error in the anisoelastic coefficient (ΔK_o) used for compensation. This error will be evaluated later when the VIALS-induced errors and the active compensation system is considered. The remaining terms in (57) are stated as (58).

$$\left. \epsilon_{cX} \right|_{sB} = K_{oX} \left[2g^2 n_y + g^2 \left(n_y^2 - n_x^2 \right) \right] \quad (58)$$

The deterministic portions of (58) are contained in the non-linear terms, and these will be compensated during the initialization process. An upper bound on this bias term is given by (59).

$$\left| M_{cX} \right| \leq \left[2695 \frac{\text{EU}}{g^2} \right] \left[2 \times \left(10^{-3} g \right)^2 \right] \cong 0.005 \text{ EU} \quad (59)$$

SECTION IX

The bias uncertainty is at least two orders of magnitude smaller and may be neglected. The remaining term in (58) is the linear term proportional to n_y . The power spectral density of low frequency (0-1 Hz) spin bearing accelerations on a one-sided basis is limited by specification to $2 \times 10^{-9} g^2/\text{Hz}$ such that the effective acceleration within the RGG bandwidth is limited to approximately $7 \times 10^{-6} g$. This results in the standard errors at the RGG output given by (60) and (61).

$$\sigma_c = (2)(2695)(7 \times 10^{-6}) \cong 0.038 \text{ EU} \quad (60)$$

$$\sigma_s = (2)(2695)(7 \times 10^{-6}) \cong 0.038 \text{ EU} \quad (61)$$

The same result will be obtained for the remaining horizontal spin axis sensor.

The vertical spin axis sensor has no first-order prime anisoelastic errors due to spin bearing excitation. The standard errors at the gravity gradient tensor are given from (60) and (61) by (62) through (67).

$$\sigma_{XX} \cong \frac{1}{3}(0.038) \cong 0.013 \text{ EU} \quad (62)$$

$$\sigma_{YY} \cong \frac{1}{3}(0.038) \cong 0.013 \text{ EU} \quad (63)$$

$$\sigma_{ZZ} \cong \frac{\sqrt{2}}{3}(0.038) \cong 0.018 \text{ EU} \quad (64)$$

$$\sigma_{XY} \cong 0 \quad (65)$$

$$\sigma_{XZ} \cong \frac{1}{2}(0.038) \cong 0.019 \text{ EU} \quad (66)$$

$$\sigma_{YZ} \cong \frac{1}{2}(0.038) \cong 0.019 \text{ EU} \quad (67)$$

SECTION IX

To evaluate the VIALS-induced prime anisoelastic errors, consideration must be given to inter-instrument correlation after compensation and system initialization. A logical first step in this development is to specialize the prime anisoelastic input error equations of (18) and (19) to the compensated output equations of each RGG channel. These specialized output error equations are expressed in the platform-fixed measurement reference frame (\overline{XYZ}) in terms of the actual and measured component accelerations as (68) through (73).

$$\epsilon_{cX} = H_e(s) \left[K_{oX} (A_Z^2 - A_Y^2) - K_{lX} (A_{Zm}^2 - A_{Ym}^2) \right] + B_{cX} \quad (68)$$

$$\epsilon_{cY} = H_e(s) \left[K_{oY} (A_X^2 - A_Z^2) - K_{lY} (A_{Xm}^2 - A_{Zm}^2) \right] + B_{cY} \quad (69)$$

$$\epsilon_{cZ} = H_e(s) \left[K_{oZ} (A_Y^2 - A_X^2) - K_{lZ} (A_{Ym}^2 - A_{Xm}^2) \right] + B_{cZ} \quad (70)$$

$$\epsilon_{sX} = H_e(s) \left[2K_{oX} A_Y A_Z - 2K_{lX} A_{Ym} A_{Zm} \right] + B_{sX} \quad (71)$$

$$\epsilon_{sY} = H_e(s) \left[2K_{oY} A_X A_Z - 2K_{lY} A_{Xm} A_{Zm} \right] + B_{sY} \quad (72)$$

$$\epsilon_{sZ} = H_e(s) \left[2K_{oZ} A_X A_Y - 2K_{lZ} A_{Xm} A_{Ym} \right] + B_{sZ} \quad (73)$$

where

$H_e(s)$ = Equivalent filter of RGG signal process

K_{oX} , K_{oY} , K_{oZ} = Prime anisoelastic error coefficients

K_{lX} , K_{lY} , K_{lZ} = Measured prime anisoelastic compensation coefficients

SECTION IX

$$\left. \begin{array}{l} B_{cX}, B_{cY}, B_{cZ} \\ B_{sX}, B_{sY}, B_{sZ} \end{array} \right\} = \text{Initial bias compensation of each instrument channel}$$

A_{Xm}, A_{Ym}, A_{Zm} = Measured VIALS accelerations

The tensor element errors are formed from the RGG channel errors according to (74) and (75).

$$\left[\begin{array}{l} \epsilon_{XX} \\ \epsilon_{YY} \\ \epsilon_{ZZ} \end{array} \right] = \frac{1}{3} \left[\begin{array}{ccc} 0 & +1 & -1 \\ -1 & 0 & +1 \\ +1 & -1 & 0 \end{array} \right] \left[\begin{array}{l} \epsilon_{cX} \\ \epsilon_{cY} \\ \epsilon_{cZ} \end{array} \right] \quad (74)$$

$$\left[\begin{array}{l} \epsilon_{XY} \\ \epsilon_{XZ} \\ \epsilon_{YZ} \end{array} \right] = \frac{1}{2} \left[\begin{array}{ccc} 0 & 0 & 1 \\ 0 & 1 & 0 \\ 1 & 0 & 0 \end{array} \right] \left[\begin{array}{l} \epsilon_{sX} \\ \epsilon_{sY} \\ \epsilon_{sZ} \end{array} \right] \quad (75)$$

The measured accelerations differ from the actual accelerations by the accelerometer instrument errors ($\Delta_X, \Delta_Y, \Delta_Z$) as in (76), (77), and (78).

$$A_{Xm} \triangleq A_X + \Delta_X \quad (76)$$

$$A_{Ym} \triangleq A_Y + \Delta_Y \quad (77)$$

$$A_{Zm} \triangleq A_Z + \Delta_Z \quad (78)$$

SECTION IX

The prime accelerations may be expressed in terms of the normalized dynamic accelerations, n_X , n_Y , n_Z , and scalar gravity, $g_o + \Delta g$, where the scalar gravity increment, Δg , is the scalar gravity change from the initialization point.

$$A_X \stackrel{\Delta}{=} g_o N_X \quad (79)$$

$$A_Y \stackrel{\Delta}{=} g_o N_Y \quad (80)$$

$$A_Z \stackrel{\Delta}{=} g_o + \Delta g + g_o N_Z \quad (81)$$

Substitution of (77), (78), (80), and (81) into (68) and (71) yields the typical prime anisoelastic RGG channel errors of the horizontal spin axis sensors as in (82) and (83).

$$\begin{aligned} \epsilon_{cX} = & H_e(s) \Delta K_{oX} \left[g_o^2 + 2g_o \left\{ \Delta g + g_o n_Z \right\} + \left\{ \Delta g + g_o n_Z \right\}^2 - g_o^2 n_Y^2 \right] \\ & - H_e(s) K_{1X} \left[2A_Z \Delta_Z - 2A_Y \Delta_Y + \Delta_Z^2 - \Delta_Y^2 \right] + B_{cX} \end{aligned} \quad (82)$$

$$\begin{aligned} \epsilon_{sX} = & H_e(s) \Delta K_{oX} \left[2g_o^2 + 2g_o \Delta g n_Y + 2g_o^2 n_Y n_Z \right] \\ & - H_e(s) K_{1X} \left[2A_Y \Delta_Z + 2A_Z \Delta_Y + 2\Delta_Y \Delta_Z \right] + B_{sX} \end{aligned} \quad (83)$$

The bias terms, B_{cX} and B_{sX} , are adjusted to null the instrument errors at the initialization site. When the initial bias correction is applied to (82) and (83) and the initial dynamic accelerations are assumed to be zero, the compensated errors are defined by (84) and (85).

SECTION IX

$$\begin{aligned}\epsilon_{cX} &= H_e(s)\Delta K_{oX} \left[2g_o \left\{ \Delta g + g_o n_Z \right\} + \left\{ \Delta g + g_o n_Z \right\}^2 - g_o^2 n_Y^2 \right] \\ &\quad - H_e(s)K_{lX} \left[2g_o n_Z \Delta_Z - 2g_o n_Y \Delta_Y + 2\Delta g \Delta_Z \right]\end{aligned}\quad (84)$$

$$\begin{aligned}\epsilon_{sX} &= H_e(s)\Delta K_{lX} \left[2g_o \Delta g n_Y + 2g_o^2 n_Y n_Z \right] \\ &\quad - H_e(s)K_{lX} \left[2g_o n_Y \Delta_Z + 2g_o n_Z \Delta_Y + 2\Delta g \Delta_Y \right]\end{aligned}\quad (85)$$

The individual output errors of each channel of the remaining instruments may be expanded by a similar process, and the results are presented as (86) through (89).

$$\begin{aligned}\epsilon_{cY} &= H_e(s)\Delta K_{oY} \left[g_o^2 n_X^2 - 2g_o \left\{ \Delta g + g_o n_Z \right\} + \left\{ \Delta g + g_o n_Z \right\}^2 \right] \\ &\quad - H_e(s)K_{lY} \left[2g_o n_X \Delta_X - 2g_o n_Z \Delta_Z - 2\Delta g \Delta_Z \right]\end{aligned}\quad (86)$$

$$\begin{aligned}\epsilon_{sY} &= H_e(s)\Delta K_{oY} \left[2g_o \Delta g n_X + 2g_o^2 n_X n_Z \right] \\ &\quad - H_e(s)K_{lY} \left[2g_o n_X \Delta_Z + 2g_o n_Z \Delta_X + 2\Delta g \Delta_X \right]\end{aligned}\quad (87)$$

$$\begin{aligned}\epsilon_{cZ} &= H_e(s)\Delta K_{oZ} \left[g_o^2 n_Y^2 - g_o^2 n_X^2 \right] \\ &\quad - H_e(s)K_{lZ} \left[2g_o n_Y \Delta_Y - 2g_o n_X \Delta_X \right]\end{aligned}\quad (88)$$

$$\epsilon_{sZ} = H_e(s)\Delta K_{oZ} \left[2g_o^2 n_X n_Y \right] - H_e(s)K_{lZ} \left[2g_o n_X \Delta_Y + 2g_o n_Y \Delta_X \right]\quad (89)$$

SECTION IX

Substitution of (84) through (89) into (74) and (75) yields the prime anisoelectric errors at the gravity gradient tensor as shown in (90) through (95).

$$\begin{aligned}
 \epsilon_{XX} &= \frac{H_e(s)}{3} \Delta K_{oY} g_o^2 \left[n_X^2 + n_Z^2 - 2n_Z - 2\frac{\Delta g}{g_o} + 2\frac{\Delta g}{g_o} n_Z + \left(\frac{\Delta g}{g_o} \right)^2 \right] \\
 &+ \frac{H_e(s)}{3} \Delta K_{oZ} g_o^2 \left[n_X^2 - n_Y^2 \right] \\
 &+ \frac{H_e(s)}{3} \left(2K_{1Y} g_o^2 \right) \left[\frac{\Delta_Z}{g_o} n_Z - \frac{\Delta_X}{g_o} n_X + \frac{\Delta g \Delta_Z}{g_o^2} \right] \\
 &+ \frac{H_e(s)}{3} \left(2K_{1Z} g_o^2 \right) \left[\frac{\Delta_Y}{g_o} n_Y - \frac{\Delta_X}{g_o} n_X \right] \tag{90}
 \end{aligned}$$

$$\begin{aligned}
 \epsilon_{YY} &= \frac{H_e(s)}{3} \Delta K_{oZ} g_o^2 \left[n_Y^2 - n_X^2 \right] \\
 &+ \frac{H_e(s)}{3} \Delta K_{oX} g_o^2 \left[n_Y^2 - n_Z^2 - 2n_Z - 2\frac{\Delta g}{g_o} - 2\frac{\Delta g}{g_o} n_Z - \left(\frac{\Delta g}{g_o} \right)^2 \right] \\
 &+ \frac{H_e(s)}{3} \left(2K_{1Z} g_o^2 \right) \left[\frac{\Delta_X}{g_o} n_X - \frac{\Delta_Y}{g_o} n_Y \right] \\
 &+ \frac{H_e(s)}{3} \left(2K_{1X} g_o^2 \right) \left[\frac{\Delta_Z}{g_o} n_Z - \frac{\Delta_Y}{g_o} n_Y + \frac{\Delta g \Delta_Z}{g_o^2} \right] \tag{91}
 \end{aligned}$$

SECTION IX

$$\begin{aligned}
 \epsilon_{ZZ} = & \frac{H_e(s)}{3} \Delta K_{oX} g_o^2 \left[n_Z^2 - n_Y^2 + 2n_Z + 2\frac{\Delta g}{g_o} + 2\frac{\Delta g}{g_o} n_Z + \left(\frac{\Delta g}{g_o}\right)^2 \right] \\
 & + \frac{H_e(s)}{3} \Delta K_{oY} g_o^2 \left[2n_Z - n_X^2 - n_Z^2 + 2\frac{\Delta g}{g_o} - 2\frac{\Delta g}{g_o} n_Z - \left(\frac{\Delta g}{g_o}\right)^2 \right] \\
 & + \frac{H_e(s)}{3} \left(2K_{lX} g_o^2 \right) \left[\frac{\Delta Y}{g_o} n_Y - \frac{\Delta Z}{g_o} n_Z - \frac{\Delta g \Delta Z}{g_o^2} \right] \\
 & + \frac{H_e(s)}{3} \left(2K_{lY} g_o^2 \right) \left[\frac{\Delta Z}{g_o} n_Z - \frac{\Delta X}{g_o} n_X + \frac{\Delta g \Delta Z}{g_o^2} \right]
 \end{aligned} \tag{92}$$

$$\epsilon_{XY} = H_e(s) \left[\left(\Delta K_{oZ} g_o^2 \right) n_X n_Y - \left(K_{lZ} g_o^2 \right) \left(\frac{\Delta Y}{g_o} n_X + \frac{\Delta X}{g_o} n_Y \right) \right] \tag{93}$$

$$\begin{aligned}
 \epsilon_{XZ} = & H_e(s) \left[\left(\Delta K_{oY} g_o^2 \right) \left(n_X n_Z + \frac{\Delta g}{g_o} n_X \right) \right. \\
 & \left. - \left(K_{lY} g_o^2 \right) \left(\frac{\Delta Z}{g_o} n_X + \frac{\Delta X}{g_o} n_Z + \frac{\Delta g \Delta X}{g_o^2} \right) \right]
 \end{aligned} \tag{94}$$

$$\begin{aligned}
 \epsilon_{YZ} = & H_e(s) \left[\left(\Delta K_{oX} g_o^2 \right) \left(n_Y n_Z + \frac{\Delta g}{g_o} n_Y \right) \right. \\
 & \left. - \left(K_{lX} g_o^2 \right) \left(\frac{\Delta Z}{g_o} n_Y + \frac{\Delta Y}{g_o} n_Z + \frac{\Delta g \Delta Y}{g_o^2} \right) \right]
 \end{aligned} \tag{95}$$

SECTION IX

Before estimating the standard errors of the gravity gradient tensor elements, it is convenient to examine the magnitudes of some of the terms with the objective of eliminating those that are clearly negligible. In this process, the following parametric bounds will be employed:

$$|\Delta K_0 g_o^2| \leq 26.95 \text{ EU} \quad (96)$$

$$|K_1 g_o^2| \leq 2695 \text{ EU} \quad (97)$$

$$|\Delta/g_o| \leq 10^{-4} \quad (98)$$

$$|\Delta g/g_o| \triangleq 3 \times 10^{-3} \quad (99)$$

First, consider terms of the forms $(\Delta g/g_o)^2$ and $[(\Delta g/g_o)(\Delta/g_o)]$. A quick calculation shows that these terms contribute less than 0.001 EU and may be neglected. Next consider terms where $(\Delta g/g_o)$ is an additive factor in the coefficient of a common term, e.g., in (90) the terms $-2n_Z(1 - \Delta g/g_o)$. Clearly, in this case the factor, $\Delta g/g_o$, can be dropped without appreciable error. Finally, terms whose coefficients are dependent on the accelerometer instrument errors (Δ/g_o) are small in comparison to the terms whose coefficients depend on the error in the prime anisotropic compensation coefficient (ΔK_0) as shown by (96) and (100).

$$|K_1 g_o^2| \times \left| \frac{\Delta}{g_o} \right| \leq 0.2695 \text{ EU} \quad (100)$$

All such terms will contribute on the order of 0.001 EU or less and may be neglected. Applying the foregoing approximations to (90) through (95) yield the simplified gradient tensor errors forms (101) through (106).

SECTION IX

$$\epsilon_{XX} \cong \frac{H_e(s)}{3} \left[\left(\Delta K_o Y g_o^2 \right) \left(n_X^2 + n_Z^2 - 2n_Z - 2 \frac{\Delta g}{g_o} \right) + \left(\Delta K_o Z g_o^2 \right) \left(n_X^2 - n_Y^2 \right) \right] \quad (101)$$

$$\epsilon_{YY} \cong \frac{H_e(s)}{3} \left[\left(\Delta K_o Z g_o^2 \right) \left(n_Y^2 - n_X^2 \right) + \left(\Delta K_o X g_o^2 \right) \left(n_Y^2 - n_Z^2 - 2n_Z - 2 \frac{\Delta g}{g_o} \right) \right] \quad (102)$$

$$\epsilon_{ZZ} \cong \frac{H_e(s)}{3} \left[\left(\Delta K_o X g_o^2 \right) \left(n_Z^2 - n_Y^2 + 2n_Z + 2 \frac{\Delta g}{g_o} \right) + \left(\Delta K_o Y g_o^2 \right) \left(2n_Z - n_X^2 - n_Z^2 + 2 \frac{\Delta g}{g_o} \right) \right] \quad (103)$$

$$\epsilon_{XY} \cong H_e(s) \left[\left(\Delta K_o Z g_o^2 \right) n_X n_Y \right] \quad (104)$$

$$\epsilon_{XZ} \cong H_e(s) \left[\left(\Delta K_o Y g_o^2 \right) \left(n_X n_Z \right) \right] \quad (105)$$

$$\epsilon_{YZ} \cong H_e(s) \left[\left(\Delta K_o X g_o^2 \right) \left(n_Y n_Z \right) \right] \quad (106)$$

It should be noted that terms of the form $(\Delta g/g_o)n$ in (94) and (95) have been neglected in the approximations of (105) and (106) on the basis that these terms are numerically smaller than other previously neglected terms.

SECTION IX

Let us now examine the gravity gradient tensor element errors for their statistical properties on the basis that the normalized accelerations are zero-mean, wide-sense stationary, gaussian random variables. For this purpose, assume that all of the prime anisoclastic error coefficients (ΔK_o) are numerically equal to the upper bound given by (97).

The tensor element bias terms may be written directly in terms of the acceleration covariances evaluated at zero time shift as in (107) through (112).

$$M_{XX} \cong \frac{\Delta K_o g_o^2}{3} \left[2C_X^{(o)} - C_Y^{(o)} + C_Z^{(o)} - 2\frac{\Delta g}{g_o} \right] \quad (107)$$

$$M_{YY} \cong \frac{\Delta K_o g_o^2}{3} \left[2C_Y^{(o)} - C_X^{(o)} - C_Z^{(o)} - 2\frac{\Delta g}{g_o} \right] \quad (108)$$

$$M_{ZZ} \cong \frac{\Delta K_o g_o^2}{3} \left[4\frac{\Delta g}{g_o} - C_X^{(o)} - C_Y^{(o)} \right] \quad (109)$$

$$M_{XY} \cong \left(\Delta K_o g_o^2 \right) C_{XY}^{(o)} \quad (110)$$

$$M_{XZ} \cong \left(\Delta K_o g_o^2 \right) C_{XZ}^{(o)} \quad (111)$$

$$M_{YZ} \cong \left(\Delta K_o g_o^2 \right) C_{YZ}^{(o)} \quad (112)$$

The trace element bias functions are characterized by a trend, i.e., the $(\Delta g/g_o)$ term whose magnitude is proportional to altitude change from the initialization point. When this term has the magnitude given by (99), a bias of 0.054 EU is contributed to the horizontal trace

SECTION IX

elements and 0.108 EU to the vertical trace element. The remaining parts of the bias terms depend on the acceleration covariances. It is estimated that all acceleration variances will be bounded by $7 \times 10^{-4} g^2$ in the operational environment. This leads to a trace element bias bound of approximately 0.013 EU and a cross-element bias bound of approximately 0.019 EU due to the acceleration variances. A summary of the total biases on each tensor element is given by (113) through (118).

$$|M_{XX}| \leq 0.067 \text{ EU} \quad (113)$$

$$|M_{YY}| \leq 0.067 \text{ EU} \quad (114)$$

$$|M_{ZZ}| \leq 0.121 \text{ EU} \quad (115)$$

$$|M_{XY}| \leq 0.019 \text{ EU} \quad (116)$$

$$|M_{XZ}| \leq 0.019 \text{ EU} \quad (117)$$

$$|M_{YZ}| \leq 0.019 \text{ EU} \quad (118)$$

Observe that the largest bias errors occur in the trace elements and that they are primarily the result of the scalar gravity trend.

To compute the tensor element variances, it is convenient to assume the normalized accelerations to be statistically independent. This assumption has a small effect on the resultant errors because the most significant errors are due to the linear term (n_Z) in the trace element error equations. Now, we consider the power spectrum of M_{XX} assuming the $(\Delta K_0 g_0^2)$ coefficients are numerically equal.

SECTION IX

$$S_{XX}(f) = \frac{1}{9} |H_e(s)|^2 \left[\Delta K_o g_o^2 \right]^2 \left[4S_X * S_X + S_Y * S_Y + S_Z * S_Z + 4S_Z \right] \quad (119)$$

When all the acceleration spectra are assumed to be of the same amplitude and shape, equation (119) reduces to (120).

$$S_{XX}(f) = \frac{1}{9} |H_e(s)|^2 \left[\Delta K_o g_o^2 \right]^2 \left[4S_n(f) + 6S_n * S_n \right] \quad (120)$$

The remaining spectra may be written on the same basis and are presented as (121), (122), and (123).

$$S_{YY}(f) = \frac{1}{9} |H_e(s)|^2 \left[\Delta K_o g_o^2 \right]^2 \left[4S_n(f) + 6S_n * S_n \right] \quad (121)$$

$$S_{ZZ}(f) = \frac{1}{9} |H_e(s)|^2 \left[\Delta K_o g_o^2 \right]^2 \left[16S_n(f) + 6S_n * S_n \right] \quad (122)$$

$$S_{XY} = S_{XZ} = S_{YZ} = |H_e(s)|^2 \left[\Delta K_o g_o^2 \right]^2 \left[S_n(f) * S_n(f) \right] \quad (123)$$

The error variances are obtained by integration of the error spectra. Two spectral forms must be considered, i.e., the acceleration spectrum itself and its convolution, as in (124) and (125).

$$I_n \triangleq \int_{-\infty}^{\infty} |H_e(j2\pi f)|^2 S_n(f) df \quad (124)$$

$$I_{nn} \triangleq \int_{-\infty}^{\infty} |H_e(j2\pi f)|^2 S_n(f) * S_n(f) df \quad (125)$$

SECTION IX

It is assumed that $S_n(f)$ is constant below 1 Hz with a "two-sided" amplitude of approximately $2.8 \times 10^{-4} g^2/\text{Hz}$. On this basis, the integral of (124) is stated as (126).

$$I_n \cong (2.8 \times 10^{-4}) \Delta f_e = 1.4 \times 10^{-5} g^2 \quad (126)$$

The integral of (125) may be approximated by assuming the acceleration spectrum, $S_n(f)$, to be constant between f_o and zero outside of this band. This approximation is stated as (127).

$$I_{nn} \cong 2f_o (2.8 \times 10^{-4} g^2/\text{Hz}) \Delta f_e^2 \quad (127)$$

The frequency, f_o , may be eliminated from (127) by its relation to the acceleration variance, σ_n^2 , as in (128).

$$\sigma_n^2 = 2f_o (2.8 \times 10^{-4} g^2/\text{Hz}) \quad (128)$$

In computing the bias terms an acceleration variance of $7 \times 10^{-4} g^2$ was employed. Substitution of this value and (128) into (127) yields the desired integral as (129).

$$I_{nn} \cong (7 \times 10^{-4} g^2) (2.8 \times 10^{-4} g^2/\text{Hz}) (0.05) \cong 10^{-8} g^4 \quad (129)$$

Comparison of the resultant integral values of (126) and (129) provides an indication of the dominance of the linear terms over the non-linear terms in the prime anisoelastic error variances.

Substitution of the integral values of (126) and (129) for the appropriate integrals of the error power spectra of (120) through (123) yields the standard "prime anisoelastic" tensor errors due to the VIALS as shown in (130) through (133).

SECTION IX

$$\sigma_{XX} \cong \left(\frac{26.95}{3} \right) \sqrt{(4)(1.4)(10^{-5}) + (6)(10^{-8})} \cong 0.068 \text{ EU} \quad (130)$$

$$\sigma_{YY} \cong \left(\frac{26.95}{3} \right) (7.5 \times 10^{-3}) \cong 0.068 \text{ EU} \quad (131)$$

$$\sigma_{ZZ} \cong \left(\frac{26.95}{3} \right) \sqrt{(16)(1.4)(10^{-5}) + (6)(10^{-8})} \cong 0.135 \text{ EU} \quad (132)$$

$$\sigma_{XY} = \sigma_{XZ} = \sigma_{YZ} \cong (26.95) \sqrt{10^{-8}} \cong 0.003 \text{ EU} \quad (133)$$

A summary of the standard anisoelastic errors at the gravity gradient tensor elements is presented as Tables IX-6 and IX-7 for RGG spin bearing excitation and for VIALS excitation.

TABLE IX-6
Anisoelastic Errors (Spin Bearing)

	σ_{XX}	σ_{YY}	σ_{ZZ}	σ_{XY}	σ_{XZ}	σ_{YZ}
Cross-Aniso	0.011	0.011	0.009	0.014	0.010	0.010
Prime-Aniso	0.013	0.013	0.018	φ	0.019	0.019
TOTAL	0.017	0.017	0.020	0.014	0.021	0.021

T834

TABLE IX-7
Anisoelastic Errors (VIALS)

	σ_{XX}	σ_{YY}	σ_{ZZ}	σ_{XY}	σ_{XZ}	σ_{YZ}
Cross-Aniso	0.013	0.013	0.010	0.016	0.011	0.011
Prime-Aniso	0.068	0.068	0.135	0.003	0.003	0.003
TOTAL	0.069	0.069	0.135	0.016	0.011	0.011

T835

SECTION IX

G. PLATFORM ORIENTATION ERROR PROPAGATION

Misalignment of the RGG system measurement frame from its nominal reference position produces errors in the measured scalar elements of the gravity gradient tensor. These errors may be calculated as the incremental changes of the scalar elements of the measured gravity gradient tensor from their values at the point of system initialization due to coordinate misalignment.

The measured gravity gradient tensor elements may be expressed as a matrix, $[\Gamma_m]$, in terms of a similarity transformation on the actual gravity gradient matrix, $[\Gamma_a]$, and the direction cosine matrix, $[C]$, which relates the measurement frame to the reference frame as in (1).

$$[\Gamma_m] = [C][\Gamma_a][C]^T \quad (1)$$

When the misalignment angles are sufficiently small, the direction cosine matrix may be approximated to first order by (2) as the sum of the identity matrix, $[I]$, and a skew symmetric matrix, $[\phi]$, defined by (3).

$$[C] \approx [I] + [\phi] \quad (2)$$

$$[\phi] \triangleq \begin{bmatrix} 0 & \phi_Z & -\phi_Y \\ -\phi_Z & 0 & \phi_X \\ \phi_Y & -\phi_X & 0 \end{bmatrix} \quad (3)$$

Also, observe that the transpose of (2) and (3) may be expressed as (4) and (5).

SECTION IX

$$[C]^T \approx [I] + [\phi]^T \quad (4)$$

$$[\phi]^T \equiv -[\phi] \quad (5)$$

Substitution of (2), (4) and (5) into (1) yields the first-order measurement increment due to angular misalignment expressed as (6).

$$[\Gamma_m] - [\Gamma_a] \approx [\phi][\Gamma_a] - [\Gamma_a][\phi] \quad (6)$$

The change in the measurement increment from the point of system initialization is defined as the gradient tensor error due to misalignment as in (7).

$$[\Gamma_e] \triangleq \{[\Gamma_m] - [\Gamma_a]\} - \{[\Gamma_{mo}] - [\Gamma_{ao}]\} \quad (7)$$

Substitution of (6) into (7) yields the expanded error form of (8).

$$[\Gamma_e] = \{[\phi][\Gamma_a] - [\Gamma_a][\phi]\} - \{[\phi_o][\Gamma_{ao}] - [\Gamma_{ao}][\phi_o]\} \quad (8)$$

Since the platform misalignment angles are specified in terms of initial misalignments and changes thereafter, it is convenient to express (8) in terms of the initial and incremental parameters defined by (9) and (10).

$$[\phi] \triangleq [\phi_o] + [\Delta\phi] \quad (9)$$

$$[\Gamma_a] \triangleq [\Gamma_{ao}] + [\Delta\Gamma_a] \quad (10)$$

Substitution of (9) and (10) into (8) yields the convenient error form of (11).

$$[\Gamma_e] = [\phi_o][\Delta\Gamma_a] - [\Delta\Gamma_a][\phi_o] + [\Delta\phi][\Gamma_a] - [\Gamma_a][\Delta\phi] \quad (11)$$

SECTION IX

Expansion of (11) yields the gravity gradient misalignment error set expressed as (12) through (17).

$$\Gamma_{eXX} = 2\phi_{Zo} \Delta\Gamma_{XY} - 2\phi_{Yo} \Delta\Gamma_{XZ} + 2\Delta\phi_Z \Gamma_{XY} - 2\Delta\phi_Y \Gamma_{XZ} \quad (12)$$

$$\Gamma_{eYY} = 2\phi_{Xo} \Delta\Gamma_{YZ} - 2\phi_{Zo} \Delta\Gamma_{XY} + 2\Delta\phi_X \Gamma_{YZ} - 2\Delta\phi_Z \Gamma_{XY} \quad (13)$$

$$\Gamma_{eZZ} = 2\phi_{Yo} \Delta\Gamma_{XZ} - 2\phi_{Xo} \Delta\Gamma_{YZ} + 2\Delta\phi_Y \Gamma_{XZ} - 2\Delta\phi_X \Gamma_{YZ} \quad (14)$$

$$\begin{aligned} \Gamma_{eXY} = & \phi_{Zo} [\Delta\Gamma_{YY} - \Delta\Gamma_{XX}] + \phi_{Xo} \Delta\Gamma_{XZ} - \phi_{Yo} \Delta\Gamma_{YZ} \\ & + \Delta\phi_Z [\Gamma_{YY} - \Gamma_{XX}] + \Delta\phi_X \Gamma_{XZ} - \Delta\phi_Y \Gamma_{YZ} \end{aligned} \quad (15)$$

$$\begin{aligned} \Gamma_{eXZ} = & \phi_{Yo} [\Delta\Gamma_{XX} - \Delta\Gamma_{ZZ}] - \phi_{Xo} \Delta\Gamma_{XY} + \phi_{Zo} \Delta\Gamma_{YZ} \\ & + \Delta\phi_Y [\Gamma_{XX} - \Gamma_{ZZ}] - \Delta\phi_X \Gamma_{XY} + \Delta\phi_Z \Gamma_{YZ} \end{aligned} \quad (16)$$

$$\begin{aligned} \Gamma_{eYZ} = & \phi_{Xo} [\Delta\Gamma_{ZZ} - \Delta\Gamma_{YY}] + \phi_{Yo} \Delta\Gamma_{XY} - \phi_{Zo} \Delta\Gamma_{XZ} \\ & + \Delta\phi_X [\Gamma_{ZZ} - \Gamma_{YY}] + \Delta\phi_Y \Gamma_{XY} - \Delta\phi_Z \Gamma_{XZ} \end{aligned} \quad (17)$$

For the purpose of statistical analysis of this error set, it is convenient to observe that the tensor element errors are linearly related to the initial and incremented misalignment errors and that the entire error set may be expressed in the state variable form of (18), wherein the $[A]$ matrix contains the gravity gradient tensor elements, Γ_{ij} , and their incremental changes, $\Delta\Gamma_{ij}$, from the initialization point.

$$\underline{\Gamma}_e \triangleq [A]\underline{\phi} \quad (18)$$

SECTION IX

The gravity gradient error covariance matrix, $[\Pi]$, may be expressed in terms of the misalignment angle covariance matrix, $[\Phi]$ as (19).

$$[\Pi] = [A][\Phi][A]^T \quad (19)$$

The trace elements of (19) correspond to the gravity gradient tensor element variances of the errors of (12) through (17). Rigorous evaluation of the trace elements of (19) requires complete knowledge of the misalignment error covariance matrix, $[\Phi]$, as a function of time. An approximate estimate of the trace elements of (19) may be obtained using the specified variances of the initial and incremental platform misalignment angles as stated in (20).

$$[\Pi]_{ii} \approx \sum_{j=1}^6 a_{ij}^2 \Phi_{jj} \quad (20)$$

Expansion of (20) in terms of the coefficients in (12) through (17) yields the set (21) through (26).

$$\sigma_{XX}^2 = 4 \left[(\Delta \Gamma_{XZ})^2 \Phi_{22} + (\Delta \Gamma_{XY})^2 \Phi_{33} + (\Gamma_{XZ})^2 \Phi_{55} + (\Gamma_{XY})^2 \Phi_{66} \right] \quad (21)$$

$$\sigma_{YY}^2 = 4 \left[(\Delta \Gamma_{YZ})^2 \Phi_{11} + (\Delta \Gamma_{XY})^2 \Phi_{33} + (\Gamma_{YZ})^2 \Phi_{44} + (\Gamma_{XY})^2 \Phi_{66} \right] \quad (22)$$

$$\sigma_{ZZ}^2 = 4 \left[(\Delta \Gamma_{YZ})^2 \Phi_{11} + (\Delta \Gamma_{XZ})^2 \Phi_{22} + (\Gamma_{YZ})^2 \Phi_{44} + (\Gamma_{XZ})^2 \Phi_{55} \right] \quad (23)$$

$$\begin{aligned} \sigma_{XY}^2 = & (\Delta \Gamma_{XZ})^2 \Phi_{11} + (\Delta \Gamma_{YZ})^2 \Phi_{22} + (\Delta \Gamma_{YY} - \Delta \Gamma_{XX})^2 \Phi_{33} \\ & + (\Gamma_{XZ})^2 \Phi_{44} + (\Gamma_{YZ})^2 \Phi_{55} + (\Gamma_{YY} - \Gamma_{XX})^2 \Phi_{66} \end{aligned} \quad (24)$$

SECTION IX

$$\begin{aligned}\sigma_{XZ}^2 &= (\Delta\Gamma_{XY})^2 \Phi_{11} + (\Delta\Gamma_{XX} - \Delta\Gamma_{ZZ})^2 \Phi_{22} + (\Delta\Gamma_{YZ})^2 \Phi_{33} \\ &\quad + (\Gamma_{XY})^2 \Phi_{44} + (\Gamma_{XX} - \Gamma_{ZZ})^2 \Phi_{55} + (\Gamma_{YZ})^2 \Phi_{66}\end{aligned}\quad (25)$$

$$\begin{aligned}\sigma_{YZ}^2 &= (\Delta\Gamma_{ZZ} - \Delta\Gamma_{YY})^2 \Phi_{11} + (\Delta\Gamma_{XY})^2 \Phi_{22} + (\Delta\Gamma_{XZ})^2 \Phi_{33} \\ &\quad + (\Gamma_{ZZ} - \Gamma_{YY})^2 \Phi_{44} + (\Gamma_{XY})^2 \Phi_{55} + (\Gamma_{XZ})^2 \Phi_{66}\end{aligned}\quad (26)$$

Evaluation of (21) through (26) is facilitated by substitution of the specified misalignment angle variances as defined by (27), (28), and (29).

$$E[\phi_{Xo}^2] \triangleq E[\phi_{Yo}^2] \triangleq [2.5 \times 10^{-4}]^2 \triangleq \Phi_{11} \triangleq \Phi_{22} \quad (27)$$

$$E[\Delta\phi_X^2] \triangleq E[\Delta\phi_Y^2] \triangleq [5 \times 10^{-5}]^2 \triangleq \Phi_{44} \triangleq \Phi_{55} \quad (28)$$

$$E[\phi_{Zo}^2] \triangleq E[\Delta\phi_Z^2] \triangleq [5 \times 10^{-4}]^2 \triangleq \Phi_{33} \triangleq \Phi_{66} \quad (29)$$

Now let us define the parameter, σ_ϕ , by (30) and the covariance parameters by (31), (32), and (33).

$$\sigma_\phi \triangleq 5 \times 10^{-5} \text{ rad} \quad (30)$$

$$\Phi_{11} = \Phi_{22} = 25\sigma_\phi^2 \quad (31)$$

$$\Phi_{33} = \Phi_{66} = 100\sigma_\phi^2 \quad (32)$$

SECTION IX

$$\Phi_{44} = \Phi_{55} = \sigma_\phi^2 \quad (33)$$

The estimated gradient tensor standard errors may be expressed as (34) through (39) by substitution of (31), (32), and (33) into (21) through (26) and taking their square roots.

$$\sigma_{XX} \cong 2\sigma_\phi \left[25(\Delta\Gamma_{XZ})^2 + 100(\Delta\Gamma_{XY})^2 + (\Gamma_{XZ})^2 + 100(\Gamma_{XY})^2 \right]^{1/2} \quad (34)$$

$$\sigma_{YY} \cong 2\sigma_\phi \left[25(\Delta\Gamma_{YZ})^2 + 100(\Delta\Gamma_{XY})^2 + (\Gamma_{YZ})^2 + 100(\Gamma_{XY})^2 \right]^{1/2} \quad (35)$$

$$\sigma_{ZZ} \cong 2\sigma_\phi \left[25(\Delta\Gamma_{YZ})^2 + 25(\Delta\Gamma_{XZ})^2 + (\Gamma_{YZ})^2 + (\Gamma_{XZ})^2 \right]^{1/2} \quad (36)$$

$$\sigma_{XY} \cong \sigma_\phi \left[\begin{aligned} & 25(\Delta\Gamma_{XZ})^2 + 25(\Delta\Gamma_{YZ})^2 + 100(\Delta\Gamma_{YY} - \Delta\Gamma_{XX})^2 \\ & + (\Gamma_{XZ})^2 + (\Gamma_{YZ})^2 + 100(\Gamma_{YY} - \Gamma_{XX})^2 \end{aligned} \right]^{1/2} \quad (37)$$

$$\sigma_{XZ} \cong \sigma_\phi \left[\begin{aligned} & 25(\Delta\Gamma_{XY})^2 + 25(\Delta\Gamma_{XX} - \Delta\Gamma_{ZZ})^2 + 100(\Delta\Gamma_{YZ})^2 \\ & + (\Gamma_{XY})^2 + (\Gamma_{XX} - \Gamma_{ZZ})^2 + 100(\Gamma_{YZ})^2 \end{aligned} \right]^{1/2} \quad (38)$$

$$\sigma_{YZ} \cong \sigma_\phi \left[\begin{aligned} & 25(\Delta\Gamma_{ZZ} - \Delta\Gamma_{YY})^2 + 25(\Delta\Gamma_{XY})^2 + 100(\Delta\Gamma_{XZ})^2 \\ & + (\Gamma_{ZZ} - \Gamma_{YY})^2 + (\Gamma_{XY})^2 + 100(\Gamma_{XZ})^2 \end{aligned} \right]^{1/2} \quad (39)$$

SECTION IX

Numerical evaluation of (34) through (39) requires definition of the error coefficients, Γ_{ij} and $\Delta\Gamma_{ij}$. For this purpose, we make the following arbitrary definitions:

1. Operating Point Values:

$$|\Gamma_{XY}| \triangleq |\Gamma_{XZ}| \triangleq |\Gamma_{YZ}| \triangleq 150 \text{EU} \quad (40)$$

$$|\Gamma_{YY} - \Gamma_{XX}| \triangleq 300 \text{EU} \quad (41)$$

$$|\Gamma_{ZZ} - \Gamma_{YY}| \triangleq |\Gamma_{XX} - \Gamma_{ZZ}|^* \triangleq 4500 \text{EU} \quad (42)$$

2. Incremental Change Values:

$$|\Delta\Gamma_{XY}| \triangleq |\Delta\Gamma_{XZ}| \triangleq |\Delta\Gamma_{YZ}| \triangleq 300 \text{ EU} \quad (43)$$

$$|\Delta\Gamma_{YY} - \Delta\Gamma_{XX}| \triangleq |\Delta\Gamma_{ZZ} - \Delta\Gamma_{YY}| \triangleq |\Delta\Gamma_{XX} - \Delta\Gamma_{ZZ}| \triangleq 600 \text{EU} \quad (44)$$

Substitution of the numerical values of (30) and (40) through (44) into (34) through (39) yields the estimated gravity gradient tensor element errors stated as (45) through (48).

$$\sigma_{XX} \approx \sigma_{YY} \approx 0.368 \text{EU} \quad (45)$$

$$\sigma_{ZZ} \approx 0.212 \text{EU} \quad (46)$$

$$\sigma_{XY} \approx 0.352 \text{EU} \quad (47)$$

$$\sigma_{XZ} \approx \sigma_{YZ} \approx 0.327 \text{EU} \quad (48)$$

* It is realized that the equality of (42) requires that (41) be zero; however, the equality of (42) is assumed for analytical simplicity.

SECTION X

SENSOR ROTOR DESIGN

The objectives in designing the rotor were to make it as small, rigid, symmetrical, and homogeneous as possible. At the same time, provision for initial assembly test and balance was necessary. The design evolved into a main circular central plate to which all other parts could be fastened symmetrically. Except for the pivots and fasteners, the rotor is entirely of 6061 aluminum, which provides good heat conductivity and symmetrical thermal expansion. The good heat conductivity reduces thermal gradients to a minimum.

All fasteners will be made of beryllium copper and will be designed so that the fastener is in tension. Since Be-Cu has a lower thermal coefficient of expansion than aluminum, when the sensor is assembled at room temperature and then raised to operating temperature, the fastener will be tightened. The pivots are made of Be-Cu because the temperature coefficient of the shear modulus of elasticity is much lower (-330 ppm/ $^{\circ}$ C) than for most other metals. This aids in keeping the thermal sensitivity of the sensor undamped natural frequency to a minimum.

A. DESCRIPTION

This paragraph refers to Fig. V-1 and the number flags of that figure. However it provides more detail than the Section V summary. The circular central plate (3) and the eight brace posts (5) are machined from a solid billet of aluminum. The pivot structure (4) is made from a single rod of beryllium copper and is attached at the center of the central circular plate. At this point the assembly appears as a circular central plate with four symmetrically arranged brace posts protruding from each side. The pivot structure appears as two more posts centered in the plate. The pivots extend slightly beyond the brace posts.

SECTION X

The arms and arm masses (7) can now be assembled onto the pivots by interleaving the arms in the proper order. Prior to this assembly, each arm has had the remote mass balance assembly (10) and the appropriate transducer stand-off posts (23) installed. The end plates (6) can now be attached to the brace posts (5) and to the outboard end of the pivots. The assembly now appears as a central plate with a cage-like structure protruding from each side. The outer end of the cage is the end plate (6). The end plate and the central plate support and hold the pivots and the pivots in turn support the arms and their end masses. Eight transducer mounting posts (23), arranged in a circle, extend through each end plate.

A holding fixture is now provided. This holding fixture is a cylindrical tube that fits into the circumferential ledge at the outer perimeter of the central plate. The holding fixture is a dummy end bell with a flat open end and access holes bored through the cylinder walls. The central assembly can now be placed on the holding fixture and one set of transducer mounting plates (22) and transducers (8) installed. The other end is completed in a similar fashion. The rotor electronics assembly (9) is installed at this point and internal wiring completed. A battery pack will be installed on the cylindrical holding fixture and temporary connections made to the electronics pack so that the FM signal can be brought out. The central rotor and arm structure can now be tested for arm unbalance, arm anisoelasticity, and transducer and test signal operation. Adjustments can be made as required.

After all internal adjustments have been made, the rotor end bells (1) are installed. These end bells have been provided previously with the female part of the spin bearing (2), the encoder disk (12), the two test signal photocells (15), the spin motor/tachometer (11) drag cup, and the FM output antenna (16). This completes the rotor assembly.

SECTION X

B. STIFFNESS, MASS, AND INERTIA CALCULATIONS

Detailed calculations for stiffness, mass, and inertia have not been made for the RGG prototype design. Preliminary values, believed to be sufficiently accurate for all but final modelling, are as follows:

Axial stiffness	175×10^6 N/m (1×10^6 lb/in.)
Mass, including arms	5.867 kg
Inertia, including arms	
$I_{xx} = I_{yy}$ I_{zz}	1.44×10^{-2} kg m ² 2.039×10^{-2} kg m ²

SECTION XI

SENSOR STATOR DESIGN

A. GENERAL

The purpose of the stator is to provide a stable, indexed mount for the sensor; to protect and restrain the rotor; and to locate the spin motor/tachometer, encoder light source, test signal light source and the FM receiver antenna.

This paragraph refers to Figure V-1 and the number flags of that drawing. The material selected for the stator is 6061 aluminum, the same as that of the rotor. A sturdy flange (18) provides a rigid flat mounting and index surface. The motor/tachometers and the male parts of the spin bearings are mounted in the end caps (19). One end cap is insulated from the remainder of the stator by a thin mica washer (20). This allows the rotor electronics power to be coupled into the rotor through the capacity between the spin bearing halves and between the motor stator to drag cup as described in Section XV. The test signal light source (14) is positioned to illuminate the two rotor mounted test signal photocells (15). The rotor position light source and photocell (13) is positioned so that the encoder disk on the rotor (12) can interrupt the light beam and produce the precise 1/8-revolution signals required by the system. The FM receiver antenna (16) is mounted on the end opposite to that just discussed.

One of the most critical sensor dimensions is the axial clearance of the spin bearings. This is adjusted during assembly by initially making the clearance too large. Then, with the sensor stabilized at operating temperature, the clearance is measured by means of the capacitor clearance gauges built into the spin bearing. The end cap is then removed and the spacer or shim ring (21) is lapped to the required dimension. A selection of spacer rings will be made initially and one near the proper dimension will be selected for the first assembly. This completes the stator assembly.

SECTION XI

B. STIFFNESS, MASS AND INERTIA CALCULATIONS

Detailed calculations for stiffness, mass, and inertia have not been made for the RGG prototype design. Preliminary values, believed to be sufficiently accurate for all but final modelling accuracy are:

Axial stiffness	$1.58 \times 10^8 \text{ N/m}$ $(9 \times 10^5 \text{ lb/in.})$
Mass	3.766 kg
Inertia	
$I_{xx} = I_{yy}$	$2.89 \times 10^2 \text{ kg m}^2$ $2.53 \times 10^2 \text{ kg m}^2$

SECTION XII

SPIN BEARINGS

The previous Hughes RGG "hard bearing" sensor experimental development program had utilized a commercially available hydrostatic air spin bearing manufactured by Professional Instruments Co., Minneapolis, Minnesota, and designed for machine-tool spindle applications. Although this program had provided promising results, no tests were conducted that allowed separation of the spin bearing contribution to the lowest sensor noise level achieved (6 EU). Realizing the importance the spin bearing would play in determining the overall sensor accuracy, we sought the best professional assistance available in selecting and designing the optimum bearing type for the prototype sensor.

Characteristics, error mechanisms, and requirements that affected the spin bearing design were studied and formed the basis of a procurement specification. These studies and the procurement specification are contained in the Semiannual Technical Report No. 1 (see Section V-C). A bearing vendor survey was made, proposals requested, and a vendor was selected. The vendor, Mechanical Technology Incorporated (MTI), Latham, New York, was placed under contract on 24 July 1972. This contract called for a bearing trade-off study and selection recommendation followed by generation of a detailed design and a design specification for the bearing.

MTI has completed this effort and has prepared a final report entitled, "Spin Bearing Selection and Design for Hughes Research Laboratory Rotating Gravity Gradiometer," Ref. No. MTI 72TR59, October 1972. In addition to this report, MTI has generated a design specification, which is included as Appendix D herein. A summary of the candidate bearings considered in the trade-off study and the rationale leading to the selection of the prototype bearing type is presented in the following subsections.

SECTION XII

A. BEARING CANDIDATES

Initially, 12 bearing types were considered: 3 bearing geometries - cylindrical, conical, and hemispherical; 4 lubrication methods - hydrostatic gas, hydrodynamic gas, hydrodynamic oil/grease, and squeeze-film. This initial group of 12 was quickly narrowed to three candidates. The squeeze-film type was found unacceptable because: (1) the power to operate it was excessive, and (2) the stiffness would be too low. The hemispherical geometry was selected over the conical and cylindrical types on the basis of the following: (1) easier alignment of the two bearings, and (2) ease of producibility.

B. BEARING SELECTION

Having narrowed the choices to three hemispherical types (hydrostatic gas, hydrodynamic gas, and hydrodynamic oil/grease), MTI proceeded to perform more detailed studies of these three types. These detailed studies indicated the design and performance characteristics of each bearing type. The performance and size of both air bearing types were virtually equal in all respects except the breakaway torque requirements. The breakaway torque for the hydrostatic bearing was virtually zero. The breakaway torque for the hydrodynamic gas bearing was 130 in.-ozs, approximately 20 times larger than the capability of a practical sized spin motor of the drag-cup type considered appropriate. Both bearings had diameters of approximately 3 in. The large breakaway torque of the hydrodynamic gas bearing (due to its large friction radius arm) resulted in its being dropped from further consideration.

The performance characteristics of the remaining two bearing types, hydrostatic gas versus hydrodynamic oil/grease, were essentially equal, again except for their breakaway torque requirements. The oil/grease bearing required 5 oz-in., which was slightly less

SECTION XII

than the expected stall torque capability of the motor. The only other performance difference was slightly in the favor of the gas bearing. Its nominal clearance was slightly greater, 240 μ -in. versus 220 μ -in. This difference would reflect in a slightly larger $2w_s$ torque ripple since it was shown by MTI that the torque ripple would be approximately inversely proportional to bearing clearance.

The remaining differences were in the areas of size and operational convenience. These differences and the advantages and disadvantages are compared in Table XII-1. Hughes made the final selection decision in favor of the oil/grease bearing. This decision was based on the following two significant advantages provided by the oil/grease bearing: (1) the size of the oil bearing was approximately 1/2 in. versus 3 in. in radius. The smaller size permits nesting of the spin motor around the bearing and, hence, results in a significantly smaller size; (2) the operational and design complexity associated with providing an air supply to the bearing would be very disadvantageous.

C. PROTOTYPE BEARING DESIGN

The final detailed design of the selected oil bearing was completed by MTI. The Spin Bearing Design Specification in Appendix D provides a detailed listing of all the physical and performance characteristics on pages 20 and 21. A cross-sectional view of the final prototype bearing design is shown in Fig. XII-1. The bearing installation is shown in the sensor assembly drawing in Section V. The female portion of the bearing is mounted to the rotor, while the male portion is mounted to the sensor case. The spiral-grooved male portion acts as a pump to pressurize the lubricant and thus provides the load carrying capability of the bearing. The lubricant is supplied from a porous reservoir via a small meniscus ring between the reservoir and the female portion of the bearing. A nonwet surface barrier film is applied over the areas indicated to prevent oil migration.

SECTION XII

TABLE XII-1

Final Spin Bearing Selection Considerations

Hydrostatic Air Bearing		Hydrodynamic Oil Bearing	
Advantages	Disadvantages	Advantages	Disadvantages
<p>1. Low break-away torque.</p> <p>2. Approximately 20% lower ripple torque.</p> <p>3. Bearing exhaust air would help cool sensor.</p>	<p>1. Very large size:</p> <ul style="list-style-type: none"> a. Difficult to design and make motor. b. Significant increase in sensor size. <p>2. Has drag and ripple torque sensitivity to supply air pressure and temperature. \therefore requires close control of both pressure and temperature of supply air.</p> <p>3. Air feed across platform gimbals very difficult and operationally inconvenient.</p> <p>4. Loss of air supply could damage bearing.</p>	<p>1. Small – easy to package motor and smaller sensor size.</p> <p>2. Convenient – no air supply problems.</p> <p>3. Cost is slightly less.</p>	<p>1. Higher break-away torque.</p> <p>2. Drag and ripple torque temperature sensitive, \therefore must control bearing temperature more closely. (Not inconsistent with temperature control requirements on sensor, however.)</p> <p>3. Must conduct all development tests at operating temperature.</p> <p>4. There is a considered risk in oil recirculation and retention. May require periodic replenishment.</p>

T873

2075-54

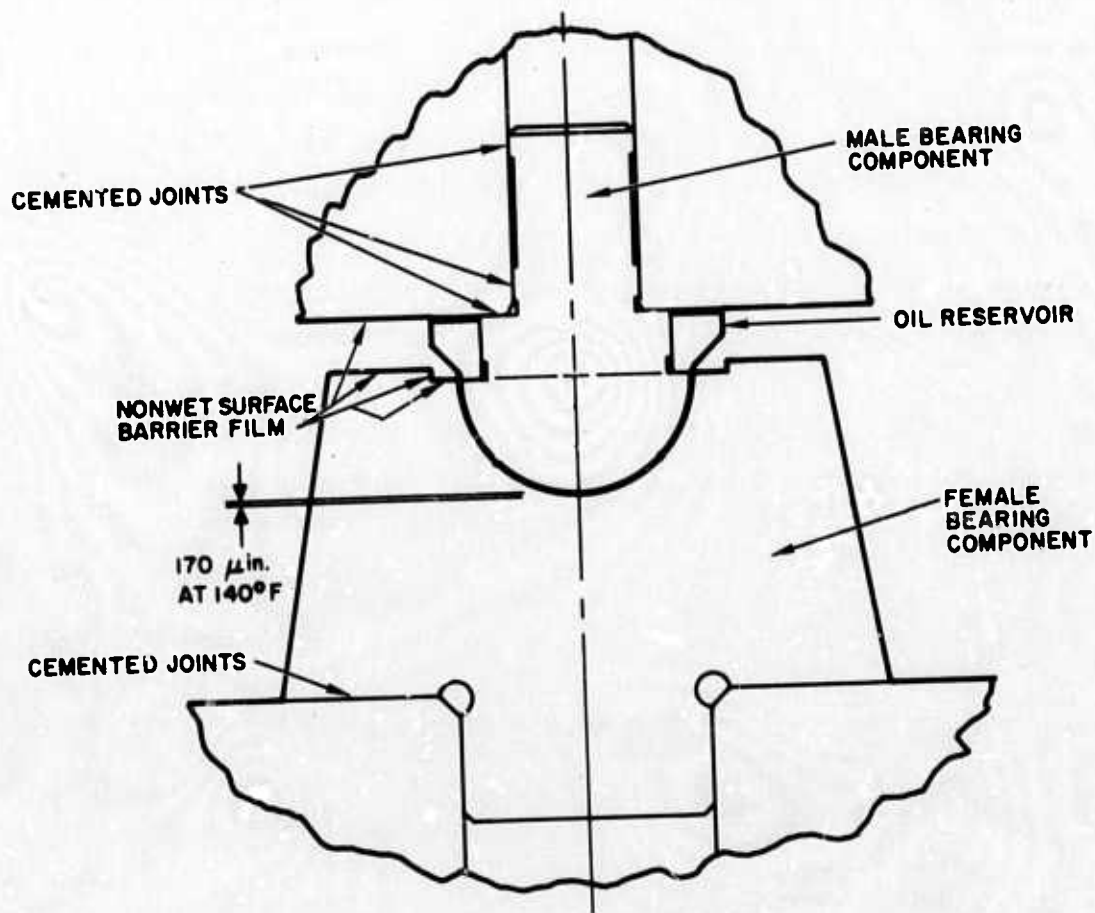


Fig. XII-1. Spin Bearing Final Design Cross-Sectional View.

SECTION XII

Some of the bearing performance requirements were restated in this final specification. These were necessary to reduce the mechanical tolerance requirements imposed by the original Hughes procurement specification. The nature of these changes was to allow specific RGG errors, induced by the spin bearing, to be increased provided the resultant RGG error would be deterministic. The allowed randomness of these errors, induced by the spin bearing, was not modified. Thus, the deterministic portion of these errors will be "biased-out" during the sensor calibration operation.

The spin bearing performance requirements imposed in the RGG sensor application are difficult, but are within the state of the art of bearing technology. Manufacture of the bearing will require close control and surveillance by competent technical personnel.

SECTION XIII

SENSOR ARM DESIGN

A. GENERAL

The following major factors were considered in selecting an optimum design configuration for the RGG sensor arm pair: thermal noise, size, weight, structural resonant frequencies, isoelasticity, mass/structural symmetry, and compatibility for mounting mass balance adjustment devices and the gradient signal transducers.

Nominal sensor design parameters, selected early in the sensor design process, allocated approximately one-third EU to thermal noise. Thus, the arm size-weight characteristics were established.

Since arm anisoelasticity was one of the potentially large error sources for the moving base environment, selection of the basic arm structural configuration was heavily influenced by this characteristic. Similarly, because of potential dynamic coupling between arm structural vibration modes and both external and internally generated vibrations, a light-weight, high stiffness arm structure, having relatively high natural frequencies, was desired.

A requirement for symmetry of each individual arm structure placed one constraint on design of the arm pair. A nonsymmetrical arm structure can cause a see-saw motion of the arm (oscillatory angular motion about an axis normal to the spin-axis), induced by external translational vibration, which results in a $2\omega_s$ differential arm gradient error torque.*

Another error source, axial arm mass unbalance, ** imposes the requirement that the center of mass of each arm be coincident, both

*See HRL Technical Proposal 71M-1593/C3755, September 1971,
pp 355-364.

**See Section IX-A.

SECTION XIII

radially and axially. This error is proportional to the product of axial center of mass separation distance and radial center of mass separation distance. Hence, it was only necessary to make this product sufficiently small.

Finally, it was necessary that the arm design provide for mounting of the mass balance adjustment devices and for connection and mounting of the output transducer. The desired location of the mass balance adjustment devices was near the center to minimize centrifugal forces imposed on them by the spin. The transducer mounting scheme was selected to minimize all mechanical loading on the transducer except that caused by axial differential arm torque.

The material selected for the arm structure is aluminum, while that for the end masses is Mallory 1000. The justification for these choices is contained in Section II.

B. FORM FACTOR TRADEOFFS

Ideally, a long slender arm structure with relatively small sized end masses would have the highest inertia efficiency, η , and the least mass. However, the requirement for an isoelastic structure with high resonant frequencies suggests a short stubby form factor, but would have a higher total mass. A solid bar of rectangular cross section can be shown to be anisoelastic no matter what its length to cross-sectional area ratio may be. Such a structure deflects in shear about three times more than in compression. See Fig. XIII-1. This is because the shear modulus is usually about one-third the Youngs modulus. Considering any flexural bending deflection just makes this ratio of lateral to longitudinal deflection even more unequal. Hence, a solid arm structure to support the high density end masses cannot be isoelastic. A structure with cutouts of some kind, to weaken it more longitudinally than laterally, is required.

Also, to keep the axial bending (end mass deflection along spin-axis direction) and see-saw stiffness high, it is desired to keep the depth

SECTION XIII

of the arm structure large. Figures XIII-2 and XIII-3 illustrate two possible arm designs which can meet these isoelastic and high stiffness requirements.

To keep the overall sensor length small and simultaneously provide for high see-saw and axial bending stiffness, it is desired to interleave the two arms. Two possible configurations are shown in Fig. XIII-4(a) and (b) for the individual arm configuration shown in Fig. XIII-2. Note that for either interleaved configuration shown, the arm width must be less than the longitudinal distance between the end masses.

The interleaved configuration shown in Fig. XIII-4(a) has the advantage that each arm can be made identical. The configuration of Fig. XIII-4(b) requires two separate arm designs to achieve equal isoelastic parameters for each. In configuration XIII-4(a), the arm centers of mass are separated axially which gives rise to an error sensitivity to angular accelerations normal to the spin-axis. However, error analyses have shown that this sensitivity is sufficiently small. In the configuration of Fig. XIII-4(a), the inner arm will have a considerably lower "see-saw" stiffness than the outer arm. This low stiffness could give rise to "see-saw" motion of the arm, induced by a small arm axial center-of-mass offset acted upon by translational acceleration normal to spin-axis, which results in a $2\omega_s$ differential gradient error torque.* The arm configuration of Fig. XIII-4(b) has been selected for the prototype arm design because of its higher achievable see-saw stiffness and because each arm is of identical design.

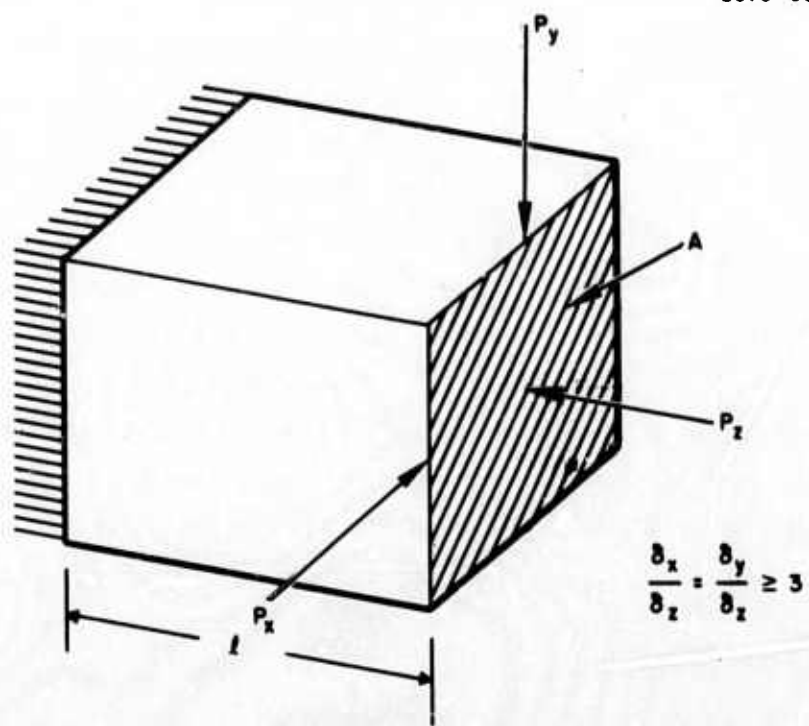
Tradeoffs between the arm configurations of Figs. XIII-2 and XIII-3 pertain to anisoelastic design considerations and are discussed in Section XIII-D.

C. ARM MASS AND INERTIA EFFICIENCY

The physical size and weight of the total RGG sensor package is, to a very large extent, dominated by the dimensions of the sensor arms.

*See HRL Technical Proposal 71M-1593/C3755, September 1971,
pp 355-364.

2075-30



$$\frac{\delta_x}{\delta_z} = \frac{\delta_y}{\delta_z} \geq 3$$

Fig. XIII-1. Solid Bar Structure of Rectangular Cross Section.

2075-31

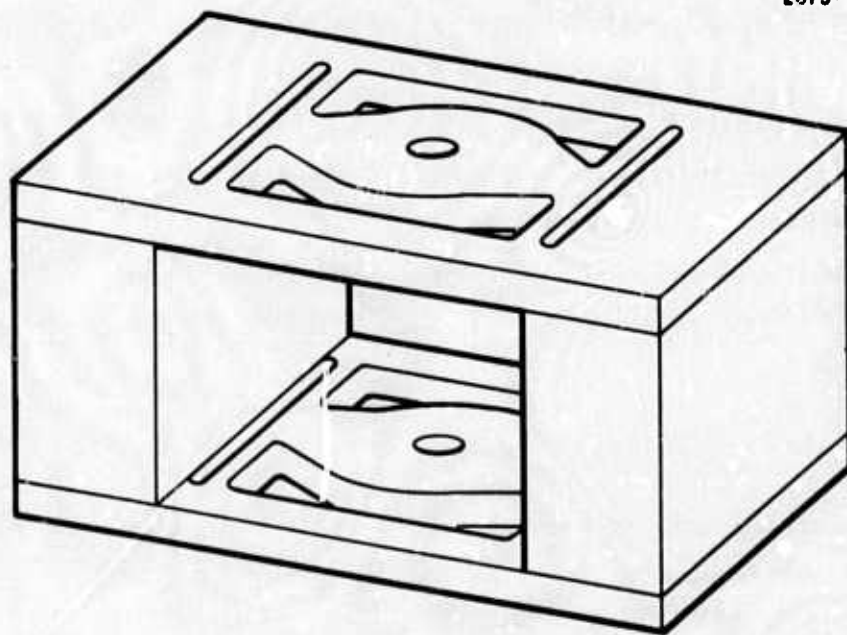


Fig. XIII-2. Arm Configuration A.

2075-32

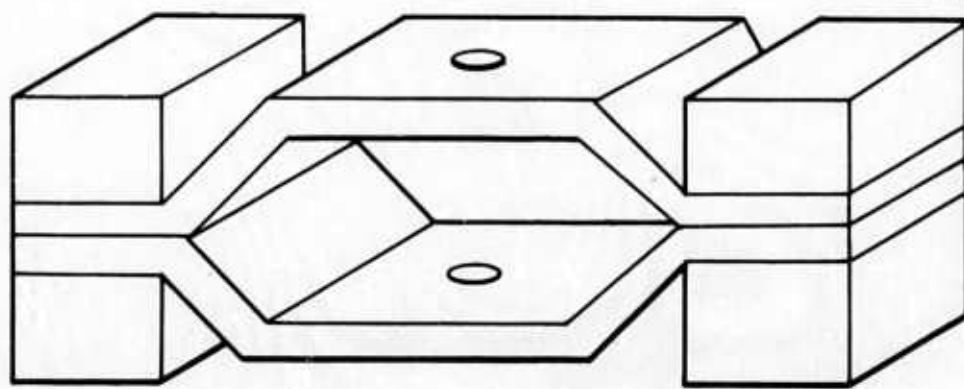
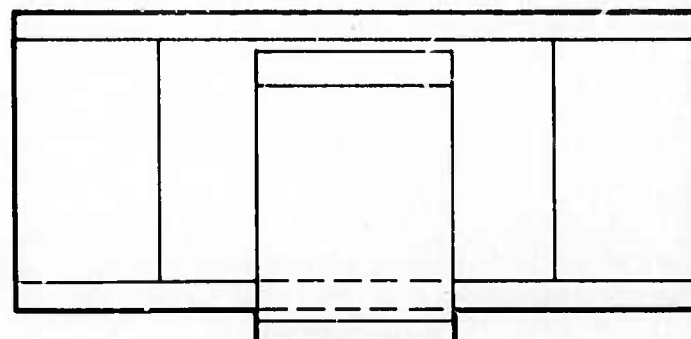
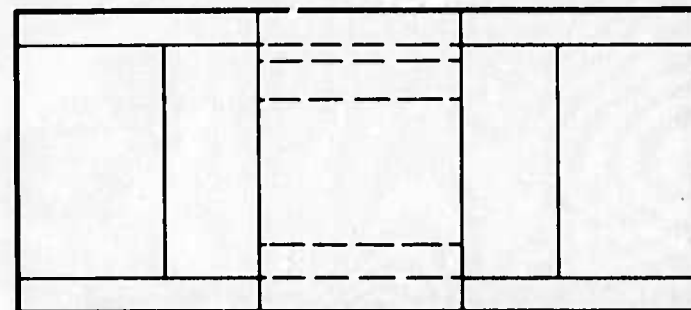


Fig. XIII-3. Arm Configuration B.

2075-33



(a)



(b)

Fig. XIII-4. Arm Configuration - Interleaved.

SECTION XIII

The allocated 1/3 EU thermal noise limit imposes the requirement that $\eta^2 C_{zz}$ be at least 26,400 gm \cdot cm²*. This requirement could be met by many combinations of arm end mass vs arm length, and hence a trade-off between these two parameters is implied. Because of the many form factor considerations, a rather short stubby arm configuration is preferred. Also, since the total sensor weight tends to be proportional to the third power of the arm's largest (radial length or axial height) dimension, arm size rather than mass has the greater influence on over-all sensor size and weight. Furthermore, an optimization study which determined the best combination of arm length, width, and height to maximize the $\eta^2 C_{zz}$ parameter indicates that a short stubby form is optimum. This would appear surprising at first glance until it is realized that the inertia efficiency factor, $\eta = (B_{yy} - A_{xx})C_{zz}$, plays a dominant role in the $\eta^2 C_{zz}$ parameter.

The results of the optimization study are depicted graphically in Fig. XIII-5. Note the strong dependency of $\eta^2 C_{zz}$ on arm width to length ratio, $a/2R$. The optimum value of width to length ratio is dependent on the ratio of the mass length to overall arm length, b/R , however for $1/3 < b/R < 2/3$, the optimum changes only very slightly. For the prototype arm design, b/R was chosen as $1/3$, and $a/2R$ as $1/2$.

It is interesting to note that height, l , and the plate thickness, t , play a very insignificant role in determining this optimization. It can be shown that $\eta^2 C_{zz}$ of the heavy weight masses alone is completely independent of their height, l . The second order effect of varying the $t\rho_1/l\rho_2$ ratio is brought about by the influence of the additional mass and inertia of the low density arm structural material. The ratio of the weight of the arm structure to the heavy weight end mass material for the prototype arm design is approximately $1/6 \underline{t}h$.

The trends determined from the optimization study are applicable to either of the arm configurations of Fig. XIII-2 or XIII-3. The dimensions of the prototype arm were chosen by: (1) selecting $a/2R$ and b/R ratios consistent with the optimization curves of Fig. XIII-5 at

*The calculations leading to the specification of this number are shown in the Semiannual Technical Report No. 1, p. 72.

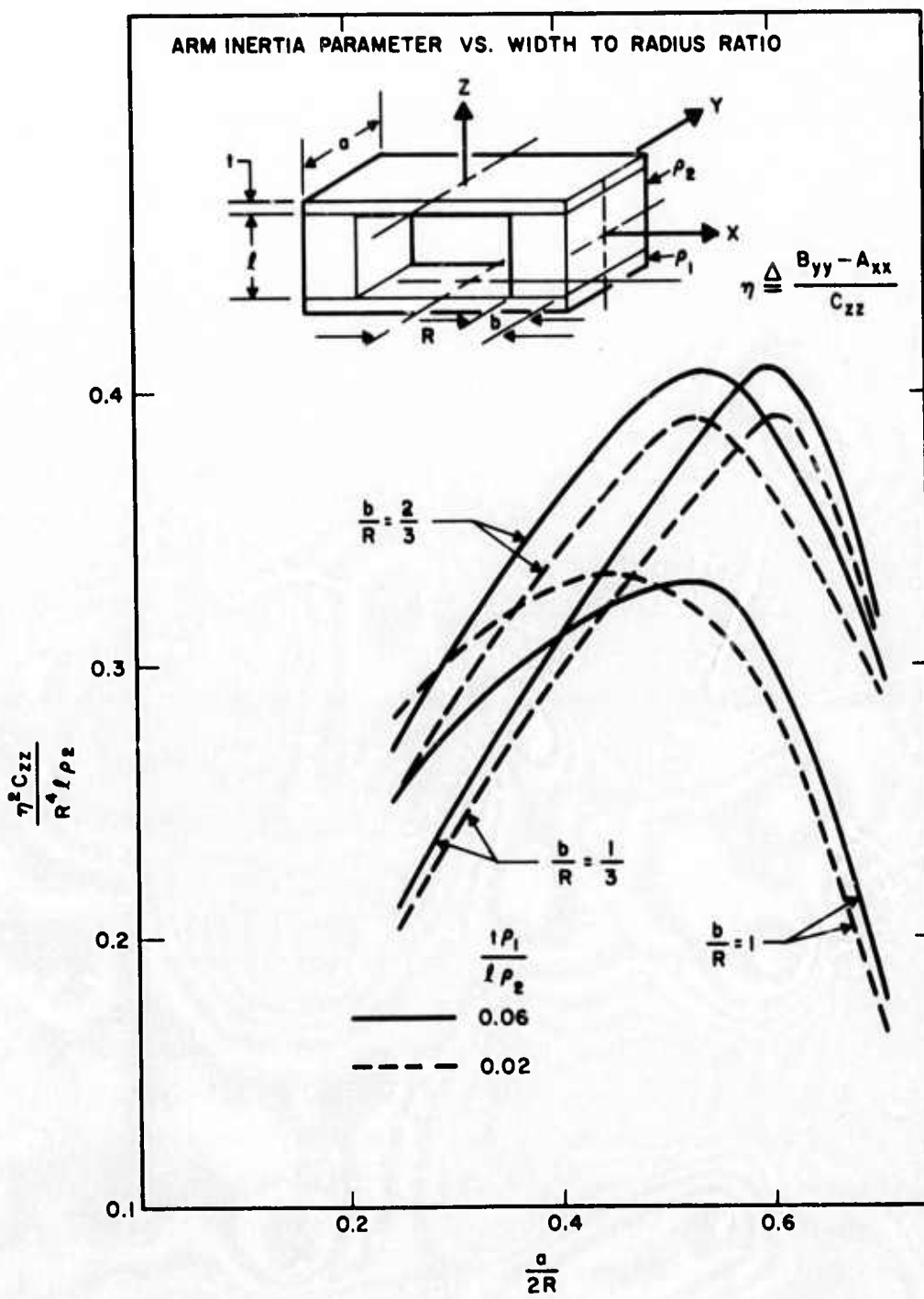


Fig. XIII-5. Arm Inertia Parameter Versus Width to Radius Ratio.

SECTION XIII

$a/2R = 0.5$ and $b/R = 1/3$, (2) selecting for the materials, aluminum for the arm structure and Mallory 1000 for the end masses, (3) selecting an arm structure thickness of 0.25 in., and (4) trading off arm radius, R , with height, l , to result in an arm configuration which provided the required $\eta^2 C_{zz}$ value and which had the appropriate ratio of R to l to minimize the radius of a circumscribed sphere. This approach was used to minimize the volume, and hence weight, of the surrounding rotor and case.

After selecting the primary arm dimensions, it was noted that if a cylindrical or spherical rotor were used to house the arms, additional inertia efficiency could be obtained by merely adding a cylindrical sector portion on each arm mass as shown by the dotted lines of Fig. XIII-6. Addition of this sector reduced the radius of the circumscribed sphere by 8% and increased the inertia efficiency, η , from 0.83 to 0.86.

Finalized dimensions, weight, and moments of inertia of the baseline arm design are summarized in Section XIII-E.

D. ISOELASTIC ARM DESIGN

Many arm structural configurations have been considered during this study, some quite simple and some, although possibly superior in concept, very complex and extremely difficult to fabricate and assemble. The goal established for selecting a suitable design was that it be relatively easy to manufacture and assemble, result in minimum structural resonant frequencies of approximately 10 to 20 times the gradient sensing frequency of 35 Hz, and be simple and straightforward to trim, in the laboratory, into final isoelastic balance.

After considering the many form factor trade-offs mentioned above, the two-arm configurations shown in Figs. XIII-2 and XIII-3 remained as suitable choices. Initially, the arm of Fig. XIII-3 appeared superior and a detailed structural deflection analysis was undertaken of this configuration. The results of this analysis showed that for a reasonable overall arm height of 2 inches, isoelasticity could not be

2076-36

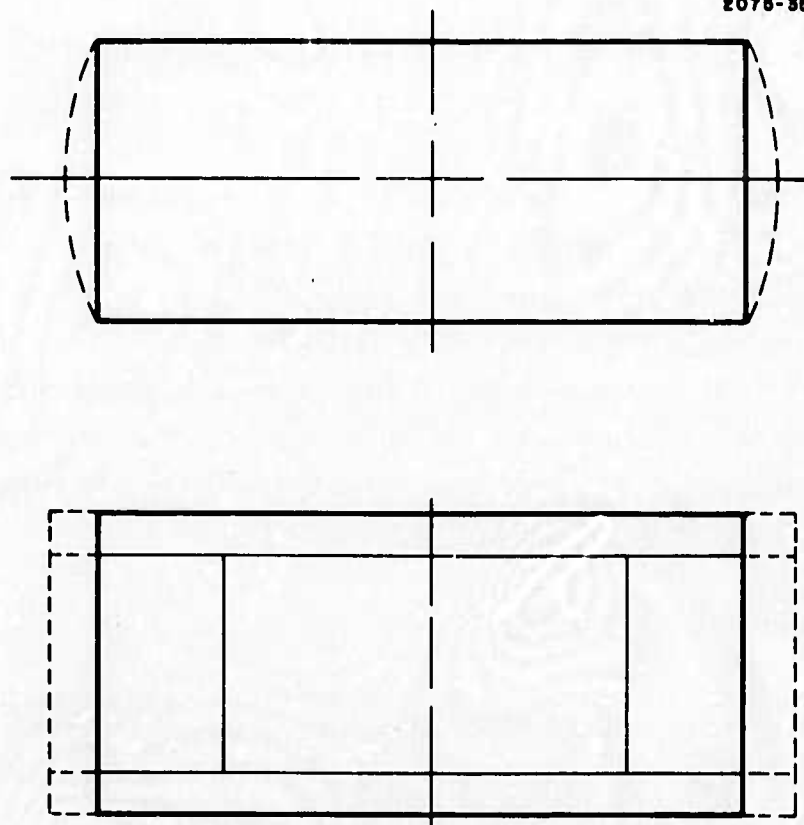


Fig. XIII-6. Arm Mass with Added Cylindrical Sector Portion.

SECTION XIII

achieved. It had been thought that by varying the inclination angle of the arm struts, the longitudinal to bending stiffness ratio could be varied sufficiently to achieve equal stiffnesses in both directions. However, it was found, even with the strut angle at 90° , that the longitudinal stiffness was still approximately 3 times greater than the bending stiffness. Variations of the strut thickness and top and bottom plate thicknesses, both together, and oppositely, did not alleviate the basic isoelastic inequality. It was apparent that the design could only hope to be made isoelastic if the arm axial height were increased. However, it could be seen from the structural deflection equations that a significant height increase would be required to achieve isoelasticity and that in so doing, the stiffnesses would become significantly lowered. Hence, this design was cast aside in favor of the configuration of Fig. XIII-2.

Deflection equations for the Fig. XIII-2 arm configuration were derived. These equations are summarized in Appendix A. Optimization studies were carried out to determine arm structure dimensions which resulted in isoelasticity and maximum stiffness. Checks were made of the axial bending stiffness. Also, structural resonant frequencies were computed for the arm first flapping mode, first see-saw mode, as well as the first lateral bending and longitudinal modes. All of the above resonant frequencies were determined considering deflection of the arm structure itself as well as deflection of the two end support pivots. All of these data are summarized in Section XIII-E.

Design of the center hub portion of the arm was chosen to minimize the induced see-saw motion. This motion gives rise to $2\omega_s$ differential arm error torques induced by acceleration normal to the spin-axis.* The center hub portion of the arm is offset axially so as to place the center of the two end support pivots directly over the arm center of mass. This, except for manufacturing error, reduces this error sensitivity to zero.

*See HRL Technical Proposal 71M-1593/C3755, September 1971,
pp 355-364.

SECTION XIII

Since all of the stiffness parameters and natural frequencies of the arm configuration were found to be reasonable and satisfactory, it has been selected as the prototype arm configuration. While detailing this design during Phase II minor modifications will be considered to maximize the lateral and longitudinal stiffnesses.

E. ARM DESIGN CHARACTERISTICS

This section summarizes the prototype arm design characteristics, including mass, inertias, stiffnesses, structural resonant frequencies, and nominal dimensions. The arm dimensions are shown in Fig. XIII-7 and the remaining parameters are listed below and pertain to one complete sensor arm.

Mass - 1563 g

$A_{xx} \triangleq$ Moment of inertia about arm length = $4,990 \text{ gm-cm}^2$

$B_{yy} \triangleq$ Moment of inertia about arm width = $35,610 \text{ gm-cm}^2$

$C_{zz} \triangleq$ Moment of inertia about spin-axis = $35,600 \text{ gm-cm}^2$

Lateral Bending Stiffness = $162,200 \text{ lb/in.} = 2.839 \times 10^{10} \text{ dynes/cm}$

Longitudinal Stiffness = $162,200 \text{ lb/in.} = 2.839 \times 10^{10} \text{ dynes/cm}$

Axial Bending Stiffness = $94,500 \text{ lb/in.} = 1.654 \times 10^{10} \text{ dynes/cm}$

Lateral Support Pivot Stiffness (one only) = $196,000 \text{ lb/in.} = 3.428 \times 10^{10} \text{ dynes/cm}$

Axial Support Pivot Stiffness (one only) = $785,000 \text{ lb/in.} = 13.73 \times 10^{10} \text{ dynes/cm}$

Arm-Pivot 1st Lateral Bending or First Longitudinal Natural Frequency = 779 Hz

Arm-Pivot 1st Flapping Mode Natural Frequency = 673 Hz

Arm-Pivot First See-Saw Mode Natural Frequency = 567 Hz

F. OPERATIONAL ANISOELASTIC ERROR COEFFICIENTS

In Section IX, the "differential anisoelastic error coefficient tensor," $\overline{\overline{K}}_0$, was developed and presented in terms of the compliance

2075-27

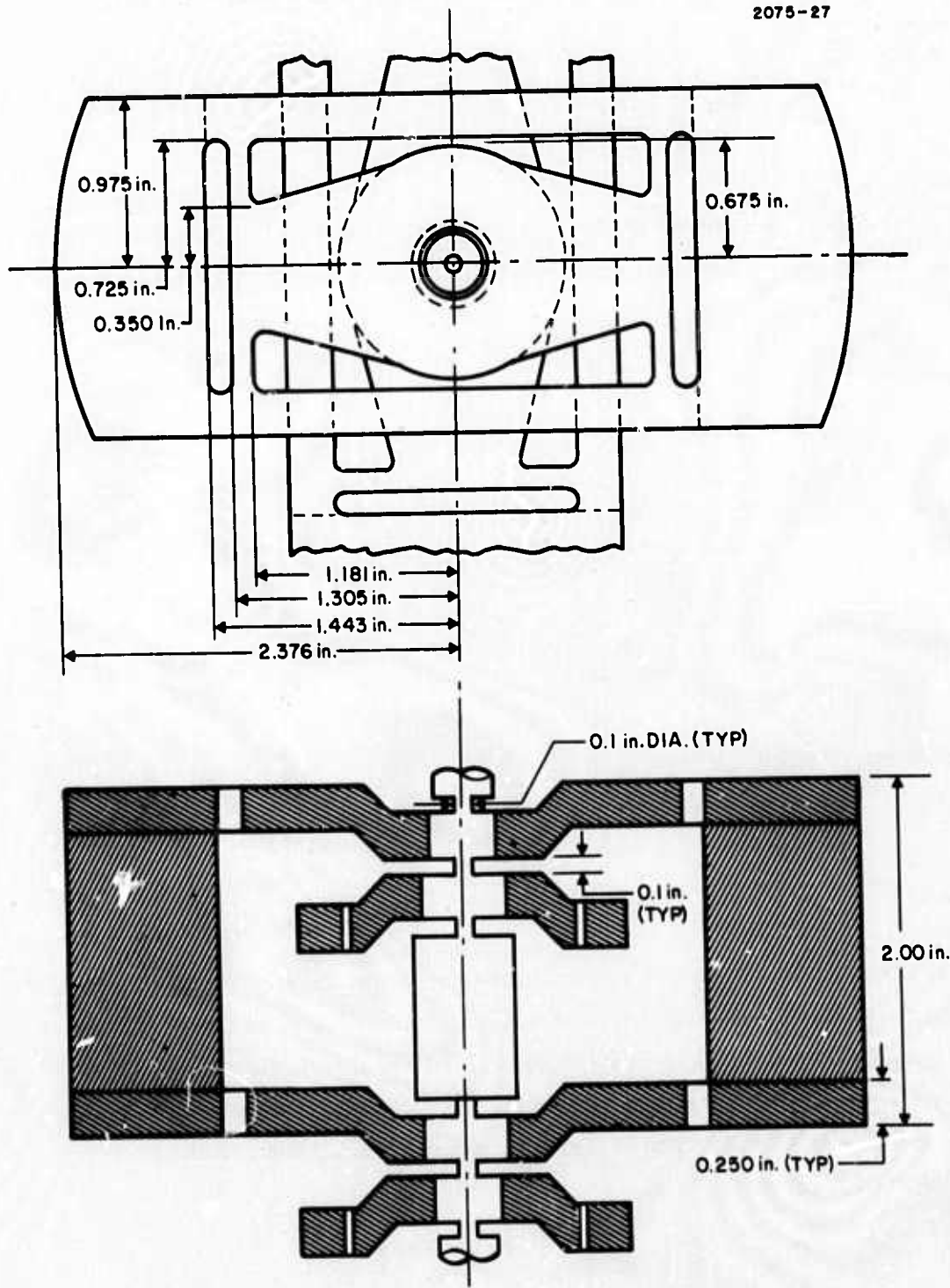


Fig. XIII-7. Prototype RGG Isoelastic Arm Design.

SECTION XIII

tensors, $\bar{\psi}_i$, of each RGG arm. This definition is repeated here as equation (1).

$$\bar{K}_0 \triangleq \frac{1}{\eta C} \left[(M_1)^2 \bar{\psi}_1 - (M_2)^2 \bar{\psi}_2 \right] \quad (1)$$

The compliance tensors of each arm may be expressed in terms of their principal elements such that each part of (1) may be expressed in the matrix forms of (2) and (3).

$$\frac{(M_1)^2 \bar{\psi}_1}{\eta C} \triangleq \begin{bmatrix} A_1 & 0 & 0 \\ 0 & B_1 & 0 \\ 0 & 0 & C_1 \end{bmatrix} \quad (2)$$

$$\frac{(M_2)^2 \bar{\psi}_2}{\eta C} \triangleq \begin{bmatrix} B_2 & 0 & 0 \\ 0 & A_2 & 0 \\ 0 & 0 & C_2 \end{bmatrix} \quad (3)$$

The inversion of the A and B coefficients between (2) and (3) is due to the orthogonal relative orientation of the RGG arms. Each arm compliance tensor may be expressed in RGG rotor-reference coordinates (ijk) by small angle similarity transformations, $[\theta_i]$, from the principal elastic axes of each arm to the rotor reference frame such that (1) may be expressed from (2) and (3) as (4).

$$\bar{K}_0 = [\theta_1]^T \begin{bmatrix} A_1 & 0 & 0 \\ 0 & B_1 & 0 \\ 0 & 0 & C_1 \end{bmatrix} [\theta_1] - [\theta_2]^T \begin{bmatrix} B_2 & 0 & 0 \\ 0 & A_2 & 0 \\ 0 & 0 & C_2 \end{bmatrix} [\theta_2] \quad (4)$$

SECTION XIII

where

$$[\theta_1] \cong \begin{bmatrix} . & 1 & \theta_{k1} & -\theta_{j1} \\ & -\theta_{k1} & 1 & \theta_{i1} \\ & \theta_{j1} & -\theta_{i1} & 1 \end{bmatrix} \quad (5)$$

$$[\theta_2] \cong \begin{bmatrix} . & 1 & \theta_{k2} & -\theta_{j2} \\ & -\theta_{k2} & 1 & \theta_{i2} \\ & \theta_{j2} & -\theta_{i2} & 1 \end{bmatrix} \quad (6)$$

Substitution of (5) and (6) into (4) yields the elements of the symmetric differential anisoelastic error coefficient tensor, K_0 , as (7) through (12).

$$K_{ii} \cong A_1 - B_2 \quad (7)$$

$$K_{jj} \cong B_1 - A_2 \quad (8)$$

$$K_{kk} \cong C_1 - C_2 \quad (9)$$

$$K_{ij} \cong (A_1 - B_1)\theta_{k1} + (A_2 - B_2)\theta_{k2} \quad (10)$$

$$K_{ik} \cong (C_1 - A_1)\theta_{j1} + (B_2 - C_2)\theta_{j2} \quad (11)$$

$$K_{jk} \cong (B_1 - C_1)\theta_{il} + (C_2 - A_2)\theta_{i2} \quad (12)$$

SECTION XIII

The dominant coefficient in the anisoelastic input error function of Section IX (eq. (15)), is stated from (7) and (8) as (13).

$$\frac{K_{ii} - K_{jj}}{2} = \left(\frac{A_1 - B_1}{2} \right) + \left(\frac{A_2 - B_2}{2} \right) \triangleq K_0 \quad (13)$$

The remaining anisoelastic error coefficients of the referenced error function are functions of the "elastic misalignment angles" of each arm, $\bar{\theta}_1$ and $\bar{\theta}_2$. The parameter defined by (13) is called the "prime-anisoelastic error coefficient," and the parameters defined by (10), (11) and (12) are called the "cross-anisoelastic error coefficients."

Ideally, the "prime anisoelastic coefficient" of (13) is zero since, by design, all of the "A" and "B" parameters are intended to be equal. However, because of the practical approximations which must be made, analysis of the arm structural deflections can be only approximate. Experience would indicate that errors as large as 10 to 15 percent could be expected for a structure like that of the baseline arm. However, this inaccuracy, in itself, is not considered a problem. A significant advantage of the baseline arm is that certain portions of the structure are known to be the primary contributors to bending deflection and other portions are known to be the primary contributors to longitudinal deflection. Thus, once fabricated, the arm will be tested to determine the required arm dimension changes to achieve isoelasticity. Thus, a "modified arm design" will result which will be nominally isoelastic.

With the modified design, a sensor arm pair will be fabricated and assembled into an operating sensor. A calibration and trimming operation will then be performed. For the prototype arm design, it is estimated that a stiffness difference of 1/10th percent can be practically achieved. This 1/10th percent stiffness mismatch corresponds to a prime anisoelastic error coefficient of approximately 2700 EU/g^2 . Thus, with the sensor operated with a horizontal spin axis, a 2700 EU signal will result. Thus, it is expected that this anisoelastic coefficient can be experimentally determined to an accuracy of at least $\pm 1\%$, or $\pm 27 \text{ EU}$.

SECTION XIII

However, trimming the mismatch factor to better than 1/10% would not be practical. After achieving this level of mismatch, the calibration and trimming must be performed with the sensor operating and thermally stabilized. Each "trim" cycle entails dismantling the sensor, trimming the arms, re-assembly, arm mass re-balancing, rotor mass re-balancing, warm-up, etc.

Because this practically attainable "prime anisoelastic coefficient" is large, it is obvious that "active compensation" of the "prime anisoelastic errors" will be required. The implementation of this type of compensation requires that the actual "prime anisoelastic error coefficient" of each RGG be determined by laboratory test. As stated above, it is estimated that the coefficient can be experimentally determined to an accuracy of one percent or better. It is shown in Section IX that this accuracy is well within the required limits. Because "active compensation" will be employed, not only the initial "accuracy" of this prime anisoelastic coefficient is of concern but its stability as well.

The primary cause of instability of the anisoelastic coefficient will be variations in operating temperature of the sensor arms over the period of one operational run. Note that effects of aging-creep, change of modulus of elasticity, density, etc. - are not significant since these changes occur very slowly compared to an operational run of even several days. This is true since such effects of aging are "biased-out" during the initialization prior to an operational run.

The variation of the anisoelastic coefficient may be computed considering thermal expansion and modulus of elasticity variation with temperature. The arm structure deflection equations, presented in Appendix A, all have a similar dimensional form. The deflection due to a load, or the compliance, is inversely proportional to the product of an arm dimension and the modulus of elasticity. Define

- C_i = arm structure compliance along i^{th} axis
- ℓ = arm length dimension parameter
- E = arm modulus of elasticity parameter
- T = average arm temperature, $^{\circ}\text{C}$

SECTION XIII

α = unit thermal expansion coefficient

ϵ = unit modulus of elasticity thermal coefficient

K_{ij} = anisoelastic error coefficient

From the above observations:

$$C_i \sim \frac{1}{E\ell}$$

Taking the rate of change with temperature,

$$\frac{dC_i}{dT} \sim C_i \left(\frac{1}{\ell} \frac{d\ell}{dt} + \frac{1}{E} \frac{dE}{dt} \right) \sim C_i(\alpha + E)$$

The prime anisoelastic error coefficient, K_{ij} , is proportional to the difference between say C_x and C_y . Thus,

$$\frac{d(C_x - C_y)}{dT} \sim (C_x - C_y)(\alpha + E) \sim K_{xy}(\alpha + E)$$

or

$$\frac{dK_{xy}}{dT} = K_{xy}(\alpha + E)$$

Hence, for a nominal prime anisoelastic error coefficient of 2700 EU/g^2 , a unit thermal expansion coefficient for aluminum of $23.4 \times 10^{-6}/^\circ\text{C}$ and a unit modulus of elasticity thermal coefficient of $-530 \times 10^{-6}/^\circ\text{C}$, the temperature sensitivity of K_{xy} is

$$\frac{dK_{xy}}{dT} = 2700(23.4 - 580) \times 10^{-6} = -1.50 \text{ EU/g}^2 - ^\circ\text{C}$$

SECTION XIII

The expected variation of the average arm temperature during sensor operation is approximately $\pm 0.005^{\circ}\text{C}$, 1σ . Hence, the standard deviation of the prime anisoelastic error coefficient will be

$$\sigma_{K_{xy}} = 1.50 \times 0.005 \cong 0.0075 \text{ EU/g}^2 - ^{\circ}\text{C}$$

The cross-anisoelastic coefficient, K_{ij} , depends on the polar non-orthogonality of the arm principal elastic axes and the anisoelastic coefficients of each arm. For example, let the angle of polar non-orthogonality be defined as θ_k such that each angle in (10) is defined by (15) and (16).

$$\theta_{k_1} \triangleq \frac{1}{2}\theta_k \quad (15)$$

$$\theta_{k_2} \triangleq -\frac{1}{2}\theta_k \quad (16)$$

Then from (10), (15), and (16), the coefficient, K_{ij} , is given by (17).

$$K_{ij} = \left[\left(\frac{A_1 - B_1}{2} \right) - \left(\frac{A_2 - B_2}{2} \right) \right] \theta_k \quad (17)$$

It is expected that the angle of "orthogonal deficiency," θ_k , will be less than one milliradian and that the magnitudes of the principal elastic differences ($A_i - B_i$) of each arm will be less 0.1% of the principal values (A_i or B_i). This leads to the upper bound defined by (18).

$$|K_{ij}| \leq 2.7 \text{ EU/g}^2 \quad (18)$$

SECTION XIII

Since this coefficient is an order of magnitude smaller than the "compensated prime anisoelastic error coefficient" (27 EU/g^2),* its error contribution is small in comparison to the "prime anisoelastic error" after active compensation.

The remaining "cross-anisoelastic coefficients," K_{ik} and K_{jk} , may be examined in terms of the "average" and "differential" angles of "tilt" of the principal elastic planes of the RGG arms as defined by (19) through (24).

$$\theta_{ja} \triangleq \frac{1}{2}(\theta_{j1} + \theta_{j2}) \quad (19)$$

$$\theta_{jd} \triangleq (\theta_{j1} - \theta_{j2}) \quad (20)$$

$$\theta_{ka} \triangleq \frac{1}{2}(\theta_{k1} + \theta_{k2}) \quad (21)$$

$$\theta_{kd} \triangleq (\theta_{k1} - \theta_{k2}) \quad (22)$$

$$K_{ik} = [B_2 - A_1 + C_1 - C_2] \theta_{ja} + \left[\frac{C_1 + C_2}{2} - \frac{A_1 + B_2}{2} \right] \theta_{jd} \quad (23)$$

$$K_{jk} = [B_1 - A_2 + C_2 - C_1] \theta_{ka} + \left[\frac{A_2 + B_1}{2} - \frac{C_1 + C_2}{2} \right] \theta_{kd} \quad (24)$$

The axial compliance coefficients, C_i , are significantly different from the radial coefficients, A_i and B_i such that the significant terms in (23) and (24) will be those associated with the differential angles, θ_{jd} and θ_{kd} . On this basis (23) and (24) may be approximated as (25) and (26).

$$K_{ik} \approx (C - A) \theta_{jd} \quad (25)$$

*See Section IX-F

SECTION XIII

$$K_{jk} \cong (A - C)\theta_{kd} \quad (26)$$

where

$$C \triangleq \frac{1}{2}(C_1 + C_2)$$

$$A \cong \frac{1}{2}(A_1 + B_2) \cong \frac{1}{2}(A_2 + B_1)$$

It is expected that the differential "tilt" angles, θ_{jd} and θ_{kd} , will be less than one milliradian such that the upper bounds of these cross-anisoelastic coefficients may be stated as (27) and (28).

$$|K_{ik}| \leq 1931 \text{ EU/g}^2 \quad (27)$$

$$|K_{jk}| \leq 1931 \text{ EU/g}^2 \quad (28)$$

Gradient errors associated with these "cross-anisoelastic error coefficients" are induced by accelerations in narrow frequency bands centered at one and three times the sensor spin frequency. Although these coefficients appear to be very large, it is shown in Section IX that the resultant tensor element bias error is less than 0.1 EU and the standard deviation is less than 0.02 EU. The bias error is the result of deterministic vibrations induced by the spin bearing and will be compensated in the system initialization process. Because these errors are so small, stability of the coefficients is relatively unimportant.

SECTION XIV

PIVOTS AND TRANSDUCER DESIGN

A. GENERAL

The pivots support the RGG sensor arms and provide the primary torsional stiffness for the mechanical resonant system. The piezoelectric transducers provide the remainder of the torsional stiffness, and also provide the electrical output signal. The output load resistor, the input resistance of the signal preamplifier, damps the very high Q mechanical system and stabilizes the effective Q of the sensor as a whole to about 300.

The electromechanical system can be represented by an electrical equivalent circuit, as shown in Figure XIV-1. In this figure

$$L_1 \equiv C_{zz}/2 \quad H$$

$$R_1 \equiv \text{ohms}$$

$$1/C_1 \equiv 1/C_p + 1/(C_m'/2) \quad F^{-1}$$

$$E_g \equiv \eta L_1 \Gamma_{eq}/2 \quad V$$

where:

C_{zz} = the moment of inertia of one sensor arm in Newton \cdot meters 2 (Ref. XIV-1)

R_1 = mechanical damping of the sensor pivots, arms, and transducers

2075-1

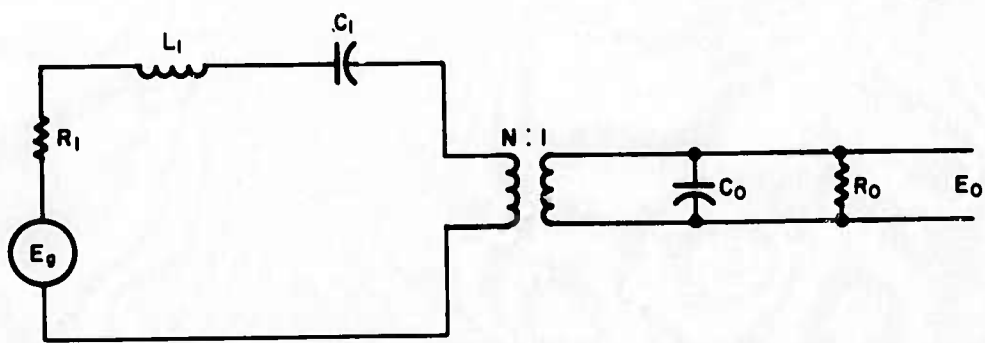


Fig. XIV-1. RGG Sensor-Transducer Equivalent Circuit.

SECTION XIV

C_p = mechanical compliance of the pivots in the differential mode, radians per Newton.

$C'_m / 2$ = mechanical compliance of the transducers in pure bending mode, radians per Newton.

E_g = torque input per EU, Newton meters/EU

N = system transformation ratio, a function of the transducer materials and dimensions
(see Section XIV-C)

η = inertia efficiency of the sensor arms $(B-A)/C$

C_o = the output capacitance of the two transducers in parallel, farads

R_o = load resistance, ohms.

The output voltage, phase and circuit impedance can be determined as follows: The input voltage and L_1 are transformed into a current source

$$I_1 \equiv \frac{E_g}{L_1 S} = \frac{\eta L_1 \Gamma_{eq}/2}{L_1 S} = \frac{\eta \Gamma_{eq}}{2 S}$$

The impedance on the output side is

$$Z_o = \frac{R_o}{1 + R_o C_o S}$$

transforming this to the input side

$$Z'_o = N^2 Z_o$$

SECTION XIV

The impedance on the input side is

$$Z_1 = \frac{1 + R_1 C_1 S}{C_1 S}$$

and the output voltage is

$$E_o = \frac{\eta \Gamma_{eq}}{N} \left[\frac{Z'_o L_1}{Z'_o + Z_1 + L_1 S} \right]$$

This is more conveniently written as the reciprocal in eq. (1)

$$\begin{aligned} \frac{\eta \Gamma_{eq}}{E_o} &= \left[\frac{N}{L_1} + \frac{1}{N} \left(\frac{R_1}{R_o L_1} + \frac{C_o}{C_1 L_1} + C_o S^2 \right) \right] \\ &+ \left[\frac{S}{N} \left(\frac{R_1 C_o}{L_1} + \frac{1}{R_o} + \frac{1}{R_o L_1 C_1 S^2} \right) \right]. \end{aligned} \quad (1)$$

Equation 1 is of the form

$$\frac{\eta \Gamma_{eq}}{E_o} = R(\omega) + jI(\omega)$$

where $R(\omega)$ and $I(\omega)$ are the real and imaginary parts, respectively, of eq. 1

$$\therefore E_o = \frac{\eta \Gamma_{eq}}{R + jI}$$

and

$$|E_o| = \frac{\eta \Gamma_{eq}}{(R^2 + I^2)^{1/2}} = \frac{\eta \Gamma_{eq}}{Z} \quad (2)$$

SECTION XIV

and

$$\tan \phi = \frac{-I}{R} \quad (3)$$

where:

$$R(\omega) = \frac{N}{L_1} + \frac{1}{N} \left[\frac{R_1}{R_o L_1} + \frac{C_o}{C_1 L_1} - C_o \omega^2 \right] \quad (4)$$

$$I(\omega) = \frac{\omega}{N} \left[\frac{R_1 C_o}{L_1} + \frac{1}{R_o} - \frac{1}{R_o L_1 C_1 \omega^2} \right] \quad (5)$$

Since these equations and their computed values will be used frequently in the following sections, they have been incorporated into a simple computer program shown in Fig. XIV-2. The output voltage and its phase angle over a narrow range of frequencies is plotted in Fig. XIV-3. The slope of the phase angle is so large that the phase angle plot appears as a nearly vertical line near the peak of the voltage response curve. $\Delta\phi/\Delta\omega$ is included as one of the printouts so that it can be evaluated more accurately. Near the resonant frequency the phase slope is nearly constant over a relatively large frequency range. Thus, if desired we can operate with a plus, flat, or negative $\Delta E_o/\Delta\omega$ coefficient.

B. PIVOTS, ARM SUPPORT

The objective of the pivot and arm design is to provide a rigid, stable structure that can be manufactured with high precision and provide the desired, sensor performance. The balancing of all the factors that must be considered was described in detail in the Semi-annual Technical Report No. 1. When the inertia and inertia efficiency of the arm was determined on the basis of thermal noise, the arm size and mass was approximately fixed. When the operating frequency was

```

100 REM" PROGRAM NAME SENS-1"
110 REM"
120 PRINT
130 REM THIS PROGRAM CALCULATES THE RGG SENSOR OUTPUT VOLTAGE
140 REM PER GAMMA EQUIVALENT INPUT. IT ALSO CALCULATES THE MECHANICAL
150 REM "Q"(Q0), THE SYSTEM Q1 BASED ON THE PHASE SLOPE OF THE
160 REM OUTPUT VOLTAGE AND THE PHASE OF THE OUTPUT VOLTAGE EO, AS
170 REM PER GAMMA EQUIVALENT INPUT.
180 REM
190 REM W = TWO * SENSOR ROTATION SPEED, RADIANS / SEC.
200 REM EO = OUTPUT VOLTAGE, VOLTS.
210 REM RO = OUTPUT LOAD RESISTOR, OHMS.
220 REM CO = XDR OUTPUT CAPACITY, FARADS.
230 REM N = SENSOR TRANSFORMATION RATIO.
240 REM CI = TOTAL MECHANICAL COMPLIANCE, RADIANS / NEWTON METER.
250 REM LI = CZZ/2, KGMETERS^2
260 REM RI = MECHANICAL DAMPING IN SENSOR, OHMS.
270 REM 0.861 IN THE FINAL EO CALCULATION IS THE INERTIA EFFICIENCY
280 REM OF ONE ARM. (B-A)/C.
290 REM B = 80 = PHASE OF EO IN RADIANS
300 REM Q0 = NOMINAL MECHANICAL " Q " OF THE SENSOR
310 REM Q1 = SYSTEM Q BASED ON THE PHASE SLOPE OF THE OUTPUT VOLTAGE.
320 REM Q1 = - DELTA B * W / 2 / DELTA W STEP.
330 REM B2 = DELTA B0
340 REM FOR AUTOMATIC INSERTION OF CO, N, AND CI EDIT MERGE WITH
350 REM PROGRAM XTD-1 AND DELETE VALUES FOR CO, N, CI THIS PROGRAM.
360 PRINT
370 PRINT " EO R I DELTA B "
380 LET CO = 3.49 E-9
390 LET CI = 1.1730459 E-2
400 LET LI = 1.78201816 E-3
410 LET RI = 6.1165992 E-4
420 LET N = 3.912 E-9
430 READ RO
440 PRINT "RO = " RO
450 DATA 9.55 E+6
460 LET Q0 = 220 * LI / RI
470 PRINT "Q0 = " Q0
480 FOR W = 219.9 TO 220.1 STEP 0.01
490 LET R = N/LI + ( RI/RO/LI + CO/CI/LI - CO*W^2 ) / N
500 LET I = W/N*(RI*CO/LI+I/RO-1/(RO*LI*CI*W^2))
510 LET Z = (R+I)^2+.5
520 LET EO = 0.861E-9/Z
530 LET B0 = ATN (-I/R)
540 IF R <= 0 THEN 560
550 GOTO 570
560 LET B0 = B0 - 3.14159265
570 LET B2 = B0 - B1
580 LET B1 = B0
590 LET Q1 = - B2 * W / 2 / .01
600 PRINT "W = " W
610 PRINT "Q1 = " Q1
620 PRINT EO, R, I, B2, B0
630 NEXT W
640 GOTO 430
650 END

```

Fig. XIV-2. Sensor Computer Program.

2075-26

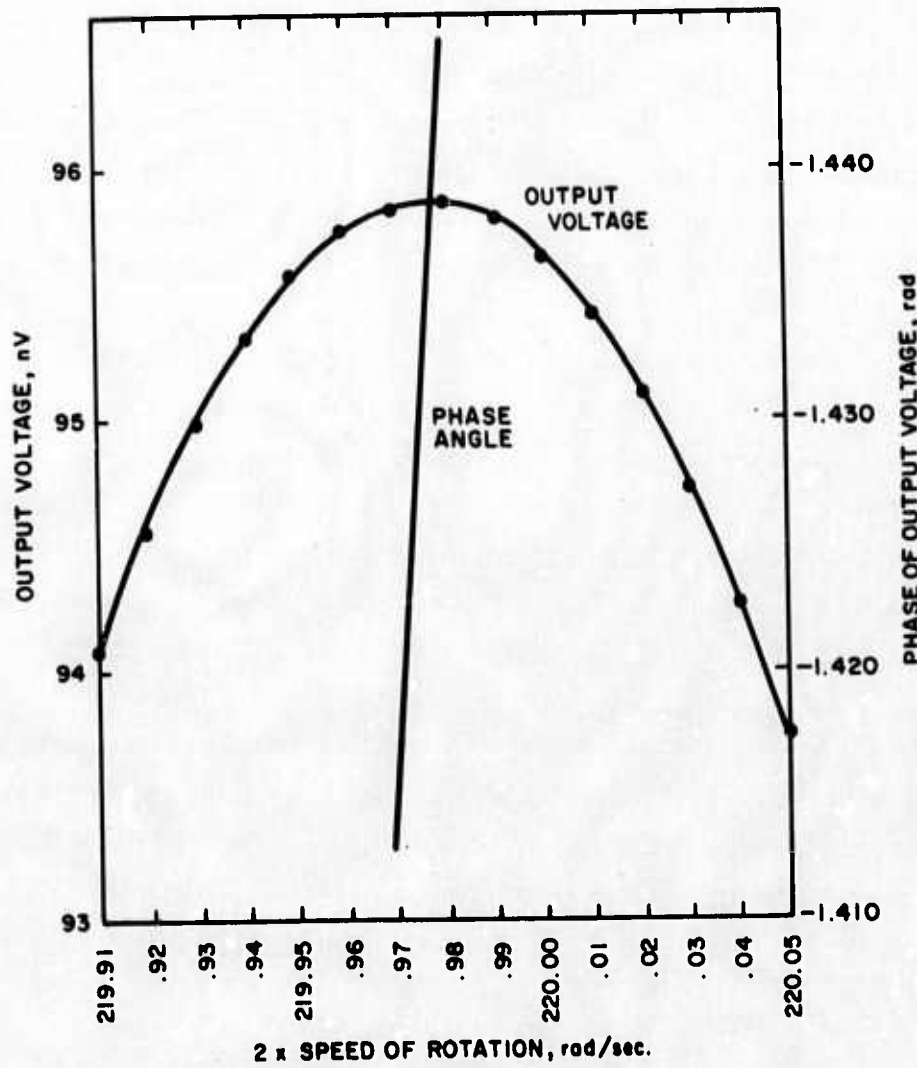


Fig. XIV-3. Voltage and Phase of Sensor-Transducer Output Voltage.

SECTION XIV

determined, the difference mode torsional stiffness was fixed. The ratio of the torsional stiffness of the end pivots to the difference mode pivots can be varied but as shown in the Semiannual Technical Report No. 1, if all pivots are made identical, a good symmetrical structure with satisfactory properties is obtained.

The detailed pivot design is completed in Section XIV-C as a part of the transducer calculation. The pivot material selected is beryllium copper which is stable and has low loss when operated as a spring. The pivots have a length-to-diameter ratio of 1, and the dimension is 0.0659 in.

The pivots are supported on one end by the central member of the rotor described in Section XI and on the other end by a brace plate.

The brace plate is attached to the central member by four brace posts. These posts can be made of a material whose coefficient of thermal expansion is higher, lower, or equal to the pivot material expansion coefficient. Thus, the pivots can be caused to be in tension, compression, or a zero longitudinal stress condition due to temperature changes. This is shown in detail in Section XIV-D.

In the prototype design, the pivots are beryllium copper, and the braces are aluminum. This puts the pivot in tension for increasing ambient temperatures, but the effect is slight and the sensor has a satisfactory temperature sensitivity as shown in Section XIV-D.

C. PIEZOELECTRIC TRANSDUCERS

1. General

Piezoelectric transducers have been selected for the baseline RGG design. They have the required sensitivity, and Hughes has used them in all previous gradiometer designs. Thus, we are continuing to build on our past experience. Detailed information on piezoelectric materials and transducers is contained in Refs. XIV-1, -2, -3, and -4.

SECTION XIV

The piezoelectric material specified is a mixture of lead-zirconate-titanate with other minor additives to improve temperature stability, aging, and other characteristics. The exact compositions are usually proprietary and unknown to the user; therefore, their performance must be specified in terms of their coefficients, as in this Section XIV-C, paragraph 5, "Transducer Specification."

After the piezoelectric material has been mixed, fired, poled, and provided with electrodes, it generates a voltage on the electrodes when it is stressed. In general, it is sensitive to tension and compression along the poling axis and along any axis at right angles to the poling axis; it is sensitive to shear along the poling axis or at right angles to the poling axis. To identify the various material stress sensitivities, the convention shown in Fig. XIV-4 has been adopted. The poling axis is designated as 3 and, since piezoelectric ceramics are homogeneous in the plane at right angles to the poling axis, axes 1 and 2 may be located arbitrarily as long as they are at right angles to 3 and to each other. The piezoelectric coefficients are defined in Table XIV-1. There is a multitude of piezoelectric symbols with an abundance of subscripts and superscripts. They provide compact equations, but the implied restrictions are not always clear to the non-expert user. The list in Table XIV-1 is minimal, but adequate, and generally the quantities have intuitive physical meaning.

The g_{31} coefficient of Table XIV-1 warrants further discussion.

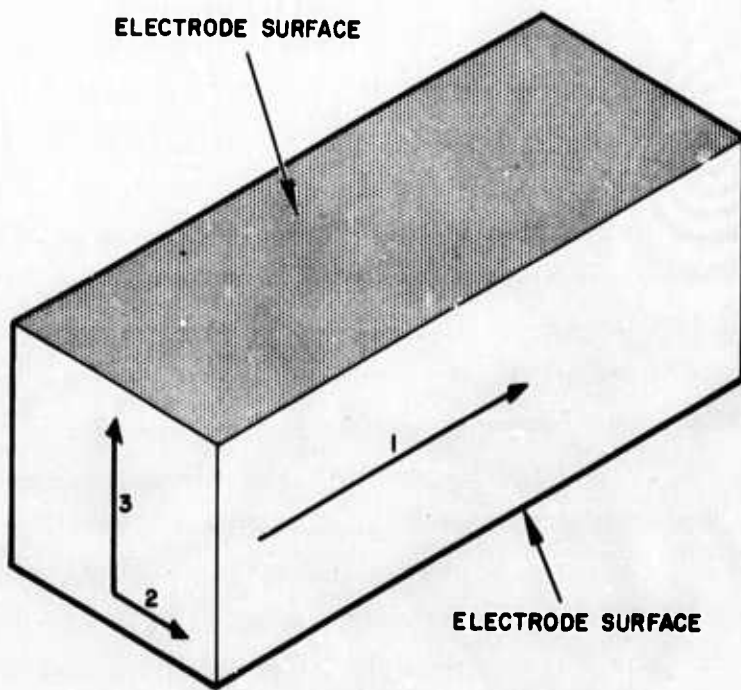
$$g_{31} = \frac{\text{electric field developed}}{\text{applied stress}} \quad (1)$$

or

$$g_{31} = \frac{\text{strain}}{\text{applied charge/electrode area}} \quad (2)$$

That is, an electric field will be developed along the 3-3 axis if a stress is applied along the 1-1 axis. Conversely, if a charge is applied to the electrodes (3-3 axis), the material will be strained along the 1-1 axis.

2075 - 2



3 IS THE POLING DIRECTION
1 AND 2 ARE AT RIGHT ANGLES TO 3 AND
EACH OTHER
1 IS USUALLY THE LONG AXIS

Fig. XIV-4. Axis Definition for Piezo-electric Ceramics.

SECTION XIV

TABLE XIV-1
Piezoelectric Symbol Definition

ϵ_{33}	indicates that all stresses are constant, for example, zero	=	free dielectric constant along the poled axis
ϵ_{11}	indicates that the electrodes are along the 3-3 axis		
Y_{11}	indicates that the modulus is measured with the electrodes shorted	=	short circuit modulus of elasticity (Young's Modulus)
ϵ_{11}	indicates that the stress or strain is along the 1-1 axis		
g_{31}	indicates that the applied stress or piezoelectric induced strain is in the 1-1 direction	=	piezoelectric voltage constant with all stresses, other than the stress involved in the second subscript, are held constant
g_{15}	indicates that the electrodes are along the 3-3 axis		
g_{15}	indicates that the stress or piezoelectric induced strain is in shear form around the 2-2 axis	=	piezoelectric shear stress constant with all stresses, other than the stress involved in the second subscript, are held constant
α_1	indicates that the electrodes are perpendicular to the 1-1 axis		
α_1	= temperature coefficient of linear expansion along the 1-1 axis		
α_3	= temperature coefficient of linear expansion along the 3-3 axis		
ρ	= density in kg/m^3		
ϵ_0	= dielectric constant of free space = $8.85 \times 10^{-12} \text{ F/m}$		

T836

SECTION XIV

2. Output Voltage Equations

If two slabs of poled piezoelectric material are provided with electrodes and rigidly fastened together as shown in Fig. XIV-5(a), they form a bender transducer. The output voltage per unit input moment can be calculated as follows: The reference axes are shown in Fig. XIV-5(b). It is apparent that the upper half of the beam is in tension and the lower half in compression and these strains have mirror-image symmetry. Thus, the output voltage can be calculated for one-half and the result doubled to find the total.

As seen in Fig. XIV-5(b), the stress does not vary along x or y , but only along z . Thus eq. (1) can be written

$$-g_{31} = \frac{\text{average field along } z}{\text{average tension stress in the } l-l \text{ axis}} \quad (3)$$

The tension stress along the $l-l$ axis is

$$\sigma = \frac{12 M_o}{w t^3} z$$

and the average stress across the thickness of one slab $t/2$ is

$$\bar{\sigma} = \frac{3 M_o}{w t^2} \quad (4)$$

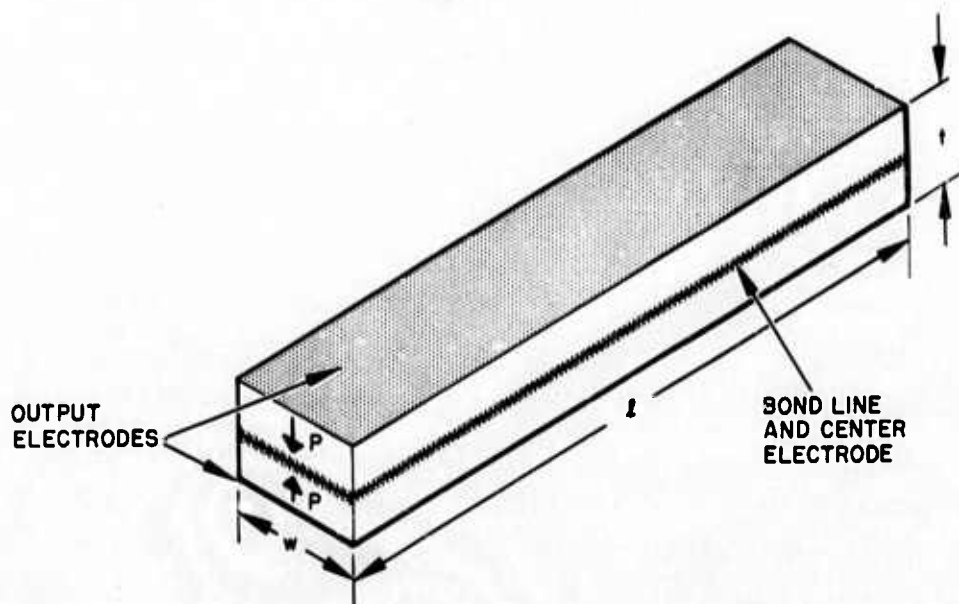
The average field along z is

$$\bar{F} = E/(t/2) \quad (5)$$

From (3), (4) and (5)

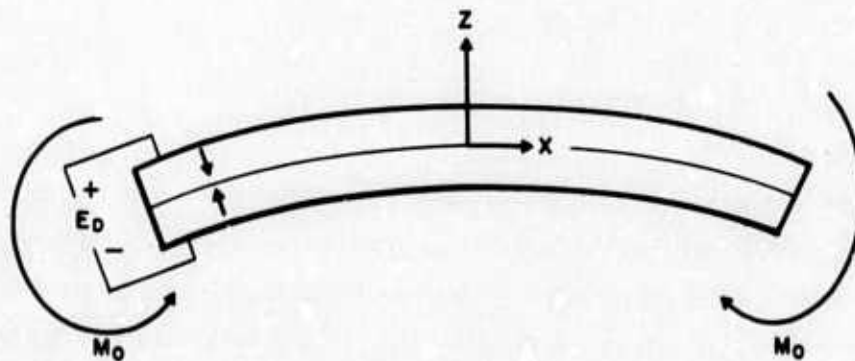
$$E_o = - \frac{3 g_{31} M_o}{2 w t} \text{ for one slab.}$$

2075-3



(a) PIEZOELECTRIC SERIES CONNECTED
BENDER TRANSDUCER

2075-4



(b) BENDING MOMENTS, AXES, AND
OUTPUT VOLTAGE

Fig. XIV-5. Piezoelectric Bender Transducer.

SECTION XIV

For the poling directions shown, the two slabs must be connected in series and the total output voltage for a series connected pure bender is

$$E_o = \frac{3g_{31}M_o}{wt} \quad (6)$$

Since the g_{31} coefficient for these materials is inherently negative, the output voltage will have the polarity shown in Fig. XIV-5(b). In many elementary texts and examples the absolute value for g_{31} is used and the minus sign omitted. This can lead to considerable confusion.

Because each transducer slab is sensitive to tension and compression, it is necessary to evaluate the output due to a longitudinal load. This output voltage sensitivity can be derived by the same method as that used for the bending sensitivity, or it can be found in any of the standard references, and it is

$$e_o = -g_{31} \frac{P}{w} \text{ for tension} \quad (7)$$

where

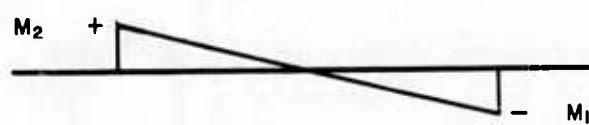
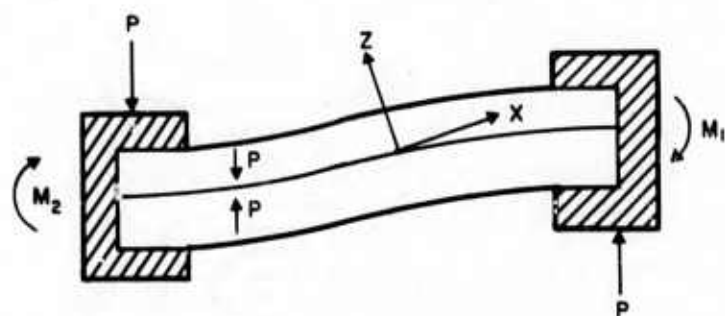
P = force in Newtons

w = width in meters

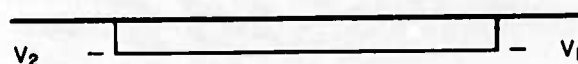
This sensitivity is significant, but note that it is exactly canceled by an equal and opposite voltage from the other slab, because for longitudinal loads both slabs are either in tension or compression. Thus, to first order, the bender transducer is not sensitive to longitudinal loading.

If one end of the clamped transducer is displaced as shown in Fig. XIV-6, it is seen from the diagram that the average moment in the transducer is zero. Because eq. (6) is exact for any element of

2075-5



MOMENT DIAGRAM



SHEAR DIAGRAM

Fig. XIV-6. Moment and Shear Diagram
for One Type of Trans-
ducer Loading.

SECTION XIV

length, it is exact for a differential length. Thus, for the beam as a whole, it represents the average moment over the length of the beam. In view of this, it is concluded that the transducer sensitivity to the type of bending shown in Fig. XIV-6 is zero. However, if M_1 is not exactly equal to M_2 , then the transducer acts as an end-loaded cantilever beam and will have a significant output. This requires careful attention to the transducer standoffs and clamps, which are discussed in a later section.

In addition to the moment, the transducer is also subjected to shear as shown in Fig. XIV-6. From Table XIV-1 it is evident that the voltage due to shear developed on an elemental transducer length will have the form

$$e_{\text{shear}} = K g_{15}$$

The exact equation for transverse shear is

$$e_{\text{shear}} = \frac{P g_{15}}{w} \quad (8)$$

on each slab where P is the shear force. The shear force in the two slabs is constant and equal throughout the active length of the slab. However, due to the opposite poling direction in the two slabs, the induced shear voltages cancel one another. Thus, the shear loading sensitivity is also zero by first-order analysis.

Another possible loading condition of the transducer is shown in Fig. XIV-7. This condition will arise when the sensors are mounted with the spin axis horizontal and the transducer is subjected to the gravity field. In this case, it is not self-evident that the average moment in the transducer is zero, and the moment equation must be written. It is

$$M = \frac{1}{2} w \left(x - \frac{x^2}{l} - \frac{1}{6} l \right)$$

2075-6

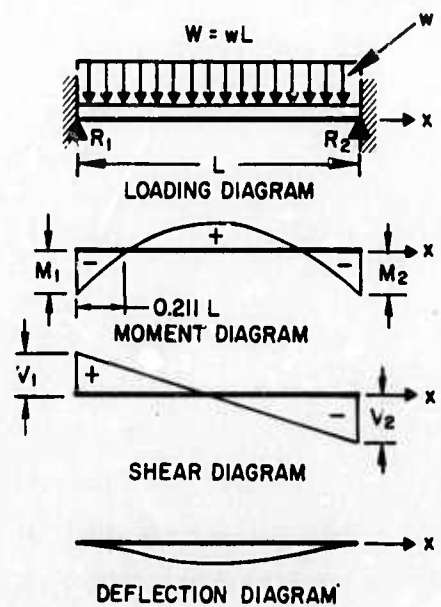


Fig. XIV-7.
Moment and Shear Diagram
for Second Type of Trans-
ducer Loading.

SECTION XIV

where

M = moment at distance x from one end

W = weight of the active section of the transducer

l = active length of the transducer

The average moment is

$$\bar{M} = \frac{W}{2l} \int_0^l \left(x - \frac{x^2}{l} - \frac{1}{6} l \right) dx = \frac{W}{12l} \left[3x^2 - x^3 - lx \right]_0^l = 0$$

Thus, this loading does not introduce an extraneous signal to a first-order estimate.

Finally, it is possible for one clamp to move along the Y direction with respect to the other (in and out of the paper) in Fig. XIV-6. This introduces a stress that is identified as the parallel shear mode and the equations and conditions are exactly the same as for eq. (8).

To a first order, the transducer is not sensitive to extraneous forces, moments, and shear.

3. Equivalent Circuits

It is shown in Refs. XIV-1, -2, and -3 that for low frequency operation piezoelectric transducers can be represented with reasonable accuracy by either of the two equivalent circuits shown in Fig. XIV-8. Some of the important defining relationships are shown on the figure. The symbols used on Fig. XIV-8 are defined in Table XIV-2. The equations are developed as follows.

Piezoelectric transducers have a fundamental coupling coefficient that defines the electrical energy and mechanical energy relationships in the transducer. For the bender transducer, this coefficient will

SECTION XIV

TABLE XIV-2
Symbol Definitions (Fig. XIV-8)

Equivalent Circuit Constants

C_e = Free electrical capacitance
 C'_e = Blocked electrical capacitance
 N = Transducer volts/moment ratio
 N' = Transducer moment/volt ratio
 C_m = Compliance, open circuit condition
 C'_m = Compliance, short circuit condition
 I = Inertia of the transducer

Piezoelectric, Dielectric and Elastic Constants

g_{31} = Piezoelectric constant relating electric field developed to applied stress
 k_b = Bender coupling factor
 Y_{11}^E = Young's modulus, short circuit conditions
 ϵ_{33}^T = Material dielectric constant, free

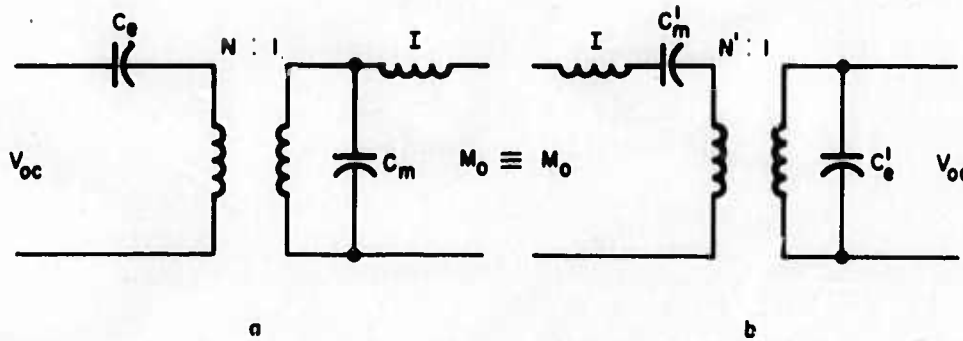
Piezoelectric Energy

U_{es} = Electrical energy stored in the transducer
 U_{ms} = Mechanical energy stored in the transducer
 U_{mi} = Total mechanical energy input to the transducer

T840

SECTION XIV

2075-7



$$V_{oc} = NM_o = \frac{-3g_{31}M_o}{wt}$$

$$N = -\frac{3g_{31}}{wt} = \frac{N'C'_m}{(N')^2C'_m + C'_e}$$

$$N' = \frac{-g_{31}\epsilon_{33}^T Y_{11} E wt}{4}$$

$$N'C'_m = NC_e$$

$$N'C_m = NC'_e$$

$$C'_m = N^2 C_e + C_m = \frac{12\ell}{Y_{11}^E wt^3} = \frac{C_m}{1 - k_b^2}$$

$$C_e = \frac{\epsilon_{33}^T wt\ell}{t} = \frac{C'_e}{1 - k_b^2}$$

$$\frac{1}{C_m} = \frac{1}{C'_m} + \frac{1}{C'_e/(N')^2}$$

$$k_b^2 = NN' = \frac{N^2 C_e}{C'_m} = \frac{(N')^2 C'_m}{C_e} = \frac{N^2 C'_e}{C_m} = \frac{3}{4} g_{31}^2 \epsilon_{33}^T Y_{11} E$$

Fig. XIV-8. Equivalent Circuits for Piezoelectric Bender Transducers with Interrelating Equations.

SECTION XIV

be designated as k_b^2 . The coefficient is defined by (1) for open circuit conditions and a mechanical input.

$$k_b^2 = \frac{\text{Electrical energy stored in the transducer}}{\text{Mechanical energy input to the transducer}} \quad (1)$$

For an electrical input with the transducer free to move the equation becomes

$$k_b^2 = \frac{\text{Mechanical energy stored in the transducer}}{\text{Electrical energy input to the transducer}} \quad (2)$$

$$k_b^2 = \frac{U_{es}}{U_{mi}} = \frac{U_{mi} - U_{ms} - \text{losses}}{U_{mi}} \quad (3)$$

neglecting losses

$$\frac{U_{ms}}{U_{mi}} = 1 - k_b^2 \quad (4)$$

It is apparent that if the electrical output of Fig. XIV-8(b) is short-circuited, all of the transducer energy is stored in the short circuit mechanical compliance, C'_m , for a given input moment. Also, for Fig. XIV-8(a) with the output open and a given input moment, all of the input energy is stored in the open circuit mechanical compliance, C_m .

Since these circuits are fully reciprocal, when viewed from the external terminals, and since the energy store is inversely proportional to the compliances, we can write

$$\frac{U_{ms}}{U_{mi}} = \frac{1/C'_m}{1/C_m} = \frac{C_m}{C'_m} = 1 - k_b^2 \quad (5)$$

SECTION XIV

and

$$C_m = C'_m \cdot 1 - k_b^2 \quad (6)$$

Using the value for N previously derived and the factors defined by the physical constants, all of the relationships of Fig. XIV-8 can be derived.

In the RGG sensor the moment of inertia of the transducer is quite small and is included as a part of the arm inertia. The equivalent piezoelectric transducer equivalent circuit for two series polarized benders connected in parallel and connected to an RGG sensor is shown in Fig. XIV-9. Note the change in use of symbol N in this diagram to reduce the complexity of the working equations.

The Semiannual Technical Report No. 1 demonstrated the method of relating the peak sensor stored energy to the peak electrical stored energy of the transducer. Briefly

$$U_{mp} = \frac{C_{ZZ}}{4} \left(\frac{\eta Q}{\omega_0} \Gamma_{eq} \right)^2 \quad (7)$$

where

U_{mp} = peak mechanical energy stored in the sensor compliances as a whole

η = sensor arm inertia efficiency ratio = 0.861

C_{ZZ} = polar moment of inertia of one arm, $3.561 \times 10^{-3} \text{ kgm}^2$

Q = effective Q of the sensor including load resistor = 300

ω_0 = sensor resonant frequency

Γ_{eq} = equivalent gravity gradient input = 10^{-9} sec^{-2}

2075-8

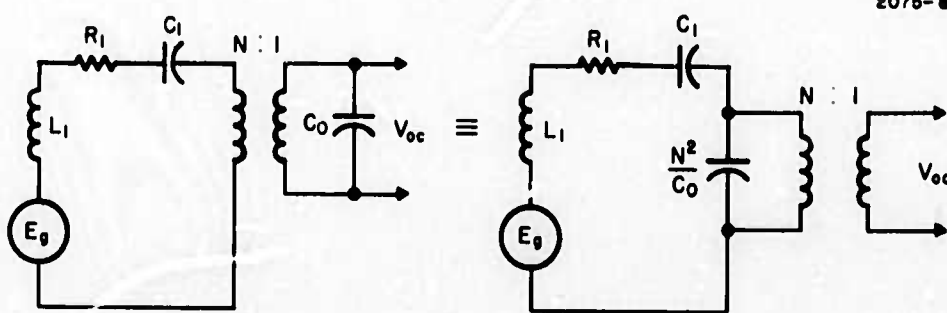


Fig. XIV-9. RGG Sensor Equivalent Circuit.

SECTION XIV

and it was shown that in the present nominal sensor

$$U_{mp} = 1.23 \times 10^{-21} \text{ joules/EU}^2$$

This energy will divide inversely as the pivot compliance, C_p , and the open circuit mechanical compliance of the transducers, $C_m/2$. That is

$$U_{mi} = \frac{U_{mp} C_2}{C_m/2} \quad (8)$$

where

$$C_2 = \text{total system compliance}$$

and

$$\frac{1}{C_2} = \frac{1}{C_p} + \frac{1}{C_m/2} \quad (9)$$

If we let the compliance ratio of eq. (8) be a fixed fraction F , then

$$F = \frac{C_2}{C_m/2} = 0.1333 \quad \text{in one example}$$

This is possible since C_2 is fixed by the relationship

$$\omega_o^2 = \frac{1}{(C_{ZZ}/2 C_2)} = \frac{1}{L_1 C_2} \quad (10)$$

SECTION XIV

and $C_{ZZ}/2$ is fixed by the thermal noise limit.

The peak electrical energy stored in the transducer is

$$U_{es} = U_{mi} k_b^2 = U_{mp} F k_b^2 = \frac{1}{2} C_o (V_{oc})^2 \quad (11)$$

Since

$$C_o = K_1 \frac{wt}{t}$$

$$V_{oc} = K_2 \frac{1}{wt}$$

$$U_{es} = K_3 \frac{l}{wt^3}$$

where the $K_1 \dots K_3$ are constants. Since U_{es} is fixed, then only certain values of C_o and V_{oc} can be used. One procedure used to determine acceptable values of C_o and V_{oc} is to plot the available values of C and V_{oc} for a given U_{es} . Select a desirable combination of these two and calculate the values for ω , l and t that are determined by this combination. If the resulting transducer is poorly proportioned, move to a different combination of C_o and V_{oc} that will alter the proportions in a favorable direction. This is repeated until a satisfactory combination of parameters is obtained.

4. Transducer Computer Program

The relationships of the previous section can be applied in a different manner. Select reasonable values for w , l and t for the individual transducers and then calculate, C_o , $C_m/2$, $C'_m/2$, N , F and C_p . If these values are satisfactory the designer can then calculate the pivot dimensions. If not, the transducer dimensions must be

SECTION XIV

adjusted within the constraints described in the preceding paragraphs and new calculations made.

Once satisfactory transducer dimensions have been established, the designer can calculate the pivot dimensions by the method described in the Semiannual Technical Report No. 1. Note that the pivot dimensions can be calculated as long as some compliance ratio is established between the end pivots and the differential pivots. Also a length-to-diameter ratio must be established for each type of pivot. The simplest preliminary assumption is to assume that all pivots have equal compliance and a length-to-diameter ratio of one.

All of the terms relating to the transducers and pivots have been combined into the simple computer program shown in Fig. XIV-10. This program uses the basic piezoelectric material characteristics, assumed transducer dimensions and pivot material shear modulus. The program calculates all of the transducer parameters and the pivot dimensions. The calculated parameters are then used in the sensor computer program previously given to calculate the sensor frequency, signal level, and phase response of the sensor as a whole.

5. Transducer Specification

Two identical series polarized piezoelectric bender transducers will be used on each RGG sensor. The dimensions of each transducer are shown in Fig. XIV-11. The outputs of the two transducers will be connected in parallel. These dimensions, with the material characteristics, provide the transducer characteristics that have been used in the previous paragraphs of this section.

The transducers will be operated in an evacuated chamber ($\sim 10^{-3}$ mm Hg) at a temperature of $55 \pm 0.01^\circ\text{C}$. The set point (55°C) may differ by $\pm 5^\circ\text{C}$ in the final device, but the temperature excursions will be maintained to $\pm 0.01^\circ\text{C}$ or better. In the nonoperating condition, the transducers will be subjected to temperatures between 5 and 70°C .

The piezoelectric material characteristics and the characteristics of the fabricated bender are shown in Table XIV-3. The material

```

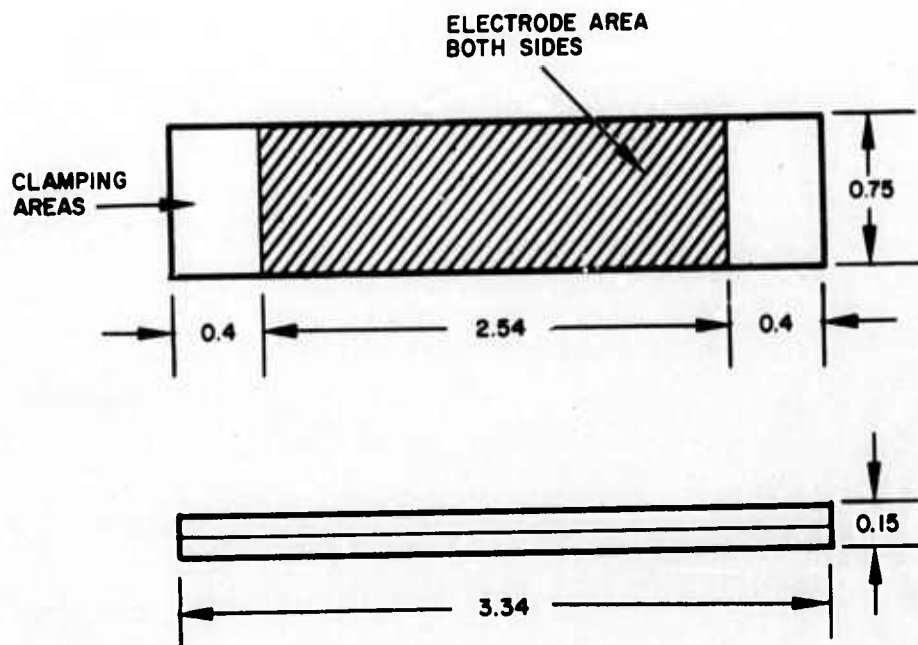
100 REM " PROGRAM NAME XTD-1"
110 REM "
120 REM
130 REM THIS PROGRAM CALCULATES THE PIEZO XDR COEFFICIENTS
140 REM OF TWO SERIES POLARIZED PURE BENDER BIMORPHS
150 REM CONNECTED IN PARALLEL. IT ALSO CALCULATES PIVOT L AND D.
160 REM W3 = WIDTH OF XDR IN METERS
170 REM L3 = ACTIVE LENGTH OF XDR IN METERS
180 REM T3 = XDR THICKNESS IN METERS
190 REM E3 = XDR FREE DIELECTRIC CONSTANT
200 REM G3 = XDR VOLTAGE TRANSFORMATION CONSTANT
210 REM Y3 = XDR MODULUS OF ELASTICITY - SHORT CIRCUIT CONDITIONS
220 REM C0 = OUTPUT CAPACITY OF PARALLEL XDRS
230 REM C1 = MECHANICAL COMPLIANCE OF SYSTEM ( $1/C1 = 1/CP + 1/C3$ )
240 REM C2 = TOTAL COMPLIANCE OF SENSOR AND XDR TRANSF. TO MECH. SIDE
250 REM C3 = MECHANICAL COMPLIANCE OF THE TWO XDRS
260 REM C9 = CP = MECHANICAL COMPLIANCE OF ALL PIVOTS IN DIFF. MODE
270 REM W0 = UNDAMPED NATURAL FREQUENCY OF SENSOR, 220 RAD/SEC
280 REM L1 = 1/2 MOMENT OF INERTIA OF ONE ARM ,
290 REM G9 = SHEAR MODULUS OF PIVOTS, 4.5 E+10 FOR BE-CU.
300 REM L9 = PIVOT LENGTH = PIVOT DIAMETER, METERS
310 REM D9 = PIVOT DIAMETER IN INCHES
320 REM F3 = FRACTION PEAK SENSOR ENERGY STORED IN XDR
330 REM F9 = FRACTION OF PEAK SENSOR ENERGY STORED IN PIVOTS
340 LET W3 = 7.5E-3
350 LET L3 = 2.54E-2
360 LET T3 = 1.5E-3
370 LET E3 = 1.5035E-8
380 LET G3 = -11E-3
390 LET Y3 = 6.3E10
400 LET G9 = 4.5 E+10
410 LET W0 = 220
420 LET L1 = 1.78201816 E-3
430 LET C0 = 2*E3*W3*L3/T3*(1-3*G3+2*E3*Y3/4)
440 LET C2 = 1 / W0*2 / L1
450 LET N = -0.5 * G3 * E3 * Y3 * W3 * T3
460 LET C1 = C0 * C2 / ( C0 - C2 * N+2 )
470 LET C3 = 6*L3/Y3/W3/T3+3
480 LET C9 = C1 * C3 / ( C3 - C1 )
490 LET F3 = 1 - C2 / C9
500 LET F9 = C2 / C9
510 LET L9 = ( 16 / 3 / 3.14159 / G9 / C9 ) +(1/3)
520 LET D9 = L9 / 2.54 E-2
530 PRINT "C0 = " C0, "C1 = " C1
540 PRINT "C2 = " C2, "C3 = " C3
550 PRINT "C9 = " C9
560 PRINT "N = " N, "F3 = " F3
570 PRINT "W0 = " W0, "L9 = " L9
580 PRINT "D9 = " D9
590 END

C0 = 3.49062 E-9          C1 = 1.17281 E-2
C2 = 1.15942 E-2          C3 = 9.55673 E-2
C9 = 1.33687 E-2
N = 5.86083 E-5
W0 = 220
D9 = 5.56351 E-2          F3 = .132729
                           L9 = 1.41313 E-3

```

Fig. XIV-10. Piezoelectric Transducer Computations.

2075-9



ALL DIMENSION IN CENTIMETERS

Fig. XIV-11. Piezoelectric Bender Transducer,
Series Polarized.

SECTION XIV

TABLE XIV-3
Piezoelectric Material Characteristics

Characteristics*	Variation with Temperature PPM/ $^{\circ}$ C at 55 $^{\circ}$ C
$\epsilon_{33}^T = 1.5035 \times 10^{-8} \pm 10\%$	$+3215 \pm 10\%$
$g_{31} = 11.00 \times 10^{-3} \pm 10\%$	$-1930 \pm 10\%$
$Y_{11}^E = 6.3 \times 10^{10} \pm 10\%$	$+643 \pm 10\%$
$\rho = 7.3 \times 10^3 \pm 5\%$	
α_1	$+1.4 \pm 20\%$
α_3	$+4.0 \pm 20\%$
$Q_{mech} = 80 \pm 20\%$	
Volume resistivity $> 10^{11}$ ohm m	
<small>* Characteristics at 25$^{\circ}$C after 1000 hr storage at 55$^{\circ}$C. Alternatively these may be specified at 55$^{\circ}$C.</small>	

T841

is of a type known as lead-zirconate-titanate, but the exact composition is unknown. One material of this type is known as PZT-5A, a trademark of Vernitron Piezoelectric Division. The detailed characteristics of PZT-5A are well documented in Vernitron (formerly Clevite) specification sheets and in the Ref. XIV-5.

Extreme values of dielectric constant, electromechanical coupling coefficient, mechanical Q, and modulus of elasticity are not required. These coefficients may vary slowly with age since we expect

SECTION XIV

to recalibrate the sensor as a whole every 10 to 100 hours. However, the smaller the coefficient variation with time the easier it will be to use the sensor.

After the transducers are received by Hughes they will be oven-aged at 55°C in a stress-free, short circuit condition for 5 weeks prior to installation in the sensor. Applied voltages during testing will never exceed 100 V/cm.

It is shown in Section XIV-D that the variations with temperature allowed in the table, the transducer variations, have little influence on the temperature sensitivity of the sensor as a whole.

SECTION XIV

D. SENSOR THERMAL SENSITIVITY

It was shown in Section XIV-A that the output voltage of the sensor-transducer system was

$$|E_o| = \frac{\eta \Gamma_{eq}}{(R^2 + I^2)^{1/2}} = \frac{\eta \Gamma_{eq}}{Z} \quad (1)$$

and the phase was

$$\phi = \tan^{-1}(-I/R) \quad (2)$$

when the rotation frequency was ω . In equations (1) and (2)

$$R(\omega) = \frac{N}{L_1} + \frac{1}{N} \left[\frac{R_1}{R_o L_1} + \frac{C_o}{C_1 L_1} - C_o \omega^2 \right] \quad (3)$$

$$I(\omega) = \frac{\omega}{N} \left[\frac{R_1 C_o}{L_1} + \frac{1}{R_o} - \frac{1}{R_o L_1 C_1 \omega^2} \right] \quad (4)$$

Taking the derivatives of (3) and (4) with respect to I and R for constant ω , we have

$$d|E_o| = -\eta \Gamma_{eq} \left[\frac{R dR + I dI}{Z^{3/2}} \right] \quad (5)$$

and

$$d\phi = \frac{IdR - RIdI}{Z^2} \quad (6)$$

SECTION XIV

From (2)

$$\cos \phi = \frac{R}{Z} \text{ and } \sin \phi = \frac{-I}{Z}$$

Equation (5) can then be written as (7)

$$d|E_o| = -E_o \left[\frac{dR \cos \phi - dI \sin \phi}{Z} \right] \quad (7)$$

and multiplying (6) by (1) we have

$$|E_o| d\phi = -E_o \left[\frac{dI \cos \phi + dR \sin \phi}{Z} \right] \quad (8)$$

Since the sensor will be operated at an ω such that ϕ is almost exactly $\pi/2$, we can evaluate (7) and (8) at this point. Any small deviations in the operating frequency and thus small changes in ϕ from this value will not materially affect the analysis. Thus

$$d|E_o| = E_o \frac{dI}{Z} \quad (9)$$

$$|E_o| d\phi = -E_o \frac{dR}{Z} \quad (10)$$

Since these represent the trace (cos) and cross trace (sin) gradient error terms, we can write directly

$$\frac{d\Gamma_c}{|2\Gamma_{ij}|} = \frac{dI}{Z} \quad (11)$$

SECTION XIV

$$\frac{d\Gamma_s}{|2\Gamma_{ij}|} = -\frac{dR}{Z} \quad (12)$$

To find the temperature induced gradient error sensitivity, the partial derivatives of all the temperature-sensitive parameters for $R(\omega)$ and $I(\omega)$ must be evaluated for constant ω . Since every parameter is temperature-sensitive to some extent they will all be evaluated. Also, since there are going to be many partials they will be assigned alphanumeric symbols where possible. Taking R first,

$$A_1 = \frac{\partial R}{\partial L_1} = \left[\frac{-1}{L_1^2} \right] \left[N + \frac{1}{N} \left(\frac{R_1}{R_o} + \frac{C_o}{C_1} \right) \right]$$

$$A_2 = \frac{\partial R}{\partial C_o} = \frac{1}{N} \left(\frac{1}{C_1 L_1} - \omega^2 \right)$$

$$A_3 = \frac{\partial R}{\partial N} = \frac{1}{L_1} - \frac{1}{N^2} \left[\frac{R_1}{R_o L_1} + \frac{C_o}{C_1 L_1} - C_o \omega^2 \right]$$

$$A_4 = \frac{\partial R}{\partial R_1} = \frac{1}{N R_o L_1}$$

$$A_5 = \frac{\partial R}{\partial R_o} = \frac{-R_1}{N R_o^2 L_1}$$

$$A_6 = \frac{\partial R}{\partial \left(\frac{1}{C_1} \right)} = \frac{C_o}{N L_1}$$

SECTION XIV

Taking the partials of I,

$$B_1 = \frac{\partial I}{\partial L_1} = -\frac{1}{L_1^2} \left(\frac{\omega}{N} \right) \left(R_1 C_o - \frac{1}{R_o C_1 \omega^2} \right)$$

$$B_2 = \frac{\partial I}{\partial C_o} = \frac{\omega R_1}{N L_1}$$

$$B_3 = \frac{\partial I}{\partial N} = -\frac{\omega}{N^2} \left[\frac{R_1 C_o}{L_1} + \frac{1}{R_o} - \frac{1}{R_o L_1 C_1 \omega^2} \right]$$

$$B_4 = \frac{\partial I}{\partial R_1} = \frac{\omega C_o}{N L_1}$$

$$B_5 = \frac{\partial I}{\partial R_o} = -\frac{\omega}{N R_o^2} \left[1 - \frac{1}{L_1 C_1 \omega^2} \right]$$

$$B_6 = \frac{\partial I}{\partial \left(\frac{1}{C_1} \right)} = -\frac{1}{N R_o L_1 \omega}$$

We can now write the error derivatives due to the derivatives of the parameters

$$\frac{d\Gamma_c}{|2\Gamma_{ij}|} = \frac{1}{Z} \left[B_1 dL_1 + B_2 dC_o + B_3 dN + B_4 dR_1 + B_5 dR_o + B_6 d\left(\frac{1}{C_1}\right) \right] \quad (13)$$

SECTION XIV

$$\frac{d\Gamma_s}{|2\Gamma_{ij}|} = \frac{-1}{Z} \left[A_1 dL_1 + A_2 dC_o + A_3 dN + A_4 dR_1 + A_5 dR_o + A_6 d\left(\frac{1}{C_1}\right) \right] \quad (14)$$

The temperature partials of the parameter derivatives must now be evaluated at their operating temperature. The temperature differentials may not be the same for all of the elements so provision will be made to account for this

$$dL_1 = \frac{\partial L_1}{\partial T_1} dT_1 \quad (15)$$

$$dC_o = \frac{\partial C_o}{\partial T_2} dT_2 \quad (16)$$

$$dN = \frac{\partial N}{\partial T_2} dT_2 \quad (17)$$

$$dR_1 = \frac{\partial R_1}{\partial T_3} dT_3 \quad (18)$$

$$dR_o = \frac{\partial R_o}{\partial T_4} dT_4 \quad (19)$$

$$d\left(\frac{1}{C_1}\right) = \frac{\partial\left(\frac{1}{C_p}\right)}{\partial T_5} dT_5 + \frac{\partial\left(\frac{1}{C_m}\right)}{\partial T_2} dT_2 \quad (20)$$

SECTION XIV

In the above equations the referred temperature differentials are as follows:

dT_1 - arms

dT_2 - transducer

dT_3 - arm-pivot loss term

dT_4 - preamplifier

dT_5 - pivots

The individual temperature partials are evaluated as follows:

L_1 is of the form

$$L_1 = \frac{1}{2} mk^2 \quad (21)$$

where

m = mass of the arm

k = radius of gyration, a linear function of temperature

$$\frac{\partial L_1}{\partial T_1} = \frac{m}{2} (2k) \frac{\partial k}{\partial T_1} \quad (22)$$

The linear temperature expansion coefficient of the arm is α_a and α_a is defined

$$\frac{\left(\frac{\partial k}{k}\right)}{\partial T} \triangleq \alpha_a \quad (23)$$

SECTION XIV

or

$$\frac{\partial k}{\partial T} = k \alpha_a \quad (24)$$

and

$$\frac{\partial L_1}{\partial T_1} = m k^2 \alpha_a = 2 L_1 \alpha_a \quad (25)$$

$$\therefore dL_1 = 2 L_1 \alpha_a dT_1 \quad (26)$$

The temperature-sensitive partials of C_o are quite complex unless a simplifying assumption is made. The equation for C_o can be written as shown in previous sections

$$C_o = \frac{2 \epsilon_{33}^\tau w \ell}{t} \left(1 - k_b^2 \right) \quad (27)$$

The k_b^2 term is small and does not vary greatly with temperature. In addition the dC_o terms are small as can be seen on the computer print-out (Fig. XIV-12). Therefore, it is satisfactory to assume k_b^2 is constant in this particular case. Following the same procedure used to evaluate dL_1 , we have for dC_o

$$dC_o = C_o \left[\alpha_w + \alpha_\ell - \alpha_t + \left(\frac{\partial \epsilon_{33}^\tau}{\epsilon_{33}^\tau} \right) / \partial T_2 \right] dT_2 \quad (28)$$

PAR-I

```
100 REM " PROGRAM NAME PAR-I "
110 REM "
120 REM -----
130 REM THIS PROGRAM CALCULATES THE GRAVITY GRADIENT ERRORS IN
140 REM THE SIN AND COS CHANNELS DUE TO THE THERMAL SENSITIVITY
150 REM OF THE SENSOR AND TRANSDUCER.
160 REM THIS PROGRAM ASSUMES A HORIZONTAL SPIN AXIS SENSOR AND
170 REM 2 GAMMA SUB IJ = 4500 EU.
180 REM -----
190 REM G4 = THERM. PARTIAL OF XDR G31
200 REM E4 = THERM. PARTIAL OF XDR E33 SUPER T
210 REM Y4 = THERM. PARTIAL OF XDR YII SUPER E
220 REM P2 = THERM. PARTIAL OF XDR ALPHA, THICKNESS
230 REM P3 = THERM. PARTIAL OF XDR ALPHA, WIDTH
240 REM P4 = THERM. PARTIAL OF XDR ALPHA, LENGTH
250 REM P1 = THERM. PARTIAL OF ARMS, ALPHA, LENGTH AND WIDTH
260 REM P5 = THERM. PARTIAL OF PIVOTS, ALPHA, LENGTH AND WIDTH
270 REM P6 = THERM. PARTIAL OF BRACE, ALPHA, LENGTH AND WIDTH
280 REM G1 = THERM. PARTIAL OF PIVOT SHEAR MODULUS
290 REM R2 = THERM. PARTIAL OF R1, ARM MECH. DAMPING
300 REM R5 = THERM. PARTIAL OF R0, OUTPUT LOAD RESISTOR
310 REM ALL THERM. PARTIALS G4,E4-----R5, ARE IN PPM /DEG C
320 REM T1 = DELTA TEMP. CHANGE OF ARMS, DEG C
330 REM T2 = DELTA TEMP. CHANGE OF XDR, DEG C
340 REM T6 = DELTA TEMP. CHANGE OF R1, DEG C
350 REM T4 = DELTA TEMP. CHANGE OF R0, DEG C
360 REM T5 = DELTA TEMP. CHANGE OF PIVOTS, DEG C
370 REM -----
380 REM
390 REM ARMS - 6061 ALUMINUM
400 REM Y = 6.8 E+10
410 REM ALPHA = 23.4
420 REM
430 REM PIVOTS - BERYLLIUM COPPER
440 REM G9 = 4.5 E+10
450 REM ALPHA = P5 = +16.6
460 REM G1 = -330
470 REM
480 REM BRACE FOR PIVOT BRACE PLATE - 6061 ALUMINUM
490 REM Y = 6.8 E+10
500 REM ALPHA = -23.4
510 REM
520 REM TRANSDUCER - PZT 5-A AT 55 DEG C
530 REM "PIEZOELECTRIC TRANSDUCER MATERIALS"
540 REM JAFFE AND BERLINGOURT
550 REM IEEE, VOL 53, NO 10, (OCT 1965), 1372-1386
560 REM
570 REM G31 = G3 = -9.5 E-3
580 REM YII SUPER E = Y3 = 6.17016 E+10
590 REM E33 SUPER T = E3 = 1.6815 E-8
```

Fig. XIV-12. Computer Program to Evaluate RGG Sensor Temperature Sensitivity.

PART-I CONTINUED

```

600 REM
610 REM
620 REM
630 REM
640 REM G5 = SIN CHANNEL GRAV. GRAD. IN EU ( PHASE ERROR )
650 REM G6 = COS CHANNEL GRAV. GRAD. IN EU ( AMPLITUDE ERROR )
660 REM G3 = -9.5 E-3
670 REM E3 = 1.6815 E-8
680 REM Y3 = 6.17016 E 10
690 REM G9 = PIVOT SHEAR MODULUS, 4.5 E+10 BERYLLIUM COPPER
700 REM ALL DATA AND COEFFICIENTS MUST BE AT THE
710 REM OPERATING TEMPERATURE = 326K = 53C = 127.6 F
720 REM DATA: T1, T2, T6, T4, T5, MUST BE IN THIS ORDER,
730 REM IN DEG C, AND MUST CARRY CORRELATED SIGNS.
740 DATA +.001, +.001, +.001, +.001, +.001
750 READ T1, T2, T6, T4, T5
760 LET G4 = -1.9289 E 3
770 LET E4 = 3214.8
780 LET Y4 = +643
790 LET P2 = +4
800 LET P3 = +1.4
810 LET P4 = +1.4
820 LET P1 = +20
830 LET P5 = + 16.6
840 LET P6 = + 23.4
850 LET G1 = -330
860 LET R2 = +50
870 LET R5 = + 40
880 LET C0 = 3.49 E-9
890 LET C1 = 1.1730459 E-2
900 LET L1 = 1.78201816 E-3
910 LET R0 = 9.55 E+6
920 LET R1 = 6.1165552 E-4
930 LET N = 5.912 E-5
940 LET W = 219.98
950 LET R = N/L1 + 1/N*( R1/R0/L1 + C0/C1/L1 - C0*W*2 )
960 LET I = W/N * ( R1*C0/L1 + 1/R0 - 1/R0/L1/C1/W*2 )
970 LET Z = ( R*2 + I*2 )^.5
980 LET C3 = 9.55673 E-2
990 LET C9 = C1 * C3 / ( C3 - C1 )
1000 LET Z2 = 4500 E-6 / Z
1010 LET A1 = -1/L1*2 * ( N + ( R1/R0 + C0/C1 )/N )
1020 LET A2 = ( I/C1/L1-W*2 )/N
1030 LET A3 = 1/L1 - ( R1/R0/L1 + C0/C1/L1 - C0 * W*2 )/N*2
1040 LET A4 = 1/N/R0/L1
1050 LET A5 = -R1/N/R0*2/L1
1060 LET A6 = C0 / N / L1
1070 PRINT " R = " R
1080 PRINT " I = " I
1090 PRINT " Z = " Z

```

Fig. XIV-12. Continued.

PART-I CONTINUED

```
1100 PRINT
1110 PRINT
1120 LET B1 = -1/L1*2*W/N*(R1*C0-1/R0/C1/W+2)
1130 LET B2 = W*R1/N/L1
1140 LET B3 = -W/N*2*(R1*C0/L1 +1/R0-1/R0/L1/C1/W+2)
1150 LET B4 = W*C0/N/L1
1160 LET B5 = -W/N/R0*2*(1-1/L1/C1/W+2)
1170 LET B6 = -1/N/R0/L1/W
1180 LET K1 = Z2 * A1 * L1 * T1
1190 LET K2 = Z2 * A2 * C0 * T2
1200 LET K3 = Z2 * A3 * N * T2
1210 LET K4 = Z2 * A4 * R1 * T6
1220 LET K5 = Z2 * A5 * R0 * T4
1230 LET K6 = Z2 * A6 / C9 * T5
1240 LET K7 = Z2 * A6 / C3 * T2
1250 LET M1 = Z2 * B1 * L1 * T1
1260 LET M2 = Z2 * B2 * C0 * T2
1270 LET M3 = Z2 * B3 * N * T2
1280 LET M4 = Z2 * B4 * R1 * T6
1290 LET M5 = Z2 * B5 * R0 * T4
1300 LET M6 = Z2 * B6 / C9 * T5
1310 LET M7 = Z2 * B6 / C3 * T2
1320 PRINT "K1 = " K1, "K2 = " K2
1330 PRINT "K3 = " K3, "K4 = " K4
1340 PRINT "K5 = " K5, "K6 = " K6
1350 PRINT "K7 = " K7
1360 PRINT
1370 PRINT "M1 = " M1, "M2 = " M2
1380 PRINT "M3 = " M3, "M4 = " M4
1390 PRINT "M5 = " M5, "M6 = " M6
1400 PRINT "M7 = " M7
1410 LET G3 = K1*2*P1 + K2*(P3+P4-P2+E4) + K3*(P3+P4+G4+Y4) + K4*R2
1420 LET G3 = G3 + K5*R5 + K6*(6*(P5-P6)+3*P5+G1) + K7*(P3+P2-P4+Y4)
1430 LET G6 = M1*2*P1 + M2*(P3+P4-P2+E4) + M3*(P3+P4+G4+E4+Y4) + M4*R2
1440 LET G6 = G6 + M5*R5 + M6*(6*(P5-P6)+3*P5+G1) + M7*(P3+P2-P4+Y4)
1450 PRINT
1460 PRINT "G5 = " G5
1470 PRINT
1480 PRINT "G6 = " G6
1490 END
```

Fig. XIV-12. Continued.

RUN

PAR-I 14:44 MON. 01/29/73

R = 1.12607 E-3
I = 8.91151 E-3
Z = 8.98238 E-3

K1 = -1.43169 E-3
K3 = 3.26768 E-5
K5 = -3.04564 E-7
K7 = 1.73656 E-4

K2 = -1.63609 E-5
K4 = 3.04564 E-7
K6 = 1.24111 E-3

M1 = 1.90730 E-4
M3 = -4.46450 E-6
M5 = -2.23149 E-6
M7 = -2.36853 E-5

M2 = 2.23301 E-6
M4 = 2.23301 E-6
M6 = -1.69277 E-4

G5 = -.437811
G6 = 4.52171 E-2

TIME: 3 SECS.

Fig. XIV-12. Continued.

SECTION XIV

where:

α_w — linear temperature coefficient of expansion of the transducer width

α_l — linear temperature coefficient of expansion of the transducer length

α_t — linear temperature coefficient of expansion of the transducer thickness

$\left(\frac{\partial \epsilon_{33}^T}{\epsilon_{33}^T} \right) / \partial T_2$ — temperature coefficient of the transducer dielectric constant

The above coefficients are tabulated in the transducer specification.

The equation for N, the transducer transformation ratio is

$$N = -\frac{1}{2} g_{31} \epsilon_{33}^T Y_{11}^E w t \quad (29)$$

The temperature sensitivity of its differential at the transducer temperature T_2 is

$$\begin{aligned} dN = N & \left[\alpha_w + \alpha_t + \left(\frac{\partial g_{31}}{g_{31}} \right) / \partial T_2 + \left(\frac{\partial \epsilon_{33}^T}{\epsilon_{33}^T} \right) / \partial T_2 \right. \\ & \left. + \left(\frac{\partial Y_{11}^E}{Y_{11}^E} \right) / \partial T_2 \right] dT_2 \end{aligned} \quad (30)$$

Where α_w and α_t are as previously defined and the coefficient partials are from the transducer specification.

SECTION XIV

The temperature sensitivity of R_1 , the internal mechanical damping of the sensor is simply the partial

$$dR_1 = R_1 \left[\left(\frac{\partial R_1}{\partial T_3} \right) / \partial T_3 \right] dT_3 \quad (31)$$

It is estimated that this will be +50 parts per million per $^{\circ}\text{C}$.

The external load resistor will be selected for low temperature coefficient, approximately +10 ppm/ $^{\circ}\text{C}$ and its partial will be

$$dR_o = R_o \left[\left(\frac{\partial R_o}{\partial T_4} \right) / \partial T_4 \right] dT_4 \quad (32)$$

The compliance derivative is made up of two parts as shown in (33)

$$d\left(\frac{1}{C_1}\right) = d\left(\frac{1}{C_p}\right) + d\left(\frac{2}{C_m}\right) \quad (33)$$

The pivot compliance, C_p , will be treated first. The defining equation for cylindrical rods in torsion is

$$\frac{1}{C_p} = \frac{3\pi D^4 G}{16l_p} = K_p \quad (34)$$

The factor of 3 appears in this equation because six identical pivots make up the total pivot system as shown in the Semiannual Technical Report No. 1. The equation is written in terms of D and l_p for the individual pivots.

SECTION XIV

Taking the stiffness partials

$$dK_p = \frac{\partial K_p}{\partial D} dD + \frac{\partial K_p}{\partial l_p} dl_p + \frac{\partial K_p}{\partial G} dG \quad (35)$$

and

$$dK_p = \frac{4K_p dD}{D} - \frac{K_p dl_p}{l_p} + \frac{K_p dG}{G} \quad (36)$$

The derivatives of D and l_p are sensitive to temperature due to two effects. First, they have their normal coefficient of linear expansion and second, they may be compressed or stretched by the pivot-arm mounting structure. In the sensor the pivots are supported and restrained by the central plate and the end plate (brace plate), which in turn are held together by the braces. If the braces have a lower thermal coefficient of expansion than the pivots, then the pivots will be compressed and shortened, and through Poisson's ratio their diameter will be increased. It can be shown that for a simple structure with one member tending to compress the other the compressive force developed is

$$F_p = \frac{(\alpha_b - \alpha_p) \Delta T}{\left(\frac{1}{A_b E_b} + \frac{1}{A_p E_p} \right)} \quad (37)$$

where

F_p = compression force developed on the pivot

α_b = temperature coefficient of linear expansion of the brace

α_p = temperature coefficient of linear expansion of the pivot

SECTION XIV

A_b, A_p = area of the brace and pivot respectively

Y_b, Y_p = Young's modulus of the brace and pivot respectively.

The total elongation (contraction) of the pivot structure in this case is found from

$$F_p = Y_p A_p \frac{e}{l_b} \quad (38)$$

and

$$e = \frac{F_p l_p}{Y_p A_p} = \frac{(\alpha_b - \alpha_p) l_b \Delta T}{\left(1 + \frac{Y_p A_p}{Y_b A_b}\right)} \quad (39)$$

or

$$de = d\ell_p = \frac{(\alpha_b - \alpha_p) l_b dT}{\left(1 + \frac{Y_p A_p}{Y_b A_b}\right)} \quad (40)$$

In eqs. (38) to (40) it is assumed that the active length of the pivots, ℓ_p , is relatively small compared to the length of the brace. It is further assumed that the active pivot area is so small that all of the pivot compression takes place within the active pivot. There are 3 pivots associated with each brace length. Therefore the compression of each individual pivot is

$$d\ell_p = \frac{1}{3} \frac{(\alpha_b - \alpha_p) l_b}{\left(1 + \frac{Y_p A_p}{Y_b A_b}\right)} dT \quad (41)$$

SECTION XIV

and the diameter of each individual pivot is increased due to Poisson's ratio by

$$dD = -\sigma d\ell_p \quad (42)$$

The total differential for D including both the force and the direct temperature effect is

$$dD = \frac{\partial D}{\partial T} dT = \left[\frac{(\alpha_p - \alpha_b) \ell_b \sigma}{3 \left(1 + \frac{Y_p A_p}{Y_b A_b} \right)} + \alpha_p D \right] dT \quad (43)$$

Similarly, for the pivot length

$$d\ell_p = \frac{\partial \ell_p}{\partial T} dT = \left[\frac{(\alpha_b - \alpha_p) \ell_b}{3 \left(1 + \frac{Y_p A_p}{Y_b A_b} \right)} + \alpha_p \ell_p \right] dT \quad (44)$$

Combining the appropriate terms and remembering that $\ell_p = D$, we have

$$d\left(\frac{1}{C_p}\right) = \left[\frac{(\alpha_p - \alpha_b)(1 + 4\sigma)\ell_b}{3 \left(1 + \frac{Y_p A_p}{Y_b A_p} \right) D} + 3\alpha_p + \left(\frac{\partial G}{G} \right) / \partial T \right] dT_5 \quad (45)$$

SECTION XIV

Since the pivot area will be quite small compared to the area of the brace and since $l_b/D \sim 9$, eq. (44) can be approximated

$$d\left(\frac{1}{C_p}\right) = \left(6(\alpha_p - \alpha_b) + 3\alpha_p + \left(\frac{\partial G}{G}\right)/\partial T\right) dT \quad (46)$$

Where

$$\left(\frac{\partial G}{G}\right)/\partial T_6 = \text{temperature coefficient of pivot shear modulus}$$

For the $2/C_m^1$ term we have

$$\frac{2}{C_m^1} = \frac{Y_{11}^E \text{wt}}{6l} \quad (47)$$

for the two transducers, again taking the partials and remembering that this is a transducer term at a temperature T_2

$$d\left(\frac{2}{C_m^1}\right) = \frac{2}{C_m^1} \left(\alpha_w + \alpha_t - \alpha_l + \left(\frac{\partial Y_{11}^E}{Y_{11}^E}\right)/\partial T_2 \right) dT_2 \quad (48)$$

The evaluation of the final temperature sensitivity is done best in a simple computer program PAR-1, shown in Figure XIV-12. The computer can not handle all of the subscripts and super scripts, so alphanumeric symbols are assigned as shown in Table XIV-4. These symbols are consistent with the other two computer programs shown in this section, and all of the programs can be merged into a single program and run as a unit.

SECTION XIV

TABLE XIV-4

Conventional Symbols, Computer Symbols, and Definitions

C_0	$= C_0$	blocked output capacitance of two transducers in parallel
w	$= W_3$	width of each transducer
l	$= L_3$	active length of each transducer
t	$= T_3$	total thickness of each transducer
$C_m^1/2$	$= C_3$	compliance of two transducers, short circuit
N	$= N$	model transformation ratio
g_{31}	$= G_3$	transducer field to stress piezoelectric constant
$\left(\frac{\partial g_{31}}{g_{31}}\right) \Big/ \partial T_2$	$= G_4$	thermal sensitivity of g_{31}
ϵ_{33}^T	$= E_3$	free dielectric constant of transducer
$\left(\frac{\partial \epsilon_{33}^T}{\epsilon_{33}^T}\right) \Big/ \partial T_2$	$= E_4$	thermal sensitivity of ϵ_{33}^T
Y_{11}^E	$= Y_3$	modulus of elasticity of transducer
$\left(\frac{\partial Y_{11}^E}{Y_{11}^E}\right) \Big/ \partial T_2$	$= Y_4$	thermal sensitivity of Y_{11}^E
α_t	$= P_2$	thermal expansion coefficient of transducer thickness
α_w	$= P_3$	thermal expansion coefficient of transducer width
α_l	$= P_4$	thermal expansion coefficient of transducer length

SECTION XIV

TABLE XIV-4

Conventional Symbols, Computer Symbols, and Definitions (Cont'd)

α_b	=	P6	=	thermal expansion coefficient of brace
α_a	=	P1	=	thermal expansion coefficient of arm
α_p	=	P5	=	thermal expansion coefficient of pivots
G_p	=	G9	=	shear modulus of pivot material
$\left(\frac{\partial G_p}{G_p}\right) \left/\right. \partial T_5$	=	G1	=	temperature coefficient of G_p
L_1	=	L1	=	1/2 the inertia of one arm
C_1	=	C1	=	mechanical compliance
C_p	=	C9	=	mechanical compliance of all pivots, differential mode
Z	=	Z	=	equivalent sensor impedance
R_0	=	R0	=	output load resistor
$\left(\frac{\partial R_0}{R_0}\right) \left/\right. \partial T_4$	=	R5	=	temperature sensitivity of R_0
R_1	=	R1	=	internal mechanical damping
$\left(\frac{\partial R_1}{R_1}\right) \left/\right. \partial T_5$	=	R2	=	temperature sensitivity of R_1
$\Delta \Gamma_c$	=	G6	=	COS channel gradient error, Eu
$\Delta \Gamma_s$	=	G5	=	SIN channel gradient error, Eu

Note: All temperature sensitive coefficients are given in parts per million/ $^{\circ}\text{C}$.

T842

SECTION XIV

Finally, from eq. (13) and (14) and all of the derivatives, the incremental changes in Γ_c and Γ_s due to the incremental temperature changes, we have

$$\begin{aligned}\Delta\Gamma_c = & \frac{|2\Gamma_{ij}| \times 10^{-6}}{Z} \left[B_1 L_1 (2\alpha_a) \Delta T_1 \right. \\ & + B_2 C_0 (\alpha_w + \alpha_l - \alpha_t + E4) \Delta T_2 \\ & + B_3 N (\alpha_w + \alpha_t + G4 + E4 + Y4) \Delta T_2 \\ & + B_4 R_1 (R2) \Delta T_3 + B_5 R_0 (R5) \Delta T_4 \\ & + B_6 \frac{1}{C_p} (6(\alpha_p - \alpha_b) + 3\alpha_p + G1) \Delta T_5 \\ & \left. + B_6 \frac{2}{C_m} (\alpha_w + \alpha_t - \alpha_l + Y4) \Delta T_2 \right] \quad (49)\end{aligned}$$

and

$$\begin{aligned}\Delta\Gamma_s = & - \frac{|2\Gamma_{ij}| \times 10^{-6}}{Z} \left[A_1 L_1 (2\alpha_a) \Delta T_1 \right. \\ & + A_2 C_0 (\alpha_w + \alpha_l - \alpha_t + E4) \Delta T_2 \\ & + A_3 N (\alpha_w + \alpha_t + G4 + E4 + Y4) \Delta T_2 \\ & + A_4 R_1 (R2) \Delta T_3 + A_5 R_0 (R5) \Delta T_4 \\ & + A_6 \frac{1}{C_p} (6(\alpha_p - \alpha_b) + 3\alpha_p + G1) \Delta T_5 \\ & \left. + A_6 \frac{2}{C_m} (\alpha_w + \alpha_t - \alpha_l + Y4) \Delta T_2 \right] \quad (50)\end{aligned}$$

SECTION XIV

These are still far too complex to allow the important terms to be easily recognized so the computer is programmed to print out the coefficients for the temperature-sensitive partials for $|2\Gamma_{ij}|$ equal 4500 EU and all ΔT equal 0.001°C . The printouts are of the form shown in (41) and (42)

$$\begin{aligned}\Delta\Gamma_s &= K1(2\alpha_a) \\ &+ K2(\alpha_w + \alpha_l - \alpha_t + E4) \\ &+ K3(\alpha_w + \alpha_t + G4 + E4 + Y4) \\ &+ K4(R2) \\ &+ K5(R5) \\ &+ K6(6(\alpha_p - \alpha_b) + 3\alpha_p + G1) \\ &+ K7(\alpha_w + \alpha_t - \alpha_l + Y4)\end{aligned}\quad (51)$$

and

$$\begin{aligned}\Delta\Gamma_c &= M1(2\alpha_a) \\ &+ M2(\alpha_w + \alpha_l - \alpha_t + E4) \\ &+ M3(\alpha_w + \alpha_t + G4 + E4 + Y4) \\ &+ M4(R2) \\ &+ M5(R5) \\ &+ M6(6(\alpha_p - \alpha_b) + 3\alpha_p + G1) \\ &+ M7(\alpha_w + \alpha_t - \alpha_l + Y4)\end{aligned}\quad (52)$$

In the printout, $G5 = \Delta\Gamma_s$, the phase error term, and $G6 = \Delta\Gamma_c$, the amplitude error term. It is evident that the sensor phase error is much more sensitive to temperature changes than the amplitude term. This has been known generally since the original proposal but this computer program provides a precise evaluation and comparison.

SECTION XIV

The computer printout evaluates $\Delta\Gamma_s = -0.438$ EU for perfectly correlated temperature differentials of 0.001°C at each point. This is considered to be a worst-case situation. It is shown in Section XVIII, Temperature Control Subsystem, that a temperature standard deviation of 0.00114°C , and probably better can be attained in the sensor. Adjusting the ΔT 's to this value gives a $\Delta\Gamma_s = -0.500$ EU. This translates to a sensor phase error of 5.55×10^{-5} rad and a $\sigma_{XY} = 0.250$ EU standard deviation gradient error at the tensor element. In Section IX-B, Phase Error Propagation in the Rotating Gravity Gradiometer, sensor phase errors of 6×10^{-5} rad and $\sigma_{XY} = 0.27$ were used in the error analysis. Thus, it is expected the RGG prototype design will have a slightly better phase error stability than is shown in the error analysis.

E. TRANSDUCER MOUNTING STRUCTURE

The transducers are mounted as shown in the layout of Section V. Four posts are fixed on each arm, in a circle around the pivot, and these posts extend through the brace plate and through the other arm if the first arm is an inside arm. An axial view along the posts shows, for both arms, the ends of eight posts arranged in a circle around the pivot. A mounting plate is fixed to the four posts of one arm and another plate to the four posts of the other arm. This arrangement is shown in the layout. The transducer is then attached to the two mounting plates.

Each set of posts and mounting plate constitute a rigid isoelastic structure that applies a pure bending moment to the end of each transducer. This stand-off structure is quite rigid in bending, torsion, and to end loading. It is quite similar to the quadrilever pivot discussed in the original technical proposal.

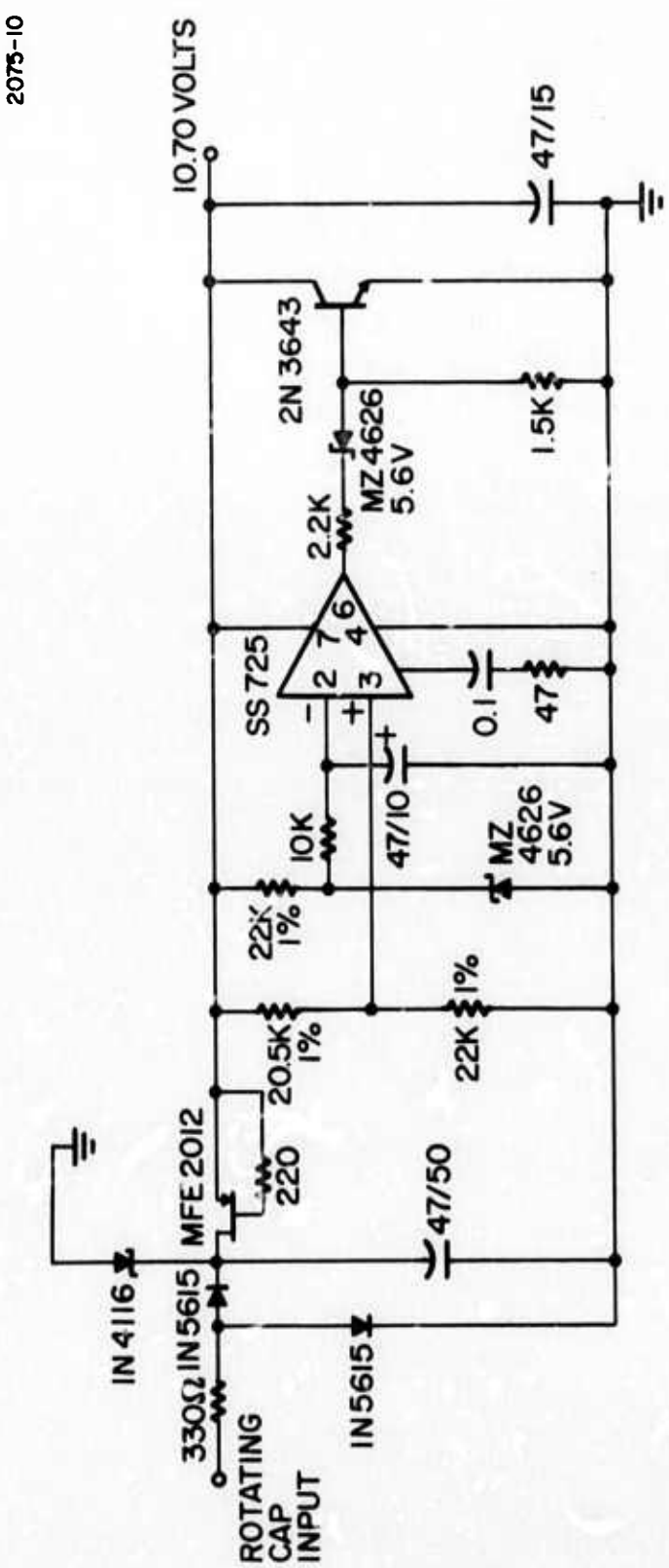
Since the stand-off structures for each of the two arms will have different length posts the diameter of these posts will have to be designed so that the bending spring rates are equal. Also the mounting plates and the transducer clamps will be designed so that they have both static and dynamic mass balance about their longitudinal axis.

SECTION XV

ROTOR POWER SUBSYSTEM

The rotor power subsystem described in the Semiannual Technical Report No. 1, has been built and tested and performs as predicted. Minor changes in component values were made to optimize the regulation capability and temperature sensitivity. The prototype design of the rotor power subsystem is shown in Fig. XV-1. The packaging of this subsystem is included in Section XIX, along with all of the other rotor mounted electronics.

Fig. XV-1 Rotor Power Subsystem.



SECTION XVI

ROTOR SPEED CONTROL SUBSYSTEM

A. GENERAL

The rotor speed control subsystem is comprised of an analog spin motor servo, spin motor, tachometer, frequency reference and a rotor-stator position pick-off. The position pick-off is also used in the digital data reduction subsystem discussed in Section XXI. Although the prototype design uses an analog spin motor servo it is expected that the final design will use a digital servo and this will be tested during Phase II. The following paragraphs discuss the subsystem components and their performance in detail.

B. SPEED CONTROL SERVO

The "speed control servo" controls the frequency of the RGG signal modulation process on the basis of the sampled phase error of this process. The continuous phase error of the process is defined as the difference between the actual position and the reference position of the RGG rotating assembly as in (1), where $\dot{\alpha}(t)$ is the actual, instantaneous angular velocity of the rotating assembly with respect to the measurement reference frame of the case.

$$\phi(t) \triangleq \int_0^t \dot{\alpha}(t) dt - \omega_R t \quad (1)$$

The sampled phase error is taken as the value of (1) which exists at the time of mechanical coincidence between rotor and stator reference points as described in paragraph E of this section.

SECTION XVI

Although the position error of the speed control servo is sampled and quantized, the remaining part of the servo proposed for the baseline design is an analog mechanization employing proportional plus integral control and tachometer feedback. A simplified functional block diagram of the servo is shown in Fig. XVI-1. The upper portion of Fig. XVI-1 depicts the tachometer feedback dynamics and the tachometer measurement noise ($\Delta\omega_t$). The lower portion of Fig. XVI-1 indicates the proportional plus integral control dynamics acting on the sampled and held position error signal. The central portion of Fig. XVI-1 represents the "plant dynamics" of the rotating assembly and the "plant disturbances" which include the normalized torque disturbances (T_d/J) and the RGG c se angular velocity (ω_c). The normalized damping coefficient (D/J) of the plant is the combined effect of the viscous damping of the spin bearing, the electromagnetic drag of the motor and tachometer, and the windage effects of the rotating assembly. The calculated damping coefficient for the baseline design is 1193 dcm-sec and the polar moment of inertia of the rotating assembly is estimated to be 2.5×10^5 gm-cm². These figures yield a normalized damping coefficient (D/J) equal to 0.0048 sec⁻¹. The constant input quantities represented in Fig. XVI-1 are the reference speed command, (ω_R), the tachometer bias (ω_b), and the normalized average running torque (To/J).

The sample and hold operation on the position error may be approximated as a simple, first-order lag (for frequencies well below the sampling frequency) with a time constant equal to one-half the sample time interval ($\tau_s \approx \frac{1}{2}t^*$). In the baseline design, the sample frequency is approximately 17.5 Hz, and the servo position loop bandwidth is less than 1 Hz. These conditions adequately satisfy the requirements for the approximate representation of the sample and hold operation with a first order lag of 28.6 msec (corner frequency = 35 rad/sec).

The tachometer feedback signal will be filtered by a first order lag to reduce the effects of tachometer noise, and a notch filter will be employed to reduce disturbances at twice the spin frequency. The notch filter is not shown in Fig. XVI-1 because its gain and phase has negligible effect within the servo bandwidth.

2078-56

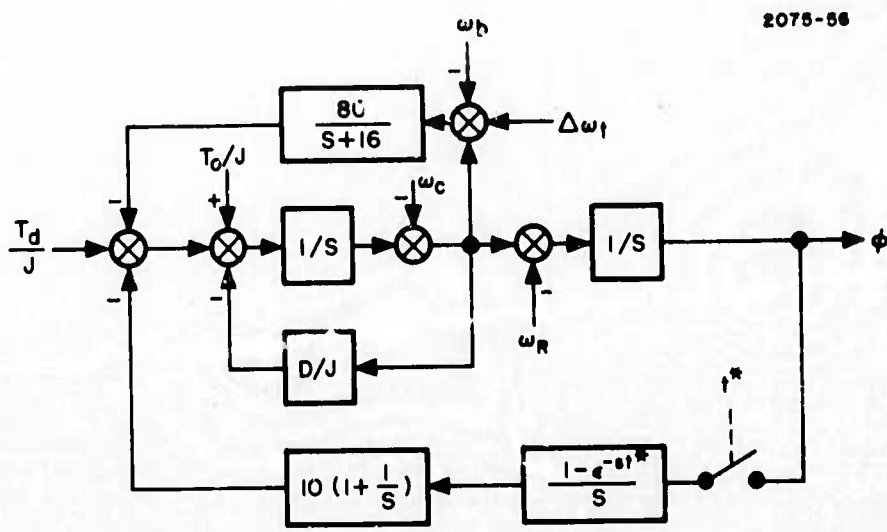


Fig. XVI-1. Functional Block Diagram of Servo.

SECTION XVI

A plot of the open loop gain vs. phase is shown in Fig. XVI-2 for the numerical parameters of Fig. XVI-1. This particular configuration has a phase margin of 46°, a gain margin of 20 dB, and a cross-over frequency of 2 rad/sec.

The position error response of the servo to normalized disturbance torques and to tachometer noise for the parameters of Fig. XVI-1 is presented in (2) and (3).

$$\frac{\phi}{T_d/J} = \frac{S(S+16)}{S^4 + 16S^3 + 90S^2 + 170S + 160} \quad (2)$$

$$\frac{\phi}{\Delta\omega_t} = \frac{80S}{S^4 + 16S^3 + 90S^2 + 170S + 160} \quad (3)$$

Plots of these disturbance responses are shown in Fig. XVI-3. The low frequency asymptotes of these transfer functions are ($S/10$) and ($S/2$), respectively. There is no steady state position error because of the integral control. These position error responses are used in the system error analysis to predict phase error induced gradient tensor errors.

C. SPIN MOTOR/TACHOMETER

Two identical motor/tachometers will be used on the prototype design, one at each end of the sensor. During run-up both motor/tachometers will be used as motors. This is necessary to obtain enough torque to overcome the breakaway torque of the hydrodynamic spin bearings. Once the sensor rotor is up to about half speed the function of one of the motor/tachometers will be switched and it will then be used as a tachometer. The tachometer provides the basic rotor velocity signal for the analog speed control servo previously discussed in this section.

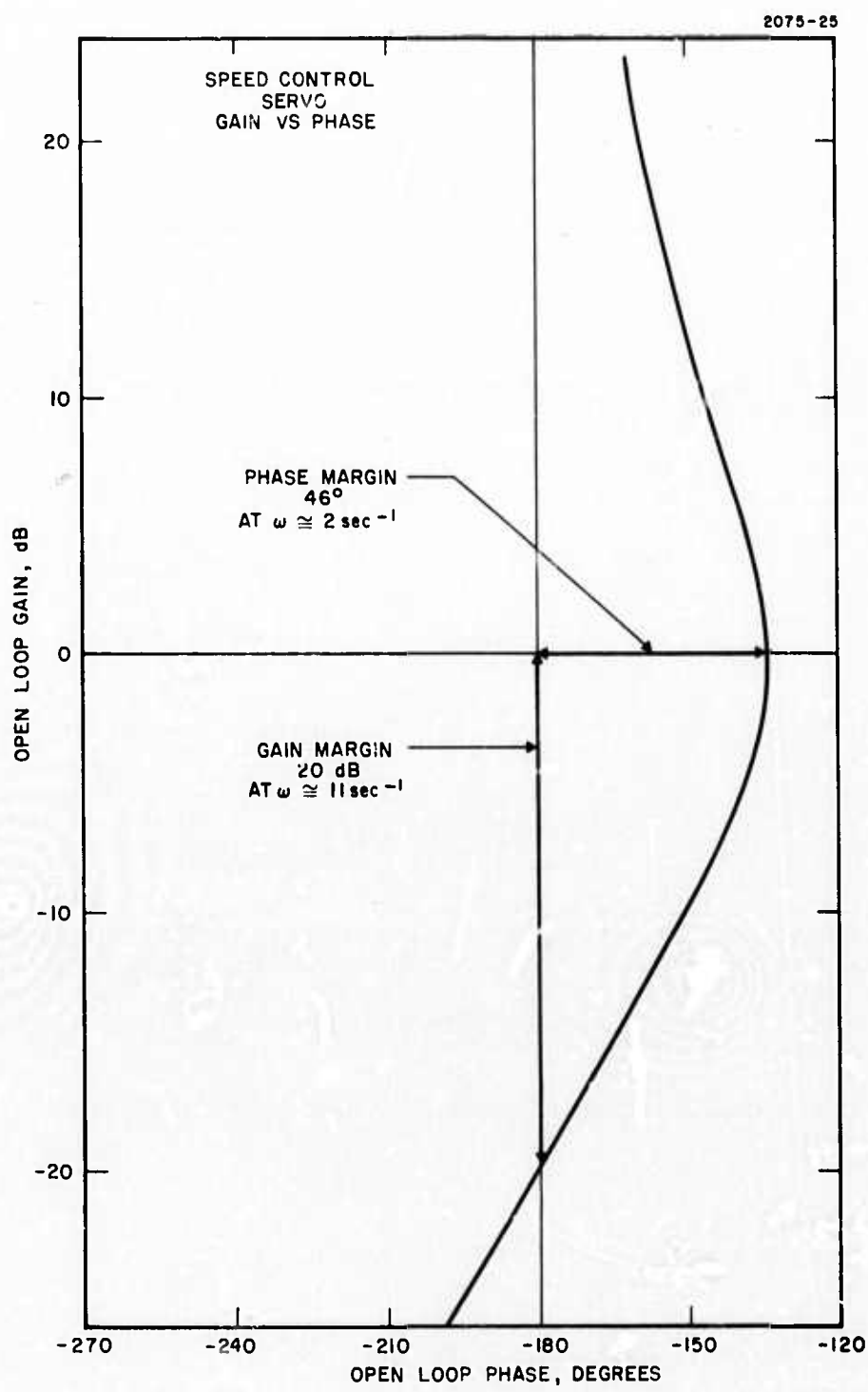


Fig. XVI-2. Speed Control Servo Gain Versus Phase.

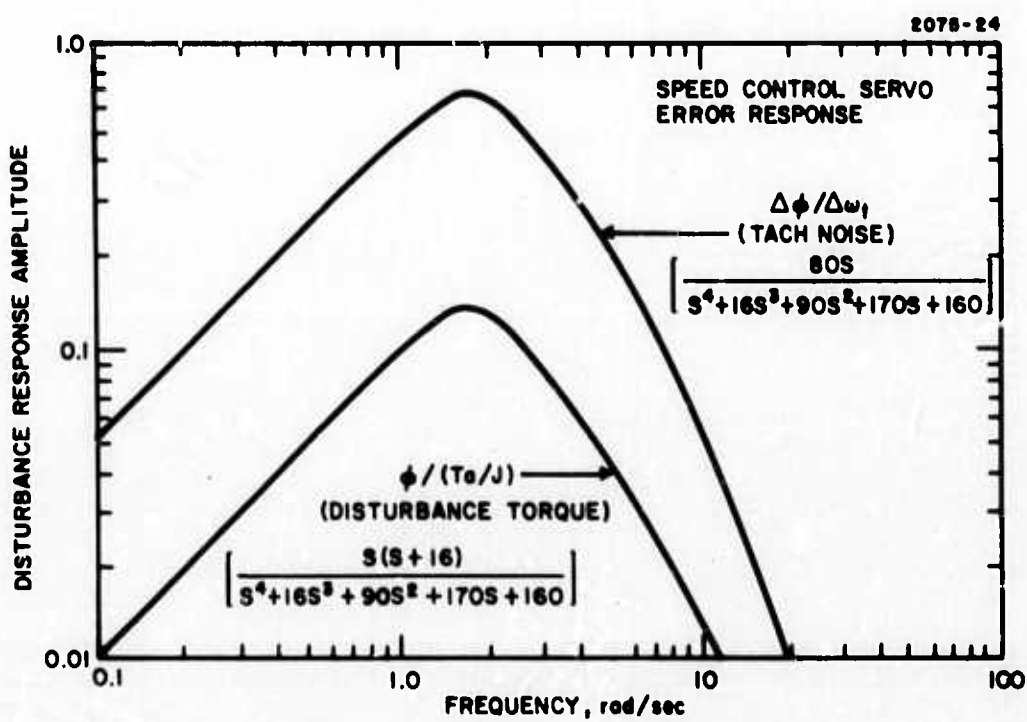


Fig. XVI-3. Speed Control Servo Error Response.

SECTION XVI

1. Motor/Tachometer Type Selection

Many types of motors and tachometers were considered for this application. The requirements are in general:

- a. Sufficient stall torque to overcome bearing friction.
- b. Low and constant self generated ripple torque at operating speed.
- c. Insensitive to external magnetic fields.
- d. Lowest possible input power.
- e. Good servo motor characteristics.
- f. Good tachometer characteristics.
- g. Size and form commensurate with the basic sensor design.

These requirements automatically exclude any motor that has ferromagnetic material on the rotor. Ferromagnetic materials can not be made sufficiently homogeneous to meet the ripple torque and external magnetic field requirements. The requirements also exclude any motor using brushes or commutators. Only the drag cup servo motor can meet the requirements. Its only drawback is that its efficiency is low, about 10% at best. It can be used interchangeably as a motor or tachometer although a good motor design is not necessarily a good tachometer design.

Motor/tachometer specifications were sent to three motor design consultants. These were:

R. H. Park, Co., Inc.
Main Street
Brewster, Mass.

Herbert C. Rotors Associates, Inc.
45 North Mall
Plainview, N. Y.

Philip H. Trickey
112 West Lavender Ave.
Durham, N. C.

SECTION XVI

All of the consultants believed that they could design a motor that would meet the specifications but only Mr. Trickey was equipped and had the background to make the ripple torque calculations without further study. Mr. Trickey is semiretired after 30 years of designing drag cup motors and tachometers. He is the author and coauthor of a number of classic papers on the subject. Also he is a part-time professor at Duke University so that he has ready access to a large computer. Mr. Trickey was selected to design the motor/tachometer. The Spin Motor/Tachometer specifications are reproduced as Appendix C.

2. Description

The main motor parameters are given in Table XVI-1. The motor is designed to operate at two different voltages. It operates at 62.2 V on both phases to provide run-up and the breakaway torque of the spin bearings. It operates at 37.86 V on both phases in the speed control servo mode.

Both the motor and the tachometer have a compensator winding that is wound in parallel with the reference phase winding. The compensator winding is of course electrically insulated from the reference winding. The voltage induced in the compensator winding is a direct measure of the magnetic field induced by the reference winding. The output of the compensator winding will be fed back to control the reference magnetic field to a constant value. This method of establishing the reference field is commonly used with high precision resolvers and is far superior to other methods of establishing a constant reference field.

Both the motor and the tachometer operate at a frequency of 140 Hz, which is locked to the basic frequency reference.

It is seen in Table XVI-1 that this is a "pancake" motor and is similar in appearance to "pancake" resolvers in common use. The inner and outer stators are made exactly the same stack height so that the inevitable fringing field at the gap is completely symmetrical.

SECTION XVI

TABLE XVI-1
Spin Motor/Tachometer Characteristics

<u>Motor</u>	
Phases	2
Poles	8
Frequency	140 Hz nominal
Start-Up, Locked Rotor	
Voltage	62.2 V
Watts	30.2 W
Torque	3.84×10^5 dcm
Servo Mode at 1050 rpm	
Voltage	37.86 V
Watts	9.94 W
Torque	6.69×10^4 dcm
Compensator Winding Output	3.78 V
<u>Tachometer</u>	
Reference Phase at 1050 rpm	
Volts	20.8 V
Watts	1.7 W
Average Drag	1.11×10^4 dcm
Compensator Winding Output	3.78 V
Output at 1050 rpm	
Volts	1.42 V
Scale Factor	1.29×10^{-2} V/rad/sec
<u>Dimensions</u>	
Stator - Outer	
Outside Dia.	4.250 in.
Inside Dia.	2.875 in.
Stack Height	0.250 in.
Winding Slots	32
Length Over-all	1.00 in.
Stator - Inner	
Outside Dia.	2.791 in.
Inside Dia.	2.0 in.
Stack Height	0.250 in.
Drag Cup (Aluminum)	
Outside Dia.	2.861 in.
Inside Dia.	2.791 in.
Length	1.00 in.
Thickness	0.035 in.

T870

SECTION XVI

The drag cup is made quite long so that the end effects are small and predictable. These two latter features reduce both motor and tachometer variations as the cup shifts with respect to the stators.

It is shown in Section IX-B, Phase Error Propagation in the RGG, that a tachometer measurement noise of 10^{-4} rad/sec in a band from 0 to 0.1 Hz is all that is allowed to meet the rotor speed control error budget. With the tachometer scale factor in Table XVI-1, the noise voltage is only 1.29×10^{-6} V. This is a formidable requirement, but the noise band of importance is at very low frequency and the band is very narrow.

The tachometer output is at 140 Hz and can be easily amplified with negligible noise and distortion to 14.2 V at 1050 rpm. This output is phase sensitive, demodulated, filtered, and used in the rotor speed control loop. The tachometer output voltage is at 140 Hz, and it inherently has only the rotation speed, 17.5 Hz, and its higher harmonics as distortion terms. Note that the rotor speed and signal frequency are harmonically related and phase locked by the use of one master reference frequency and a frequency synthesizer. The only means by which a 0 to 0.1 Hz signal can be generated is to modulate the tachometer output voltage or phase by one of the following mechanisms:

- a. Reference voltage modulation
- b. Translation of the drag cup with respect to the stator (axial, radial)
- c. Resistance variation of the drag cup due to temperature variation
- d. Stator iron loss change due to temperature variation
- e. Stator permeability change due to temperature variation
- f. Dimensional changes of stator and drag cup due to temperature variation
- g. Thermal noise of the winding resistance component.

SECTION XVI

Although final design calculations have not been made, it is believed that the tachometer will meet the noise voltage specification. Other tachometers have been designed to perform with an accuracy of 0.1% over a range of $\pm 10^{\circ}\text{C}$ and with 0.001 in. radial and axial rotor play. Allowing for temperature variations at the motor of $\pm 0.1^{\circ}\text{C}$ and radial and axial play of 10^{-4} in., this would scale to one part in 10^6 , a little better than required. The actual temperature variation should be less than $\pm 0.01^{\circ}\text{C}$ and the radial and axial play will not exceed about $\pm 10^{-5}$ in.

This tachometer has been designed with a compensator winding and large drag cup overhang. Also, the output load will be a very high resistance and can be temperature compensated. These features help ensure that the tachometer will meet its specifications.

D. FREQUENCY REFERENCE

Two secondary standard frequency references are available. Both of these are so accurate that the error due to the frequency reference is negligible in the error analysis.

The Hewlett-Packard No. 10544A, 10 MHz Quartz Crystal Oscillator, ages less than 5×10^{-10} per day, and less than 1.5×10^{-7} per year. This oscillator warms up in 15 min to within 5×10^{-9} of the final stabilized frequency. This same unit is incorporated as the clock in all Hewlett-Packard frequency counters. One of these counters will be used as a basic component of the prototype design.

The General Radio Type 1115-B, 5 MHz, Standard Frequency Oscillator, ages less than 5×10^{-10} parts per day and less than 5×10^{-8} parts per year.

The General Radio Frequency Synthesizer is not quite as good as the above two secondary standards but it is provided with terminals that allows it to use an external frequency reference. The Hewlett-Packard Frequency Counter will be used as the basic reference in the Prototype Design. Its 10 MHz output will be used directly by the speed

SECTION XVI

control servo, and the digital data reduction subsystem. In addition the 10 MHz signal will be divided by two to obtain a 5 MHz reference with an accuracy and stability equal to that of the reference. This 5 MHz will be used as the reference for the General Radio Frequency Synthesizer. The Frequency Synthesizer will be used to provide the low frequency, 35 Hz locked to the standard, that is required by the analog data reduction subsystem. This same Frequency Synthesizer will also generate the 140 Hz required by the spin motor and tachometer.

The above combination of equipments will eliminate the frequency reference as a significant source of error in the prototype design.

E. POSITION PICKOFF

A precision pickoff is required to detect coincidence, or the error angle, of the rotor and stator reference points once each revolution. This will be accomplished in the prototype design by the use of a pulsed light emitting diode (LED) as a light source, and a high speed photocell to read the position of an encoder disc.

1. Requirements

The relative error between the rotor and stator must be detected once each revolution with an instantaneous position uncertainty of no more than 2.2×10^{-5} radians (1 sigma) and an average uncertainty of no more than 2×10^{-5} radians (1 sigma). The mean position error will be held to less than one part in 10^7 over periods of up to 10 hours by means of the frequency reference previously discussed in paragraph D of this section.

SECTION XVI

The position error requirements, 1 sigma values, in radians are

Reference frequency change	1.5×10^{-7}
Center of rotation uncertainty due to "g" loads on bearing	1×10^{-5}
Sensor Arm Alignment to Rotor Case	1×10^{-5}
Encoder Disk to Rotor Case	1×10^{-5}
Photo Cell to Stator Alignment	1×10^{-5}
RSS Alignment Variations, 1 sigma	2×10^{-5}

The initial values of these terms are not important, except as a convenience, since they will all be calibrated prior to a test. It is only their variation during a 3 to 10 hr test that are significant. The above values are estimates, of course, but based on experience with optical autocollimators, gyro and accelerometer pick-off stability and alignment stability of precision devices in general, they are considered to be realistic.

The long-term speed error (zero mean speed error) is met by the use of the precision frequency reference previously described and through the speed control servo forcing the average speed to equal the set speed. The reference frequency is 10^7 Hz and the nominal speed is 110 radians per second. The exact rotor speed for optimum performance will be found by test and set to seven significant figures for each sensor but the use of the nominal illustrates the technique.

A register is set in the computer that represents the number of 10 MHz counts that should occur during one revolution. This counter is set to seven significant digits on a decimal base. A counter, that counts the actual number of 10 MHz pulses during each revolution is started and stopped by the reference slot on the encoder disk. This actual count is compared with the ideal count and an error signal of the proper polarity is generated and sent to the speed control servo. Thus the long time speed error is forced to zero. The counters just mentioned

SECTION XVI

are clocked so that no bit of the 10 MHz count is ever lost. Thus even if there should be exact coincidence between an encoder disk slot pulse and a 10 MHz count, that count will be added to the count for the next revolution.

The encoder disk is also used for digital data reduction which is a considerably more complicated task than that just described. The actual speed control counters and registers are incorporated within the computer used for digital data reduction and the diagrams therefore appear in Section XXI.

2. Encoder Disk

The encoder disk is glass and is opaque except for eight light slots as shown in Fig. XVI-4. The reference slot is made significantly wider than the others so that it can be identified by the computer.

At the pick-off point the encoder disk has a radius of 1.625 in. Rotating at 110 rad/sec the slot velocity is

$$v = R \omega_s = 179 \text{ inches per second} \quad (1)$$

The light source is focused to a spot 0.001 in. in diameter at the slot. Thus the light fall time on the photocell is

$$\text{Fall Time} = \frac{10^{-3}}{R \omega_s} = 5.6 \times 10^{-6} \text{ sec.}$$

The photocell saturated level will be set to 10 V and the gate will be set to 5 ± 0.2 V giving time resolution of 1.1×10^{-7} sec and a position resolution of 1.2×10^{-5} rad. This will meet the pulse jitter requirement of 2.2×10^{-5} radians previously stated as a requirement.

2075-16

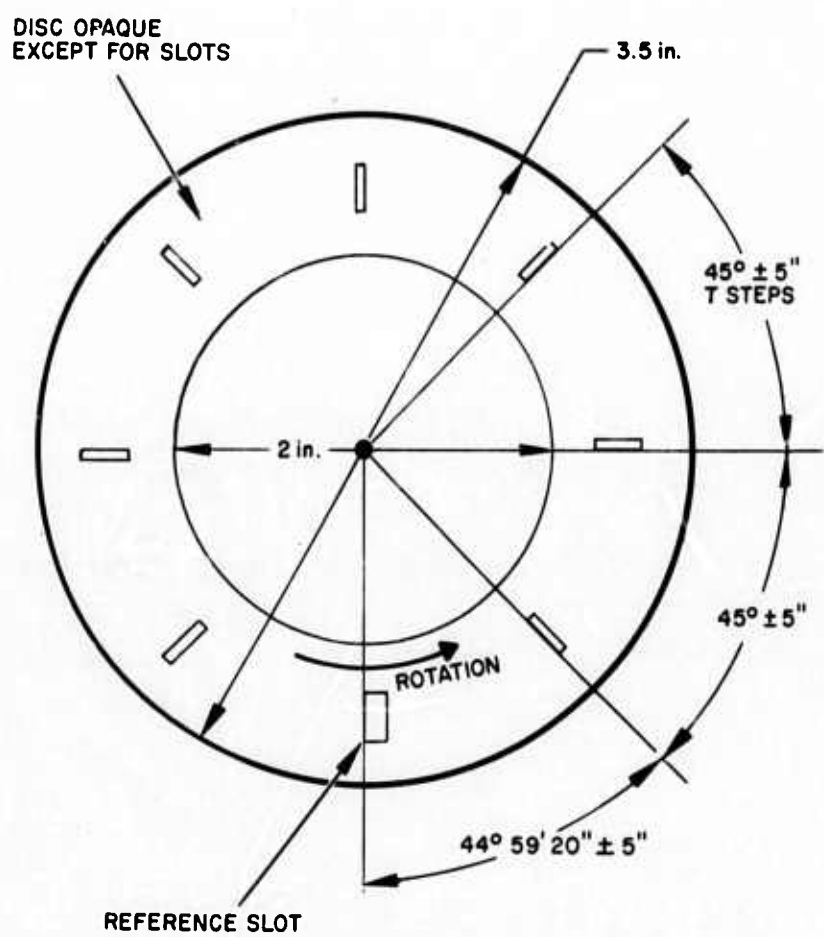


Fig. XVI-4. Encoder Disk.

SECTION XVI

For the single reference slot used for speed control, position accuracy has no meaning since it is the reference. However as shown in the figure there will be seven other slots on the disk. These slots can be spaced and positioned to an accuracy of ± 5 arc sec for a modest cost disk. As shown in the section on digital data reduction, this accuracy is entirely adequate. However, there is one other important characteristic of the placement of these seven slots. They are placed 20 arc sec ahead of the exact one-eighth of a rotation position based on the reference slot. The reason for this slot positioning is given in Section XXI.

Operation of the light source, photocell and encoder disk is as follows: The light source is pulsed to high intensity just prior to the leading edge of each slot and is extinguished immediately after the slot has passed. This keeps the average dissipation of the LED to a low level but provides a high intensity source at the time that it is needed. The computer can be programmed to turn the LED on and off at the proper time. The computer also recognizes the reference slot by its greater width and then keeps track of the other seven slots. When the trailing edge of the slot passes through the light beam, the photocell output goes to zero and this generates the position signal previously discussed.

SECTION XVII

REMOTE ARM BALANCE SUBSYSTEM

The remote arm balance subsystem allows the mass balance of the sensor arms to be adjusted while the sealed sensor is operating. In addition the same logic system that controls the mass balance adjustment provides a logic state that adjusts the gain of the signal preamplifier and FM transmitter to provide "Normal" and "Low" gain settings. The "Low" gain is used during initialization and coarse adjustment. This same logic is also used to turn the sensor test signal on and off. The subsystem diagram is shown in Fig. XVII-1. A discussion of the packaging of the electronics of this subsystem is included in Section XIX.

A. GENERAL

The arm balance subsystem consists of a power supply, the same as that used for the sensor electronics, a logic section, a sequencer, mass transport devices and three vibration drivers.

While the system is operating in a static environment each of the three vibration drivers will be excited in sequence to vibrate the sensor along a known axis at a known amplitude. The phase and magnitude of the change in the output signal will be measured and recorded. The magnitude and direction of the mass shift required to correct the differential mode arm mass unbalance will be calculated. By use of the sequencer and logic the subsystem will be commanded to shift a small precisely known mass a precisely known distance. It has been shown in the Semiannual Technical Report No. 1 that the adjustment can easily be made to one-hundredth the allowable residual unbalance. The subsystem is essentially the same as previously described. It has been refined in some areas.

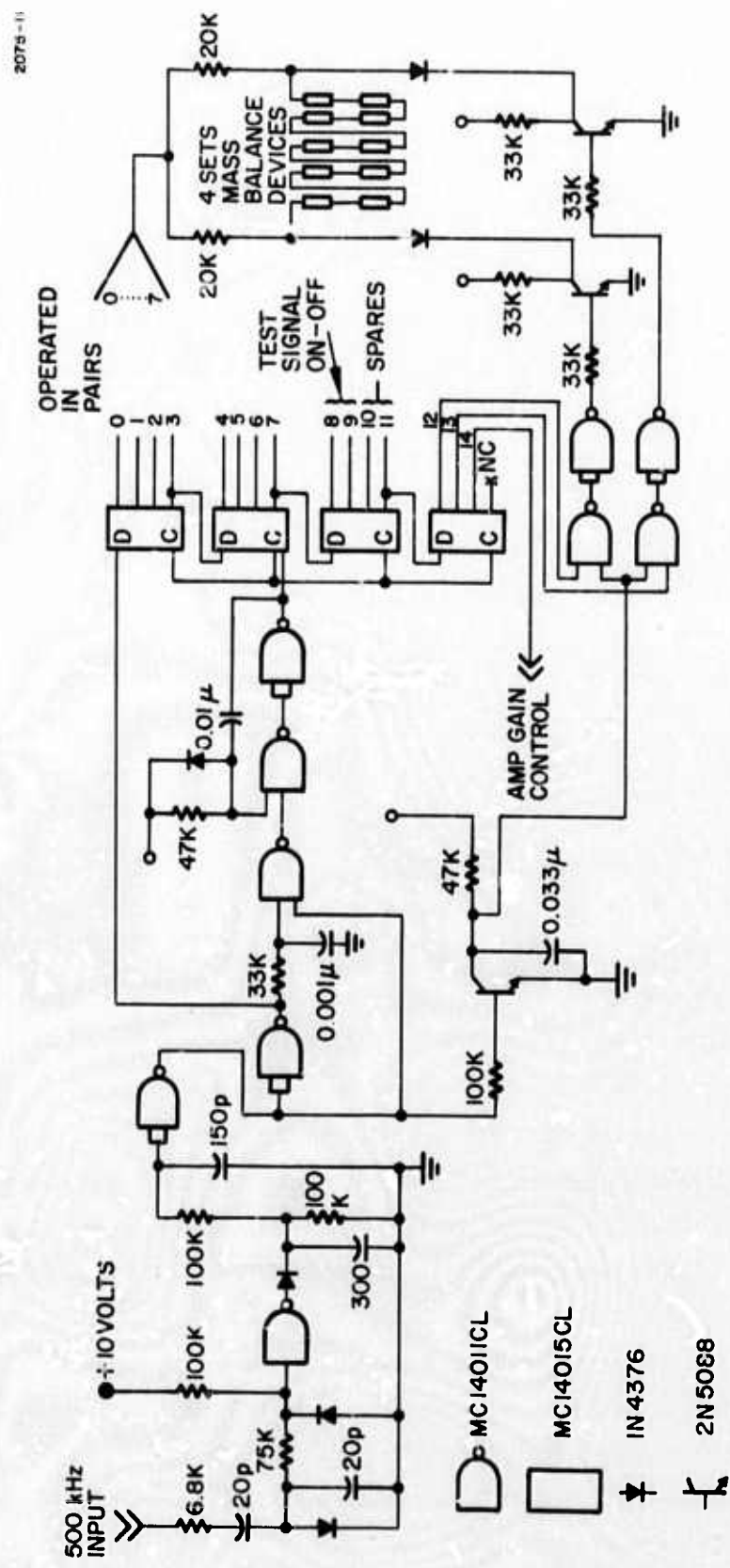


Fig. XVII-1. Remote Arm Balance Subsystem.

SECTION XVII

The mass balance device logic commands are given by interrupting the high voltage high frequency rotor power supply for 0.1 ms = logic "1", 0.3 ms = logic "0". The power supply, logic sequencer, and balance logic have all been built and tested. They are stable, do not generate false logic and drive the mass balance devices as predicted.

B. MASS TRANSPORT DEVICES

1. Requirements

It was shown in the Semiannual Technical Report No. 1 that the mass balance devices were required to have a mass times distance transport capability of

$$\Delta mh = \pm 56 \times 10^{-4} \text{ gm cm/arm/axis}$$

It must be possible to position the mass to an accuracy of

$$\Delta mh = \pm 4 \times 10^{-5} \text{ gm cm}$$

The mass balance devices have an inherent "g" limitation that must not be exceeded. They must be capable of operating over the temperature range anticipated for the sensor.

2. Description

The mass transport devices selected are small glass capillary tubes, filled with mercury except for a small gap of electrolyte and a gas pocket. A gas pocket, filled with dry nitrogen, will be left at the

SECTION XVII

"low g" end of the glass tube. This gas can absorb the expansion and contraction of the mercury due to ambient temperature changes in the non-operating condition. The tubes are sealed and provided with electrodes at each end. When an electric current is passed between the electrodes, mercury is plated from one side of the electrolyte gap to the other and the gap is transported along the tube. The direction of transport is controlled by the direction of the current, and the position of the gap is proportional to the time integral of the current through the balance device.

Devices similar to this have been described in a number of patents and have been manufactured by Sprague Electric Co.; Plessey Inc., Electrochemical Division (Formerly Bissell-Berman Corp.); and Curtis Instruments, Inc. Currently, Curtis Instruments is in commercial production on a current integrator tube almost identical to the one required for the RGG sensor. Curtis has quoted, to Hughes, a fixed price development and production contract for the balance tubes that we will require, made to Hughes specification. Hughes has studied the literature and has decided that we could make the balance tubes in our own laboratories. This would not be efficient, due to learning problems, but it provides a backup source.

A drawing of the specified balance tube is shown in Fig. XVII-2. A sketch of the mass balance device mounting arrangement is shown in Fig. XVII-3. Ten tubes in series, in two groups of five each, will be placed along each axis of each arm. The voltage drop across each tube will be approximately 0.15 V or a total of 1.5 V at a current of 0.5 mA. The electrolyte gap has an apparent negative mass of 7×10^{-4} g and a travel of ± 0.814 cm (± 0.32 in.). Since there are ten gaps on each axis the mass shift available is

$$\Delta m_h = \pm 57 \times 10^{-4} \text{ g cm}$$

as required by the previous paragraph. At a current of 0.5 mA the gap moves at a rate of 0.254 cm (0.1 in.) per hour. Thus an end to end

2075-12

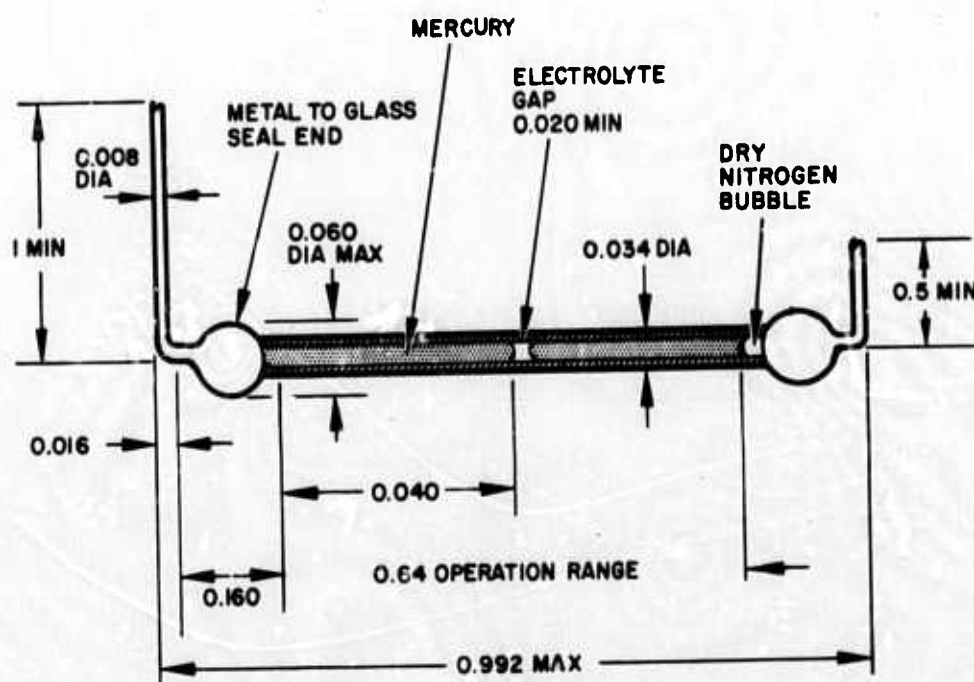


Fig. XVII-2. Mass Balance Device.

2075-13

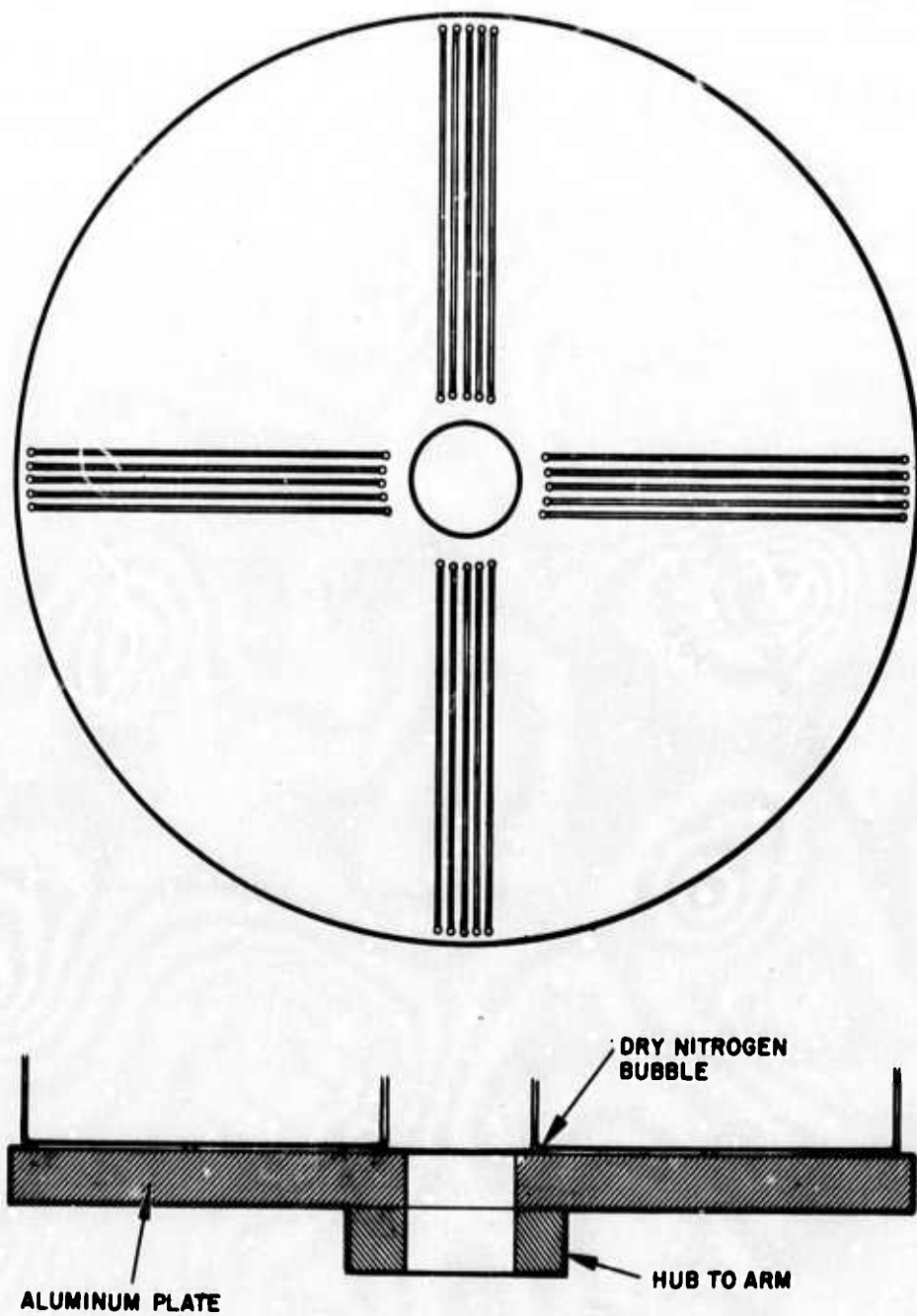


Fig. XVII-3. Mass Balance Device Mounting.

SECTION XVII

shift would require 6.4 hr. It is evident that by timing the current integration time, very fine resolution can be obtained.

The centrifugal acceleration near the pivot end (gas bubble end) will be about 15 g. At the outer limit of gap travel, 1.02 in. from the center the acceleration will be 39 g. These are safely within the theoretical and tested acceleration capability of over 60 g.

The device is completely satisfactory for the intended application.

3. Specification

A condensed specification for the mass transport device is given in Table XVII-1. In addition, the following inspections and tests will be made:

a. Characteristics

Voltage drop

Travel range

Accuracy

Gap size

b. Environmental

Acceleration

Temperature cycle

c. Inspection

Gap size

X-ray for extraneous gas and gaps

Bubble size

Leak detection

Seals

SECTION XVII

TABLE XVII-1
Mass Balance Device Specification

Tube material	Hard glass or quartz
Tube fill material	Mercury
1 in. lead	0.008 in platinum
1 in. lead seal	Glass to metal
1 in. lead Hg fill	< 0.50 mm Hg
Electrolyte	Perchlorate (valence 1 with Hg)
1/2 in. lead	0.008 in platinum
1/2 in. lead seal	Epoxy-room temp. cure
1/2 lead end fill	0.20 in. dry nitrogen bubble
Electrolyte gap size	0.20 to 0.23 in.
Tube ID	0.15 in.
Length overall (Leads bent 90°)	1.00 in.
Max OD	0.60 in.
Mass transport constant	0.1 in./Hr at 0.5 mA
Mass transport constant	Accuracy ±2%
Usable transport distance	±0.32 in.

T871

C. VIBRATION DRIVER

Three small vibration drivers will be mounted on orthogonal axes of the RGG mounting platform. These are small commercially available units that weigh 2 lb and can provide a force of 0.5 lb at 10 W

SECTION XVII

input power. This is sufficient force to vibrate the sensor mounting platform on the vibration isolation system to the 5×10^{-3} g level. This is adequate to provide the excitation required to adjust the arm mass unbalance.

D. SENSOR TEST SIGNAL

If an insulated plate is placed near some part of the sensor arm, the plate and arm form a capacitor. If a voltage is applied to this plate it will attract the arm with a force, F, acting at a lever arm, L. The moment acting on the arm is

$$M_t = F L = \frac{V^2 C L}{2d} = \frac{V^2 A \epsilon_0 L}{2d^2} \quad (1)$$

where

M_t = torque on the sensor arm, Nm

V = potential difference, volts

A = area of the plates, m^2

ϵ_0 = permittivity of free space, 8.85×10^{-12}

L = lever arm, m

d = spacing between the arm and plate, m

The sensor design includes an insulated plate 1 cm square, with a lever arm of 5 cm at the tip of each arm, which provides 4 capacitors. The voltage applied to each plate will be 10 volts, off of the rotor power

SECTION XVII

supply, the spacing will be 0.1 cm and these capacitors will produce a moment of

$$M_t = 8.85 \times 10^{-9} \text{ Nm}$$

The sensor torque due to an input gravity gradient is

$$M_o = \eta C_{zz} \Gamma_{eq}/2 = 1.533 \times 10^{-11} \text{ Nm/EU} \quad (2)$$

Thus the test capacitors can introduce a test gradient Γ_t which has an effective value of

$$\Gamma_t = \frac{M_t}{2M_o} = 228 \text{ EU} \quad (3)$$

The voltage required to excite the test capacitors will be obtained from the Rotor Power Subsystem. The loading, due to test capacitor excitation will be trivial, and it will be turned on and off with the same logic circuitry and sequencer that are used to shift the mass balance devices as previously described. These capacitors merely provide an excitation voltage source that can be turned on or off by external commands.

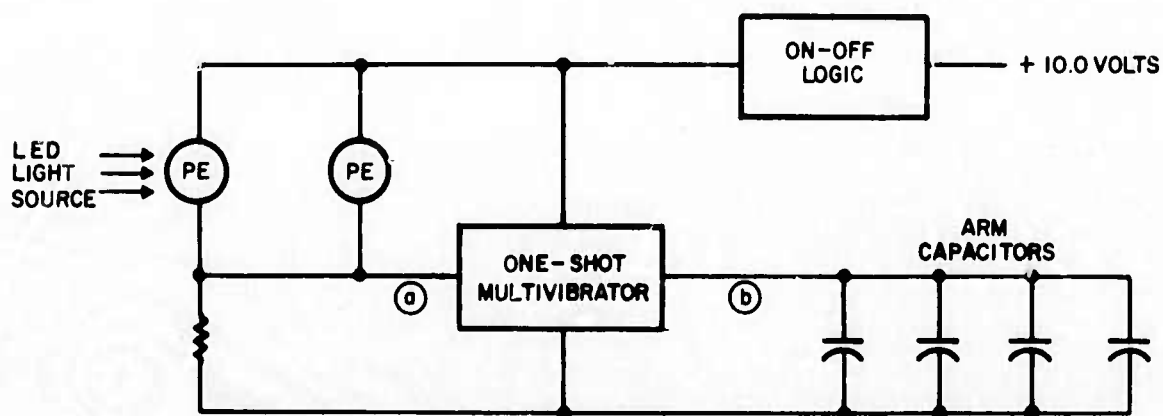
A $2\omega_s$ ($=\omega_o$) frequency will be obtained inside the rotor by using two photocells on the rotor that are excited by a LED (light emitting diode) mounted on the stator. These photocells will produce output pulses at a frequency of ω_o with their phase determined exactly by the mechanical position of the sensor rotor with respect to the stator. The photocell output pulses go to a single-shot multivibrator that has an

SECTION XVII

output pulse width of exactly $4\pi/\omega_0$ sec. The circuit and the wave forms at various points are shown in Fig. XVII-4.

It is evident that a precisely phased and constant amplitude test signal of approximately 228 EU can be introduced and removed by external logic commands. The exact phase and amplitude are not believed to be important. It is important that the phase and amplitude remain constant over a reasonable period of time such as an hour. Due to the temperature control and power supply regulation required by other subsystems the stability of this test signal will easily meet all of its requirements.

2075-14



SCHEMATIC DIAGRAM

2075-15

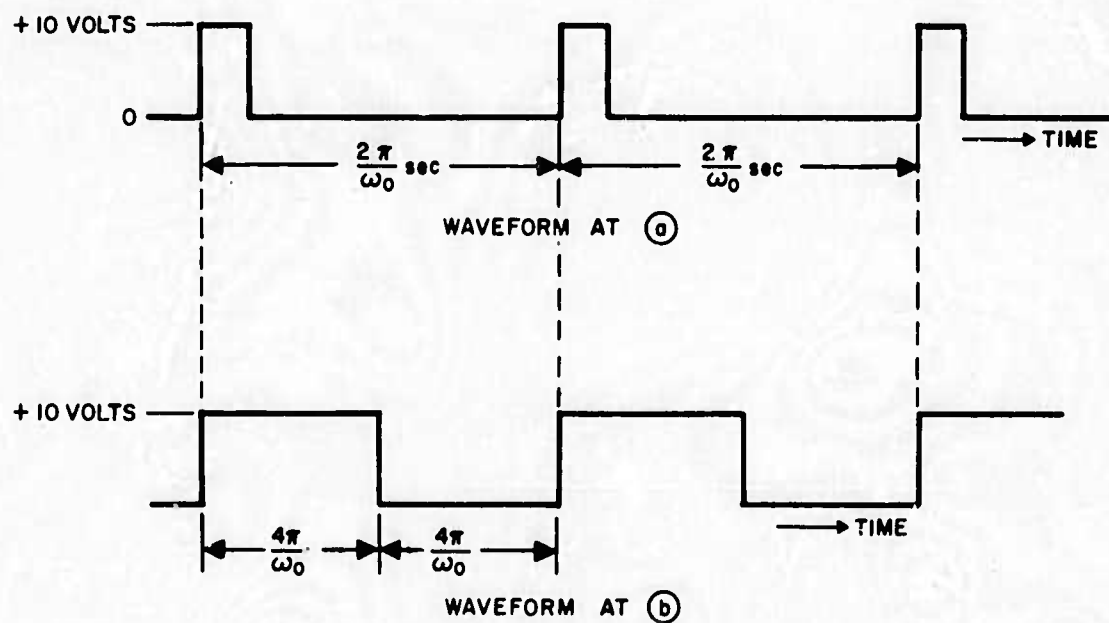


Fig. XVII-4. Test Signal Generator, Schematic and Waveforms.

SECTION XVIII

TEMPERATURE CONTROL SUBSYSTEM

A. TEMPERATURE CONTROL REQUIREMENTS ON CRITICAL COMPONENTS

There are two basic temperature requirements and an additional dimensional stability requirement which establish the basic temperature control parameters.

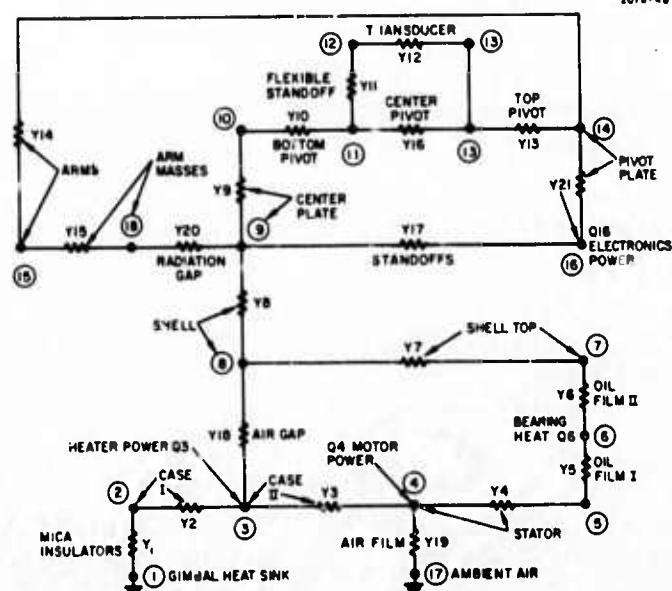
1. Analysis in Section XIV-D shows that the temperature of the transducers must not drift greater than $\approx \pm 10^{-3}^{\circ}\text{C}$ in order to maintain phase error signal at a level well below 1 EU.
2. The bearing design requires a temperature stability at the oil film of the bearing within $\pm 0.03^{\circ}\text{C}$ in order to maintain proper torque control on the drive system (see Section XII).
3. The bearing design also requires a dimensional stability of each oil film gap of $\pm 5 \mu\text{ in.}$ or a total tolerance of $\pm 10 \mu\text{ in.}$

B. THERMAL MODEL

The thermal model chosen for this analysis consists of one or two resistances for each basic part of the sensor. Since this analysis is preliminary to the finalized design and finalized dimensions were not known this level of detail appears realistic for a first cut at the problem. It is expected that a more detailed analysis will be run during the next phase of this program.

The thermal model chosen is shown in Fig. XVIII-1(a). Here all Y's are thermal conductances of individual components and the nodes between the conductances represent the thermal masses of the components. (Obviously some small mass components are considered to have no thermal capacity).

SOTB-48



(a)

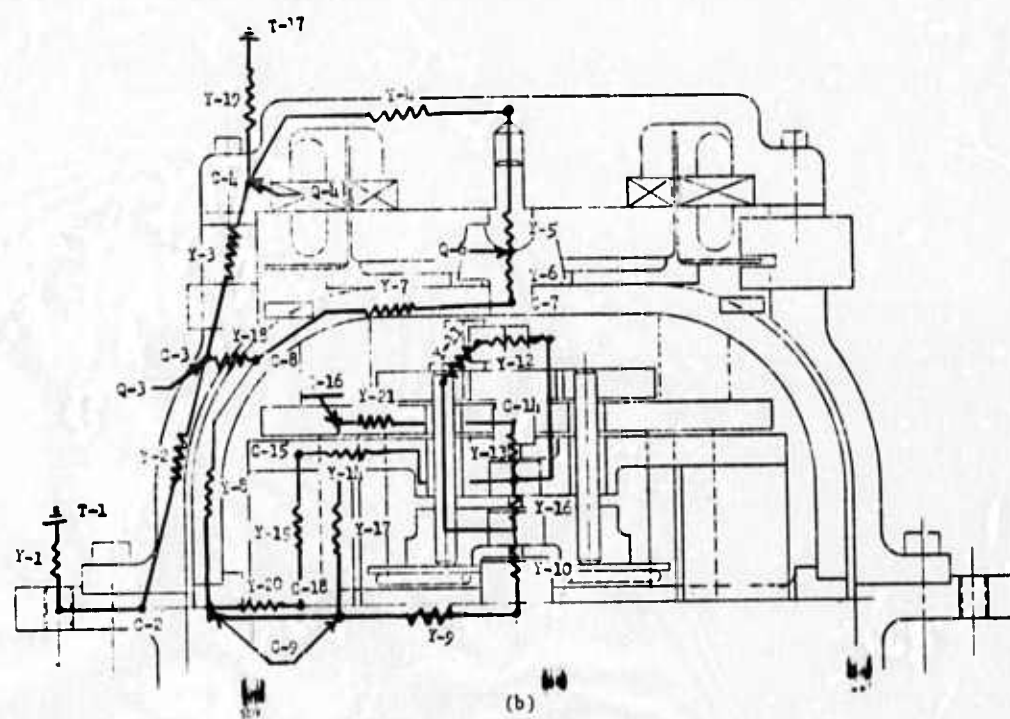


Fig. XVIII-1. Thermal Model.

SECTION XVIII

The principal heat inputs shown in Figure XVIII-1(b) are:

Q3 - Heater Power (a parametric variable)

Q4 - Motor Power

Q6 - Friction loss in the bearing oil film

Q16 - Electronics Power

The computer program chosen to provide the thermal analysis is the Hughes TAP-3 Thermal Analysis Program. The data was written with a "bang-bang" heater function with a specified dead band, but could easily be modified to a proportional controller type function. Thermal runs were made assuming both a constant ambient environment, and sinusoidally varying air temperature and gimbal heat sink temperature (T_1 and T_{17}). Initial conditions were set at 70°F and a transient analysis was run for each heater power level for the first 10 hr of operation. Readout was made of each node temperature each 0.02 hr for the last 2 hr of each run.

Data for the program was as follows:

1. All thermal conductances and capacities are as listed in the *010 and *020 Data Sections and were not changed (see Fig. XVIII-2).

2. Heat Inputs

Q4 - 1.7072 BTU/hr (Motor Power)

Q6 - 0.751 BTU/hr (Bearing Losses)

Q16 - 1.366 BTU/hr (Electronics Power)

$T_1 = 0.250 \sin(2\pi t)^{\circ}\text{F}$ (Gimbal Temperature)

$T_2 = 1.000 \sin(26.8t)^{\circ}\text{F}$ (Air Temperature)

3. Sensor Operating Temperature

$T_3 = 135^{\circ}$ and 90°

4. Heater Control Dead Band

$\pm 0.001^{\circ}\text{F}$ ($\pm 0.01^{\circ}\text{F}$ used in early runs)

RUN NUMBER 1

ALL NEW INPUT DATA FOR THIS RUN

• 1	0	0	0	0.	0	0	0	0	101
THIS PROGRAM CALCULATES THE TRANSIENT INTERNAL TEMPERATURES OF									102
THE DESIGN MODEL OF THE ROTATING GRAVITY GRADIOMETER CURRENTLY									103
BEING DESIGNED UNDER CONTRACT F19628-72-L-0222									104
T3 HAS REACHED CYCLING TEMPERATURE (135.02 DEG. F.)									R-105
• 10	NETWORK DESCRIPTION								105
1	14	0	0	0.	0.	1	2	1	106
15	0	0	0.	0.632910E 02	0.	15	18	0	107
16	0	0	0.	0.625000E 00	0.	11	13	0	108
17	0	0	0.	0.769230F 02	0.	9	16	0	109
18	0	0	0.	0.405000E 00	0.	8	3	0	110
19	0	0	0.	0.625000E 00	0.	4	17	0	111
20	0	0	0.	0.572000E-01	0.	18	9	0	112
21	0	0	0.	0.708000E 01	0.	14	16	0	113
• 20	0	0	0.	0.	0.	0	0	0	114
INITIAL VALUES									
T 2	18	0	0.	0.700000E 02	0.	0	0	0	115
Y 1	0	0	0.	0.101500E 01	0.	0	0	0	116
Y 2	0	0	0.	0.699300E 02	0.	0	0	0	117
Y 3	0	0	0.	0.285710E 02	0.	0	0	0	118
Y 4	0	0	0.	0.333333E 03	0.	0	0	0	119
Y 5	0	0	0.	0.341300E 02	0.	0	0	0	120
Y 6	0	0	0.	0.341300E 02	0.	0	0	0	121
Y 7	0	0	0.	0.667600E 01	0.	0	0	0	122
Y 8	0	0	0.	0.285710E 02	0.	0	0	0	123
Y 9	0	0	0.	0.716300E 01	0.	0	0	0	124
Y 10	0	0	0.	0.625000F 00	0.	0	0	0	125
Y 11	0	0	0.	0.414000E 00	0.	0	0	0	126
Y 12	0	0	0.	0.144000E-02	0.	0	0	0	127
Y 13	0	0	0.	0.625000F 00	0.	0	0	0	128
Y 14	0	0	0.	0.892900E 01	0.	0	0	0	129
C 1	0	0	0.	0.	0.	0	0	0	130
C 2	0	0	0.	0.273600E 00	0.	0	0	0	131
C 3	0	0	0.	0.251000E 00	0.	0	0	0	132
C 4	0	0	0.	0.765400E 00	0.	0	0	0	133
C 5	0	0	0.	0.	0.	0	0	0	134
C 6	0	0	0.	0.	0.	0	0	0	135
C 7	0	0	0.	0.188000F 00	0.	0	0	0	136
C 8	0	0	0.	0.251000E 00	0.	0	0	0	137
C 9	0	0	0.	0.230000E 00	0.	0	0	0	138
C 10	0	0	0.	0.	0.	0	0	0	139
C 11	0	0	0.	0.	0.	0	0	0	140
C 12	0	0	0.	0.	0.	0	0	0	141
C 13	0	0	0.	0.	0.	0	0	0	142
C 14	0	0	0.	0.154000E 00	0.	0	0	0	143
C 15	0	0	0.	0.108000E 00	0.	0	0	0	144
C 16	0	0	0.	0.	0.	0	0	0	145
C 17	0	0	0.	0.	0.	0	0	0	146
C 18	0	0	0.	0.208800E 00	0.	0	0	0	147
D 4	0	0	0.	0.170720E 02	0.	0	0	0	148
D 6	0	0	0.	0.751000F 00	0.	0	0	0	149
D 16	0	0	0.	0.134600E 01	0.	0	0	0	150
D 1	0	0	0.	0.135000E 03	0.	0	0	0	151
T 1	0	-1	0.	0.700000E 02	0.	0	0	0	152
T 17	0	-1	0.	0.700000F 02	0.	0	0	0	153
D 3	0	0	0.	0.200000E-02	0.	0	0	0	B-153
D 11	0	0	0.	0.700000F 02	0.	0	0	0	C-153
D 4	0	0	0.	0.135020E 03	0.	0	0	0	D-153

Fig. XVIII-2. Hughes TAP-3 Thermal Analysis Program.

U 12	0	0	0.134000E 03	0.	0	0	0	0	0	E-153	
* 30	0	0	0.	0.	0	0	0	0	0	154	
FUNCTIONS											
0 2	0	51	0.	0.	T 3	0	1	0	0	DEAD BAND FUNCTION	155
0 3	0	78	0.	0.100000E 03	0	2	0	3	0	FREQ,1 DEG./HR.	156
0 5	0	1	0.	0.360000E 03	0	0	0	0	0	FREQ,2 DEG./HR.	B-156
0 6	0	1	0.	0.153657E 04	0	0	0	0	0	SINE FUNCTION 1	C-156
0 7	0	20	0.	0.	R 5	0	0	0	0	SINE FUNCTION 2	D-156
0 8	0	20	0.	0.	R 6	0	0	0	0	AMPLITUDE 1	E-156
0 9	0	1	0.	0.250000E 00	0	0	7	0	0	AMPLITUDE 2	F-156
0 10	0	1	0.	0.100000E 01	0	6	0	0	0	TEMP, 1	G-156
T 1	0	50	0.	0.	R 11	0	9	0	0	TEMP, 17	H-156
T 17	0	50	0.	0.	R 11	0	10	0	0	MESSAGE TRIGGER	I-156
1	0	90	0.	0.	T 3	C	4	0	0		J-156
D101	118	51	0.	0.	T 1	D	12	1	0		K-156
* 70	0	0	0.	0.	0	0	0	0	0		157
SPECIAL CONSTANT VALUES											
1	0.416700E-02	SPECIFY DELTA-TIME								B-157	
2	0.100000E-03	MINIMUM ALLOWED DELTA-TIME								C-157	
4	0.416700E-05	CONVERGENCE TEST DELTA-TEMPERATURE								D-157	
6	0.100000E401	FLAG >1.0 FOR DYTOD DUMP AT RUN END								E-158	
12	0.100000F 01	CORE DUMP AFTER ERROR STOP								G-158	
* 80	0	0	PRINT OUT SPECIFICATIONS								H-159
D101	118	0	0.	0.	0	0	0	0	0		160
0 3	0	0	0.	0.	0	0	0	0	0		B-160
* 90	0	0	0.	0.	0	0	0	0	0		161
RUN CONTROL											
0	0	0	0.	0.800000E 01	0	0	0	0	0		162
0	0	0	0.500000E 01	0.200000F-01	0	0	0	0	0		B-162
0	0	0	0.100000F 02	0.	0	0	0	0	0		163
* 96	1	0	0.	0.	0	0	0	0	0		164
PLOT SPECIFICATIONS											
***** Y AXIS LABEL *****											
1	0112	0	TEMP.-DEG.F.								***** X AXIS LABEL *****
0113	0									TIME-HRS.	
0106	0										
999	0	0									

Fig. XVIII- 2. Continued.

SECTION XVIII

5. Heater Power

100, 150, 200, 250, 300, 400 and 500 BTU/hr
for $T_3 = 135^\circ$; 20, 40, 60, 80 and 100 BTU/hr
for $T_3 = 90^\circ\text{F}$

C. TRANSIENT ANALYSIS RESULTS

The important results of the analysis are contained in the following graphs.

1. Graph (Fig. XVIII-3) shows the temperature of node 12 (one end of the transducer) over the 10th hour of operation with a heater power input of 100 BTU/hr and a control temperature of 135° (± 0.001 dead band). The mean temperature at this point is 134.5547°F with a standard deviation about the mean of $2.06 \times 10^{-3}^\circ\text{F}$ or $1.144 \times 10^{-3}^\circ\text{C}$. The periodicity and amplitude of this fluctuation is directly related to the two periodic boundary temperatures (T_1 and T_{17}).
2. Fig. XVIII-4 shows a comparable curve but without boundary temperature fluctuation note that the fluctuations are considerably reduced.
3. Fig. XVIII-5 is a lower heater power curve with a lower control temperature. Heater power was 2⁰ BTU/hr and the control temp was 90° (± 0.001 dead band). Note here that there is little difference in the fluctuation pattern from that of Fig. XVIII-3 (both curves have identical boundary temp fluctuations).
4. Fig. XVIII-6 is a graph of the oil film temp ($T-6$) with the same conditions as in Fig. XVIII-3. (Note the change in vertical scale.) Here we can see the over-all range in temperature fluctuation is $< \pm 0.02^\circ\text{F}$. This is below the bearing design requirement of $\pm 0.03^\circ\text{F}$ discussed above.
5. A careful examination of the data showed no temperature in the thermal model varied more than $\pm 0.1^\circ\text{F}$ except for the control temperature itself. ($T-3$)

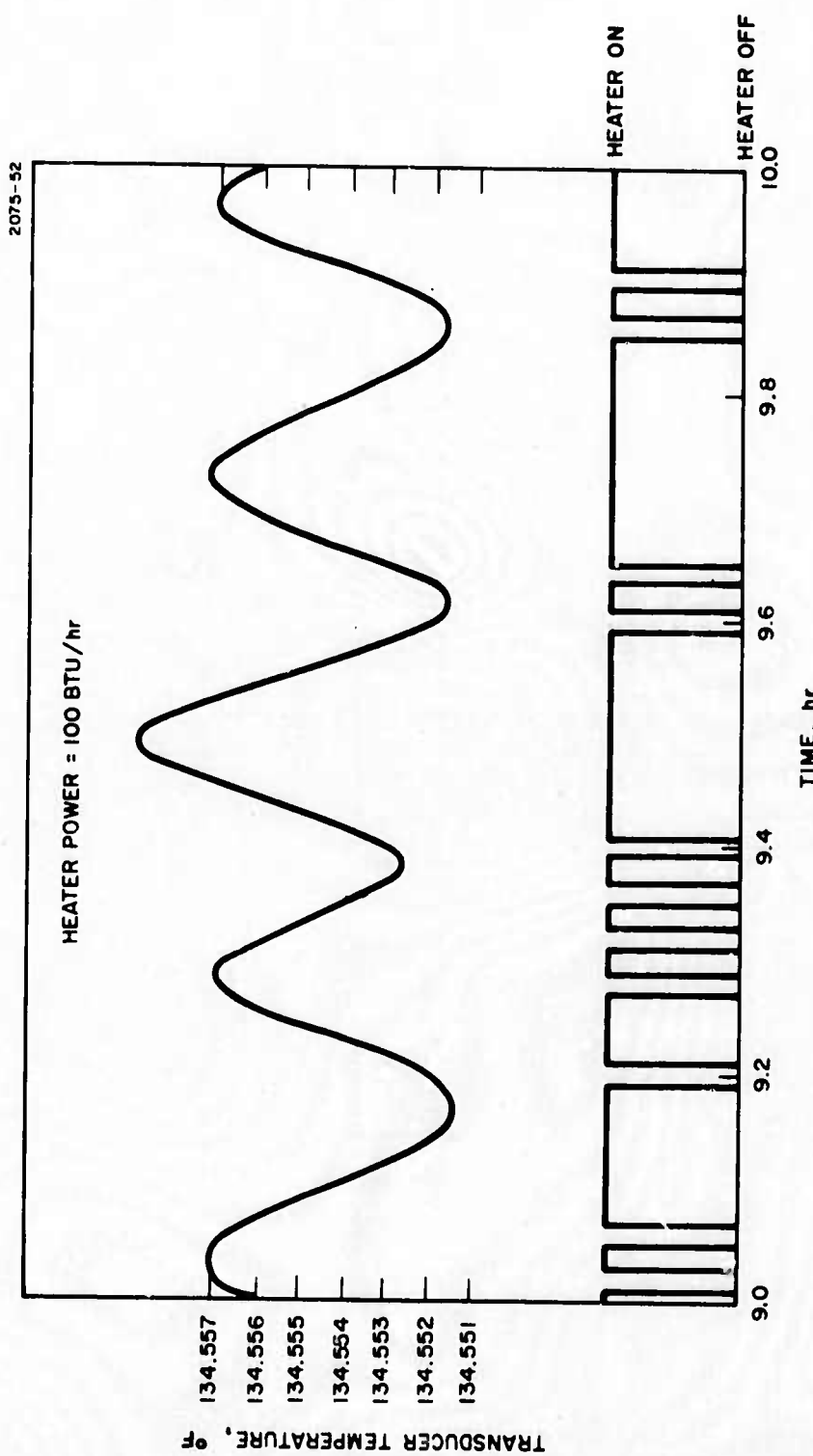


Fig. XVIII-3. Node 12 Temperature Curve (10th Operational Hour).

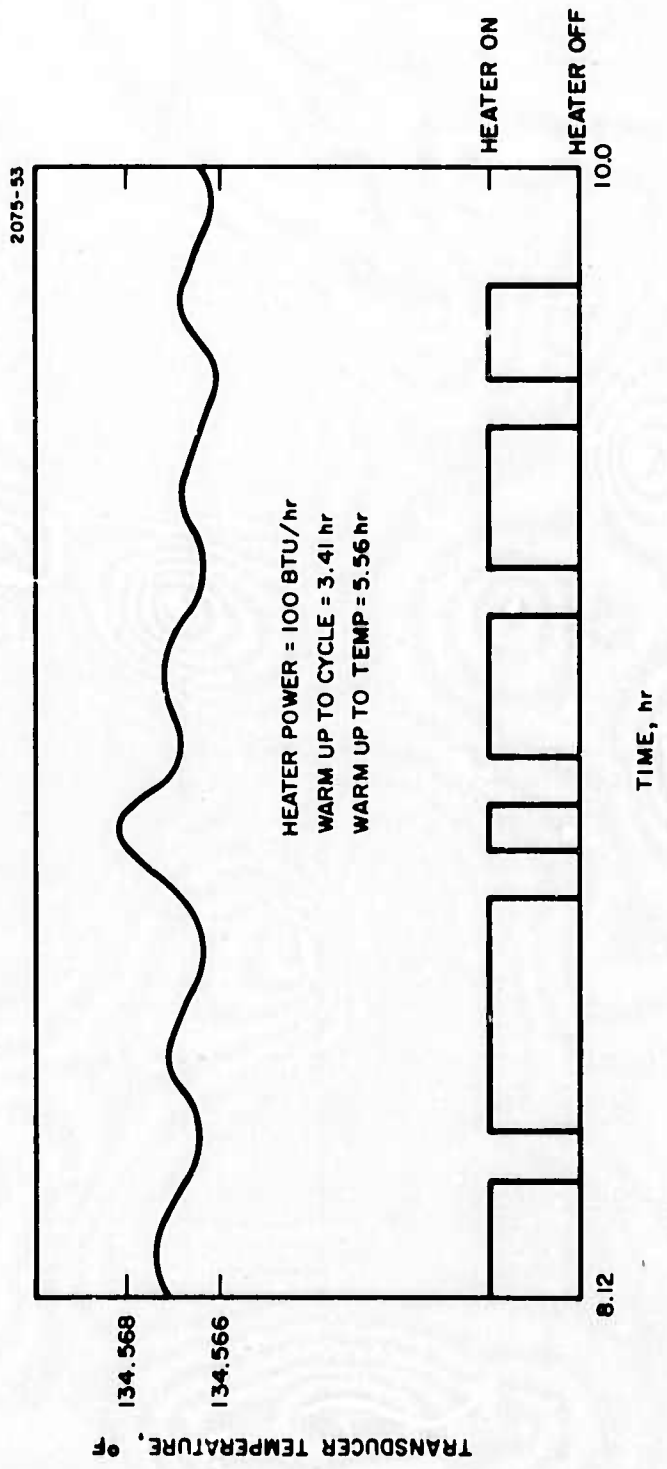


Fig. XVIII-4. Node 12 Temperature Curve (10th Operational Hour) Without Boundary Temperature Fluctuation.

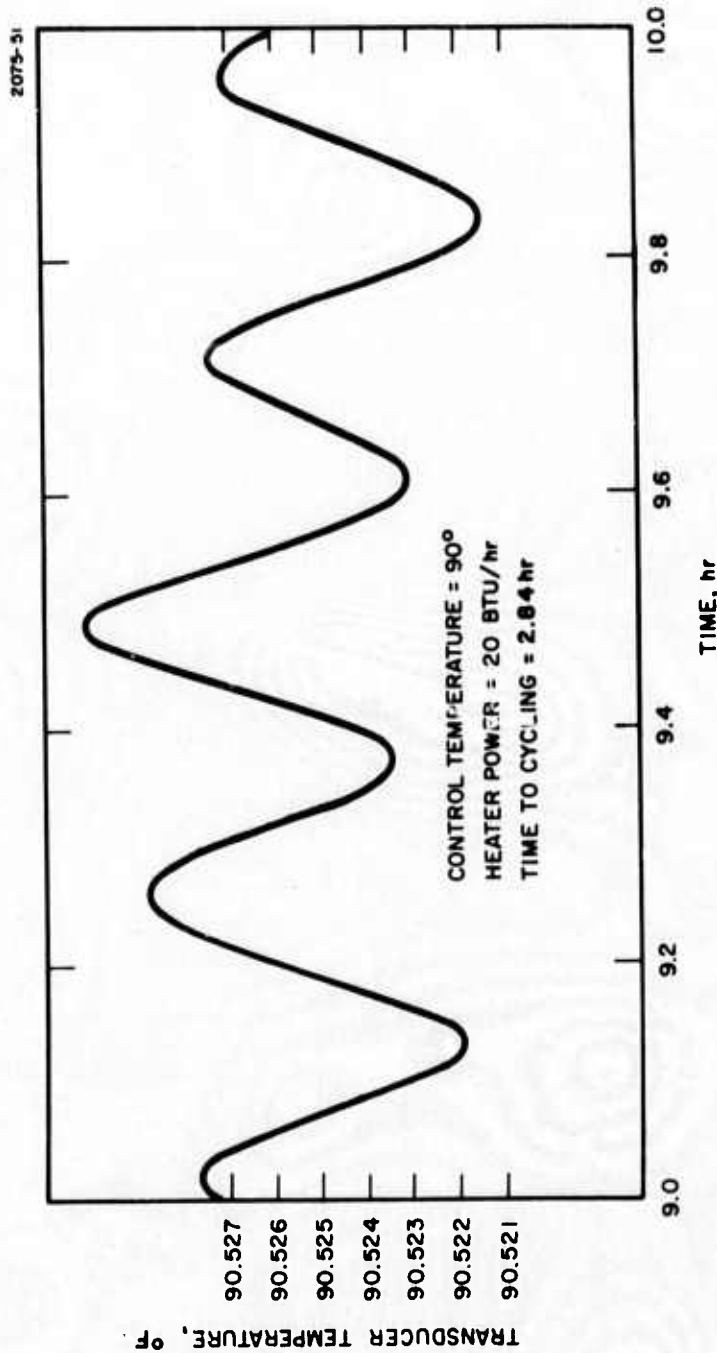


Fig. XVIII-5. Lower Heater Power Curve with Lower Control Temperature.

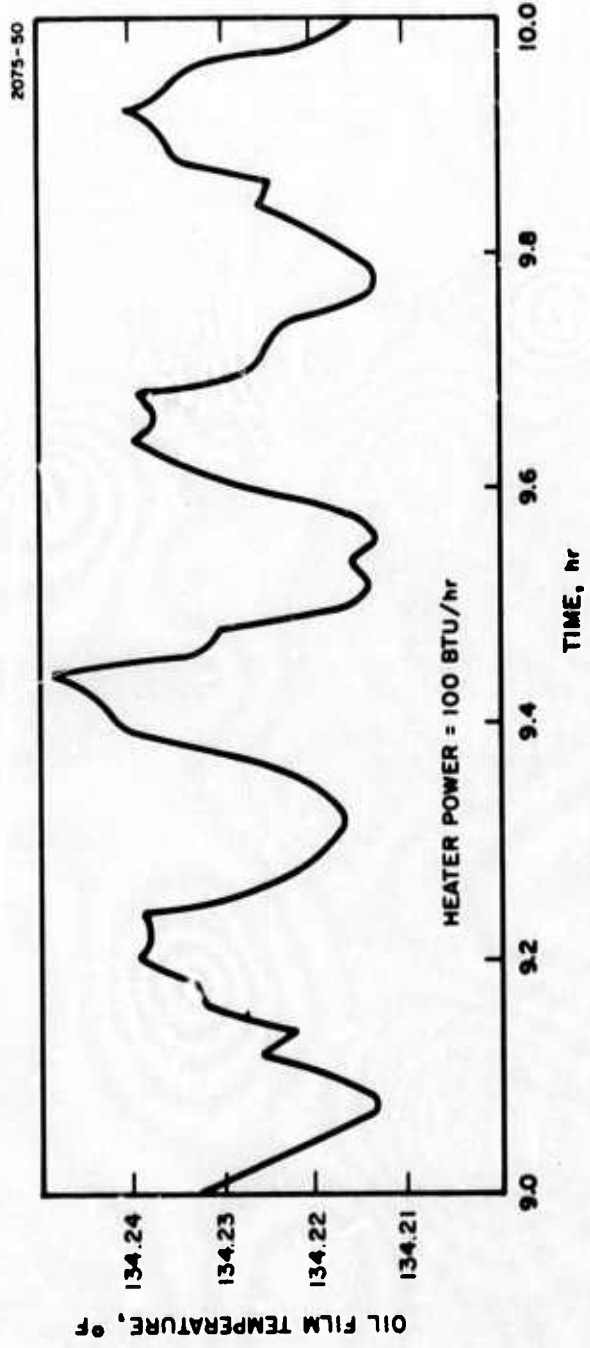


Fig. XVII-6 Oil Film Temperature (conditions same as Fig. XVII-3)

SECTION XVIII

A plot of the control temperature during the 10th hour of the run is shown in Fig. XVIII-7 (again note a change in scale).

The variation on the control temperature is a maximum of $\pm 0.235^{\circ}\text{F}$ about the nominal temperature.

This temperature variation will produce a length change of $\pm 4.6 \times 10^{-6}$ in. over the 1.5 in. length of the case. This length change is doubled because of a similar temperature variation on the other end of the sensor. Therefore, the total length change is $\Delta l = 9.2 \times 10^{-6}$ in.

D. SUBSYSTEM SPECIFICATIONS

Specifications for the thermal control subsystem are as follows:

1. Heater type and power.

Wrap-around molded rubber heaters with output to the sensor of 100 to 200 BTU/hour (based on 135°F operating temperature).

2. Operating temperature is noncritical but should be no higher than 135°F (operating temperature will probably be determined by bearing operation considerations).

3. Controller type.

The "bang-bang" type of controller with a dead band no greater than 0.001°F is satisfactory, however, additional analysis may show that a proportional type controller would lead to better operation.

4. Temperature sensors.

At least four thermistors on each half of the gradiometer case. (Disk thermistors $\approx 1/4$ in. dia. and $1/16$ in. thick.) All 8 inputs paralleled into the temperature controller.

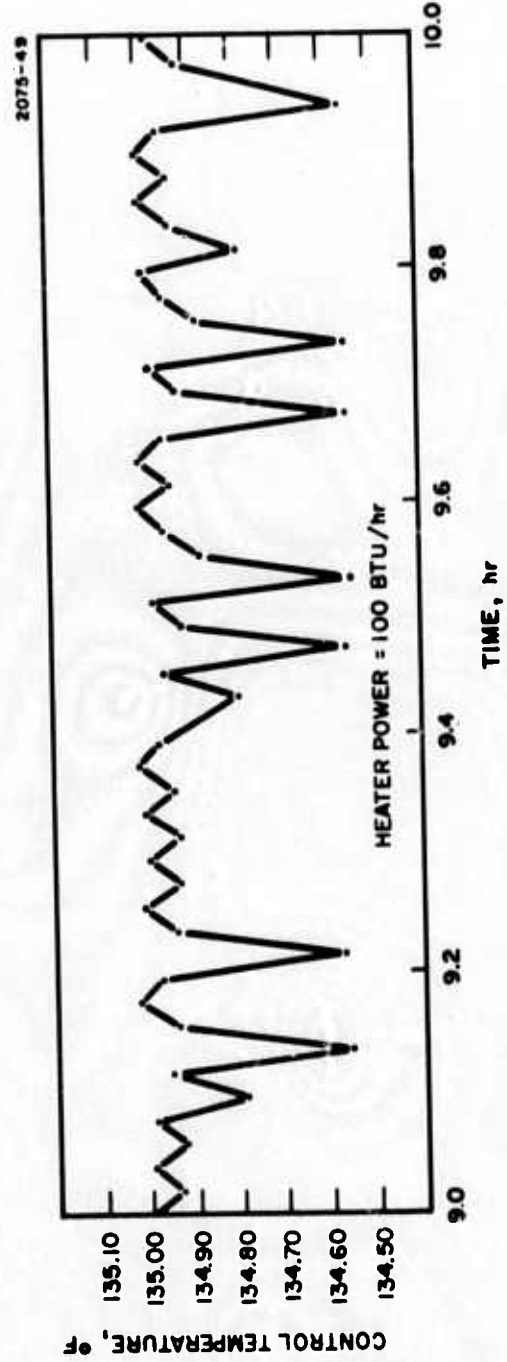


Fig. XVIII-7. Plot of Control Temperature During 10th Operational Hour.

SECTION XVIII

E. CONCLUSIONS

Conclusions are stated for each of the tolerance requirements outlined in Section XVIII-A

1. Transducer Temperature

Analysis of the 135°F run with varying boundary conditions showed temperature variation near the upper limit of that which could be allowed by signal phase shift considerations. However, in a run with constant boundary temperatures the fluctuation of the transducer temperature is well within requirements. Changes in operating temperature seem to have little effect on this problem.

Although the specification is met care must be taken that the actual operating conditions are no worse than those postulated in this model. Any possible improvements in control such as proportional thermal control or a reduction in boundary value fluctuations should be investigated.

2. Oil Film Temperature Variations

Oil film temperature variations were within the specifications established by a reasonable margin.

3. Length Stability

Temperature fluctuations are just low enough to maintain the bearing oil film gap within specifications. However, there is much room for improvement in this temperature control system and serious consideration will be given to modifications which will reduce these fluctuations. In this case, more detailed modeling may give a more accurate picture of the actual temperature-length relationship existing in the sensor case.

SECTION XVIII

F. RECOMMENDATIONS

It is recommended that the thermal studies be continued as follows:

1. Modify the model to reflect near final design parameters.
2. Model a proportional controller for use in the thermal control subsection.
3. Refine the model by subdividing the thermal parameters to reflect the accuracy of the completed design.
4. Add additional thermal insulation to the outside of the sensor to reduce the effect of boundary layer fluctuation.

SECTION XIX

SIGNAL READOUT SUBSYSTEM

The signal readout subsystem is the same as that shown in the Semiannual Technical Report No. 1. The circuit diagram is reproduced here for convenience as Fig. XIX-1. The signal readout circuit is in the upper part of Fig. XIX-1. The power supply and remote arm balance logic circuits are shown in the lower part of the figure. These latter circuits are shown in more detail and discussed in other appropriate sections of this report.

A. GENERAL DESCRIPTION

The input stage consists of two high-input-impedance, low noise, field effect transistors with a constant current common drain return. This first stage provides some gain but its primary purpose is to voltage buffer the transducer signal and provide a low impedance output. The next stage provides the gain required to drive the AM-FM converter. The gain of this stage can be set to "normal" or "low" by external commands through the remote arm balance digital logic circuits. "Normal" gain provides for full, 10%, FM frequency deviation with a 10,000 EU input signal. The "low" gain provides full FM frequency deviation with a 100,000 EU input signal. The "low" gain will be used during initial balance and alignment tests.

The AM-FM converter is a standard integrated circuit that is generally called a function generator in the literature. The converter is adjusted to provide a center frequency of approximately 200 kHz with peak to peak frequency swings of 180 to 220 kHz. The FM output is buffered and then fed to an output transformer to couple between the sensor rotor and stator. The output of the stator side of the FM transformer is buffered out to two channels. One channel goes to the Digital

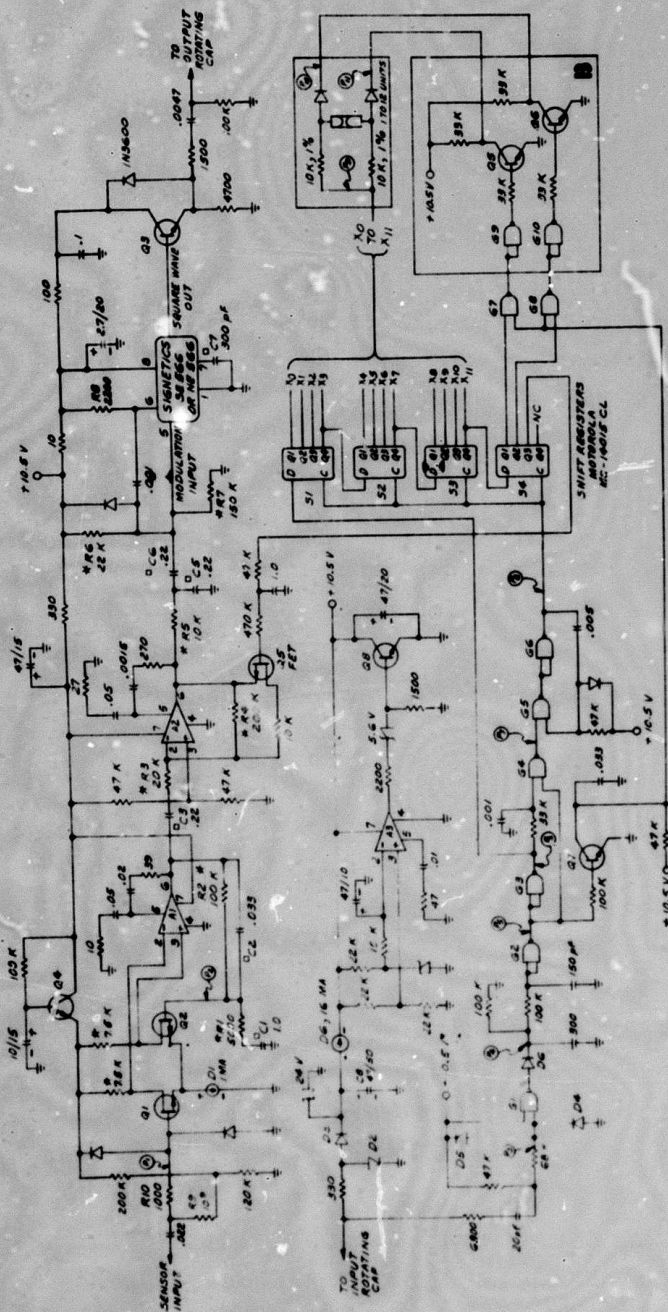


Fig. XIX-1. Signal Readout Subsystem Schematic Diagram.

- NOTES
 1. ALL RESISTORS MARKED WITH Δ ARE METAL.
 2. ALL CAPACITORS MARKED WITH Δ HAVE $< 10^{-4}$
 3. ALL OF AMPS ARE PRECISION MONOLITHICS
 5537ASC
 4. ALL NAND GATES ARE MOTOROLA MC NOVIC
5. IF ONLY ONE BALANCE TIME WILL BE OBTAINED
 AT ONE TIME, BOX B MAY BE ELIMINATED

SECTION XIX

Data Reduction Subsystem and the other to the Analog Data Reduction Subsystem. These two channels are completely independent and do not interact or interfere with one another in any way.

This signal readout subsystem has been used for all Hughes RGG sensor experiments and is considered to be completely satisfactory for the RGG Prototype Design. The specific circuit shown in Fig. XIX-1 has been breadboarded and given preliminary tests. In general the tests results have been satisfactory. The generation of low noise test signals of a few tens of nanovolts with adequate phase and amplitude stability has been more difficult than adjusting the Signal Readout Subsystem to perform as required.

B. ROTOR MOUNTED ELECTRONICS SIZE ESTIMATES

The preamplifier, transmitter, rotor power supply and digital logic circuits are all mounted in a toroidal package mounted on the sensor rotor brace plate. The location of this toroid in the rotor is shown in Section V, RGG Layout Drawing.

The schematic diagram has been studied by the Hughes Microelectronics Division. The engineers at the Microelectronics Division are experts in design and manufacture of precision integrated circuits. They have stated that they could build the complete rotor electronics as one single integrated circuit. However, due to possible yield problems and manufacturing convenience the Microelectronics Division has recommended that the circuit be divided into its four basic functional parts and that some discrete components be used. A mockup of the complete rotor mounted electronics package is shown in Fig. XIX-2. This has been assembled from dimensionally accurate, commercially available components and includes the four "flat-pack" integrated circuits recommended by the Microelectronics Division. The size, weight, and form factor for the rotor mounted RGG Prototype Design electronics is not considered to be a problem.

M9285

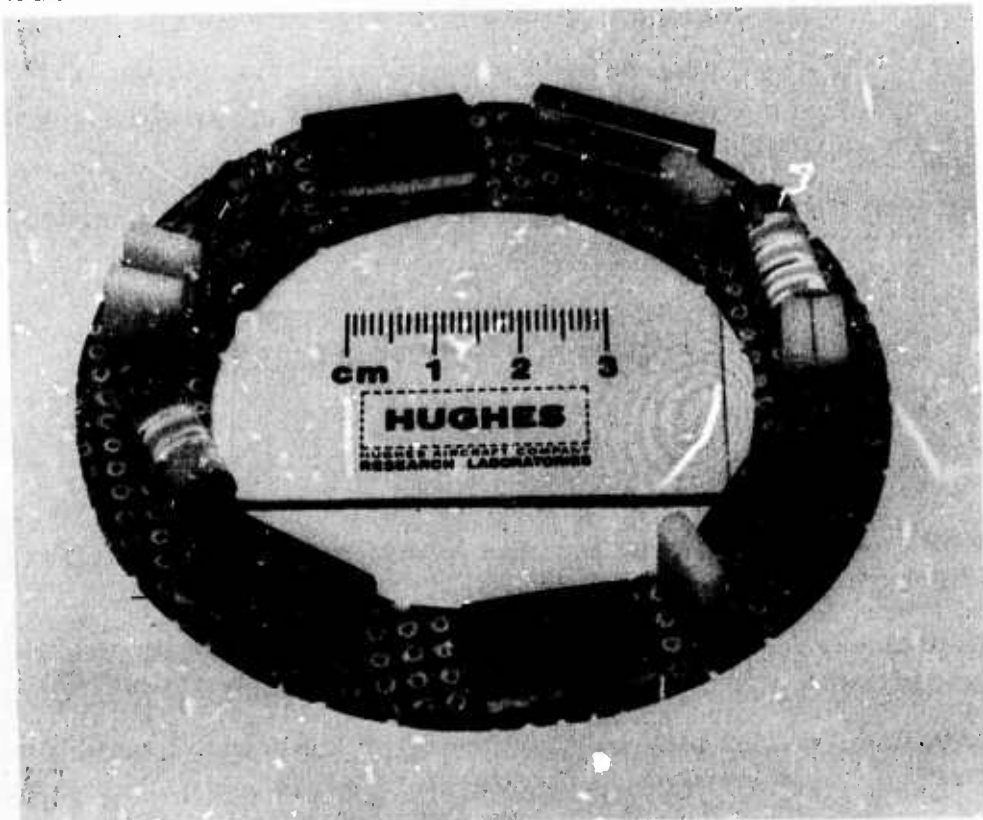


Fig. XIX-2. Full Scale Mockup of Rotor Mounted Electronics.

SECTION XX

ANALOG DATA REDUCTION SUBSYSTEM

The output of the signal readout subsystem is a frequency modulated carrier with a carrier frequency of about 200 kHz. This signal will be demodulated by a phase-locked loop with synchronous amplitude modulation lock detection. This will be accomplished by a single integrated circuit which will also buffer the output with a power stage. The device is called a Tone Decoder in the literature and they are commercially available with excellent characteristics. The Signetics No. 567 will be used in the prototype design.

The output of the Tone Decoder will be a phase and amplitude modulated signal at twice the sensor rotor spin frequency. This signal is an accurate simulation of the gravity gradient input to the RGG sensor. This signal will be passed through a phase sensitive demodulator and filtered with an appropriate time constant to produce an overall sensor signal integration time of 10 sec. The filtered sine and cosine channel gradient signals as well as the root-sum-square will be available to drive a recorder.

The foregoing paragraphs describe the analog data reduction process that Hughes has used in the past for all of the RGG tests. It is fast, versatile and convenient. It provides for initial sensor adjustment and testing in a simple nonambiguous manner. Also, such a data reduction subsystem is entirely adequate for RGG's with vertical spin axis. However, for horizontal spin axis RGG's we have been unable to locate phase sensitive demodulators and amplifiers which have sufficient phase and amplitude accuracy to allow the one EU required sensor accuracy to be conclusively demonstrated.

Therefore, the analog data reduction system will be retained for the Prototype Design, but it will be used for initial adjustment and system monitoring. The primary data reduction will be accomplished by means of a digital computer. The procedure is discussed in the following section.

SECTION XXI

DIGITAL DATA REDUCTION SUBSYSTEM

As discussed in Section II, Sensor Design Integration, it became apparent that digital speed control and digital data reduction was the most cost-effective method of attaining the required resolution and dynamic range for the output signals. Preliminary designs of digital subsystems were made using discrete components. The requirements were simple and straightforward but the number of individual components became excessive even when the largest integrated circuits available as discrete packages were used. It was found that a relatively inexpensive digital computer of the class known as "minicomputers" could handle about 99% of the requirements. Only some relatively simple input/output circuits were required in addition to the minicomputer.

Once a minicomputer was established as a prototype design subsystem it was found that it could be beneficially utilized for a number of tasks. The operation of the digital system is discussed in detail in the following paragraphs.

A. GENERAL

The digital computer will be utilized to perform the following tasks:

1. Maintain the average sensor rotor speed constant to one part in 10^8 .
2. Perform phase sensitive demodulation of the sensor output signal.
3. Perform the filtering of the signal.
4. Provide the " g^2 " compensation required to compensate for the residual arm aniselasticity.
5. Print out in decimal notation the gravity gradient tensor components.

SECTION XXI

The method of maintaining a constant average rotor speed was described in Section XVI, Rotor Speed Control and will not be repeated here.

B. FM SIGNAL DECODING

The encoder disk used in the rotor speed control is reproduced here for convenience in Fig. XXI-1. It is convenient to describe the data signal handling if it is assumed that the light slots on the encoder disk are perfectly placed. In this case, as each slot passes the light source an output pulse is obtained at exactly each 1/8th revolution. Note that this is 1/8 rotor revolution exactly and is physically locked to the rotor and stator reference points regardless of either long or short time speed variations. Therefore the photocell output pulses are physically related to the phase of the input gravity gradient signal. At this point we have 8 output pulses per rotor revolution representing two full cycles of the gravity gradient signal. The gravity gradient signal is alternating at a frequency of twice the spin speed ($f_o = 2 f_s$). The positive going gravity gradient signal causes the frequency of the FM transmitter to increase above the 200 kHz carrier and the negative going gravity gradient signal causes the FM transmitter frequency to be reduced below 200 kHz. This conversion is illustrated in Fig. XXI-2(a). Thus, if the FM transmitter output cycles are counted during 1/4 rotor revolution an FM cycle count for the positive going half of the gravity gradient signal will be obtained. A count for the next 1/4 rotor revolution will give a cycle count for the negative going gravity gradient signal. If these two counts are made alternately, each 1/4 revolution for a full revolution of the rotor we have:

$$\text{Count } S_{CI1} = \text{Carrier counts} + \text{counts due to positive GG signal} \quad (1)$$

$$\text{Count } S_{CI2} = \text{Carrier counts} - \text{counts due to negative GG signal} \quad (2)$$

2075-16

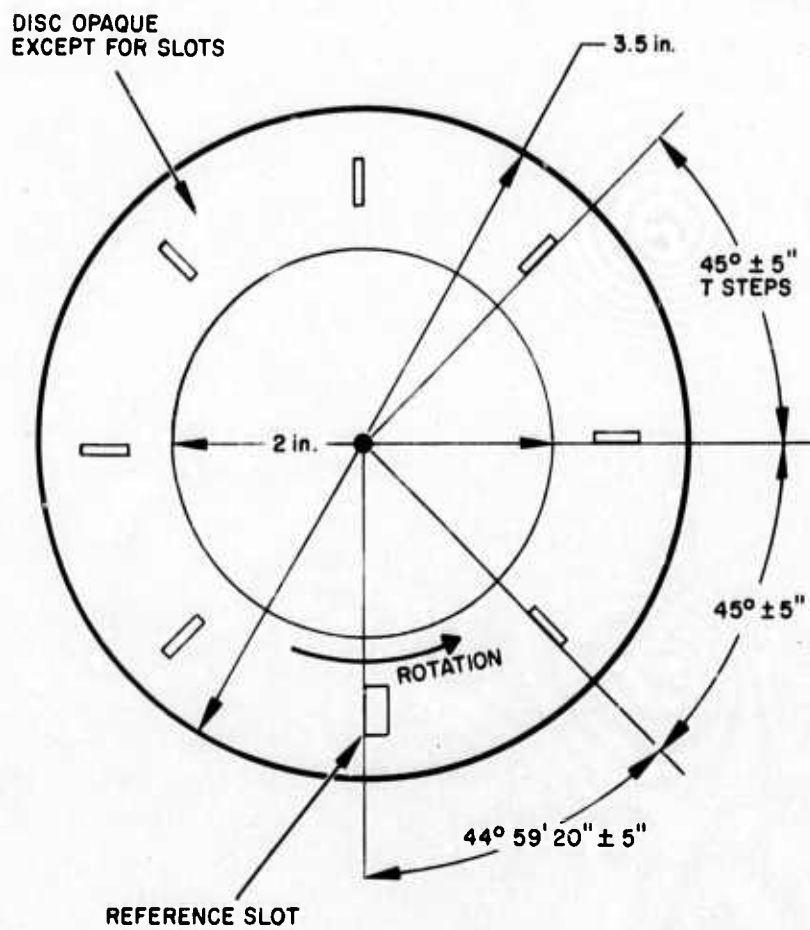
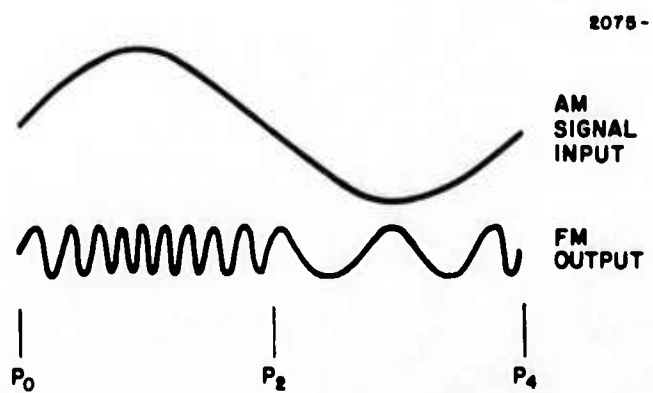
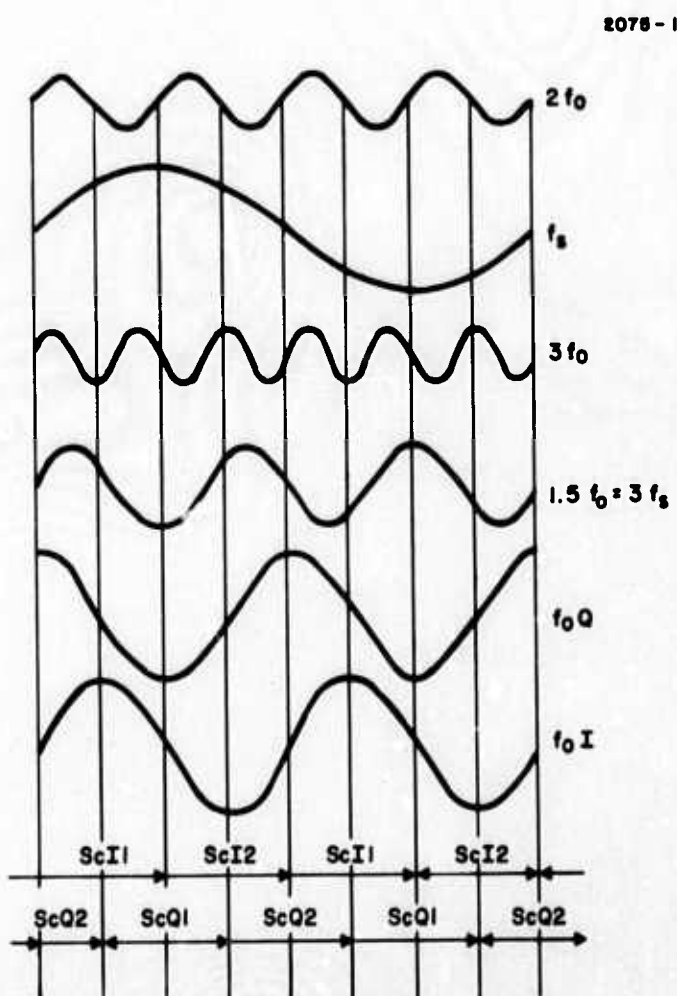


Fig. XXI-1. Encoder Disk.



(a) AM TO FM CONVERSION



(b) I AND Q COUNTER SWITCHING POINTS

Fig. XXI-2.
AM to FM and Signal Counter Switching.

SECTION XXI

Adding the two counts

$$S_{CI1} + S_{CI2} = 2 \times \text{carrier counts} \quad (3)$$

Subtracting the two counts

$$S_{CI1} - S_{CI2} = 2 \times \text{counts due to GG signal} \quad (4)$$

In addition to these two counters, which are designated I for inphase, two similar counters are set to count on the encoder disk slots 1/8 revolution removed from the I phase and these are designated Q phase.

Figure XXI-2(b) illustrates the operation of these counters at the encoder disk pulse points designated P_0 - - P_7 .

It is also evident from Fig. XXI-2(b) that by taking the counts in the registers over a full revolution that signals with frequencies of f_s , $3f_s$, $2f_o$ and $3f_o$ all average to zero. That is, interfering signals harmonically related to f_o will all be rejected.

In the computer the two component counts of the I phase are combined and fed to a running average calculation. The length of the running average calculation is such that when it is combined with the inherent sensor time delay gives a signal integration time of 10 sec. The contents of the running average register will be read every 32 revolutions of the rotor - slightly faster than once every 2 sec - divided by the appropriate scaling factor and printed. The Q phase will be treated in a similar fashion. These printouts of 5 significant decimal figures have adequate resolution and accuracy to allow the RGG to be evaluated to the 1 EU level.

C. ROTOR POSITION

In the previous paragraphs it was assumed that the slots in the encoder disk were perfectly position. It is not practical to make and install an encoder disk with the required accuracy. Therefore the

SECTION XXI

encoder slots are deliberately moved ahead. The photocell output indicates 1/8 rotor revolution has occurred before the rotor actually reaches this position. The amount of this lead will be measured on the completed sensor and the lead, in terms of the 10 mHz reference signal, will be stored in a computer register for each slot. Then, when the computer receives a slot pulse, it will wait the proper number of 10^7 Hz counts before it outputs the true pulse to the signal counting registers. Calculations show that in the short time between the photocell pulse and the stored delay the rotor cannot possibly speed up or slow down enough to cause even one error count in the 10^7 Hz signal reference.

This signal handling technique is considered to be completely satisfactory for the prototype design.

D. ANISOELASTIC COMPENSATION

It is shown in Section XIII that it is unlikely that the RGG sensor arms can be made so nearly isoelastic that compensation will not be required. In Section IX the method of calculating the compensation is shown. In this section the actual method of accomplishing this compensation will be described.

Three orthogonal accelerometers will be mounted on the same base as the RGG sensor. It is expected that the inertial navigation system accelerometer outputs will be available for this purpose. The accelerometer outputs will be converted A to D at 50 times per second and these will be read by the minicomputer. The computer will normalize, square and take the products of the appropriate acceleration components. These terms must be stored in registers for a time equal to the time constant of the sensor, about 2.71 sec. The correction terms are then subtracted from the I and Q signal cycle count registers previously described.

SECTION XXI

E. COMPUTER INTERFACE AND SPECIFICATION

Figure XXI-3 is a functional block diagram of the minicomputer and its Input/Output (I/O) unit. It is evident that the I/O is quite simple but it is not so evident that these I/O components must be high speed and synchronous. That is, the counters and latches must be able to count, without error, at a rate considerably above 10^7 Hz so that read and switching functions can occur between the 10^7 Hz cycles. Also, the counters must be clocked (synchronous counters) so that neither a 10^7 Hz input or a signal input count is lost or misread. These requirements present no particular problem since such components are readily available.

Although the counters and latches must be fast the speed requirements on the minicomputer are minimal. Once the data is in the latches the computer read in and the data processing functions can be done at a relatively low speed.

The requirements for the minicomputer are listed in Table XXI-1.

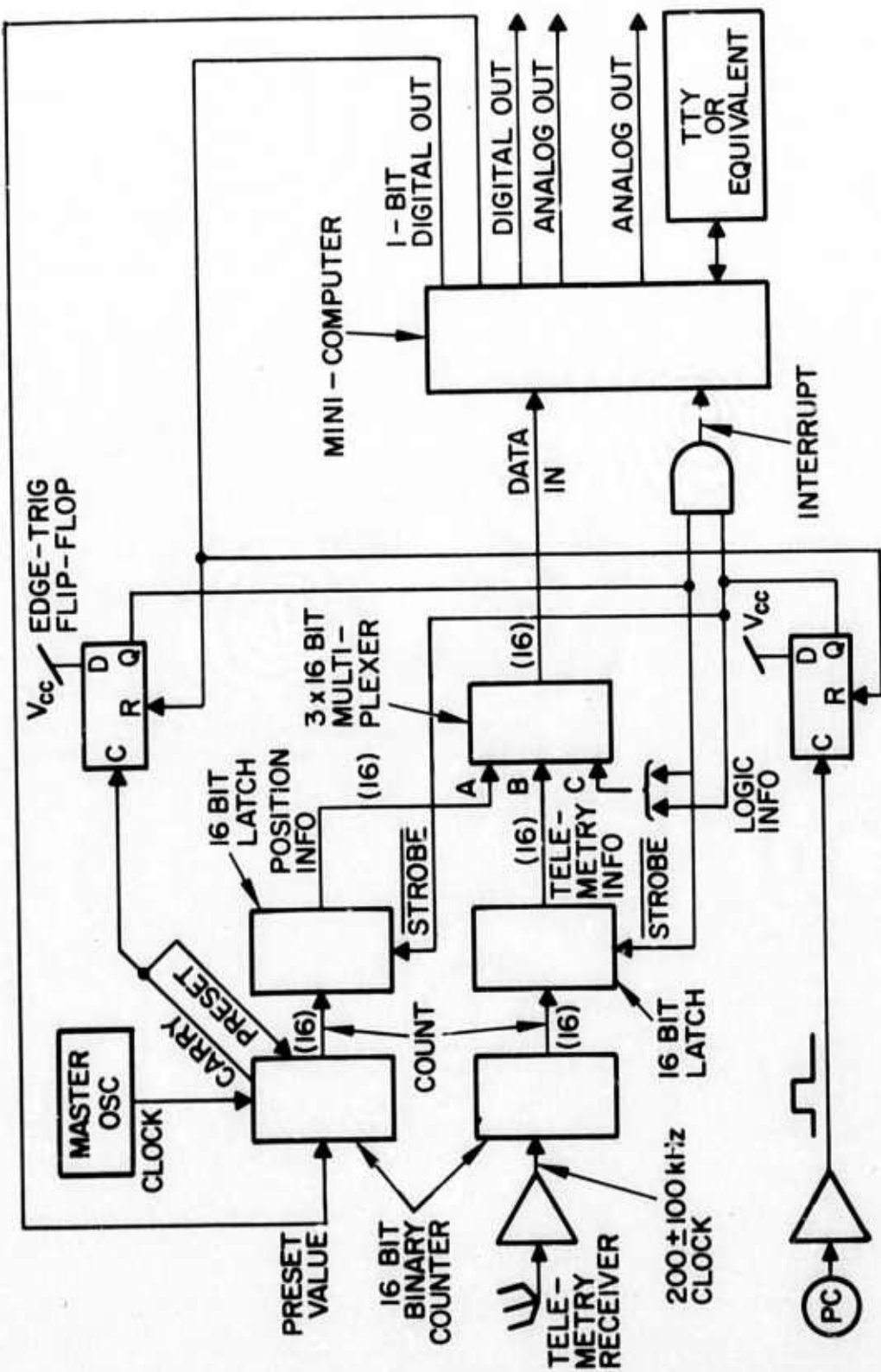


Fig. XXI-3. Minicomputer and I/O for RGG Prototype Design.

SECTION XXI

TABLE I
Minicomputer Specifications

<u>Word Length</u>	16 bits	<u>Maximum Time per Instruction</u>
<u>Instruction Types Required</u>		
Add, Subtract, logical and, logical or		2.5 μ sec
Shift one bit right or left		2.5 μ sec
Memory fetch and store		2.5 μ sec
Jump and conditional jump		5 μ sec
Multiply		12 μ sec
Divide		15 μ sec
Access IO channels		5 μ sec
<u>Storage Required</u>		
8K of 16-bit words		
<u>I/O Ports</u>		
2-16 bit input ports } preferable but not necessary		
1-4 bit input ports } 1-16 bit input is minimum requirement		
2-16 bit output ports		
1 interrupt input		
1 teletype interface		
<u>Software</u>		
Cross-assembler (preferably compiler) for IBM 370/165 – paper tape output		
Core-resident paper-tape loader (preferably ROM backup)		
<u>Peripherals</u>		
1 Teletype ASR such as ASR 33		

T872

SECTION XXII

PHASE II DIGITAL SYSTEM BENEFITS

A digital data reduction subsystem is required to obtain the accuracy and resolution necessary to measure gradients of ± 4500 EU to an accuracy of 1 EU. Although it would be possible to build the digital data reduction subsystem using discrete components, a minicomputer is a more cost-effective solution. Once a minicomputer was made a part of the prototype design, it became apparent that it would provide significant benefits during Phase II of this development program. These benefits are discussed in the following paragraphs.

A. COMPUTATIONAL REQUIREMENTS COORDINATION

Sub-Line Item 0002AC of the Statement of Work for this development program requires the following: "Determine operational and computational procedures to obtain average gradients for 10-second intervals in terms of EU such that the procedure will not contribute more than 0.1 EU error." This has been accomplished already. The procedure required to obtain any gravity gradient tensor component from individual gradiometer outputs was shown in the original proposal. These gradiometer outputs have been established in digital form and can be combined easily by the digital computer.

B. DIGITAL ROTOR SPEED CONTROL

It was stated in Section XVI, Rotor Speed Control Subsystem, that the prototype design was based on an analog speed control servo loop using a tachometer as the basic velocity feedback. This, although satisfactory, requires extreme care in amplifying the tachometer signal.

SECTION XXII

It was shown in Section XXI, Digital Data Reduction Subsystem, that an output pulse would be generated each 1/8 revolution (~ 140 per sec) of the sensor rotor with an instantaneous position uncertainty of no more than 2.2×10^{-5} rad, 1 sigma. Since the average speed of the rotor is known to seven significant figures, the number of cycles of the 10 MHz reference that should occur during 1/8 revolution of the rotor can be calculated and prestored in a computer register. A counter can count the number of 10 MHz cycles that actually occur during each 1/8 revolution as determined by the above mentioned position pulses. The difference between these two counts is the position error accumulated during 1/140 second, or an error rate signal. The average of this error rate signal is excellent, but each output is noisy due to discrete quantization levels.

If the demands on the rotor speed control servo were not so severe, the noise in the above mentioned error rate signal could be ignored and a straightforward digital servo designed. However, presently available analysis methods are not adequate to predict the performance to the level required in this application.

It is estimated by some digital servo experts that satisfactory performance can be obtained by experimentation after the sensor is built and operating. However, this is not sufficiently certain to be used as a prototype design. Therefore, the prototype design will include a digital servo and an analog servo. The analog will be used in initial tests and then the digital servo will be mechanized. It is expected that the digital rotor speed control will be used in the final tests.

C. ACTIVE COMPENSATION OF THE RGG

Because a digital computer is now a part of the prototype design, active compensation concepts now are attractive and feasible. Active compensation, as defined by Dr. Dan DeBra of Stanford University, uses a computer model of the RGG sensor to correlate

SECTION XXII

casual inputs with sensor outputs and correct the sensor or the data output on a real-time basis for changes in the sensor. For example, there will be a continuous variation in the acceleration along the sensor X axis. Ideally, the sensor will not respond to this variation; however, if the sensor output contains a signal that is exactly correlated with this casual acceleration input, output could be caused by imperfect arm anisoelastic compensation. The computer would be instructed to change the compensation calculations until the effect disappeared.

Another example of active compensation that may be used is as follows: The sensor test signal described in Section XVII would be turned on and off at 1 sec intervals. If the sensor is operating at exactly the proper frequency and therefore the proper output signal phase, this test signal will all appear in one channel and can be subtracted out of the data. However, if some of the test signal appears in the other channel, the computer will know that the reference spin frequency is incorrect and also how it should be changed to correct the phase angle. The computer can be instructed to make this frequency change automatically.

The active compensation concept will be studied during Phase II.

SECTION XXIII

RGG CALIBRATION TECHNIQUES

The RGG is a new inertial sensor, and standardized test, calibration, and evaluation procedures have not been established. Some of these procedures have been developed by Hughes during the earlier experimental development work on the RGG. Standardized procedures have been developed for gyroscopes and accelerometers and many of these concepts are believed to be applicable to the RGG. The following paragraphs illustrate some procedures that Hughes expects to utilize during test and calibration of the RGG.

A. BIAS ADJUSTMENT

The sensor will be mounted on a level, vibration-free base and allowed to stabilize, first with the spin axis vertical. The sensor case will then be rotated in 32 precisely indexed steps about the spin axis. The sensor output, averaged over a period of 1 min, will be recorded at each index position. Since sensor biases are case fixed, they will not change as the sensor is indexed around. The local gravity gradient, local earth's magnetic field, local masses, and initial spin axis tilt (if any) will remain constant and earth-fixed as the sensor is rotated. A 32 point Fourier analysis will allow determination of the sensor bias coefficients in terms of direction and magnitude of the local gravity gradient.

Once the sensor bias has been determined, the operating temperature will be changed slightly and the sensor retested. The change in temperature will aid in determining the following five characteristics: temperature sensitivity of the sensor undamped natural frequency, temperature phase shift sensitivity, spin bearing drag temperature coefficient, and the phase and scale factor sensitivity of the signal readout subsystem.

SECTION XXIII

The sensor will be turned to place the spin axis in a horizontal plane and the above procedure repeated. In addition to the parameters previously mentioned, the anisoelastic torques of the sensor arms are added to the fixed torques.

B. SCALE FACTOR CALIBRATION

Accurate calibration of the absolute scale factor of the RGG is accomplished best by introducing accurately known angular rates at right angles to the sensor spin axis. These rates can be introduced best by mounting the sensor on a precision rate table or on a stable platform that is commanded to precess at a specific rate in inertial space. In either case, a completed operating sensor is required.

The sensor can be calibrated to an accuracy of about 2.5 to 5% during assembly by adding accurate amounts of arm mass unbalance or arm inertia unbalance. The sensor is then vibrated as appropriate to excite the desired unbalance mode. These methods are simple and convenient, but the overall accuracy is not adequate for the completed RGG.

There are a number of other methods of obtaining approximate RGG calibrations, but none so far discovered can approach the accuracy of the two just described.

C. ARM MASS AND INERTIA BALANCING

Three unbalance parameters are of importance in precision balancing the sensor arm pair. These are: (1) arm sum mass unbalance, (2) arm differential mass unbalance, and (3) arm sum mode mismatch.

The first, arm sum mass unbalance, is defined as the sum of the individual arm unbalance vectors. The individual unbalance vector is defined as the distance between the individual arm center of

SECTION XXIII

mass and the elastic (torsional) axis of its support pivots. Thus the sum of these two unbalance vectors must be initially adjusted to a specified minimum value (8×10^{-3} gm-cm).

Arm differential mass unbalance is defined as the difference between the individual arm mass unbalance vectors and also must be adjusted to a specified minimum value. Because of the sensor's considerably larger sensitivity resulting from differential mass unbalance, it must be adjusted to very close tolerances, and this is accomplished in two steps. First, it is adjusted via mechanical balance screw adjustments to within the specified limit of $\pm 8 \times 10^{-4}$ gm-cm. Then fine balancing is accomplished using the mercury balance tubes discussed in Section XVII.

The third unbalance parameter, arm sum-mode mismatch, is due to a mismatch of the ratio of support pivot spring rate to arm mass moment of inertia between the two arms. This error may be reduced by adjusting either the support pivot spring rates or the moment of inertia. Spring rate matching is difficult because it would require trimming material from the support pivots that is relatively inaccessible. Moment of inertia balancing achieves the desired result and is considerably less difficult. Mechanical balance adjustment screws can be used to adjust the sum-mode mismatch to the required level of $\Delta I/I = 10^{-7}$.

The three unbalance parameters result in RGG sensor error sensitivities to different types of vibrational inputs. The arm sum mass unbalance gives rise to a sensor error proportional to angular vibration normal to the sensor's spin axis. Sensor arm differential mass unbalance produces sensor errors proportional to the translational vibration normal to the sensor's spin axis. Sum mode mismatch results in sensor errors proportional to angular vibration about the spin axis. Thus, by exposing the sensor to the excitation sources, one at a time, the sensor output signal can be used as a means of sensing the amount of unbalance present. Thus, adjustments of the

SECTION XXIII

balance screws can be made to null the sensor output for each of these three types of excitation.

Hughes has developed experimental techniques that can produce these separate excitations at the required levels. These techniques are discussed in detail in the HRL Technical Proposal (see Section V-D), pp 143-147.

For fine adjustment of the differential mass unbalance, the same test techniques will apply. In this case, the entire rotating sensor and its temperature-controlled housing will be exposed to a pure translational vibration, the output signal monitored, and the mercury balance adjustment device driven until the sensor signal is nulled.

D. ROTOR MASS BALANCING

Hughes also has developed laboratory techniques for achieving accurate static and dynamic mass balance of the sensor rotor. The sensor stator is suspended on very low mass, compliant spring supports. Static and dynamic mass unbalance is sensed by use of sensitive geophone pickups (velocity meters), one oriented normal to the spin axis direction and one displaced from and parallel with the spin axis. The phase of the unbalance is determined by use of a strobe light, triggered at the zero crossing of the geophone signal output. Static mass unbalance has been adjusted to a 1-microinch accuracy using this procedure.

SECTION XXIV

LABORATORY EXPERIMENTS

A. VIBRATION SENSITIVITY MEASUREMENTS

Testing on the prior test model of the RGG indicated a sensitivity to acceleration applied along the sensor spin axis. Recent quantitative testing indicated the magnitude of this effect was approximately 2×10^8 EU/g (under an applied 0.001 g drive input acceleration).

Two mechanisms each of which could have caused such sensitivity are analyzed in the following discussion. The first mechanism is simple tension and compression in the central transducer structure, generated by a mismatch in the tensile spring properties of the arm supports. The second mechanism is moment loading of the transducer ends due to congruent mass unbalance on each of the arms. Each of these mechanisms is capable of generating greater than 10^8 EU/g under quite reasonable assumptions of the magnitude of the existing errors.

B. ANALYSIS OF GRADIENT STRAIN LEVEL

To establish the magnitude of these effects we should first calculate the equivalent gradient-strain level scale factor. The maximum bending stress in the quadrilever pivot for a unit torsional input has been calculated by D. W. Rouse to be

$$\frac{\sigma_B}{\theta} = \frac{6Erc}{l^2} \quad (1)$$

and the associated strain $(\sigma_B/\theta)/E$ (maximum)

$$\frac{\epsilon_B}{\theta} = \frac{6rc}{l^2}$$

SECTION XXIV

however, a transducer which covers 1/4 in. of the 1-in. long leaf
senses the average strain or 3/4 of the maximum

$$\left(\frac{\epsilon_B}{\theta}\right)_{avg} = \frac{3}{4} \frac{6rC}{l^2} \quad \text{or} \quad \frac{\theta}{\epsilon_B} = \frac{4l^2}{18rc}$$

where

$$l = 1 \text{ in.}$$

$$r = 0.40625 \text{ in.}$$

$$c = 0.0205 \text{ in.}$$

$$\frac{\theta}{\epsilon_B} = 26.683 \frac{\text{in.}}{\text{rad}} \quad (2)$$

The gradient sensitivity (angular deflection) of the sensor
is given by

$$\frac{\theta_\Gamma}{\Gamma} = \frac{T_\Gamma}{K_T} \quad (3)$$

where T_Γ = gradient torque = $\eta J_a \Gamma_{eq}/2$ and

$$K_T = \frac{K_e}{2} + K_o$$

where

$$K_e = \text{end pivot spring rate}$$

$$K_o = \text{central transducer spring rate}$$

SECTION XXIV

Therefore

$$\theta_{\Gamma} = \frac{\eta J_a \Gamma_{eq}}{K_e + 2K_o} \quad (4)$$

$$\text{or } \frac{\theta}{\Gamma_{eq}} = \frac{\eta J_a}{K_e + 2K_o} \quad \text{or} \quad \frac{\Gamma_{eq}}{\theta} = \frac{K_e + 2K_o}{\eta J_a} \quad (5)$$

We can now multiply (5) by (2) to obtain the gradient-strain level scale factor (EU per in./in.). We obtain

$$\frac{\Gamma_{eq}}{\epsilon_B} = \left[\frac{K_e + 2K_o}{\eta J_a} \right] \left[\frac{4l^2}{18rc} \right] \times 10^9 \quad (6)$$

Sensor parameters were measured as follows:

$$K_e = 4.5 \times 10^8 \text{ dyne cm/rad}$$

$$K_o = 4.86 \times 10^8 \text{ dyne cm/rad}$$

$$\eta = 0.7$$

$$J_a = 28,600 \text{ gm cm}^2$$

$$l = 1 \text{ in.}$$

$$r = 0.5 - \frac{3}{32} \text{ in.} = 0.40675 \text{ in.} = 1.032 \text{ cm}$$

$$c = 0.0205 \text{ in.} = 0.0521 \text{ cm}$$

SECTION XXIV

Inserting these values into (6) we can evaluate the scale factor:

$$\frac{\Gamma_{eq}}{\epsilon_b} = 1.895 \times 10^{15} \frac{EU}{in./in.} \quad (7)$$

C. ANALYSIS OF TRANSDUCER MISMATCH

The effect of dimensional tolerance of the transducer itself depends on the type of strain being sensed. For pure tension and compression in the leaf, the voltage equation is

$$\frac{V}{T} = \frac{F}{TW} g_{31} = \sigma g_{31}$$

so a 10% variation on the transducer thickness will produce a 10% variation on the voltage output. In addition, of course, the output voltage varies with changes in transducer output impedance, but these changes produce only a 1% variation in voltage per the rms dimensional variation of the transducer, and can be neglected.

For bending strain, the transducer no longer senses a constant strain level, but an average strain under its area. Therefore the length and position of the transducer are both important. A 10% length variation (0.025 in 1/4 in.) will cause a 5% variation on the average strain sensed, whereas a 10% change in position will cause a 10% change in average strain. If we rms these with the 10% thickness variation we get a $\pm 15\%$ variation on the output voltage.

SECTION XXIV

D. TENSION-COMPRESSION DUE TO AXIAL ACCELERATION

Ideally the RGG would be insensitive to axial acceleration because of its axially symmetric construction. However, the two outer supporting plates do not have the same thickness and this thickness assymetry causes strain to appear on the central flexure under axial acceleration.

The sensor model for this effect is shown in Fig. XXIV-1.

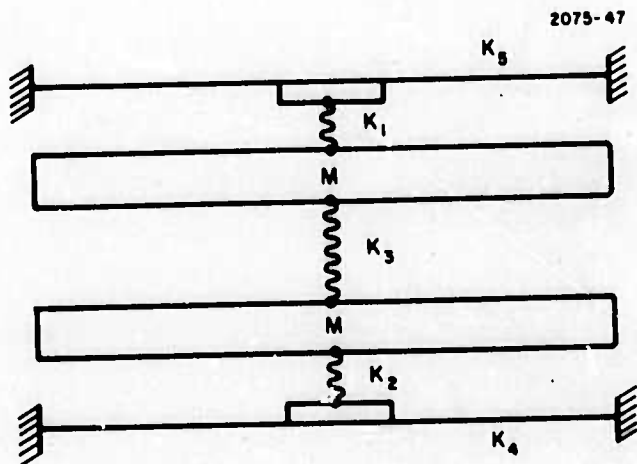


Fig. XXIV-1.
Sensor Model Axial
Acceleration Effect.

Here

$K_1 = K_2$ = end pivot axial stiffness

K_3 = quadrilever pivot stiffness

K_4, K_5 = diaphragm stiffnesses of end mounting plate
 $(K_4 \neq K_5)$

for the end pivots the axial stiffness is given by

$$K_1 = K_2 = \frac{EA}{l} \quad (8)$$

SECTION XXIV

where

$$A = \pi r^2 = \pi(0.030)^2$$

$$l = 0.040$$

$$E = 30 \times 10^6$$

$$K_1 = K_2 = 2.12 \times 10^6 \frac{\text{lb}}{\text{in.}} \quad (9)$$

For the central flexure

$$K_3 = \frac{4AE}{l} \quad (10)$$

where

$$A = \text{leaf cross section} = (0.041) \left(\frac{3}{16}\right)$$

$$l = 1 \text{ in.}$$

$$K_3 = 9.23 \times 10^5 \frac{\text{lb}}{\text{in.}} \quad (11)$$

K_4 and K_5 are diaphragm spring constants of the form

$$K = \frac{2\pi E m^2 t^3}{\left(3 m^2 - 1\right)} \cdot \frac{1}{\frac{1}{2}\left(a^2 - \gamma_o^2\right) - \gamma_o^2 \log \frac{a}{\gamma_o}} \quad (12)$$

where

$$m = \frac{1}{\nu_{\text{alum}}} = 3$$

$$a = \text{radius of plate} = 3 \text{ in.}$$

SECTION XXIV

t = thickness of plate $t_1 = 0.5, t_2 = 0.75$

$E = 10 \times 10^6$

$$r_0 = \text{Effective radius} = \sqrt{1.6(r)^2 + (t)^2} - 0.675t \quad (13)$$

where r = radius of applied load = 0.5 in.

when $t = 0.75$

$$r_0 = 0.475$$

$$K_4 = 2.363 \times 10^6 \quad (14)$$

and when $t = 0.5$

$$r_0 = 0.469$$

$$K_5 = 0.699 \times 10^6 \quad (15)$$

SECTION XXIV

Combining these diaphragm springs with the end pivot spring rates, we obtain

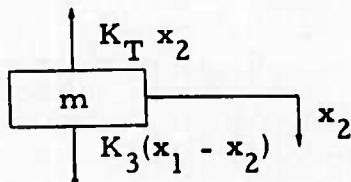
$$\frac{1}{K_B} = \frac{1}{K_2} + \frac{1}{K_4} \quad K_B = 1.117 \times 10^6 \text{ lb/in.} \quad (16)$$

$$\frac{1}{K_T} = \frac{1}{K_1} + \frac{1}{K_5} \quad K_T = 0.526 \times 10^6 \text{ lb/in.} \quad (17)$$

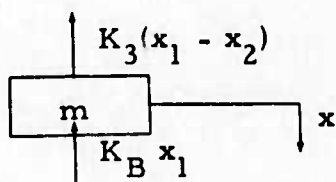
We can now find the strain in the center pivot by putting the system under constant acceleration and writing force equations from free body analysis

$$+ K_3(x_1 - x_2) - K_T x_2 = ma \quad (18)$$

$$- K_3(x_1 - x_2) - K_B x_1 = ma \quad (19)$$



$$2K_3(x_1 - x_2) - K_T x_2 + K_B x_1 = 0$$



$$2K_3 x_1 + K_B x_1 = 2K_3 x_2 + K_T x_2$$

$$\frac{x_1}{x_2} = \frac{2K_3 + K_T}{2K_3 + K_B}$$

It is simpler now to solve for this ratio and then complete the solution

$$\frac{x_1}{x_2} = \frac{2(0.924) + 1.117}{2(0.924) + 0.526} = 1.249$$

$$\text{or } x_1 = 1.249 x_2$$

SECTION XXIV

Therefore

$$K_3(1.249 x_2 - x_2) - K_T x_2 = -ma$$

$$(0.249 K_3 - K_T) x_2 = -ma = -W \text{ (for } g \text{ acceleration)}$$

$$x_2 = \frac{-W}{0.249 K_3 - K_T} = 2.054 \times 10^{-6} \text{ in.} \quad (20)$$

and

$$x_1 = 2.565 \times 10^{-6} \text{ in.} \quad (21)$$

$$x_1 - x_2 = 0.511 \times 10^{-6} \text{ in.} \quad (22)$$

which is the strain in the quadrilever.

If we multiply this strain by the gradient strain factor determined earlier, we obtain an equivalent gradient signal

$$\Gamma_{eq} = (0.511 \times 10^{-6})(1.895 \times 10^{15}) = 9.683 \times 10^8 \text{ EU/g} \quad (23)$$

If we assume that 10% of that signal is not rejected by transducer matching (see Section XXIV-B above) this would leave an axial tension-compression sensitivity of

$$\Gamma_{eq} = 0.968 \times 10^8 \frac{\text{EU}}{\text{g}} \quad (24)$$

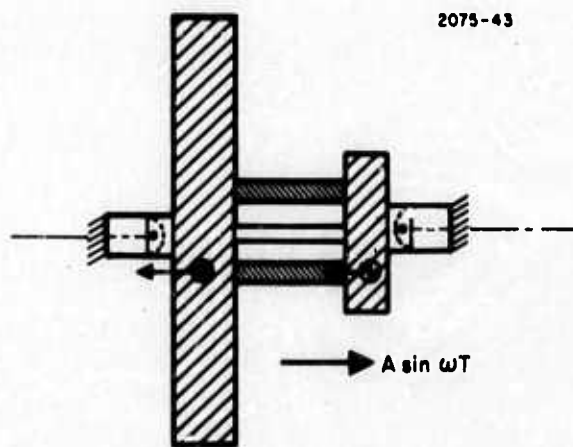
SECTION XXIV

E. ANALYSIS OF CONGRUENT ARM MASS UNBALANCE EFFECTS

The method of balancing which was used to adjust the arm balance of this model of the RGG was designed to eliminate only the differential unbalance between the two arms. After the complete balancing operation there could still be a large common unbalance where each arm C of M was offset from the pivot support. This unbalance, when excited by axial vibration could excite a parallelogram type bending in the center flexure and the resultant S shaped bending in the leaves of the flexure would generate gradient error signals in the transducer.

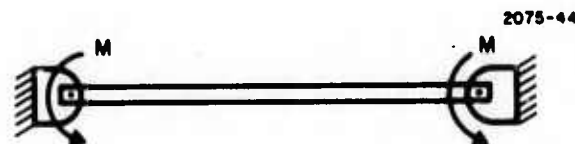
Analysis:

The model chosen for this analysis is to replace the end pivots with pin supports (the pivots are much stronger in tension and compression than in bending) (see below). Each arm has an unbalance of the same magnitude and sense away from the pivot support line.

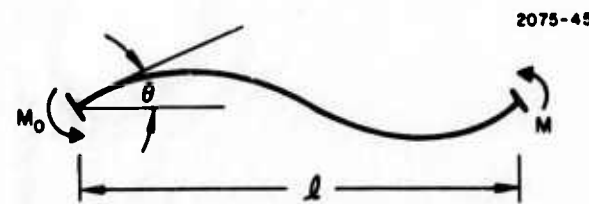


SECTION XXIV

Each beam of the center flexure could be analyzed as though it were pin supported with moments of



similar sense about each pin. The deflection of the beam would be



with a moment diagram



The angle θ is given by

$$\theta = \int_0^{\frac{l}{2}} \frac{M(x)dx}{EI} = \frac{M_0 \left(\frac{l}{2}\right)}{2EI} = \frac{M_0 l}{4EI}$$

SECTION XXIV

now when we consider the actual 4-leaf central pivot arrangement each beam has a different I and consequently a different end moment. The deflection angles are all equal and the total moment is equal to the product of the mass unbalance and axial acceleration = $(m_a e)a$. For the i^{th} leaf ($i = 1, 2, 3, 4$)

$$\theta_i = \frac{M_i l}{4EI_i} \quad (25)$$

$$\sum_{i=1}^4 M_i = M = (m_a e)a \quad (26)$$

$$\theta_1 = \theta_2 = \theta_3 = \theta_4 \quad (27)$$

$$\left. \begin{array}{l} M_1 = M_3 \\ M_2 = M_4 \end{array} \right\} \text{by symmetry} \quad (28)$$

from eq. (25)

$$\frac{M_i}{I_i} = \frac{4E\theta_i}{l} \quad \text{which is constant}$$

and therefore

$$\frac{M_2}{I_2} = \frac{M_1}{I_1} \quad \text{or} \quad M_2 = \frac{I_2}{I_1} M_1$$

from eq. (26)

$$\sum_i M_i = M = 2M_1 \left[1 + \frac{I_2}{I_1} \right] = (m_a e)a$$

SECTION XXIV

therefore

$$M_1 = \frac{(m_a e) a}{2 \left[1 + \frac{I_2}{I_1} \right]} ; M_2 = \frac{I_2}{I_1} \left[\frac{(m_a e) a}{2 \left[1 + \frac{I_2}{I_1} \right]} \right]$$

The root strain in the leaves is given by

$$\epsilon_i = \frac{M_i c_i}{EI_i}$$

and since the transducers are placed in such a way as to read the strain in the thinner bending section leaf only, this is the strain which is seen in the output

$$\epsilon_1 = \frac{(m_a e) a c}{2 \left[1 + \frac{I_2}{I_1} \right] EI_1}$$

$$I_1 = \frac{bh^3}{12} , \quad I_2 = \frac{hb^3}{12}$$

where

$$h = 0.041 \text{ in.}$$

$$b = \frac{3}{16} \text{ in.}$$

$$c = 0.020 \text{ in.}$$

$$m_a = 1.87 \text{ lb}$$

$$I_1 = 1.077 \times 10^{-6} \text{ in.}^4$$

$$I_2 = 2.252 \times 10^{-5} \text{ in.}^4$$

SECTION XXIV

We assume a mass unbalance eccentricity of 0.01 in. and calculate the per g strain

$$\frac{\epsilon_1}{a} = 2.6416 \times 10^{-7} \text{ in./in./g}$$

or the average strain under the transducer

$$\frac{3}{4} \epsilon_1 = 1.981 \times 10^{-7} \text{ in./in./g}$$

when we multiply by the strain sensitivity calculated previously

$$(1.895 \times 10^{15} \text{ EU/in./in.})$$

we obtain a signal level of

$$3.754 \times 10^8 \text{ EU/g}$$

The transducer matching to within 15% discussed in Section B leaves an uncompensated signal of

$$0.5631 \times 10^8 \text{ EU/g}$$

The rms of this effect with the tension compression effect previously calculated (Section XXIV-D)

$$1.120 \times 10^8 \text{ EU/g}$$

certainly close to the experimental results.

REFERENCES

- XIV-1. W. P. Mason, Editor, *Physical Acoustics, Part A-Methods and Devices*, 1964, Academic Press.
- XIV-2. W. P. Mason, *Electromechanical Transducers and Wave Filters*, 2nd Ed., 1948, D. Van Nostrand and Co.
- XIV-3. H. W. Katz, Editor, *Solid State Magnetic and Dielectric Devices*, 1959, John Wiley & Sons, Inc.
- XIV-4. E. G. Thurston, *Theoretical Sensitivity of Three Types of Rectangular Bimorph Transducers*, *Journal Acoustical Society of America*, Vol. 25, No. 5, (Sept 1953), pages 870-872.
- XIV-5. H. Jaffe and D. A. Berlincourt, *Piezoelectric Transducer Materials*, *Proceedings of the IEEE*, Vol 53, No. 10 (Oct 1965), pages 1372-1386.

APPENDIX A

SENSOR ARM ANISOELASTIC DEFLECTION ANALYSIS

This appendix presents the assumptions and results of an arm structure deflection analysis for the baseline arm configuration. These results have been used to determine an optimum set of arm dimensions to achieve anisoelasticity as well as high structural stiffness.

1. Arm Configuration

The sensor arm configuration analyzed herein is shown in Fig. A-1. It consists of two parallel plates whose ends are fastened together via heavyweight end masses. Fastening of each plate to the end masses is accomplished using multiple screws through each plate end into tapped holes in the heavyweight material. The plates have cutouts as shown to reduce the longitudinal stiffness in order to make it equal to the lateral bending stiffness.

2. Assumptions

In this analysis, the compliance of only the center of mass of each arm end mass is computed. The anisoelastic error coefficient is a function of the distributed mass-deflection characteristic of the total arm structure as well as the end masses. The structure mass-deflection has been ignored in the analysis. This is justified since the mass of the structure is only 1/6th that of the end masses and only a small portion of the structure mass undergoes a significant proportion of the end mass deflections. This will be taken into account during the assembly and trimming operation mentioned in the text of Section XIII.

Any internal deflections of the end masses have been ignored because of the relatively larger elastic moduli.

2075-27

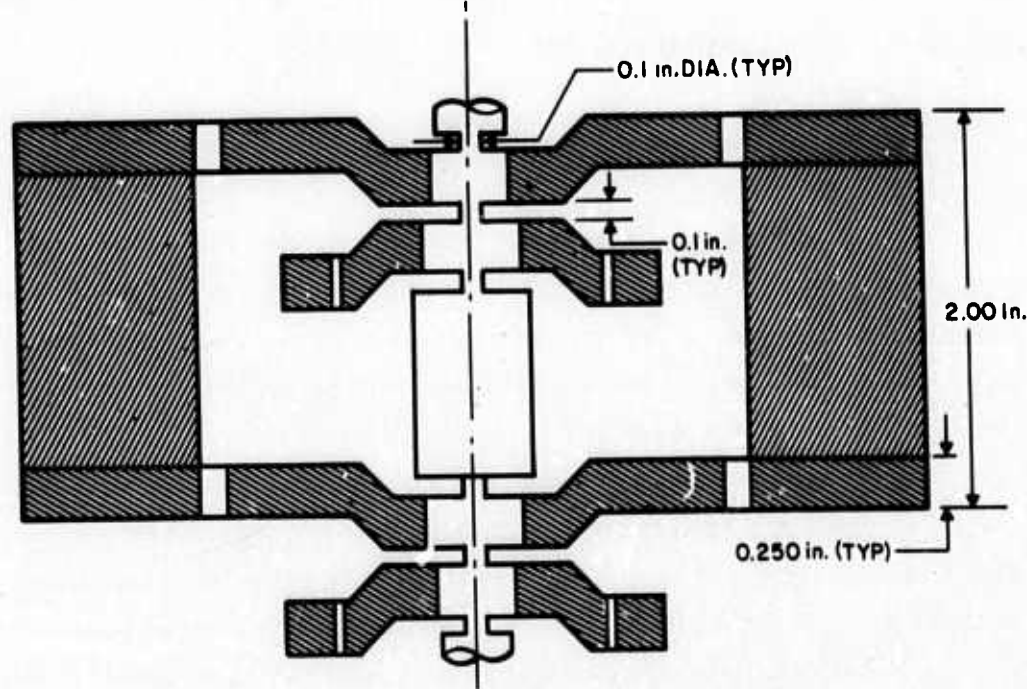
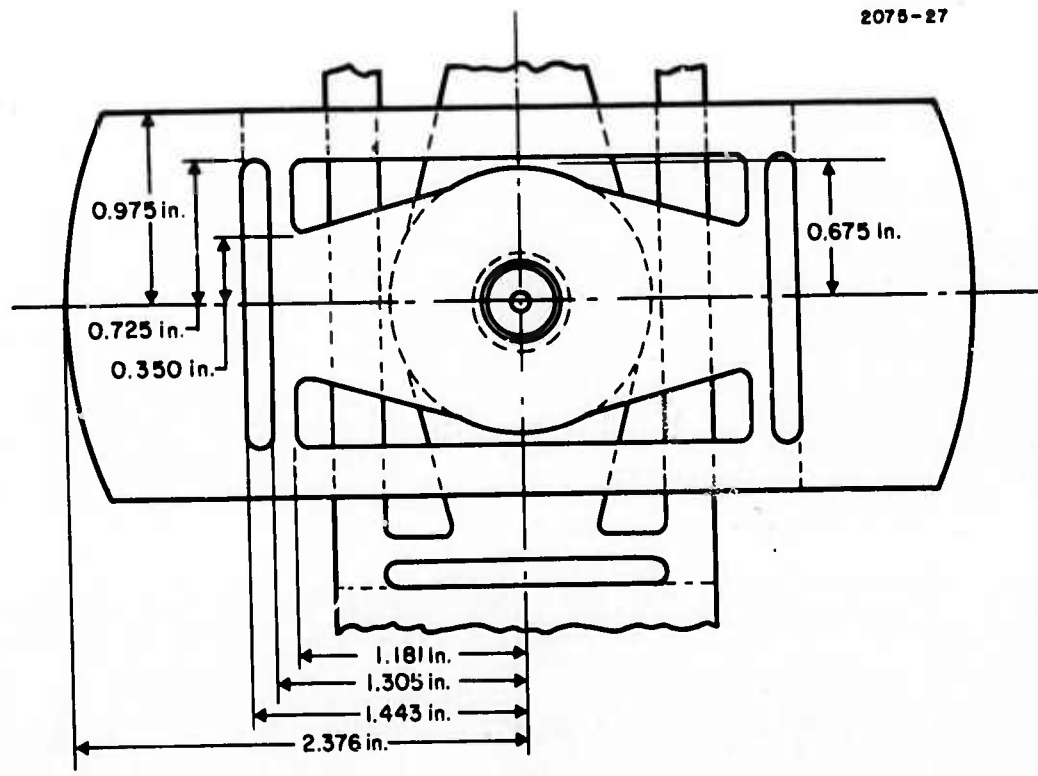


Fig. A-1. RGG Isoelastic Arm Design.

APPENDIX A

3. Idealized Structure

The baseline arm configuration depicted in Fig. A-1 has been simplified to allow straightforward analysis of each component member of the structure. The idealized arm structure considered in this analysis is illustrated in Fig. A-2. The heavy dotted lines represent the elastic axis location for the members considered to deflect elastically. The shaded portions were considered infinitely rigid. The dimension symbols represent the length of each of the elastic members. In the analysis, the width of each member is denoted by w_i , i being chosen consistent with the member's length dimension symbol. The thickness of the arm plate is denoted by t . Dimension d denotes the spanwise location of the center of mass of the heavyweight end mass. An x, y coordinate frame is shown for reference. All interconnections between the elastic and the infinitely rigid members are assumed to be "fixed" or "cantilevered" joints. In computing deflections of component members of the idealized arm structure, stiffness contributions of fillets have been ignored; however, flexure as well as vertical shear effects are included in all bending computations.

For member e, its width has been assumed to vary linearly with its span in all deflection calculations.

Arm anisoelastic error torques are induced by static or vibratory accelerations of the arm support pivots. In deriving these compliance equations, the induced inertia loads of the end masses have been replaced by static loads and similarly, the support pivot acceleration induced loads replaced by static reaction forces. No account has been made for dynamic structural deflections in replacing the "acceleration-induced" loads with "static" loads. For analytical convenience, all compliances were computed considering only half of one arm plate. The boundary conditions assumed in deriving each compliance equation are illustrated in Fig. A-3.

The equations for arm end mass deflection have been derived based upon the above stated assumptions. The compliances in each of

2078-28

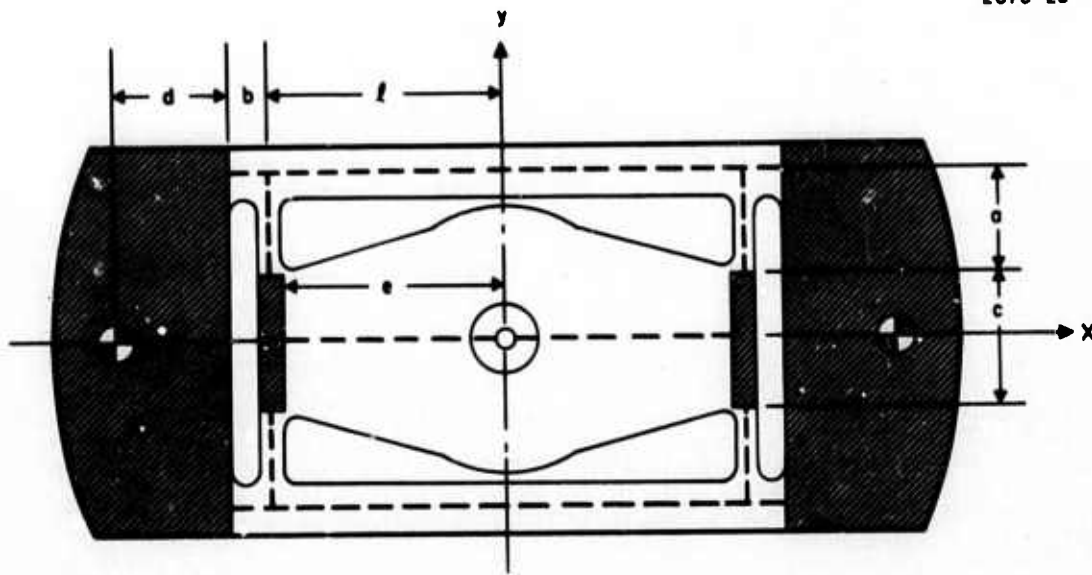


Fig. A-2. Idealized Arm Structure.

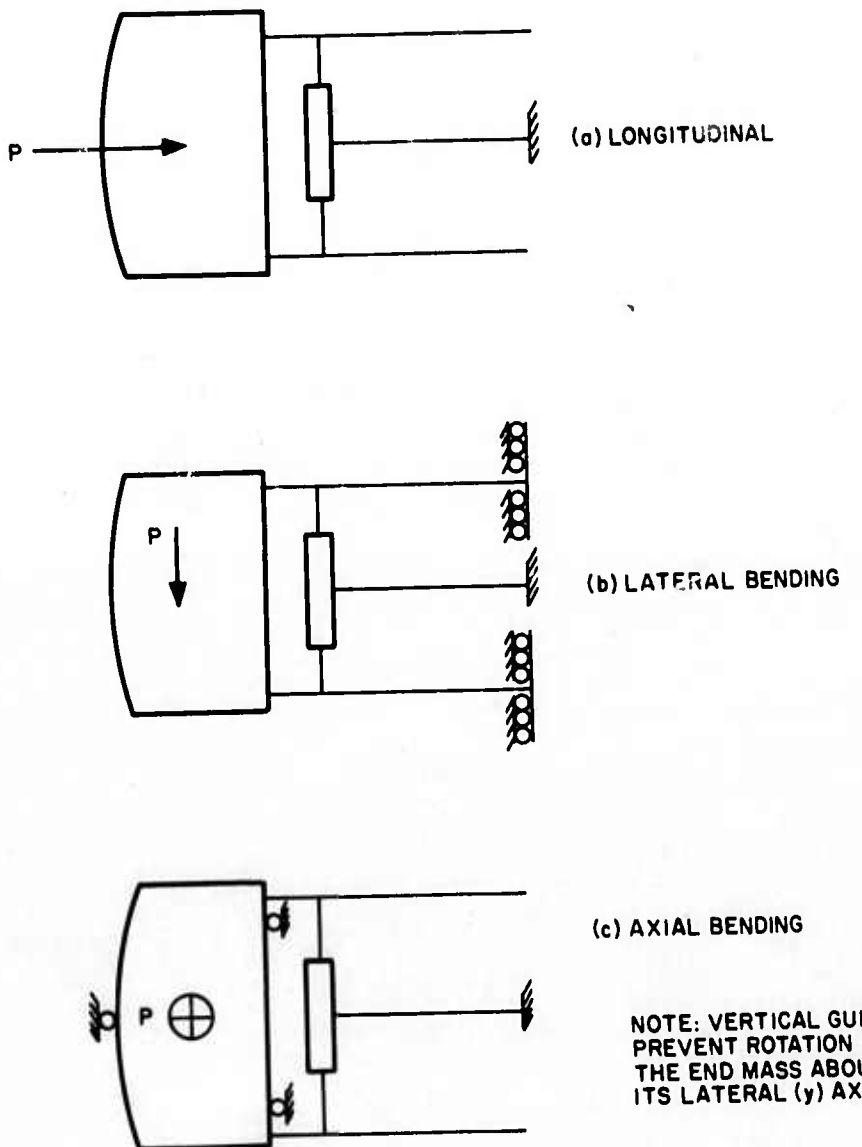


Fig. A-3. Assumed Boundary Conditions and Loads for Compliance Evaluation.

APPENDIX A

the three principal axis directions are defined by the ratio of the end mass deflection, δ_i , to the applied load, P_i :

$$C_x = \frac{\delta_x}{P_x}, \quad C_y = \frac{\delta_y}{P_y}, \quad C_z = \frac{\delta_z}{P_z}$$

The resulting compliance equations are:

$$C_x = \frac{1}{Et} \left[\frac{a^3}{2w_a^3} + \frac{b}{2w_\ell} - \frac{a\ell n(1 - \rho_e)}{w_{eo}\rho_e} \right] \quad (A-1)$$

$$C_y = \frac{1}{Et} \left[\frac{d^2}{2(a + c/2)^2} \left(\frac{b + \ell}{w_\ell} \right) + \frac{bE}{2Gw_\ell} + \frac{a}{2w_a} + \frac{2b^3}{w_b^3} + \frac{6e^3}{w_{eo}^3} K_E \right] \quad (A-2)$$

where

a, b, c, d, e, ℓ = length of members (see Fig. A-2)

w_i = width of members (see Fig. A-2)

w_{eo} = width of member e at root, or center of arm

w_{el} = width of member e at tip $\triangleq c$

ρ_e = taper ratio of member e

$$= \frac{w_{eo} - c}{w_{eo}}$$

E = Young's modulus of elasticity

G = shear modulus of elasticity

$$K_E = \left(\frac{2}{\rho_e^3} + \frac{b}{e} \right) \ell n(1 - \rho_e) + \frac{2 - \rho_e(1 - \rho_e) + \frac{b}{e}\rho_e^3}{\rho_e^2(1 - \rho_e)}$$

An explicit equation for the axial bending compliance is too unwieldy, hence intermediate parametric functions and a final equation in terms of these parametric functions is presented.

APPENDIX A

Define:

$$K_{\delta b}^P \triangleq \frac{b^3}{12EI_b} \left[1 + \frac{3EI_b}{b^2 A_b G} \right]$$

$$K_{\delta b}^M \triangleq \frac{b^2}{2EI_b}$$

$$K_{\theta b}^P \triangleq \frac{b^2}{8EI_b}$$

$$K_{\theta b}^M \triangleq \frac{b}{EI_b}$$

$$K_{\alpha b} \triangleq \frac{b}{GK_b}$$

$$K_{\delta a}^P \triangleq \frac{a^3}{12EI_a} \left[1 + \frac{3EI_a}{a^2 A_a G} \right]$$

$$K_{\delta a}^M = \frac{a^2}{2EI_a}$$

$$K_{\theta a}^P \triangleq \frac{a^2}{8EI_a}$$

$$K_{\theta a}^M \triangleq \frac{a}{EI_a}$$

$$K_{\alpha a} \triangleq \frac{a}{GK_a}$$

$$K_{\delta e}^P \triangleq \frac{e^3}{2EI_e^{\delta P}} \left[1 + \frac{EI_e^{\delta P}}{e^2 A_e^* G} \right]$$

$$K_{\delta e}^M \triangleq \frac{e^2}{EI_e^{\delta M}}$$

$$K_{\theta e}^P \triangleq \frac{e^2}{2EI_e^{\theta P}}$$

$$K_{\theta e}^M \triangleq \frac{e}{EI_e^{\theta M}}$$

where in the above, the following definitions apply

$I_i \triangleq$ section inertia of i^{th} member

$K_a, K_b \triangleq$ Torsional section inertia parameter given by

APPENDIX A

$$K_i \triangleq \frac{tw_i^3}{3} \left[1 - 0.63 \frac{w_i}{t} \left(1 - \frac{w_i^4}{12t^4} \right) \right] \quad i = a, b$$

$$I_e^{\delta p} \triangleq \frac{w_{eo} t^3 \rho_e}{6 \left[-\frac{1}{2} + \frac{\rho_e - 1}{\rho_e} \ln(1 - \rho_e) \right]}$$

$$I_e^{\delta M} \triangleq \frac{w_{eo} t^3 \rho_e}{12 [\rho_e + (1 - \rho_e) \ln(1 - \rho_e)]}$$

$$I_e^{\theta p} \triangleq \frac{w_{eo} t^3 \rho_e}{12 \left[1 + \frac{1 - \rho_e}{\rho_e} \ln(1 - \rho_e) \right]}$$

$$I_e^{\theta M} \triangleq -\frac{w_{eo} t^3 \rho_e}{12 \ln(1 - \rho_e)}$$

$$A^* \triangleq -\frac{w_{eo} t \rho_e}{\ln(1 - \rho_e)}$$

The final expression for axial bending compliance is:

$$\begin{aligned} C_z &= K_{\delta a}^p - \frac{K_{\delta a}^M K_{\theta a}^p}{K_{\alpha b}^M + K_{\theta a}^M} + K_{\delta b}^p + K_{\delta e}^p \\ &\quad + \frac{(K_{\theta b}^p - K_{\theta e}^p)(K_{\delta e}^M - K_{\delta b}^M)}{K_{\theta b}^M + K_{\alpha a}^M + K_{\theta e}^M} \end{aligned} \quad (A-3)$$

APPENDIX B

ESTIMATION OF UPPER BOUND OF STABLE PLATFORM ANGULAR RATE

The second order gradient of the specific force field at a point in a gravity field (as viewed by an observer in rotating frame of reference) is a linear combination of the second order gradients of the gravity and rotational fields. All so-called gravity gradiometers are actually specific force gradiometers; and because of this, the measurements of such instruments are contaminated by the inertial angular velocity of their measurement frames of reference. To obtain the second order gravity gradient tensor elements from a system of such instruments, it is necessary to correct for the rotational field effects on the measurements of these instruments. The differences between the actual rotational field gradients and the quantities employed for compensation are defined as the "rotational field measurement errors."

In the present application, it is desired to estimate the rotational field errors which would occur if the gradiometers were directly mounted to the platform stable element. In this case, the inertial angular velocity of the stable element is the angular velocity of the measurement reference frame. This inertial angular velocity may be considered to be made up of the sum of two components, a deterministic portion and a random portion. It is intended that the gravity gradient measurements are to be compensated for the gradient of the deterministic portion of the rotational field and that the remaining portion of the rotational field gradient be classed as a rotational field error.

The deterministic portion of the platform stable element inertial angular rate would be, for example, the carrying vehicle's transport rate plus the earth's rate for a north referenced, locally level platform mechanization. Measurements of these quantities would be the gyro precession command signals obtained from the platform's management computer. The random portion of the platform stable element inertial

APPENDIX B

angular velocity will be made up of various disturbances including gyro drift rate, gyro signal noise, and oscillatory angular rates induced by mechanical torque disturbances such as gimbal bearing friction, acceleration induced platform mass unbalance torques, etc.

Rigorous calculation of the rotational field errors in the measured gravity gradient tensor elements requires a complete knowledge of the angular rate spectra of the stable element, i.e., the three co-spectra and the three cross-spectra. Although rigorous calculation of the rotational field errors is not possible in the absence of these data, it is possible to estimate the upper bounds on these errors from the limiting values of stable platform disturbing functions.

One of the predominant sources of platform disturbance is a result of interactions of angular rates of the platform's base with the coulomb-type friction torque associated with the platform gimbal bearings, slip rings, residual torque motor torques, etc., and the platform's stabilization servo. The manner in which this disturbance propagates into platform stable element angular velocity depends on its spectrum and on the stabilization servo's response to torque disturbance. Precise analysis to generate the required angular velocity motion spectra is very difficult and would require development of a complex and costly computer simulation model and accurate knowledge of the angular rate motion co-spectra and cross-spectra of the stable platform's base.

In the absence of this data and the computer simulation model, an upper bound of the platform angular rate variance may be determined on the basis of the following heuristic argument. First, an upper bound can be placed on the variance of the normalized disturbance torque. For example, consider the normalized disturbance torque to be a zero-mean, random variable, x , with probability density, $p_x(x)$. The variance, σ_x^2 , is just the second moment of the density function as in (1).

$$\sigma_x^2 = \int_{-\infty}^{\infty} x^2 p_x(x) dx \quad (1)$$

APPENDIX B

When the random variable is bounded to a maximum value, x_{\max} , then its variance is bounded to x_{\max}^2 . The limit is reached when the probability density functions, $p_x(x)$, consist of a pair of impulses located at $\pm x_{\max}$ as in (2).

$$p_x(x) \underset{\text{limit}}{=} 1/2 \left[\delta(x_{\max}) + \delta(-x_{\max}) \right] \quad (2)$$

for any other probability density function bounded by $\pm x_{\max}$, the variance will be less than x_{\max}^2 as stated in (3).

$$\sigma_x^2 \leq x_{\max}^2 \quad (3)$$

This bounds the variance of the torque disturbance by its maximum value. Next consider the platform angular rate response to normalized disturbance torques as in (4).

$$\omega_p(s) \triangleq H_p(s) \left(\frac{T_d}{J} \right) \quad (4)$$

From (4) the angular rate power spectrum is stated in terms of the torque disturbance spectrum, $S_d(f)$ as (5).

$$S_\omega(f) = \left| H_p(j2\pi f) \right|^2 S_d(f) \quad (5)$$

The rate variance is obtained by integration of (5) as in (6).

$$\sigma_\omega^2 = \int_{-\infty}^{\infty} S_\omega(f) df = \int_{-\infty}^{\infty} \left| H_p(j2\pi f) \right|^2 S_d(f) df \quad (6)$$

APPENDIX B

An upper bound on the rate variance of (6) may be determined by forcing the disturbance torque spectrum to have all of its power at a frequency where the platform response, $H_p(s)$, is a maximum. Thus the rate variance is bounded as in (7).

$$\sigma_{\omega}^2 \Big|_{\max} \leq \left| H_p(s) \right|_{\max}^2 \sigma_d^2 \Big|_{\max} \quad (7)$$

An estimate of the peak disturbance torque response is given by (8) where ω_b is the platform servo bandwidth and ζ is its damping coefficient.

$$\left| H_p(s) \right|_{\max} = \frac{1}{\sqrt{2}\zeta\omega_b} \quad (8)$$

Using eqs. (7) and (8), the estimated upper bound of rate variance is given by (9).

$$\sigma_{\omega}^2 \leq \frac{1}{2\zeta^2\omega_b^2} \sigma_d^2 \Big|_{\max} \quad (9)$$

where $\sigma_d^2 \Big|_{\max}$ is taken to be the coulomb friction torque level normalized by platform inertia. Thus, the standard deviation of this bounded angular rate estimate for coulomb-type friction disturbance is

$$\sigma_{\omega} \leq \frac{1}{\sqrt{2}\zeta\omega_b} \frac{T_f}{J} \quad (10)$$

A method of computing an upper bound for the standard deviation of platform angular rate has been established. This upper bound was established in the absence of any knowledge of the form of the disturbance spectra using a probabilistic argument. This approach did not

APPENDIX B

lead to an estimate of the form of the angular rate spectra necessary for rigorous calculation of the rotational field errors of the gravity gradient tensor elements; however, by a similar probabilistic argument in Section IX, Error Analysis, using the angular rate bound developed here, an upper bound of the gravity gradient component rotational field errors is demonstrated.

APPENDIX C
SPIN MOTOR SPECIFICATION

PROCUREMENT SPECIFICATION

for

SPIN MOTOR FOR HUGHES
PROTOTYPE ROTATING GRAVITY GRADIOMETER

Date: September 5, 1972

No. RGG 1

Revision B October 4, 1972

Approved by:

Robert R. Brown / for
C. B. Ames

Philip M. Lafue
P. M. Lafue

Adrian J. Robinson
A. Robinson

D. W. Rouse
D. W. Rouse

Hughes Research Laboratories
3011 Malibu Canyon Road
Malibu, California 90265

Page 1 of 14
373

Preceding page blank

TABLE OF CONTENTS

	<u>Page</u>
1. 0 Scope	
2. 0 Applicable Documents	
3. 0 Requirements	
3. 1 Conflicting Requirements	
3. 2 Materials, Parts and Processes	
3. 3 Gravity Gradiometer Description	
3. 3. 1 Sensor Physical Parameters	
3. 4 Spin Motor Performance Requirements	
3. 4. 1 Second Harmonic Torque Ripple	
3. 4. 1. 1 Deterministic Torque Oscillation	
3. 4. 1. 2 Random Torque Variations	
3. 4. 2 Torque Oscillations at Other Frequencies	
3. 4. 3 Spin Motor Full Load Speed	
3. 4. 4 Spin Motor Torque	
3. 4. 5 Torque Speed Curves	
3. 4. 6 Rotor Vibration	
3. 4. 7 Input Power	
3. 4. 8 Spin-Axis Alignment Reference	
3. 4. 9 Electrical Insulation	
3. 5 Environmental Conditions	
3. 5. 1 Operating Performance Condition	
3. 5. 2 Operating Standby Condition	
3. 5. 3 Non-Operating Condition	
3. 6 Reliability Objectives	
4. 0 Quality Assurance Provisions	

Figure 3.3 Rotating Gravity Gradiometer
Baseline Configuration

Figure 3.5.3 Acceleration Spectra

Table 3.5 Environmental Conditions

REVISION B CHANGES

<u>Page</u>	<u>Para.</u>	
4	1. 0	The gradiometer design has been changed to use two identical spin motors in parallel. This specification is for a single motor. Thus many of the limits, such as full load torque, torque ripple allowed, etc., have been halved in the body of the specification. However, Hughes has also elected to use oil lubricated spin bearings - the total sensor running torque has not changed - and the starting (break-away) torque requirement has approximately doubled.
6	3. 4	"harmonics" has been clarified to show that it is torque harmonics that are of interest to Hughes.
8&9	3. 4. 1. 1 3. 4. 1. 2 3. 4. 2 3. 4. 4, a, b, c 3. 4. 6, a, b	These paragraphs changed to reflect the requirements on a per motor basis.
10	3. 4. 7	The locked rotor power is not especially important. Nor are torque variations, waveform distortion or heating during sensor breakaway and run up. However, Hughes is interested in the highest practical efficiency after the sensor has stabilized at running speed. Motor losses will heat the sensor and thus make it more difficult to maintain extremely accurate temperature control of the sensor which is required. *
12	Fig. 3. 3	This figure has been changed to show the use of two small oil lubricated bearings. Both the inner and outer stator radial thickness can be increased as shown in the figure if this is desirable. It is desired that the outer diameter of the outer stator ring be limited to 3. 0 inches unless this leads to a very unwieldy motor design. The axial length of the motor may be increased if required but again the shortest practical length is desired.

* Pole changing for break-away torque and initial runup may be considered if switching is not too complicated.

PROCUREMENT SPECIFICATION
FOR
SPIN MOTOR
FOR
PROTOTYPE ROTATING GRAVITY GRADIOMETER

1.0 SCOPE

This specification covers the requirements for a spin-axis drive motor for a prototype moving-base rotating gravity gradiometer, which may be herein referred to as the "sensor." The spin motor will be used as a part of a servo control loop to drive the sensor rotor at a speed of exactly 1050 RPM. Two identical spin motors, connected in parallel, will be used on each sensor as shown in Fig. 3.3. This specification gives the requirements for each individual motor. The sensor constitutes the basic sensing element in a system designed to precisely measure gradients of the gravitational field from a moving vehicle. The requirements and environmental conditions associated with the sensor necessitate that the spin motor perform its function with great precision as well as being rugged, reliable and reproducible.

2.0 APPLICABLE DOCUMENTS

The following documents in their latest issue at contract date form a part of this specification to the extent specified herein.

Specifications -

3.0 REQUIREMENTS

3.1 Conflicting Requirements — Any conflicting requirements arising between this specification and any specifications or drawings listed herein shall be referred in writing, to the Hughes Research Laboratories (HRL) for interpretation and clarification.

3.1.1 Request for Deviation — Any deviation from the requirements specified herein shall be considered a deviation and shall not be allowed except by written authorization from HRL.

3.2 Materials, Parts and Processes — Materials, parts and processes used in the design, fabrication and assembly of the products covered by the specification shall be in accordance with sound and proven engineering and manufacturing practices. The manufacturer's selection shall assure the highest uniform quality and conditions of the product, suitable for the intended use. It is desired but not required that the motor rotor parts and fasteners shall have a magnetic permeability not greater than 1.010 cgs units.

3.3 Gravity Gradiometer Description — A conceptual design sketch of the baseline configuration Rotating Gravity Gradiometer is attached as Fig. 3.3. The motor shown in Fig. 3.3 illustrates the space and configuration problem but it is not intended to precisely specify the motor size or configuration. The basic gravity gradient sensor consists of a crossed pair of mass quadrupoles coupled by a torsional spring and enclosed in a sealed, evacuated case. This case is then rotated at a spin frequency which is adjusted to precisely one half the inertia-spring resonant frequency of the coupled mass quadrupoles. The spinning system is enclosed within a nominally spherical shell which is, in turn, suspended within its mounting frame

with two degrees of angular freedom for base motion isolation. The baseline sketch shows a drag cup motor driving the rotor.

3.3.1 Sensor Physical Parameters - Preliminary design estimates of various sensor physical parameters, which influence spin motor selection and detailed design, are as follows:

Rotor Mass	7000 gms
Rotor Polar Inertia	2.5×10^5 gm-cm ²
Rotor Transverse Inertia	2.0×10^5 gm-cm ²
Rotor Shell Diameter	15.5 cm
Stator shell Diameter	18 cm
Stator Mass	5000 gms
Stator Polar Inertia	3.0×10^5 gm-cm ²
Stator Transverse Inertia	3.5×10^5 gm-cm ²

3.4 Spin Motor Performance Requirements - Gravity gradient sensor performance requirements impose specific performance requirements on the sensor spin motor. The sensor is particularly sensitive to 1, 2 and 3 torque harmonics of the full load speed (17.5 Hz) and this should be considered in the selection of number of poles, number of slots, magnetic field harmonics, excitation frequency and slip frequency.

The sensor spin-motor shall be capable of meeting the performance requirements set forth herein when driving the rotor mass and moment of inertia load specified in paragraph 3.3.1 and rotating at the spin speed specified in paragraph 3.4.3 while the sensor is operating under the environmental conditions defined in paragraph 3.5.1 after the motor is thermally stabilized. The required thermal stabilization time shall not exceed the following limits.

<u>Beginning Soak Temperature</u>	<u>Stabilization Time</u>
40°F	3 Hrs [1 Hr]
70°F	2 Hrs [1/2 Hr]
140 ± 10°F	5 Min [1/2 Min]

The spin motor shall be capable of meeting these performance requirements following exposure to the conditions set forth in paragraph 3.5.2 or 3.5.3.

In addition, the spin motor shall meet these performance requirements throughout a 10,000 hour operating life with a minimum of 500 rotor start-stop cycles. Furthermore, the spin motor shall meet the performance requirements at any time during a minimum one year period following assembly into the sensor.

In addition to the values assigned to the performance requirements, desired goals are indicated by values in brackets [].

3.4.1 Second Harmonic Torque Ripple -- Torque oscillations about the spin axis in a narrow frequency band centered at twice the spin frequency ($2\omega_s$) may cause significant errors in the sensor output. To the extent that these torque oscillations are deterministic, they can be compensated, however, the random portion of these torque oscillations cannot. The deterministic portion is made up of oscillation occurring at exactly $2\omega_s$ and whose phase is precisely fixed relative to the mechanical phase of the motor rotor. It is required that the magnitude of the deterministic torque oscillation not exceed the values specified in paragraph 3.4.1.1. Random torque variations are characterized by variations in both amplitude and phase relative to the above defined deterministic torque oscillation. As a consequence, the allowable random torque variations must be specified in terms of the magnitude of two mutually orthogonal components. It is required that the standard deviation of the magnitude of either of these orthogonal components within a narrow frequency band centered at $2\omega_s$ not exceed the value specified in paragraph 3.4.1.2. The requirements of paragraphs 3.4.1.1, 3.4.1.2 and 3.4.2 shall be met with the reference field voltage held at ± 5 percent of nominal and the control field within ± 25 percent of nominal.

3.4.1.1 Deterministic Torque Oscillation — The deterministic value of the torque oscillation shall be defined as the average value over a ten (10) hour operation following thermal stabilization. This value shall not exceed 500 dyne-cm. In addition the mean value of the deterministic torque oscillation when averaged over the first hour of operation following thermal stabilization shall not differ from the ten (10)-hour mean value by more than 25 dyne-cm.

3.4.1.2 Random Torque Variation — The standard deviation of either orthogonal component of the random torque variation within a 0.1 Hz wide frequency band centered at $2\omega_s$ shall not exceed 25 dyne-cm over a ten (10) hour operation following thermal stabilization.

3.4.2 Torque Oscillations at Other Frequencies — The root-mean-square value of spin-axis torque oscillations within any 0.1 Hz wide frequency band outside the band specified in paragraph 3.4.1.2 shall not exceed 250 [25] dyne-cm.

3.4.3 Spin Motor Full Load Speed — The full load speed of the spin motor shall be 1050 RPM.

3.4.4 Spin Motor Torque — The spin motor may be designed to operate at two different excitation levels. A high level during run-up and a lower level during constant speed operation.

- a. The starting torque shall not be less than 2.5×10^5 dyne-cm.
- b. The mean running torque shall be 2.5×10^4 dyne-cm.
- c. If the running torque is at a reduced reference field excitation the control field shall have a torque capability of 3.75×10^4 dyne-cm at rated speed.

3.4.5 Torque Speed Curves - For either high level or low level excitation the torque speed curves shall have the following characteristics.

- a. The torque speed curve shall be single valued from 0 to at least 1525 RPM.
- b. The slope of the torque speed curve shall not deviate from the mean slope by more than $\pm 25\frac{1}{2}$ percent of the mean slope between 750 and 1250 RPM.
- c. The slope of the low excitation torque speed curve shall not be less than 25 percent of the slope of the high excitation torque speed curve.

3.4.6 Rotor Vibration

- a. The integrated power spectrum of spin motor induced rotor translational acceleration neglecting bearing stiffness shall not exceed $0.005[0.0005]$ cm/sec² rms in the frequency range $1/2 \omega_s$ to $4 \omega_s$. Outside this frequency range, the power spectral density shall not exceed $0.5[0.005]$ cm²/sec⁴/Hz.
- b. The integrated power spectrum of spin-motor-induced rotor angular rate, normal to the spin axis, neglecting bearing stiffness shall not exceed $2.5 \times 10^{-11}[5 \times 10^{-12}]$ sec⁻².

3.4.7 Input Power - The input power may be selected to have any frequency from 140 to 2100 Hz and any voltage from 20 to 100 volts per phase. The frequency selected shall be an integral multiple 35 Hertz. The frequency will be held to better than one part per million of the value selected and the distortion in

the reference and control field will not exceed 0.5 percent.
Input power limits are shown below.

- a. The locked rotor power input 10 [5] watts maximum.
- b. Full load speed running power input 5 [2.5] watts maximum.

3.4.8 Spin-Axis Alignment Reference — A spin-axis alignment reference shall be provided which permits location of the spin reference axis to an accuracy of one mrad.

3.4.9 Electrical Insulation — [It shall be possible to electrically insulate each of the motor components from its mechanical mount(s). The insulation resistance shall not be less than 5 megohms at 500 volts and 60 Hz].

3.5 Environmental Conditions — During the specified life requirements of paragraph 3.4, and while driving the moment of inertia rotor load specified in paragraph 3.3.1, the spin motor may be subjected to the following environmental conditions. These conditions are summarized in Table 3.5.

3.5.1 Operating Performance Condition — This condition represents the most extreme environments under which the bearing is required to operate and meet the specified performance of paragraph 3.4.

3.5.2 Operating Standby Condition — This condition represents the most extreme environments under which the spin motor is required to operate and survive without damage.

3.5.3 Non-Operating Condition — This condition represents the most extreme environments to which the spin motor may be subjected while in a non-operating state. It must survive these environments without damage. The non-operating state is

defined as not rotating and not energized.

3.6 Reliability Objectives - The sensor spin motor shall have a reliability objective of 0.995 when operated under the environmental conditions set forth in paragraph 3.5.1 at any time during 10,000 hours of operation.

4.0 QUALITY ASSURANCE PROVISIONS

Assurance that the sensor spin motor meets the performance requirements set forth in paragraph 3.4 will be provided by means of (a) the Vendors Quality Control Program; (b) an adequate Testing Program; and (c) a Reliability Verification Program.

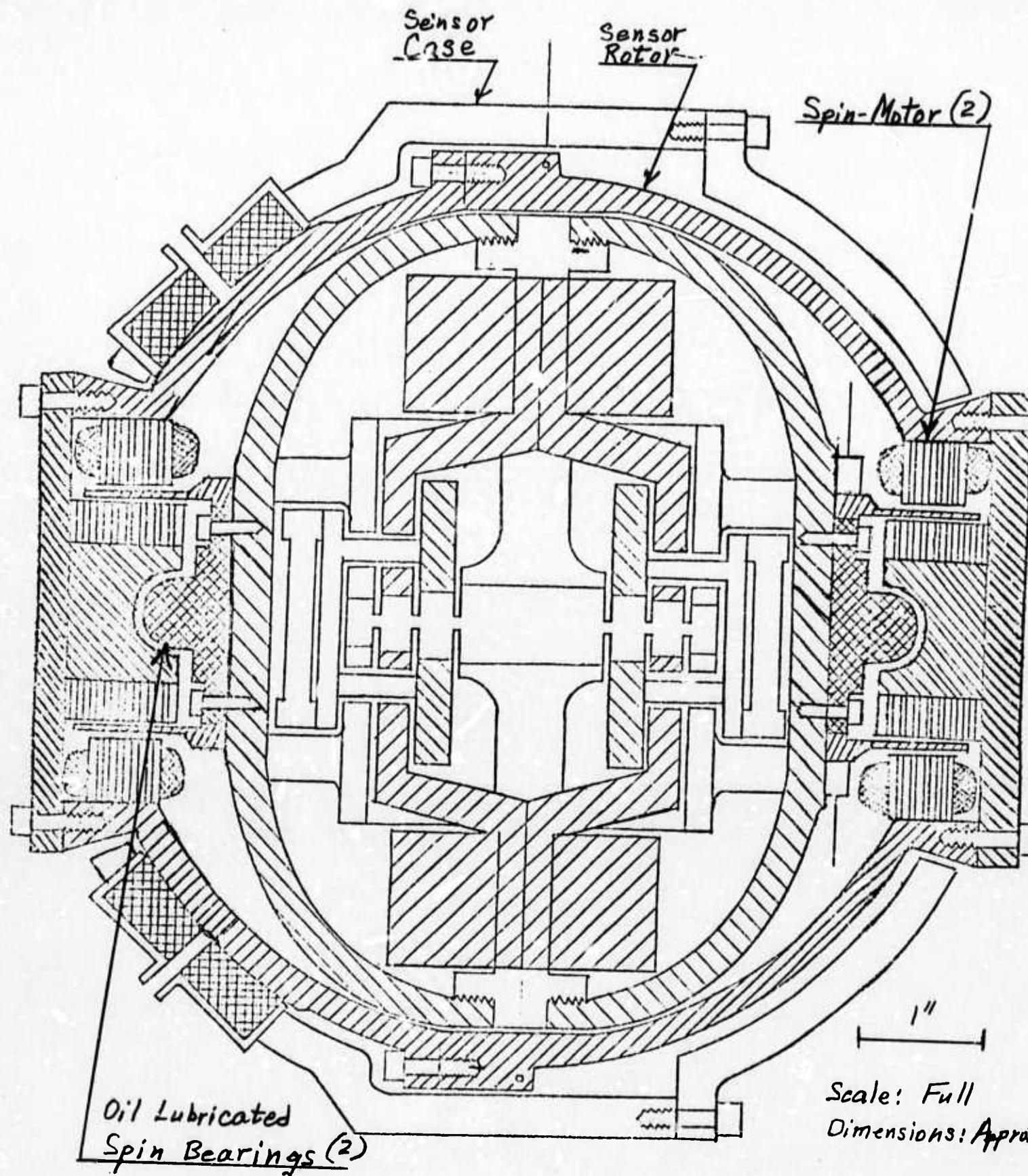


Fig. 3.3. Rotating Gravity Gradiometer Baseline Configuration

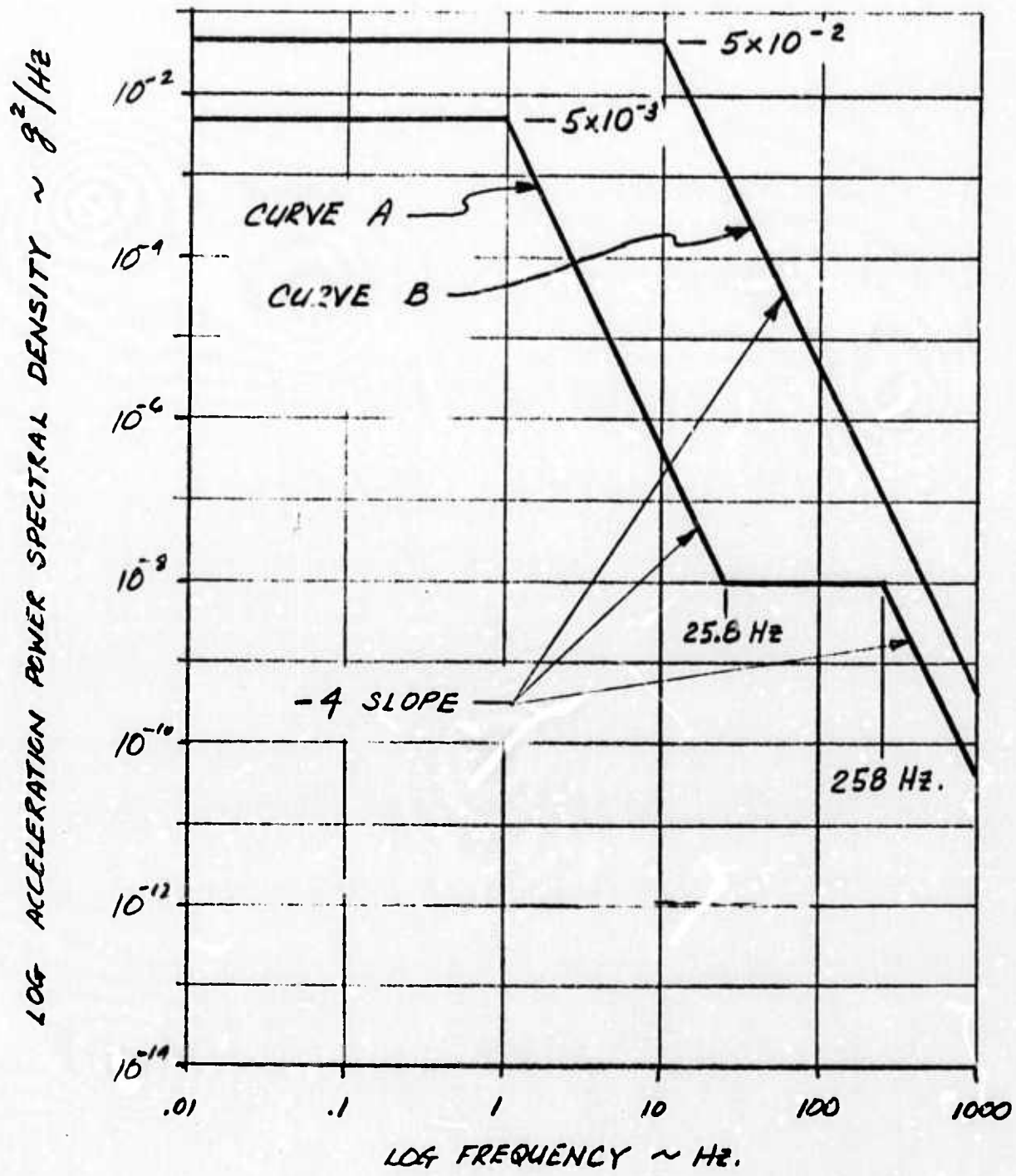


FIGURE 3.5.3

Page 13 of 14

Table 3.5. Environmental Conditions

Environment	Operating	Non-Operating
	<p>3.5.1 Operating Performance Condition: (Rotating at specified spin speed and energized, if applicable)</p> <p>Ambient air and structure temperature surrounding the bearing shall be controlled to a set point of $1400 \pm 10^{\circ}\text{F}$ within $\pm 0.5^{\circ}\text{F}$. If a gas bearing is used, the supply gas temperature will be maintained at $40^{\circ}\text{F} + \underline{\hspace{1cm}}$ F. Vendor to specify set point and limit.</p>	<p>3.5.2 Operating Standby Condition: (Rotating 0 to 5,000 rpm, and energized, if applicable)</p> <p>Ambient air and structure temperature between 40°F to 130°F. If a gas bearing is used, the supply gas temperature may vary from 40°F to 130°F.</p>
1. Temperature		
2. Humidity	<p>Ambient air 10% to 80% R. H. at temperatures specified above. If a gas bearing is used, the relative humidity of the supply gas may be controlled, if necessary. Vendor to specify.</p>	<p>Ambient air 10% to 95% R. H. at temperatures specified above. If a gas bearing is used, the supply gas humidity may vary from 10 to 95% at supply pressure whose temperature is between 40°F to 130°F.</p>
3. Pressure Altitude	0 - 10,000 ft.	40,000 ft max.
4. Mechanical Shock	Negligible	<p>Not to exceed 100 terminal sawtooth shocks at 50°G for 11 ms in any direction at temperatures and pressures specified above.</p>
5. Acceleration (D. C.)	Static acceleration not to exceed $\pm 1.1^{\circ}\text{G}$ in the vertical direction and $\pm 0.1^{\circ}\text{G}$ in the horizontal direction. Bearing spin-axis may be anywhere between a vertical to a horizontal orientation during simultaneous application of above specified acceleration levels.	<p>Static total vector acceleration not to exceed 3 g's in any direction with respect to the bearing spin axis.</p>
6. Vibration	Acceleration power spectral density not to exceed the levels shown in curve A of FIG. 3.5.3.	<p>Acceleration power spectral density not to exceed ten times the levels shown in curve B of FIG. 3.5.3.</p>

APPENDIX D

SPIN BEARING DESIGN SPECIFICATION FOR HUGHES' PROTOTYPE ROTATING GRAVITY GRADIOMETER

**(Prepared by Mechanical Technology Incorporated,
Latham, New York)**

SPIN BEARING
DESIGN SPECIFICATION
FOR
HUGHES
PROTOTYPE ROTATING GRAVITY GRADIOMETER

Date : January 5, 1973

MTI Number: 283A05

Approved By:

C. H. T. Pan
Dr. C.H.T. Pan
Director of Research Center

J. M. McGrew
J. M. McGrew
Manager, Advanced Technology Department

Richard Smith
R.L. Smith, Senior Project Engineer

Prepared Under Hughes Subcontract 01-180871-4

MECHANICAL TECHNOLOGY INCORPORATED
968 Albany-Shaker Road
Latham, New York 12110

TABLE OF CONTENTS

	<u>Page</u>
1.0 INTRODUCTION	4
1.1 Gravity Gradiometer Description	4
1.2 Design Criteria	4
1.2.1 Thermal Stability	6
1.2.2 Rotor Windage Power Loss	6
1.2.3 Materials of Construction	6
1.2.3.1 Bearing Component Magnetic Permeability	6
1.2.3.2 Isotropic Creep Stability	6
1.2.3.3 Composite Construction	7
1.2.4 Rotor Balancing	7
1.3 Revised System Requirements	7
1.4 Applicable Documents	7
1.5 Quality Assurance Provisions	8
1.6 Conflicting Requirements	8
1.7 Bearing Operating Reliability	8
1.8 Sensor Operational Definitions	8
1.8.1 Operating Performance Condition	8
1.8.2 Operating Standby Condition	9
1.8.3 Non-Operating Deviation	9
2.0 PHYSICAL DESIGN PARAMETERS OF GRADIOMETER ROTOR BEARINGS	10
2.1 Physical Parameter of Rotor	10
2.2 Environmental Conditions of Bearing Exposure	10
3.0 BEARING OPERATING REQUIREMENTS	13
3.1 Second Harmonic Torque Ripple	13
3.1.1 Deterministic Torque Oscillation	13
3.1.2 Random Torque Variations	13
3.2 Torque Oscillations at Other Frequencies	14
3.3 Bearing Torque	14
3.4 Spin Bearing Load Capacity	14
3.5 Spin Bearing Compliance	14
3.6 Bearing-Induced Vibration	14
3.6.1 Bearing-Induced Translational Acceleration	15

TABLE OF CONTENTS (Continued)

	<u>Page</u>
3.6.2 Bearing-Induced Angular Motion Normal to Spin Axis _____	16
3.6.2.1 Induced Angular Rate _____	16
3.6.2.2 Induced Angular Acceleration _____	17
3.7 Spin-Axis Alignment Reference _____	18
4.0 BEARING DESIGN REQUIREMENTS _____	19
4.1 Bearing Component Construction _____	19
4.1.1 Material _____	19
4.1.2 Component Sizing _____	19
4.1.2.1 Radial Sizing _____	23
4.1.2.2 Total Indicated Spherical Runout _____	23
4.1.2.3 Second Harmonic Runout _____	23
4.1.2.4 Third Harmonic Runout _____	23
4.1.2.5 Marking of Runout Peaks _____	23
4.1.2.6 Stability of Sphericities _____	23
4.1.3 Assembled Clearances _____	24
4.1.4 Spiral Grooves _____	24
4.1.5 Mating Interface Finish _____	24
4.1.6 Bearing Lubricant _____	24
4.1.7 Bearing Inspection _____	25
4.1.8 Design Drawings _____	25

SPIN BEARING DESIGN SPECIFICATION FOR
HUGHES PROTOTYPE ROTATING GRAVITY GRADIOMETER

1.0 INTRODUCTION

This specification includes operating as well as physical characteristics of a set of bearings intended for use in a moving base rotating gravity gradiometer system. The rotor bearings are one element of a sensing system designed to measure gravitational field gradients from a moving vehicle. The requirements associated with the sensor necessitate that the bearings perform their spin function with extreme precision and reliability.

1.1 Gravity Gradiometer Description

The latest conceptual cross sectional sketch of the intended gravity gradiometer rotor and bearings is shown in Figure 1. The basic gravity gradient sensor consists of a crossed pair of mass quadrupoles coupled by a torsional spring and enclosed in a sealed, evacuated case. This case is then rotated at a spin frequency which is adjusted to precisely one-half the inertia-spring resonant frequency of the coupled mass quadrupoles. The spinning system is enclosed within a nominally spherical shell supported at each end by a bearing complement.

1.2 Design Criteria

The final bearing design discussed in the paragraph 4.0 was based upon the procurement requirements generated by the Hughes Research Laboratory (listed for reference in the applicable documents of paragraph 1.4). The set of bearing operation requirements is complex and will necessitate control of the allowed range of physical operating parameters which must be maintained for proper operation. The allowed range of variation in the design parameters for the most critical bearing operating requirements are reviewed in paragraph 4.0 related to the bearing physical requirements. The bearing design concept was developed with certain basic assumptions related to final environmental parameters to which it will be subjected which could not explicitly be defined at this time. The most pertinent of these parameters are listed in the succeeding subparagraphs below. If the assumed design criteria are shown at a future

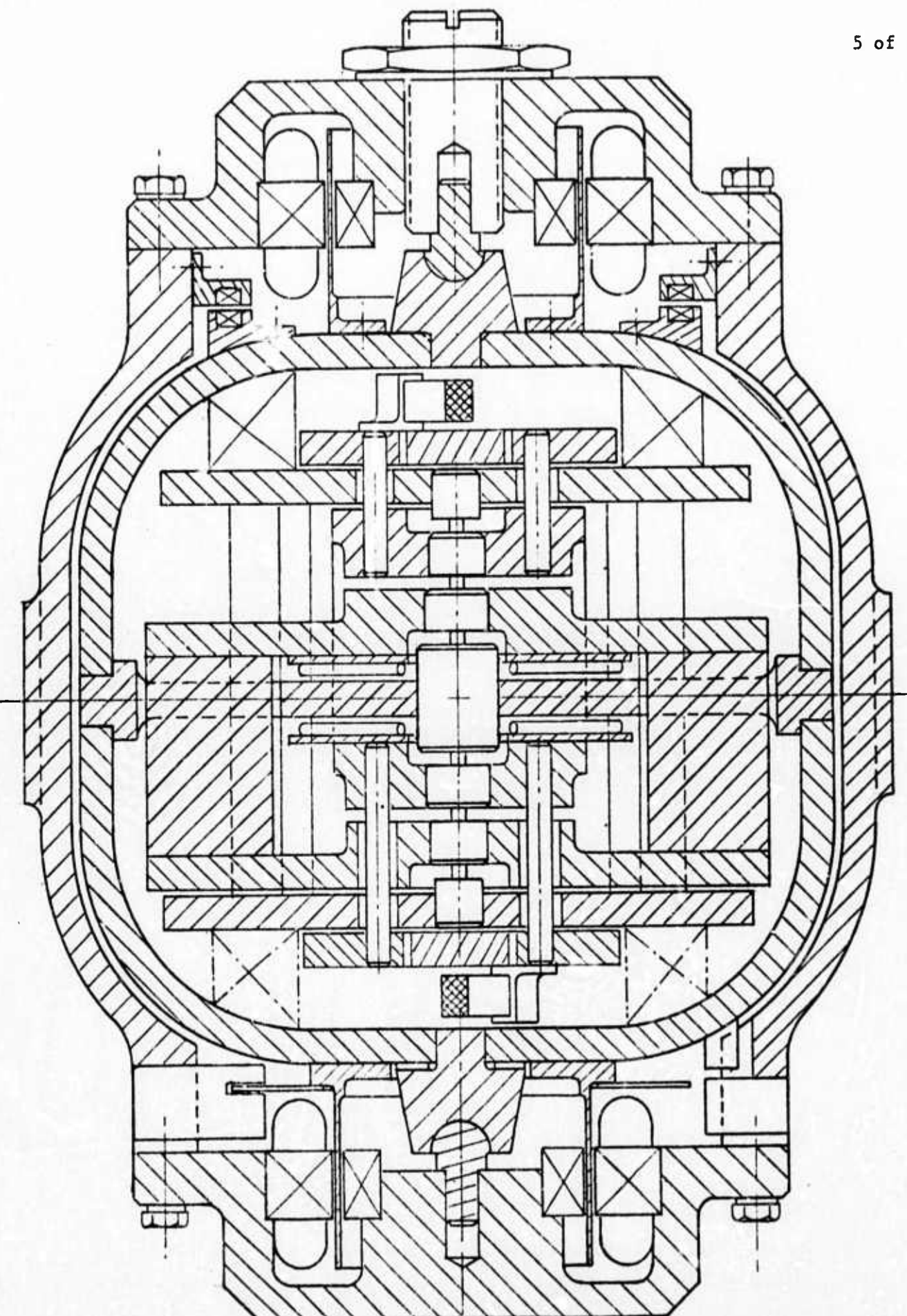


Fig. 1 Conceptual Sketch of Gravity Gradiometer Rotor and Bearings

date to be a limiting factor in the sensing aspects of the sensor design, then the bearing design would have to be re-examined for operability under the new, more extreme environmental conditions.

1.2.1 Thermal Stability

The dependent thermal gradients which could be imposed upon or generated by the bearings are not considered to be a limiting factor to the design. No thermal mappings or transient analysis was conducted prior to or during this design phase which could be used to indicate a cyclic or time dependent bearing operational problem caused by temperature variations in the gravity gradiometer system. Typical limiting variations of $\pm .032^{\circ}\text{F}$ for the operating oil temperature range of 140°F were calculated to be required for successful operation of the bearing design. It was assumed that the system surrounding the bearings could be maintained within the limits dictated by the oil chosen to lubricate the bearing system.

1.2.2 Rotor Windage Loss

Although the cavity surrounding the rotor is to be filled with air or helium, it was assumed that the windage drag of all rotor components was less than .039 oz-in and constant at the design spin frequency.

1.2.3 Materials of Construction

It was assumed that a suitable material for construction of the final concept could be found when required.

1.2.3.1 Bearing Components Magnetic Permeability

The bearing components, coatings, and fasteners will have a magnetic permeability less than 1.010 cgs units. This limit is generated on the basis of cyclic torques which are caused by the rotation of the bearing in the earth's magnetic field.

1.2.3.2 Isotropic Creep Stability

The material of bearing construction will not creep anisotropically during any temperature stabilized ten-hour operation period over

the 10,000-hour life of the bearings. The limits of differential and absolute growth along any three mutually orthogonal axes of the bearing components is given by the allowed maximum asphericities and size limits listed in paragraph 4.1.2.

1.2.3.3 Composite Construction

Aluminum 2024-T4 HARDCOATED was the assumed material choice. Present day state-of-the-art manufacturing techniques may dictate for the "optical polish" and tolerances required by this application an alternate material or combination of materials. An alternate choice would require an assessment of the ability to construct the rotor from two or more materials with different rates of thermal expansion.

1.2.4 Rotor Balancing

The design assumption that sufficient rotor mass balance could be maintained from within the rotor which would impose no excessive unstable whirl motion onto the rotor bearings. Center of rotor mass relative to spin axis shall be within 1 microinch and not be affected by shock and vibration loading.

1.3 Revised System Requirements

Every effort was made to provide a bearing design which was consistent with state-of-the-art techniques as well as the bearing operating requirements produced by Hughes Research Laboratory as this design work was being completed. New advances both in bearing and gravity gradiometer technology may occur in the future which could alter completely the bearing design approach taken at this time.

1.4 Applicable Documents

The following pertinent documents were used in making the design choices discussed in this specification:

- (a) Hughes: Procurement Specification for Spin Bearings for Hughes Prototype Rotating Gravity Gradiometer, Revision A, No. AR-772 dated August 1, 1972.
- (b) Hughes: Telex message from L.A. Hornbeek to John G. Wichser of MTI dated October 5, 1972.

- (c) MTI: Technical Report 72TR59 dated October 27, 1972.
- (d) MTI: Design Drawing Series No. 283.
- (e) Hughes: Letter from David Rouse to R.L. Smith of MTI dated December 15, 1972.

1.5 Quality Assurance Provisions

Assurance that the sensor spin bearings meet the performance requirements set forth in paragraph 3.0 will be provided by: (a) the Vendors Quality Control Program, (b) an adequate Testing Program, and (c) a Reliability Verification Program.

1.6 Conflicting Requirements

Any conflicting requirements arising between this specification and any document or drawings listed herein shall be referred in writing to the Hughes Research Laboratories (HRL) for interpretation and clarification.

1.7 Bearing Operating Reliability

The sensor spin bearings shall be capable of meeting the performance requirements set forth herein when supporting the rotor mass and moment of inertia load specified and rotating at the spin speed specified while the sensor is operating in the performance condition after thermal stabilization. In addition, the spin bearing shall meet these performance requirements throughout a 10,000 hour operating life with a minimum of 500 rotor start-stop cycles. The bearing shall meet the performance requirements at any time during a minimum one-year period following assembly into the sensor. The spin bearing shall be capable of meeting the performance requirements following exposure to the environmental and design conditions set forth in paragraph 2.0.

1.8 Sensor Operational Definitions

Three operational states of performance under different environmental conditions are listed here for reference.

1.8.1 Operating Performance Condition

This condition represents the most extreme environments under which the

bearing is required to operate and meet the specified performance of paragraph 3.0. When subjected to the environments of this condition, the bearing will be energized (if applicable), thermally stabilized, and rotating at the specified spin speed.

1.8.2 Operating Standby Condition

This condition represents the most extreme environments under which the bearing is required to operate and survive without damage. When subjected to the environments of this condition, the sensor supported on the bearings will be energized (if applicable) and may be stationary or rotating at frequencies up to 5,000 rpm.

1.8.3 Non-Operating Condition

This condition represents the most extreme environments to which the bearing may be subjected while in a non-operating state. It must survive these environments without damage. The non-operating state is defined as not rotating and not energized (if applicable). A rotation locking device may be employed if necessary.

1.9 Request for Deviation

Any deviation from the requirements specified herein shall be considered a deviation and shall not be allowed except by written authorization from Hughes Research Laboratory and Mechanical Technology Incorporated.

2.0 PHYSICAL DESIGN PARAMETERS OF GRADIOMETER ROTOR BEARINGS

The design of the rotor bearings was based upon several physical and environmental conditions which are here listed as stated at the time of the design.

2.1 Physical Parameters of Rotor

The spin bearing selection was based upon the following:

Rotor Mass	7,000 gms
Rotor Polar Inertia	2.5×10^5 gm-cm ²
Rotor Transverse Inertia	2.0×10^5 gm-cm ²
Rotor Shell Diameter	15.5 cm
Stator Shell Diameter	18 cm
Rotor Spin Speed	1050 rpm
Rotor Windage Power Loss	.03 watts (max.)

2.2 Environmental Conditions of Bearing Exposure

The bearing and rotor will be subjected to various environmental conditions which will be limited as explained in the succeeding subparagraphs.

2.2.1 Temperature Exposure

Under the operating performance condition the structure surrounding the bearings shall be controlled within $\pm .03^{\circ}\text{F}$ of a fixed operating temperature of 140°F . In the operating standby condition, the structure may be between 40°F and 130°F . If in the non-operating condition, the expected temperature exposures may be from -30°F to $+200^{\circ}\text{F}$.

2.2.2 Humidity

Under the operating performance condition, the bearings may be exposed to relative humidities ranging from 10 percent to 80 percent. Maximum variation of humidity under all other conditions is to be held within 10 percent to 95 percent.

2.2.3 Pressure

Bearing ambient pressure shall be atmospheric pressures which occur between sea level and 10,000 feet altitude during the operating performance condition. Under all other conditions, the pressure range may be from

sea level atmospheric to 40,000 feet altitude.

2.2.4 Mechanical Shock

Negligible under the operating performance condition. Not to exceed 100 terminal sawtooth shocks of 50 g for 11 milliseconds in any direction for all other conditions.

2.2.5 Acceleration (D.C.)

During the operating performance condition, the static acceleration is not to exceed ± 1.1 g in the vertical direction and ± 0.1 g in the horizontal direction. The bearing spin axis may be anywhere between a vertical to a horizontal orientation during simultaneous application of above specified acceleration levels.

During the operating standby condition, the static total vector acceleration is not to exceed 3 g's in any direction with respect to the bearing spin axis.

During the non-operating condition, the static total vector acceleration is not to exceed 20 g's in any direction with respect to the bearing spin axis.

Except during the operating performance condition, the period over which any D.C. acceleration will be applied shall be less than 10 minutes.

2.2.6 Vibration

During the operating performance condition, the bearings will not experience an acceleration power spectral density greater than the levels shown in Curve A of Figure 2. During all other conditions, the exposed acceleration power spectral density shall not exceed the levels shown in curve B of Figure 2.

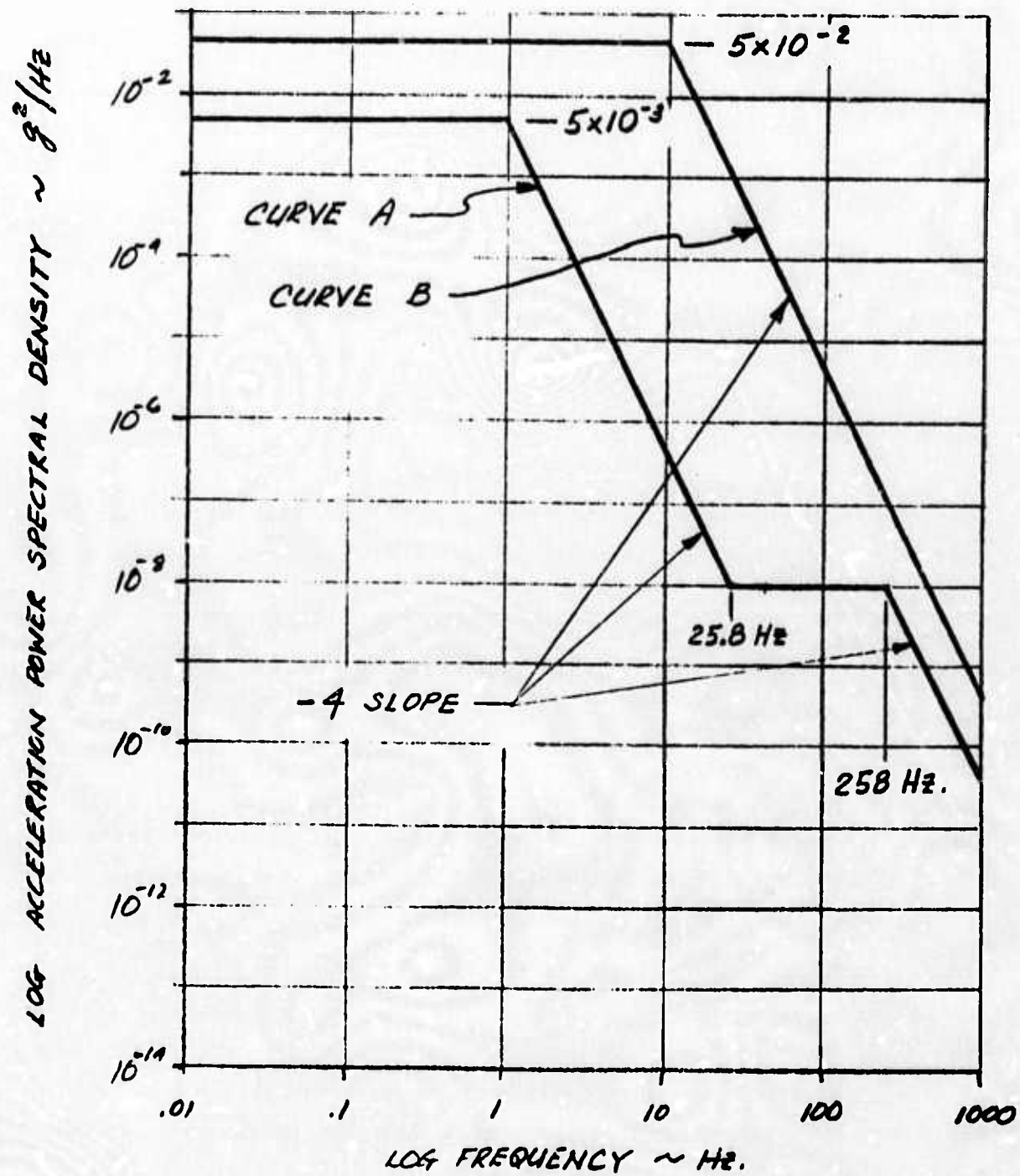


Fig. 2 Power Spectral Density Plot

3.0 BEARING OPERATING REQUIREMENTS

The gravity gradient sensor requirements necessitate certain bearing operational characteristics which must be maintained to provide a signal which may be discerned from possible noise elements. The pertinent requirements are reviewed in depth in the paragraph.

3.1 Second Harmonic Torque Ripple

Torque oscillations about the spin axis in a narrow frequency band centered at twice the spin frequency ($2\omega_s$) may cause significant errors in the sensor output. To the extent that these torque oscillations are deterministic, they can be compensated; however, the random portion of these torque oscillations cannot. The deterministic portion is made up of oscillation occurring at exactly $2\omega_s$ and whose phase is precisely fixed relative to the mechanical phase of the spin bearing. It is required that the magnitude of the deterministic torque oscillation not exceed the values specified in paragraph 3.1.1. Random torque variations are characterized by variations in both amplitude and phase relative to the above defined deterministic torque oscillation. As a consequence, the allowable random torque variations must be specified in terms of the magnitude of two mutually orthogonal components. It is required that the standard deviation of the magnitude of either of these orthogonal components within a narrow frequency band centered at $2\omega_s$ not exceed the value specified in paragraph 3.1.2.

3.1.1 Deterministic Torque Oscillation

The deterministic value of the torque oscillation will be defined as the average value over a ten-hour operation following thermal stabilization. This value will not exceed 1,000 dyne-cm. In addition, the mean value of the deterministic torque oscillation, when averaged over the first hour of operation following thermal stabilization, will not differ from the ten-hour mean value by more than 50 dyne-cm.

3.1.2 Random Torque Variation

The standard deviation of either orthogonal component of the random torque variation within a 0.1 Hz wide frequency band centered at $2\omega_s$ will not exceed 50 dyne-cm over a ten-hour operation following thermal stabilization.

3.2 Torque Oscillations at Other Frequencies

The root-mean-square value of spin-axis torque oscillations within any 0.1 Hz wide frequency band outside the band specified in paragraph 3.1.2 will not exceed 500 dyne-cm.

3.3 Bearing Torque

- Mean running torque will not exceed 5×10^4 dyne-cm when the mean applied load is 15 pounds.
- Running torque sensitivity to variation in applied load will not exceed 5.0×10^{-4} in-lb/lb along an orthogonal or parallel axis relative to the spin axis of the bearings when the mean applied load is 15 pounds.
- Bearing breakaway torque will not exceed 7 in-oz while starting with a mean load of 15 pounds and at an operating temperature of 140°F.
- Bearing running torque under operating performance conditions will not exceed .7 in-oz torque.

3.4 Operational Bearing Load Capacities

- Nominal load-carrying capacity will be 15 pounds.
- Axial and radial load capacities will not permit bearing touchdown when loaded as stated under paragraph 2.0 at speeds not less than 1,050 rpm. At lower speeds, the maximum acceleration load without causing bearing touchdown will be not more than .002857 g/rpm.
- A cross axis torsional loading equivalent to .1 g or less will not permit bearing touchdown.

3.5 Spin Bearing Compliance

- Axial and radial compliances will not exceed 5×10^{-11} cm/dyne.
- Torsional compliance will not exceed 10^{-12} rad/dyne-cm.

3.6 Bearing-Induced Vibration

Oscillatory forces or torques generated within the spin bearing pair which

produce rotor accelerations with respect to the stator can cause significant errors in the sensor output. To the extent that these accelerations are deterministic, the sensor output errors can be compensated; however, the sensor output errors due to the random portion of these accelerations cannot be compensated. In the following subparagraphs limits are specified for both deterministic and random portions of the bearing-induced translational and angular vibrations.

3.6.1 Bearing-Induced Translational Acceleration

The translational acceleration of the rotor center of mass (herein defined to be located midway between the two mounting planes of the bearing rotor-sensor interface) will be limited as follows.

3.6.1.1. The peak value of the $2\omega_s$ frequency component of the radial acceleration in a rotor-fixed frame along any radial direction fixed in the rotor will not exceed 10^{-4} g.

3.6.1.2. For any given radial direction, the average over the first hour of operation following thermal stabilization of the peak value of the $2\omega_s$ frequency component of radial acceleration in a rotor-fixed frame will not differ from the ten-hour average by more than 10^{-5} g. This requirement holds for each and every radial direction.

3.6.1.3. For any given rotor-fixed radial direction, random variations of this given radial acceleration may be characterized by time variations of both its amplitude and phase, or alternatively, by time variations of the magnitude of two mutually orthogonal components (e.g., "in phase" and "quadrature phase"). Thus, the allowable random portion of radial acceleration for any given rotor-fixed radial direction may be specified in terms of the magnitude variations of its two mutually orthogonal components. It is required that the standard deviation of either of these orthogonal components within a 0.05 Hz wide frequency band centered at $2\omega_s$ not exceed 10^{-5} g. Since the angular orientation of the sensor's acceleration-sensitive axis is unknown, the above requirement will apply for each and every rotor-fixed radial direction.

3.6.1.4. The total mean-square translational acceleration of the rotor in any (radial or axial) direction will not exceed 10^{-6} g^2 . The mean-square acceleration is defined as the value of the integrated acceleration power spectrum over all frequencies.

3.6.1.5. The power spectral density of translational acceleration of the rotor in any (axial or radial) direction will not exceed $2 \times 10^{-9} \text{ g}^2/\text{Hz}$ over the frequency range 0 to 1.0 Hz.

3.6.2 Bearing-Induced Angular Motion Normal to Spin Axis

Oscillatory angular motion about axes normal to the sensor's spin axis can excite two types of sensor output error. In one type, known as rotational field error, error is produced which is a nonlinear function of angular rate components normal to the sensor spin axis. In the second type, error is produced which is proportional to the angular acceleration over the specific narrow-band frequencies harmonically related to the spin frequency. Both types of errors can have both deterministic and random portions. Allowable limits of the applicable deterministic and random functions are specified in the following subparagraphs.

3.6.2.1 Induced Angular Rate

For the purpose of specifying limits on the induced angular rate error, the following parameters are defined:

$\bar{\omega} \triangleq$ Instantaneous angular rate vector of the sensor rotor relative to the stator.

$x, y, z \triangleq$ Orthogonal coordinate frame fixed in the stator with z along the average spin axis direction and x and y normal to z .

$\omega_x, \omega_y \triangleq$ Instantaneous angular rate components of the rotor with respect to the stator expressed in the x, y frame.

$\omega'_x, \omega'_y \triangleq$ Apparent rates of (ω_x, ω_y) relative to the rotor.

$$E \triangleq 2\omega'_x \omega'_y$$

$$\epsilon_C(t) \triangleq \frac{1}{T} \int_t^{T+t} 2E \cos 2\omega_s \tau d\tau$$

$$\epsilon_S(t) \triangleq \frac{1}{T} \int_t^{T+t} 2E \sin 2\omega_s \tau d\tau$$

$$T = 20 \text{ secs}$$

The induced angular rate error will be limited by the following criteria applied to either ϵ_C or ϵ_S . The average value of ϵ_C over the first hour of operation following thermal stabilization will not exceed $\pm 0.4 \times 10^{-8}$ (rad/sec)². In addition, the difference between the first one-hour average and the average of ϵ_C over the first ten-hour period will not exceed 0.4×10^{-10} (rad/sec)². The standard deviation of ϵ_C over the ten-hour period will not exceed 0.4×10^{-10} (rad/sec)². This same criteria applies similarly to ϵ_S .

3.6.2.2 Induced Angular Acceleration

3.6.2.2.1. The peak value of $2\omega_s$ frequency component of transverse angular acceleration in a rotor-fixed frame about any radial direction fixed in the rotor will not exceed 10^{-2} rad/sec².

3.6.2.2.2. For any given radial direction, the average over the first hour of operation following thermal stabilization of the peak value of the $2\omega_s$ frequency component of the angular acceleration about the given rotor-fixed radial direction will not differ from the ten-hour average by more than 10^{-3} rad/sec². This requirement holds for each and every radial direction.

3.6.2.2.3. For any given rotor-fixed radial direction, random variations of angular acceleration about this given radial direction may be characterized by time variations of both its amplitude and phase or, alternatively, by time variations of the magnitude of two, mutually orthogonal components (e.g., "in phase" and "quadrature phase"). Thus, the allowable random portion of angular acceleration

about any given rotor-fixed radial direction may be specified in terms of the magnitude variations of its two mutually orthogonal components. It is required that the standard deviation of either of these orthogonal components within an 0.05 Hz wide frequency band centered at $2\omega_s$ not exceed 10^{-3} rad/sec². Since the radial orientation of the sensor's angular acceleration-sensitive axis is unknown, the above requirement will apply for each and every rotor-fixed radial direction.

3.6.2.2.4. The power spectral density of angular acceleration of the rotor about any axis normal to the spin axis will not exceed 10^{-4} (rad/sec²)²/Hz, excluding all discrete spectra components.

3.7 Spin-Axis Alignment Reference

A spin-axis alignment reference will be provided which permits location of the spin reference axis to an accuracy of one mrad.

4.0 BEARING DESIGN REQUIREMENTS

The desired operational requirements of the gravity gradiometer as described above depend upon the acquisition of bearing components finished and assembled as described below. A set of proposed bearings with the properly designed characteristic are described in MTI design drawing series 283, as well as in this specification.

It should be evident from the content of this specification that bearings produced for this application must be inspected with metrology techniques at the extrapolated limits of any present day state-of-the-art fabrication capabilities. Bearing parts fabricated to date with tolerance limits close to those specified herein have been made only from coated beryllium. In addition, any bearings which are produced with the care and control required to insure that the tolerances as specified herein are achieved will, when assembled and operated, produce sensor noise errors of two types. These error signals will be deterministic (those which are repetitive and discriminable) and/or non-deterministic (random in nature). Some of the requirements may be beyond present day inspection techniques of quality assurance which can provide the desired minimization of the non-deterministic error signals present in an assembled operating sensor. A minimization of the error signals produced by the bearing, in light of these critical construction and assembly problems, can only be obtained through superior engineering practices related to the sensor bearing design, construction, assembly, and check***

4.1 Bearing Component Construction

4.1.1 Material

The bearing material of construction must be compatible with requirements specified herein. Beryllium or aluminum 2024-T4 hardcoated are the recommended choices. If beryllium is the final selection choice, it may have to be coated with an appropriate substance to provide the polish needed in the present application.

4.1.2 Component Sizing

Tables 1 and 2 provide a list of nominal bearing characteristics for references. Critical rotor bearing component characteristics are provided in Table 3. All tolerances specified are to be assured by inspection at

TABLE 1
NOMINAL BEARING PHYSICAL CHARACTERISTICS

Material	:	Aluminum 2024-T4 hardcoated
Radius	:	.2128 at 70°F
Clearance	:	170 microinches (radial)
Allowed Asphericity	:	TIR 1.5 microinches maximum (radial)
Number of Spiral Grooves	:	19
Groove Depth	:	350 microinches
Surface Finish	:	Less than .2 microinches rms
Equivalent Surface Hardness	:	60 to 70 Rockwell C range
Hard Coat Thickness	:	0.5 - 2 mils finished
Lubricant Volume Required		
Bearing Clearance	:	4.8×10^{-5} in ³
Reservoir	:	8.0×10^{-4} in ³
Amount Present at Bearing Edge:	:	4.8×10^{-4} in ³
Bearing Reservoir Volume	:	.016 in ³
Spin Axis Alignment Reference	:	Bore of Dia "A" or "B" (see Figure 14)
Electrical Insulation		
Male to Female	:	> 5 meg ohm
Female to Rotor	:	None
Male to Stator	:	None
Assumed Ambient Bearing Pressure	:	14.7 psi
Assumed Gas in Stator Housing	:	Air at 15 psi

TABLE 2
NOMINAL BEARING OPERATING CHARACTERISTICS

Design Spin Frequency	:	1,050 rpm
Design Carrying Load	:	15 \pm 1.5 pounds per pair
Stiffness		
Axial	:	3.0×10^5 lbs/in
Radial	:	2.11×10^5 lbs/in
Rotational	:	1.9×10^6 in-lbs/rad
Running Eccentricity		
Axial	:	.35
Radial	:	.50
Torque at 1,050 rpm		
at 140°F	:	.57 in-oz (for pair)
Starting Torque		
at 140°F	:	6.5 in-oz (for pair)
Estimated Rotor Windage Torque	:	.038 in-oz
Torque/Load Sensitivity		
Axial	:	1.4×10^{-4} in-lbs/lb
Radial	:	5.0×10^{-4} in-lbs/lb
Deterministic Torque Ripple	:	Less than 500 dyne-cm
Power Loss at 1,050 rpm	:	.44 watts (for pair)
Critical Design Restraint	:	Bearing load

TABLE 3
SPECIFICATION TOLERANCES FOR ROTOR BEARING

<u>Reference Paragraph</u>	<u>Physical Variable</u>	<u>Data Input</u>	<u>Freq. Range</u>	<u>Limit</u>	<u>Critical Tolerance ** of Rotor Bearing</u>
3.6.1					
3.6.1.1	Translational Acceleration Radial	Peak	35 Hz	10^{-4} g	3rd harmonic run-out < 0.25×10^{-6} in.
3.6.1.2	Radial	Ave. (1-hr) - Ave (10-hr)	35 Hz	10^{-5} g	
3.6.1.3	Radial	Std. Dev. (10-hr)	35 ± 0.05 Hz	10^{-5} g	
3.6.1.4	Radial or Axial	Mean Square	All	10^{-6} g ²	2nd harmonic run-out < 1.5×10^{-6} in. rms (excl. 2nd & 3rd harmonics) run-out < 0.25×10^{-6} in.
3.6.1.5	Radial or Axial	Power Spectral Density	0 - 1.0 Hz	2×10^{-9} g ² /Hz	
3.6.2.1*	ϵ_c or ϵ_s	Ave. (1-hr) of peak	35 Hz	$0.4 \times 10^{-8} (r/s)^2$	2nd harmonic run-out < 1.5×10^{-6} in.
3.6.2.1		1 Ave (1-hr)-Ave (10-hr)	35 Hz	$0.4 \times 10^{-10} (r/s)^2$	
		Std. Dev. (10-hr)	35 ± 0.05 Hz	$0.4 \times 10^{-10} (r/s)^2$	
3.6.2.2*					
3.6.2.2.1	Angular Acceleration	Peak	35 Hz	10^{-2} r/s ²	3rd harmonic run-out < 0.25×10^{-6} in.
3.6.2.2.2		1 Ave (1-hr)-Ave (10-hr)	35 Hz	10^{-3} r/s ²	
3.6.2.2.3		Std. Dev. (10-hr.)	35 ± 0.05 Hz	10^{-3} r/s ²	
3.6.2.2.4		Power Spectral Density		$10^{-4} (r/s)^2 / r_z^{***}$	

* Bearing span equal or longer than 6 inches.

** Bearing stiffness under 1-g load must be greater than 200,000 lb/in per bearing pair

*** Exclusive of all discrete spectra components.

the intended bearing operating temperature. In addition, a minimum of three widely separated orbits about the bearing mating surfaces will be used to demonstrate compliance with the required tolerances.

4.1.2.1 Radial Sizing

The absolute dimensions of the bearing radius will be within 100 microinches of the nominal radial dimensions of .2130 inches at 140°F. Male and female bearing components will be match mated to comply with clearance tolerances required at the operating temperatures.

4.1.2.2 Total Indicated Spherical Runout

Total indicated spherical runout will not exceed a root-mean-square value of .25 microinches, exclusive of the second and third harmonics of the sphericity. Total indicated runout will not exceed 1.5 microinches maximum.

4.1.2.3 Second Harmonic Runout of Rotor Bearing

Second harmonic runout will not exceed 1.5 microinches total indicated spherical runout about any orbit on the bearing mating surface about the bearing spin axis.

4.1.2.4 Third Harmonic Runout of Rotor Bearing

Third harmonic runout will not exceed .25 microinches total indicated spherical runout about any orbit on the bearing mating surface about the bearing spin axis.

4.1.2.5 Marking of Runout Peaks

The location of the angular positions of rotor aspherical bearing peaks of both second and third harmonics about the spin axis will be made within \pm 2 degrees.

4.1.2.6 Stability of Sphericities

Assembly of bearing parts or related components will not be overstressed in any way to prohibit tolerances being maintained in the

assembled bearings. The tolerances given are to be met in the assembled condition. Long-term anisotropic material creep must be sufficiently low to maintain sphericities stated over the operating life temperature cycling to be experienced by the sensor.

4.1.3 Assembled Clearances

The nominal bearing radial clearance of 170 microinches will be maintained within + 0 microinches and - 10 microinches during the operating performance condition of the sensor. Precise control of the axial gap is critical to maintain spherical bearing radial stiffness. If axial clearance tolerances cannot be maintained, a journal-thrust bearing is recommended.

4.1.4 Spiral Grooves

The number of spiral grooves present on the stationary half of the bearing components will be 19. The depth of the spiral grooves will be held within 15 microinches of the nominal specified depth of 350 microinches over the central 90 percent extent of the length and width of the grooves. The grooves will be generated in the usual log normal spiral fashion.

4.1.5 Mating Interface Finish

The land portions of the bearing components will have an "optical polished" surface finish. The equivalent surface roughness of these land areas will not exceed a value of .25 microinches rms. Surface hardness will be between 60 to 70 Rockwell C. The Rockwell test will not be made on components intended for operation.

4.1.6 Bearing Lubrication

The successful operation of the bearings upon assembly depends upon the lubricant for which the bearings were designed to be used. A highly refined oil (Apiezon C) with a viscosity of 31 cps and a viscosity temperature gradient of .56 cps/°F at the 140°F operating temperature was used for design purposes. The lubricant chosen for operation in the bearing specified must be within 10 percent of the absolute viscosity used to size the bearing at all operating temperatures or the bearing must be resized. In addition, the viscosity temperature gradient of any other

oil chosen for this application must not exceed that used for designing the bearings specified herein. Long-term retention of a fixed small quantity of lubricant in bearing gaps (10^4 hours) is not a proven practice and provisions for re-oiling the bearings during their operating life should be made.

4.1.7 Tolerance Inspection

Verification of compliance with the specified limits must be performed at the design operating temperatures of the bearings.

4.1.8 Bearing Design Drawings

Drawings of component parts of a nominal bearing design intended for use in the gravity gradiometer are contained in MTI design drawing series 283.